

**02 INFORMATION ABOUT PRINCIPAL INVESTIGATORS/PROJECT DIRECTORS(PI/PD) and
co-PRINCIPAL INVESTIGATORS/co-PROJECT DIRECTORS**

Submit only ONE copy of this form for each PI/PD and co-PI/PD identified on the proposal. The form(s) should be attached to the original proposal as specified in GPG Section II.B. Submission of this information is voluntary and is not a precondition of award. This information will not be disclosed to external peer reviewers. **DO NOT INCLUDE THIS FORM WITH ANY OF THE OTHER COPIES OF YOUR PROPOSAL AS THIS MAY COMPROMISE THE CONFIDENTIALITY OF THE INFORMATION.**

PI/PD Name: David T Sandwell

Gender: Male Female
Ethnicity: (Choose one response) Hispanic or Latino Not Hispanic or Latino

Race:
(Select one or more)
 American Indian or Alaska Native
 Asian
 Black or African American
 Native Hawaiian or Other Pacific Islander
 White

Disability Status:
(Select one or more)
 Hearing Impairment
 Visual Impairment
 Mobility/Orthopedic Impairment
 Other
 None

Citizenship: (Choose one) U.S. Citizen Permanent Resident Other non-U.S. Citizen

Check here if you do not wish to provide any or all of the above information (excluding PI/PD name):

REQUIRED: Check here if you are currently serving (or have previously served) as a PI, co-PI or PD on any federally funded project

Ethnicity Definition:

Hispanic or Latino. A person of Mexican, Puerto Rican, Cuban, South or Central American, or other Spanish culture or origin, regardless of race.

Race Definitions:

American Indian or Alaska Native. A person having origins in any of the original peoples of North and South America (including Central America), and who maintains tribal affiliation or community attachment.

Asian. A person having origins in any of the original peoples of the Far East, Southeast Asia, or the Indian subcontinent including, for example, Cambodia, China, India, Japan, Korea, Malaysia, Pakistan, the Philippine Islands, Thailand, and Vietnam.

Black or African American. A person having origins in any of the black racial groups of Africa.

Native Hawaiian or Other Pacific Islander. A person having origins in any of the original peoples of Hawaii, Guam, Samoa, or other Pacific Islands.

White. A person having origins in any of the original peoples of Europe, the Middle East, or North Africa.

WHY THIS INFORMATION IS BEING REQUESTED:

The Federal Government has a continuing commitment to monitor the operation of its review and award processes to identify and address any inequities based on gender, race, ethnicity, or disability of its proposed PIs/PDs. To gather information needed for this important task, the proposer should submit a single copy of this form for each identified PI/PD with each proposal. Submission of the requested information is voluntary and will not affect the organization's eligibility for an award. However, information not submitted will seriously undermine the statistical validity, and therefore the usefulness, of information received from others. Any individual not wishing to submit some or all the information should check the box provided for this purpose. (The exceptions are the PI/PD name and the information about prior Federal support, the last question above.)

Collection of this information is authorized by the NSF Act of 1950, as amended, 42 U.S.C. 1861, et seq. Demographic data allows NSF to gauge whether our programs and other opportunities in science and technology are fairly reaching and benefiting everyone regardless of demographic category; to ensure that those in under-represented groups have the same knowledge of and access to programs and other research and educational opportunities; and to assess involvement of international investigators in work supported by NSF. The information may be disclosed to government contractors, experts, volunteers and researchers to complete assigned work; and to other government agencies in order to coordinate and assess programs. The information may be added to the Reviewer file and used to select potential candidates to serve as peer reviewers or advisory committee members. See Systems of Records, NSF-50, "Principal Investigator/Proposal File and Associated Records", 63 Federal Register 267 (January 5, 1998), and NSF-51, "Reviewer/Proposal File and Associated Records", 63 Federal Register 268 (January 5, 1998).

List of Suggested Reviewers or Reviewers Not To Include (optional)

SUGGESTED REVIEWERS:

Not Listed

REVIEWERS NOT TO INCLUDE:

Not Listed

COVER SHEET FOR PROPOSAL TO THE NATIONAL SCIENCE FOUNDATION

PROGRAM ANNOUNCEMENT/SOLICITATION NO./CLOSING DATE/if not in response to a program announcement/solicitation enter NSF 08-1 PD 98-1620 02/15/08					FOR NSF USE ONLY	
FOR CONSIDERATION BY NSF ORGANIZATION UNIT(S) (Indicate the most specific unit known, i.e. program, division, etc.) OCE - MARINE GEOLOGY AND GEOPHYSICS					NSF PROPOSAL NUMBER	
DATE RECEIVED	NUMBER OF COPIES	DIVISION ASSIGNED	FUND CODE	DUNS# (Data Universal Numbering System)	FILE LOCATION	
				175104595		
EMPLOYER IDENTIFICATION NUMBER (EIN) OR TAXPAYER IDENTIFICATION NUMBER (TIN) 956006144		SHOW PREVIOUS AWARD NO. IF THIS IS <input type="checkbox"/> A RENEWAL <input checked="" type="checkbox"/> AN ACCOMPLISHMENT-BASED RENEWAL 0326707		IS THIS PROPOSAL BEING SUBMITTED TO ANOTHER FEDERAL AGENCY? YES <input type="checkbox"/> NO <input checked="" type="checkbox"/> IF YES, LIST ACRONYM(S)		
NAME OF ORGANIZATION TO WHICH AWARD SHOULD BE MADE University of California-San Diego Scripps Inst of Oceanography			ADDRESS OF AWARDEE ORGANIZATION, INCLUDING 9 DIGIT ZIP CODE University of California-San Diego Scripps Inst of Oceanography 9500 Gilman Drive La Jolla, CA. 92093			
AWARDEE ORGANIZATION CODE (IF KNOWN) 0013177010						
NAME OF PERFORMING ORGANIZATION, IF DIFFERENT FROM ABOVE			ADDRESS OF PERFORMING ORGANIZATION, IF DIFFERENT, INCLUDING 9 DIGIT ZIP CODE			
PERFORMING ORGANIZATION CODE (IF KNOWN)						
IS AWARDEE ORGANIZATION (Check All That Apply) (See GPG II.C For Definitions)		<input type="checkbox"/> SMALL BUSINESS <input type="checkbox"/> FOR-PROFIT ORGANIZATION		<input type="checkbox"/> MINORITY BUSINESS <input type="checkbox"/> WOMAN-OWNED BUSINESS		<input type="checkbox"/> IF THIS IS A PRELIMINARY PROPOSAL THEN CHECK HERE
TITLE OF PROPOSED PROJECT High-Resolution Gravity, Tomography, and Seafloor Roughness						
REQUESTED AMOUNT \$ 166,505		PROPOSED DURATION (1-60 MONTHS) 24 months		REQUESTED STARTING DATE 09/01/08		SHOW RELATED PRELIMINARY PROPOSAL NO. IF APPLICABLE
CHECK APPROPRIATE BOX(ES) IF THIS PROPOSAL INCLUDES ANY OF THE ITEMS LISTED BELOW						
<input type="checkbox"/> BEGINNING INVESTIGATOR (GPG I.G.2)			<input type="checkbox"/> HUMAN SUBJECTS (GPG II.D.6) Human Subjects Assurance Number _____			
<input type="checkbox"/> DISCLOSURE OF LOBBYING ACTIVITIES (GPG II.C)			Exemption Subsection _____ or IRB App. Date _____			
<input type="checkbox"/> PROPRIETARY & PRIVILEGED INFORMATION (GPG I.D, II.C.1.d)			<input type="checkbox"/> INTERNATIONAL COOPERATIVE ACTIVITIES: COUNTRY/COUNTRIES INVOLVED (GPG II.C.2.j)			
<input type="checkbox"/> HISTORIC PLACES (GPG II.C.2.j)			_____			
<input type="checkbox"/> SMALL GRANT FOR EXPLOR. RESEARCH (SGER) (GPG II.D.1)			<input type="checkbox"/> HIGH RESOLUTION GRAPHICS/OTHER GRAPHICS WHERE EXACT COLOR REPRESENTATION IS REQUIRED FOR PROPER INTERPRETATION (GPG I.G.1)			
<input type="checkbox"/> VERTEBRATE ANIMALS (GPG II.D.5) IACUC App. Date _____						
PHS Animal Welfare Assurance Number _____						
PI/PD DEPARTMENT Inst. of Geophysics & Planetary Physics			PI/PD POSTAL ADDRESS 8795 Biological Grade, Room 1104			
PI/PD FAX NUMBER 858-534-2902			La Jolla, CA 920930225 United States			
NAMES (TYPED)		High Degree	Yr of Degree	Telephone Number	Electronic Mail Address	
PI/PD NAME David T Sandwell		PhD	1980	858-534-7109	dsandwell@ucsd.edu	
CO-PI/PD						
CO-PI/PD						
CO-PI/PD						
CO-PI/PD						

CERTIFICATION PAGE

Certification for Authorized Organizational Representative or Individual Applicant:

By signing and submitting this proposal, the Authorized Organizational Representative or Individual Applicant is: (1) certifying that statements made herein are true and complete to the best of his/her knowledge; and (2) agreeing to accept the obligation to comply with NSF award terms and conditions if an award is made as a result of this application. Further, the applicant is hereby providing certifications regarding debarment and suspension, drug-free workplace, and lobbying activities (see below), nondiscrimination, and flood hazard insurance (when applicable) as set forth in the NSF Proposal & Award Policies & Procedures Guide, Part I: the Grant Proposal Guide (GPG) (NSF 08-1). Willful provision of false information in this application and its supporting documents or in reports required under an ensuing award is a criminal offense (U. S. Code, Title 18, Section 1001).

Conflict of Interest Certification

In addition, if the applicant institution employs more than fifty persons, by electronically signing the NSF Proposal Cover Sheet, the Authorized Organizational Representative of the applicant institution is certifying that the institution has implemented a written and enforced conflict of interest policy that is consistent with the provisions of the NSF Proposal & Award Policies & Procedures Guide, Part II, Award & Administration Guide (AAG) Chapter IV.A; that to the best of his/her knowledge, all financial disclosures required by that conflict of interest policy have been made; and that all identified conflicts of interest will have been satisfactorily managed, reduced or eliminated prior to the institution's expenditure of any funds under the award, in accordance with the institution's conflict of interest policy. Conflicts which cannot be satisfactorily managed, reduced or eliminated must be disclosed to NSF.

Drug Free Work Place Certification

By electronically signing the NSF Proposal Cover Sheet, the Authorized Organizational Representative or Individual Applicant is providing the Drug Free Work Place Certification contained in Exhibit II-3 of the Grant Proposal Guide.

Debarment and Suspension Certification

(If answer "yes", please provide explanation.)

Is the organization or its principals presently debarred, suspended, proposed for debarment, declared ineligible, or voluntarily excluded from covered transactions by any Federal department or agency?

Yes

No

By electronically signing the NSF Proposal Cover Sheet, the Authorized Organizational Representative or Individual Applicant is providing the Debarment and Suspension Certification contained in Exhibit II-4 of the Grant Proposal Guide.

Certification Regarding Lobbying

The following certification is required for an award of a Federal contract, grant, or cooperative agreement exceeding \$100,000 and for an award of a Federal loan or a commitment providing for the United States to insure or guarantee a loan exceeding \$150,000.

Certification for Contracts, Grants, Loans and Cooperative Agreements

The undersigned certifies, to the best of his or her knowledge and belief, that:

- (1) No federal appropriated funds have been paid or will be paid, by or on behalf of the undersigned, to any person for influencing or attempting to influence an officer or employee of any agency, a Member of Congress, an officer or employee of Congress, or an employee of a Member of Congress in connection with the awarding of any federal contract, the making of any Federal grant, the making of any Federal loan, the entering into of any cooperative agreement, and the extension, continuation, renewal, amendment, or modification of any Federal contract, grant, loan, or cooperative agreement.
- (2) If any funds other than Federal appropriated funds have been paid or will be paid to any person for influencing or attempting to influence an officer or employee of any agency, a Member of Congress, an officer or employee of Congress, or an employee of a Member of Congress in connection with this Federal contract, grant, loan, or cooperative agreement, the undersigned shall complete and submit Standard Form-LLL, "Disclosure of Lobbying Activities," in accordance with its instructions.
- (3) The undersigned shall require that the language of this certification be included in the award documents for all subawards at all tiers including subcontracts, subgrants, and contracts under grants, loans, and cooperative agreements and that all subrecipients shall certify and disclose accordingly.

This certification is a material representation of fact upon which reliance was placed when this transaction was made or entered into. Submission of this certification is a prerequisite for making or entering into this transaction imposed by section 1352, Title 31, U.S. Code. Any person who fails to file the required certification shall be subject to a civil penalty of not less than \$10,000 and not more than \$100,000 for each such failure.

Certification Regarding Nondiscrimination

By electronically signing the NSF Proposal Cover Sheet, the Authorized Organizational Representative is providing the Certification Regarding Nondiscrimination contained in Exhibit II-6 of the Grant Proposal Guide.

Certification Regarding Flood Hazard Insurance

Two sections of the National Flood Insurance Act of 1968 (42 USC §4012a and §4106) bar Federal agencies from giving financial assistance for acquisition or construction purposes in any area identified by the Federal Emergency Management Agency (FEMA) as having special flood hazards unless the:

- (1) community in which that area is located participates in the national flood insurance program; and
- (2) building (and any related equipment) is covered by adequate flood insurance.

By electronically signing the NSF Proposal Cover Sheet, the Authorized Organizational Representative or Individual Applicant located in FEMA-designated special flood hazard areas is certifying that adequate flood insurance has been or will be obtained in the following situations:

- (1) for NSF grants for the construction of a building or facility, regardless of the dollar amount of the grant; and
- (2) for other NSF Grants when more than \$25,000 has been budgeted in the proposal for repair, alteration or improvement (construction) of a building or facility.

AUTHORIZED ORGANIZATIONAL REPRESENTATIVE		SIGNATURE	DATE
NAME			
TELEPHONE NUMBER	ELECTRONIC MAIL ADDRESS	FAX NUMBER	

*SUBMISSION OF SOCIAL SECURITY NUMBERS IS VOLUNTARY AND WILL NOT AFFECT THE ORGANIZATION'S ELIGIBILITY FOR AN AWARD. HOWEVER, THEY ARE AN INTEGRAL PART OF THE INFORMATION SYSTEM AND ASSIST IN PROCESSING THE PROPOSAL. SSN SOLICITED UNDER NSF ACT OF 1950, AS AMENDED.

PROJECT SUMMARY

Intellectual Merit

Over the past 5 years we have been funded from agencies and corporations, including NSF, to construct global marine gravity and bathymetry grids at 1-minute resolution and to perform scientific investigations using these new data. We retracked the raw altimeter waveforms from 1 year of ERS-1 and 1.5 years of Geosat; these are the only satellite altimeter data with the dense track spacing needed for gravity field recovery. This analysis has resulted in a 40% improvement in the accuracy of the global marine gravity field, which has enabled new scientific investigations of transform faults, seamounts, seafloor fabric, and ocean mixing. In addition the improved gravity, combined with a new assembly of global depth soundings, is resulting in a new global bathymetry grid at 1 minute resolution. The funded gravity and bathymetry efforts are nearing completion but there are still significant tasks remaining. Here we propose to:

- Merge the 1-minute resolution marine gravity model with a soon-to-be-published global gravity model (EGM08) complete to spherical harmonic degree 2160 (5 minute resolution). This will result in a seamless gravity field across the shorelines.
- Construct a grid of uncertainty in the marine gravity based on altimeter data density, altimeter noise, and comparisons with shipboard gravity.
- Finish the construction of a matching bathymetry/topography grid with a focus on shallow ocean (< 1000 m) areas where new soundings are rapidly becoming available.
- Develop a 1-minute data source grid that provides the link to the original sounding data.
- Provide web access to all of these data products including: grids, cleaned soundings, and images/maps.
- Use the new data assemblies to investigate the effects of spreading rate on ridge segmentation, lithospheric strength, and crustal structure.

There are several reasons why this analysis should be completed now. First, the EGM08 gravity model is becoming available in April 2008 so this is an optimal time to merge this with the recently retracked altimetry data. Second, we have recently obtained global shallow water soundings that will improve the accuracy of bathymetry grids on continental margins. These improvements will mainly benefit scientific and petroleum exploration studies of continental margins. Finally, these data are foundational to many scientific studies supported by NSF so completing the upgrade of these products based on feedback from peers will benefit a wide range of ocean science investigations. Significant funding from NSF for these analyses will ensure the data are freely available to everyone.

Broader Impacts

Global bathymetric charts are used in many areas outside of the scientific community including: K-12 teaching of earth science and seafloor geography; undergraduate-level earth science and plate tectonics; law of the sea; mineral exploration; planning of fiber-optic cable routing and general interest by the public. This information is available on our web site <http://topex.ucsd.edu> in a variety of formats for expert, intermediate, and novice users.

TABLE OF CONTENTS

For font size and page formatting specifications, see GPG section II.C.

	Total No. of Pages	Page No.* (Optional)*
Cover Sheet for Proposal to the National Science Foundation		
Project Summary (not to exceed 1 page)	1	_____
Table of Contents	1	_____
Project Description (Including Results from Prior NSF Support) (not to exceed 15 pages) (Exceed only if allowed by a specific program announcement/solicitation or if approved in advance by the appropriate NSF Assistant Director or designee)	10	_____
References Cited	2	_____
Biographical Sketches (Not to exceed 2 pages each)	2	_____
Budget (Plus up to 3 pages of budget justification)	4	_____
Current and Pending Support	2	_____
Facilities, Equipment and Other Resources	1	_____
Special Information/Supplementary Documentation	0	_____
Appendix (List below.) (Include only if allowed by a specific program announcement/ solicitation or if approved in advance by the appropriate NSF Assistant Director or designee)	_____	_____
Appendix Items:		

*Proposers may select any numbering mechanism for the proposal. The entire proposal however, must be paginated. Complete both columns only if the proposal is numbered consecutively.

ACCOMPLISHMENT-BASED RENEWAL PROPOSAL

1. RESULTS FROM PRIOR NSF SUPPORT AND 6 REPRINTS

Over the past 5 years we have been funded by NSF, NASA, and ONR to construct global marine gravity and bathymetry grids at 1-minute resolution and to perform scientific investigations using these new data. The NASA funding (expired 9/06) was mainly for the development and implementation of a new algorithm to retrack the raw altimeter waveforms from the ERS-1 Spacecraft (European Space Agency). The NSF funding (expires 8/08) was mainly used to retrack the raw waveforms from the Geosat altimeter collected during its non-repeat orbit phase and to construct global grids. The ONR funds (expire 7/08) are currently being used to assemble and edit publicly available depth soundings for construction of a new global bathymetry/topography grid. As discussed below, this research resulted in a 40% improvement in the accuracy of the global marine gravity field. Similarly we are making a significant improvement in the accuracy of the global bathymetry, especially on the shallow continental margins, through assembly and editing of all types of existing sounding data. This is a group effort involving SIO (David Sandwell, JJ Becker, Seung-Hee Kim, and Breanna Binder), NOAA (Walter Smith, John Lillibrige, and Karen Marks), the National Geospatial-intelligence Agency (NG-ia) (Sarah Ingalls, Ron Trimmer, John VonRosenburg, and Gary Wallace), and the Naval Meteorology and Oceanography Command (METOC & NAVO) (James Braud, Jan Depner, David Fabre, and John Factor). The gravity grid construction is about 90% complete and the bathymetry grid assembly is about 60% complete. ONR may continue to fund the development of a bathymetric uncertainty grid to be used as an electronic cautionary overlay for Naval operations in poorly surveyed areas. That additional analysis will be performed in a secure environment at the NG-ia and SIO will not be directly involved. This proposal is to finish and fully document these developments as well as to perform some basic scientific investigations that can only be addressed using global bathymetry/topography and gravity. The proposed developments will benefit the MARGINS community because the new research is focused on the accuracy of the grids at the land-ocean boundary.

1.1 HIGH-RESOLUTION MARINE GRAVITY, SEAFLOOR TOPOGRAPHY, AND SEAFLOOR ROUGHNESS; SANDWELL; OCE0326707; \$367,567; 07/15/03-063008. The following publications were supported by this NSF grant. Under the guidelines of the Accomplishment-Based Renewal proposal, six of these reprints are included in the supplementary documents section also discussed briefly here.

- 1) Sandwell, D. T., and W.H.F. Smith, Retracking ERS-1 Altimeter Waveforms for Optimal Gravity Field Recovery, *Geophys. J. Int.*, 163, 79-89, 2005.

This paper on retracking of ERS-1 altimeter waveforms provides the theoretical foundation for the 40% improvement in gravity field accuracy. The standard distribution of products from all radar altimeters (Seasat, Geosat, ERS-1, Topex, . . .) is based on a waveform-tracking algorithm that meets the objectives of a broad science community. Three parameters are estimated from each waveform: arrival time (sea surface height), rise time (significant wave height), and amplitude (wind speed). The problem with the standard method is that estimates of arrival time are inherently correlated with estimates of rise time because of the noise characteristics of the returned waveform. We developed a retracking algorithm that reduces this correlation and improves the precision of the arrival time estimate by 40%. The main assumption is that the significant wave height varies smoothly along the satellite track over wavelengths of 90 km. Much of the work was to assemble the raw waveform data (provided by the European Space Agency on 152 Exabyte tapes), upgrade the waveform and ancillary information, optimize the parameters of the retracking algorithm, and retrack/edit the 2.5 billion waveforms.

- 2) Sandwell, D. T., and Y. Fialko, Warping and Cracking of the Pacific Plate by Thermal Contraction, *J. Geophys. Res.*, 109, B10411, doi:10.1029/2004JB003091, 2004.

The retracked ERS-1 data were combined with Geosat Geodetic Mission data and stacks of repeat profiles from ERS-2, Geosat/ERM, and Topex to form a new gravity field V11.1. This gravity field was a

significant improvement over V9.1 and provided better resolution of linear volcanic ridges in the troughs of the Haxby gravity lineations. We show that the large thermoelastic stress produced by top-down cooling is optimally released by lithospheric flexure between regularly spaced parallel cracks. Both the crack spacing and approximate gravity amplitude are predicted by elastic plate theory and a variational principle. The hypothesis is that cracks along the troughs of the gravity lineaments provide conduits for the generation of volcanic ridges in agreement with new observations from satellite-derived gravity. This model suggests that gravity lineaments are a natural consequence of lithospheric cooling so that convective rolls or mantle plumes are not required.

- 3) Lillibridge, J., W. H.F. Smith, D. Sandwell, R. Scharroo, F. Lemoine, and N. Zelensky, 20 Years of improvements to Geosat altimetry, paper presented at 15 Years of Progress in Radar Altimetry Symposium, European Space Agency, Venice Lido, Italy, 2006.

This paper represents the group effort involved in assembly and retracking the raw radar altimeter waveforms from the geodetic phase of the Geosat altimeter mission. When these data were first assembled at the Johns Hopkins Applied Physics Laboratory in 1986, the raw altimetry data were segmented into two products which were written onto separate 9-track tapes: Sensor Data Records (SDRs), containing 10-Hz measurements of range, AGC, and SWH along with instrumental corrections; and the Waveform Data Records (WDRs) which contained only the 10-Hz (binary) waveform data. The WDRs alone are insufficient to provide range information since they are relative to the absolute range provided in the SDR, and hence were never classified. The SDRs contain all the information necessary to compute marine gravity anomalies, but without the accompanying waveform data, the ranges cannot be retracked. The declassification of the SDRs in 1995 resulted in a dramatic improvement in the global marine gravity models. This group rejoined the two data streams and retrack the original waveforms. This data merging operation was performed at the NOAA laboratory for satellite altimetry where they also added more accurate orbital and ancillary information. The waveforms were retracked at SIO using an algorithm similar to the algorithm developed for the ERS-1 retracking. These combined improvements resulted in a 27% reduction in short-wavelength altimeter noise (see Figure 11 of *Lillibridge et al.*, 2006). More importantly, the new analysis corrected a 0.25s (1.75 km) along-track shift that caused a mislocation and blurring of sharp gravity features such as seamounts and fracture zones.

The retracked Geosat/GM data combined with the retracked ERS-1 data and stacked profiles from other missions was used to construct a new gravity (V16.1) model that provides a 40% improvement in gravity anomaly accuracy with respect to the version available prior to this investigation (V9.1). Examples of the incremental improvements are provided in Figures 1 and 2. The V16.1 gravity field also extends the latitude range to +/- 81° from +/- 72°.

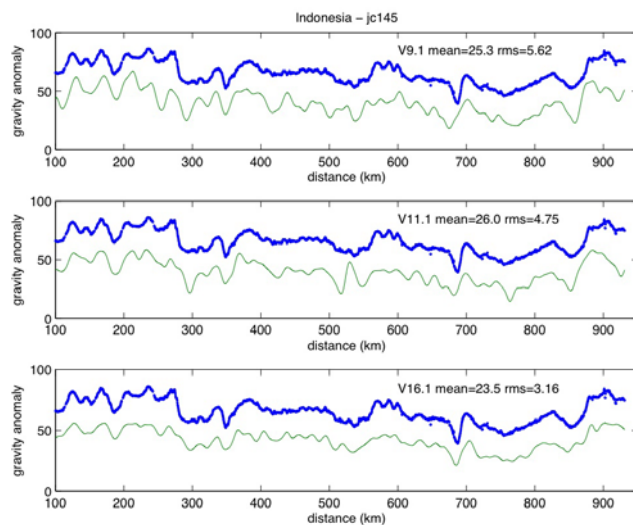


Figure 1. Comparison between satellite-derived gravity models (thin lines) and a shipboard gravity profile (points) across the Java Sea. (top) Gravity model version 9.1 does not use retracked altimeter data and has an rms misfit of 5.62 mGal. The mean difference of 25 mGal is due to a mean error commonly found in shipboard gravity [Wessel and Watts, 1988]. (middle) Gravity model version 11.1 uses retracked ERS-1 altimeter data but the Geosat data were not retracked; the rms misfit is improved to 4.75 mGal. (bottom) Gravity model version 16.1 is based on both retracked ERS-1 and Geosat altimeter profiles and also uses the biharmonic spline interpolation method. The rms is improved further to 3.16 mGal, which is a 44% reduction in rms.

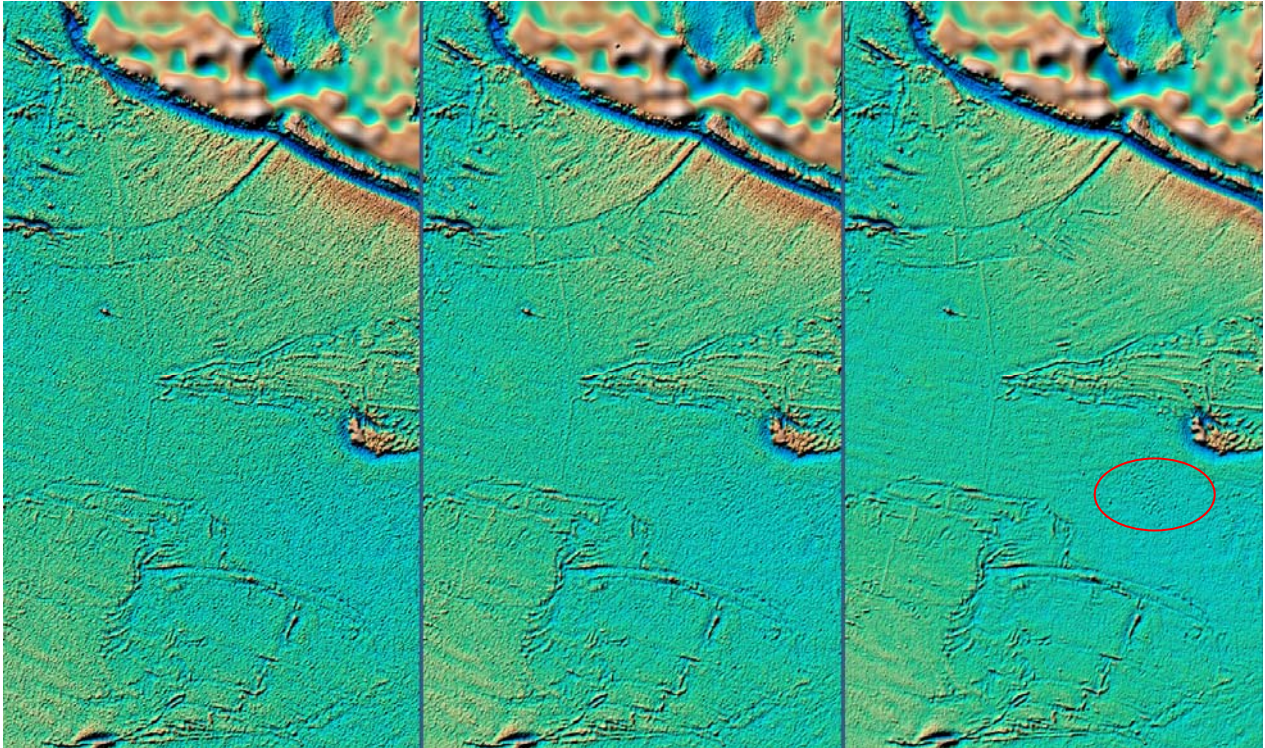


Figure 2. Shaded gravity anomaly for a large region in the Central Pacific Ocean centered at the Galapagos Triple Junction. The visual noise level decreases as one moves from V9.1 (left) to V11.1 (center) to V16.1 (right). The axis of the East Pacific Rise is well defined in V16.1 but more difficult to trace in V9.1 because of the higher noise level. The red oval outlines a patch of small-uncharted seamounts not apparent in V9.1. The gravity anomalies on the land areas reflect the anomalies from the reference gravity field EGM96 [Lemoine and al., 1998]. We propose to replace the land gravity with a new 5-minute resolution reference gravity model called EGM08 [Pavlis et al., 2007].

- 4) Watts, A. B., D. T. Sandwell, W. H. F. Smith, and P. Wessel, Global gravity, bathymetry, and the distribution of submarine volcanism through space and time, *J. Geophys. Res.*, *111*, B08408, 2006.

This study used the new global gravity model averaged to 2-minute resolution (V16.2) along with a matching 2-minute resolution bathymetry grid (V8.2) to estimate elastic thickness T_e beneath all large seamounts in the deep ocean. To avoid using predicted bathymetry in the least-squares estimate, we used the method of Lyons *et al.* [2000] to predict bathymetry from gravity and only perform the model comparisons using areas containing actual ship soundings. These new estimates of T_e are in basic agreement with more limited previous studies and show that bathymetric prediction is a robust way to estimate T_e and its upper and lower bounds. T_e at sites where there is both a sample and crustal age show considerable scatter, however, and there is no simple relationship between T_e and age. Nevertheless, we are able to tentatively assign a tectonic setting to each T_e estimate. The most striking results are in the Pacific Ocean where a broad swath of “on-ridge” volcanism extends from the Foundation seamounts and Ducie Island/Easter Island ridge in the southeast, across the equator, to the Shatsky and Hess rises in the northwest. We estimate the volume of on-ridge volcanism to be $\sim 1.1 \times 10^6 \text{ km}^3$ which implies a mean seamount addition rate of $\sim 0.007 \text{ km}^3 \text{ yr}^{-1}$. Rates appear to have varied through geological time, reaching their peak during the Late/Early Cretaceous and then declining to the present-day.

- 5) Sandwell, D. T., W. H. F. Smith, S. Gille, E. Kappel, S. Jayne, K. Soofi, B. Coakley, and L. Geli, Bathymetry from Space: Rationale and requirements for a new, high-resolution altimetric mission, *Comptes Rendus de l'Académie des Sciences*, 338, p. 1049-1062, 2006.

The detailed evaluation of the new gravity grid further highlighted the scientific contributions that could be achieved by a new altimeter mission with a focus on gravity field recovery. In October 2002, the NSF, NASA, NOAA and ConocoPhillips provided funding for a 2-day workshop at SIO convened by David Sandwell, Sarah Gille, and Walter Smith. During the 2-day workshop, the 46 participants discussed the broad scientific requirements for improved global bathymetry at moderate resolution. The workshop report is published at the following site http://www.igpp.ucsd.edu/bathymetry_workshop/. More recently, the French Space Agency (CNES) has been investigating the science requirements for this mission and the French Academy of sciences asked us to provide a more comprehensive report for their main publication *Comptes Rendus de l'Académie des Sciences*.

- 6) Becker, J. J., and D. T. Sandwell, Global Estimates Of Seafloor Slope From Single-Beam Ship Soundings, *in press J. Geophys. Res. - Oceans*, January, 2008.

This 6th publication included in the supplementary documents section fully documents the lack of short wavelength resolution available in the predicted bathymetry grids. More importantly it represents the hand editing and evaluation of 5000 cruise files of single-beam echo sounding data. The main scientific analysis of these cleaned-up data forms the body of a Ph.D thesis by Joseph Becker.

These following three publications were also partly supported by our NSF grant. The *Sandwell et al.* [2005] paper provides global maps of gravity, bathymetry, seafloor age, seismicity, and plate boundaries as consistent set of figures and data files that are useful for teaching and location maps. The *Wei and Sandwell* [2006] study uses seafloor subsidence rate as a proxy for global heat flow. They demonstrate that the subsidence rate data are entirely consistent with previous estimates of global oceanic heat output [*Pollack et al.*, 1993; *Sclater et al.*, 1980] and inconsistent with a recently-published reevaluation of global heat flow by *Hofmeister and Criss* [2005]. Matt Wei is a graduate student under the direction of Sandwell. The study by *Luttrell et al.* [2006] uses combined land and ocean bathymetry to estimate the changes in stress along the San Andreas Fault system caused by the time-varying load of Lake Cahuilla. Karen Luttrell is a graduate student working under the direction of Sandwell. The main focus of her proposed research is to calculate crustal stress due to static and time varying topographic loads on the oceanic and continental lithosphere.

Sandwell, D. T., D. Anderson, and P. Wessel, Global Tectonic Maps, *in Foulger, G. L., Natland, J. H., D. C. Presnall and D. L. Anderson, eds. Plates, Plumes & Paradigms: GSA Special Paper 388*, p. 1-10, 2005.

Wei, M. and D. Sandwell, Estimates of heat flow from Cenozoic seafloor using global depth and age data, *Tectonophysics*, 417, p. 325-335, 2006.

Luttrell, K., D. Sandwell, B. Smith-Konter, B. Bills, and Y. Bock (2007), Modulation of the earthquake cycle at the southern San Andreas fault by lake loading, *J. Geophys. Res.*, 112, B08411, doi:10.1029/2006JB004752.

1.2 HUMAN RESOURCES DEVELOPMENT

Accomplishment-Based Renewal proposals must include information on human-resources development at the postdoctoral, graduate and undergraduate levels as part of Results from Prior NSF Support. This may involve, but is not limited to, the role of research in student training, course preparation and seminars (particularly for undergraduates). Special accomplishments in the development of professional scientists and engineers from underrepresented groups should be described. Graduate students who participated in the research should be identified by name.

Most of the funding (~80% of the direct costs) provided by NSF through OCE0326707 was used to support graduate students, undergraduate students, course and seminar development, and part of a postdoc. The graduate students directly supported under this investigation are: **Bridget Smith** completed her Ph.D in 2005 under the direction of Sandwell, did a 6-mo. postdoc at SIO followed by a 1-year postdoc at JPL and is currently an assistant professor at the University of Texas at El Paso; **JJ Becker** is a 6th year Ph. D. student under the direction of Sandwell using single-beam bathymetry profiles to estimate seafloor slope globally and relate this to deep ocean mixing caused by tidal flow over rough topography; **Karen Luttrell** is a 5th year Ph.D. graduate student under the direction of Sandwell using global topography/bathymetry and gravity to calculate the static and time varying stress in the crust and its influence on earthquake rupture; **Matt Wei** is a 4th year Ph.D. graduate student under the direction of Sandwell mainly using InSAR from a new Japanese satellite called ALOS to investigate fault creep.

In terms of course preparation, Sandwell teaches two lecture-based classes and is involved in several seminar-based classes. All of these classes benefit from ongoing research funded by this and other NSF grants. In particular, SIO 135 is a **Satellite Remote Sensing** class for upper division physics and engineering majors (<http://topex.ucsd.edu/rs/>). The course includes a computer lab where the students analyze remote sensing data from the latest satellite instrumentation. New lectures are developed each year based on our satellite altimeter research as well as recently published research. Sandwell attends international remote sensing meetings to keep abreast of the latest developments in instrumentation and scientific applications.

The remote sensing class has been used to recruit top undergraduate physics students to work in our research lab. For the past two years, **Seung-Hee Kim** (senior physics major) has been editing seafloor bathymetry data and performing a variety of computer related tasks. He is currently being recruited for geophysics graduate studies at Yale University. **Breanna Binder** (senior physics major) has also been working with seafloor data and has offers from several graduate programs in astrophysics. Sandwell also teaches a lecture-based graduate class in **Geodynamics** (<http://topex.ucsd.edu/geodynamics/>). This class is constantly evolving based on the latest research. Finally Sandwell teaches a one-credit **freshman seminar** class designed to acquaint UCSD students with research activities at SIO (<http://topex.ucsd.edu/ps/>). All of these courses involve research and presentations by the students as part of their career development.

2. PLANS FOR PROPOSED SUPPORT PERIOD

2.1 INTELLECTUAL MERIT

Our proposed research has 3 main components. The first is to merge the retracked altimetry data with a soon-to-be published global geoid/gravity model at 5-minute resolution called Earth Gravity Model 2008 (EGM08). As discussed next, this merge must be done using the original altimeter profile data in order to construct a gravity model that is seamless at the shoreline. The complete gravity analysis will be documented and published in a leading journal. Second we propose to use the new funding to help complete the construction and documentation of a matching global bathymetry/topography grid at 1-minute resolution. For this component we will emphasize the shallow areas (< 1000 m) where we are compiling a global database. Finally we are most interested in continuing scientific investigation of these data in collaboration with other researchers.

To help guide this continued research we have asked a small number of investigators to comment on our current grids and make recommendations for improvement. The areas of investigation include: ridge studies (Gregg and Behn), tectonic studies (Mueller, and Stock), seamount studies (Wessel), physical oceanography (Jayne), tides (Padman), seismology (Das), and exploration geophysics (Soofi). The comments, provided in the supplementary documents section, are interesting and diverse and we have added most of these suggestions to this proposal. Through discussions with the exploration geophysics community who have been funding our efforts at a low level for the past decade, they are most interested in the seamless merging of land and ocean gravity and are willing to support a greater part of the research in exchange for placing the margins data on proprietary hold. We would like to see all of the data completely open but this will require that most of the funding comes from public sources. For example, the V16.1 gravity model was partly funded by ConocoPhillips and ExxonMobil and was on proprietary hold for 1 year. This 1-year hold period (April 1, 2005 to April 1, 2006) also provided the students in our lab with lead-time for scientific analyses using the data. We would like to continue a similar arrangement under this new investigation. However, if ConocoPhillips ends up supporting all of the investigation they are asking for a longer hold period for the gravity analysis.

2.1.1 MERGE OF RETRACKED ALTIMETRY WITH EGM08

We propose to merge profiles of retracked altimetry used in constructing the Version 16.1 global marine gravity model (V16.1) with a soon-to-be published global geoid/gravity model at 5-minute resolution [Pavlis *et al.*, 2007]. Our group at SIO has participated in the development of the EGM08 global gravity model, which will be published during the General Assembly of the European Geosciences Union, to be held in Vienna, Austria, 13-18 of April 2008. The model is represented as spherical harmonic coefficients complete to degree and order 2160 (5 minute grid resolution). A beta version of this model is shown in Figure 3 (right) for a region around West Africa. The left panel of the figure shows our 1-minute V16.1 gravity model where EGM96 was used as a reference field. The new EGM08 model has much improved resolution in the land areas but lower resolution over the ocean. We propose to recompute the marine gravity model at 1-minute resolution using the EGM08 model as a reference. This merge must be done at the level of the original altimeter profile data to ensure a seamless gravity field at the shoreline.

In addition to making this merged grid publicly available, we propose to provide more complete documentation as well as companion grid of marine gravity field uncertainty. The uncertainty grid (suggested by Paul Wessel in the supplementary documents section) will be based on the weighted rms difference between the along track slopes from each altimeter profile and the slope from the final north and east vertical deflection grids. They will show the spatial variations in uncertainty associated with factors such as track density, regions of high sea state, and regions of high mesoscale ocean variability (e.g. Gulf stream). As suggested in the letter from Trish Gregg and Mark Behn (supplementary

documents section) we will provide a GMT script to seamlessly combine higher accuracy shipboard gravity data with the global gravity grid.

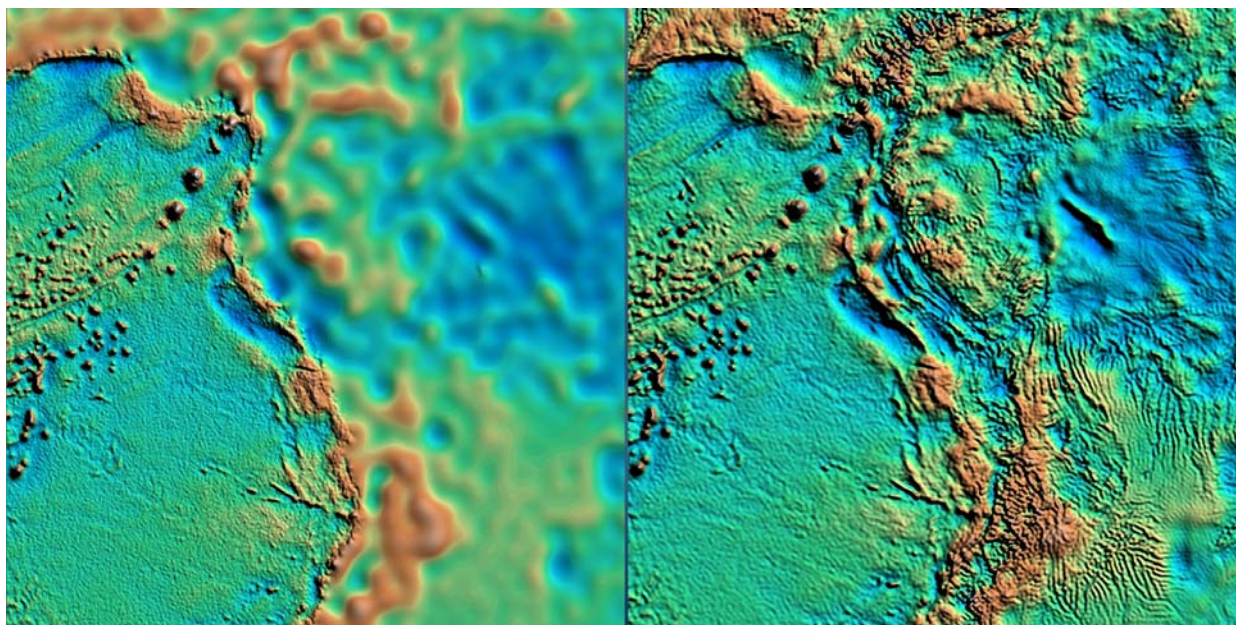


Figure 3. (left) Gravity anomaly from V16.1 analysis has 1 minute pixel size and ~ 8 km $1/2$ wavelength resolution over the ocean. Land data are constrained to match the EGM96 gravity model complete to degree and order 360 [Lemoine and al., 1998] or a ~ 111 km spatial resolution. (right) Beta version of the EGM08 gravity model complete to spherical harmonic degree and order 2160 corresponding to a $1/2$ wavelength resolution of 19 km.

2.1.2 CONSTRUCTION AND DOCUMENTATION OF 1-MINUTE GLOBAL TOPOGRAPHY/BATHYMETRY

The second component of our proposed research will be to continue the construction and documentation of a global bathymetry/topography grid. This work is a collaborative effort between SIO, the National Geospatial-intelligence Agency (NG-iA), the Naval Meteorology and Oceanography Command (METOC & NAVO), and the National Oceanic and Atmospheric Administration (NOAA). Each of these partners has pledged to contribute unclassified soundings to this effort. We are assembling all of the sounding data on a group-accessible computer at SIO in our lab (seasat.ucsd.edu). Our effort has been mainly funded by the Office of Naval Research under a contract that expires in July, 2008. So far we have completed the following tasks: assembly of an array of publicly available depth soundings from a wide variety of sources; statistical and visual assessment of all soundings through a comparison with a previously published 2-minute global bathymetry grid; hand editing of all suspect data (single beam trackline, multibeam swaths, sparse sounding, and contributed grids); and finally using these soundings to modify global satellite bathymetry based on the latest altimeter-derived gravity models. The [IBCAO, 2003] arctic bathymetry is used north of 80 degrees. In addition, the global bathymetry grid is merged with global elevations based on a combination of SRTM30 topography (latitude < 55 deg), GTOPO30 [USGS, 1997] in the Arctic, and IceSAT-derived topography of Antarctica [DiMarzio et al.].

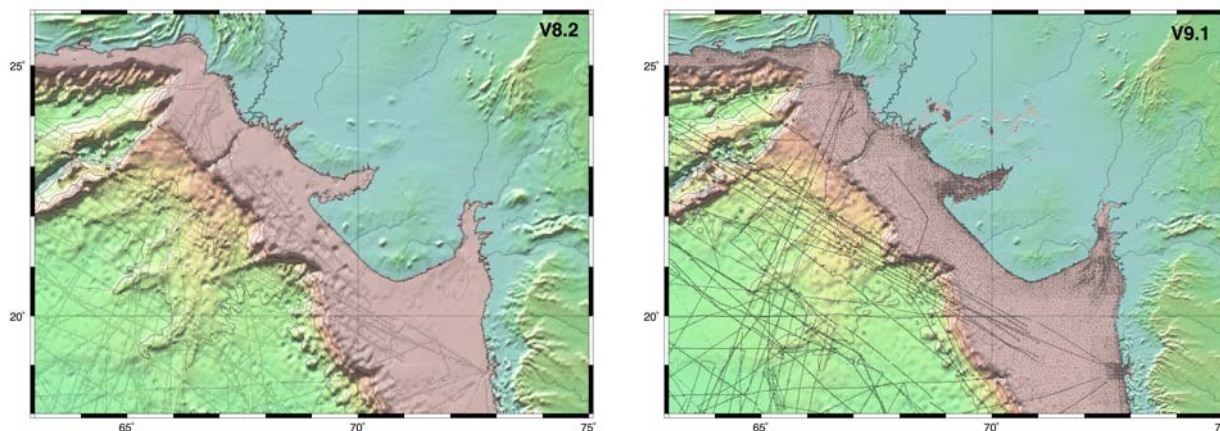


Figure 4. (left) Bathymetry of western India and northern Arabian Basin from V8.2 grid [Smith and Sandwell; 1997] at 2-minute resolution. Small gray dots show locations of available ship soundings. (right) same area from V9.1 grid at 1-minute resolution. The shallow continental margin bathymetry is much better constrained by many new electronic nautical soundings available from Pauline Weatherall British Oceanographic Data Centre (BODC). Note that the V8.2 bathymetry has artifacts on the shallow margin that have been corrected in V9.1 by using more data constraints.

An important new development is the contribution of many new shallow water (< 1000 m) soundings from Digital Nautical Chart (DNC) and Electronic Navigation Chart (ENC) data files. DNC data were contributed by NG-iA and ENC data by member agencies the International Hydrographic Organization contributing their data to BODC for the use of GEBCO, the project for the General Bathymetric Charts of the Oceans. GEBCO has adopted our new effort as the basis for its next revision, and so a variety of international sources of data are now flowing to our project. This has resulted in a major improvement in the bathymetry of all continental margins. Our previous grid (Figure 4 left) had few shallow-water depth soundings and since the gravity-to-topography prediction method is not effective on the shallow continental margins, this V8.2 grid was very inaccurate. Now the ENC data provided by the BODC results in a vastly improved global grid at 1-minute resolution (Figure 4, right). One issue related to the DNC soundings (not shown) is that most of the soundings are proprietary data at NG-iA. NG-iA has allowed us to use these data in our bathymetric grids but we cannot reveal the digital locations of the data constraints. Shallow water data constraints from the DNC soundings are global and similar in density to the non-proprietary ENC soundings shown in Figure 4.

Under this investigation we propose to continue and complete this bathymetry effort. In particular, we will produce two companion grids. The first (already under construction) is a grid providing a source identification (SID) number for each 1-minute grid cell. The SID number provides the information needed to identify, and possibly correct or edit, the individual depth soundings. When the grids are completed we will also assemble and distribute these raw sounding data at > 500 m resolution. Approximately 5000 of these data files are from the NGDC GEODAS database. For these files, we propose to merge the editing flags that we have already assembled back with the original NGD77 files and apply the crossover corrections that have been computed by Chandler and Wessel [Chandler and Wessel, 2007]. The second grid will contain the uncertainty in the depth soundings. The 1-minute bathymetry and SID grids will be compared with a much more complete bathymetric data set that is only available at the National Geospatial Agency. Walter Smith and NG-iA scientists will develop a function that uses parameters such as the mean ocean depth and distance to the nearest actual ship sounding to estimate the uncertainty in the predicted grid cells.

2.1.2 GLOBAL ANALYSIS OF RIDGE SEGMENTATION AND MORPHOLOGY

The third component of our proposed research will be to continue scientific analysis of these data. For example, these improved resolution grids provide a clearer image of the segmentation of the global spreading ridge (Figure 5). An example of the vertical gravity gradient used as shading on the new global bathymetry grid at 1 minute resolution helps to delineate the first and second order segmentation of the mid ocean ridges [Macdonald *et al.*, 1988]. A recent study of residual mantle Bouguer anomaly by [Gregg *et al.*, 2007] using this new V16.1 gravity grid reveals the spreading dependence of gravity anomalies along oceanic transform faults. Their study combined with previous investigations on the variations in ridge-axis morphology with spreading rate [Menard, 1967; Small, 1994] variations in abyssal hill morphology/seafloor roughness with spreading rate [Goff, 1991; Goff *et al.*, 2004; Small and Sandwell, 1992; Smith, 1998] and the order of magnitude variations in seismic moment release with spreading rate [Bird *et al.*, 2002] highlight the importance of spreading rate in lithospheric strength and crustal structure. This is a first-order aspect of plate tectonics that deserves a more comprehensive analysis and literature review.

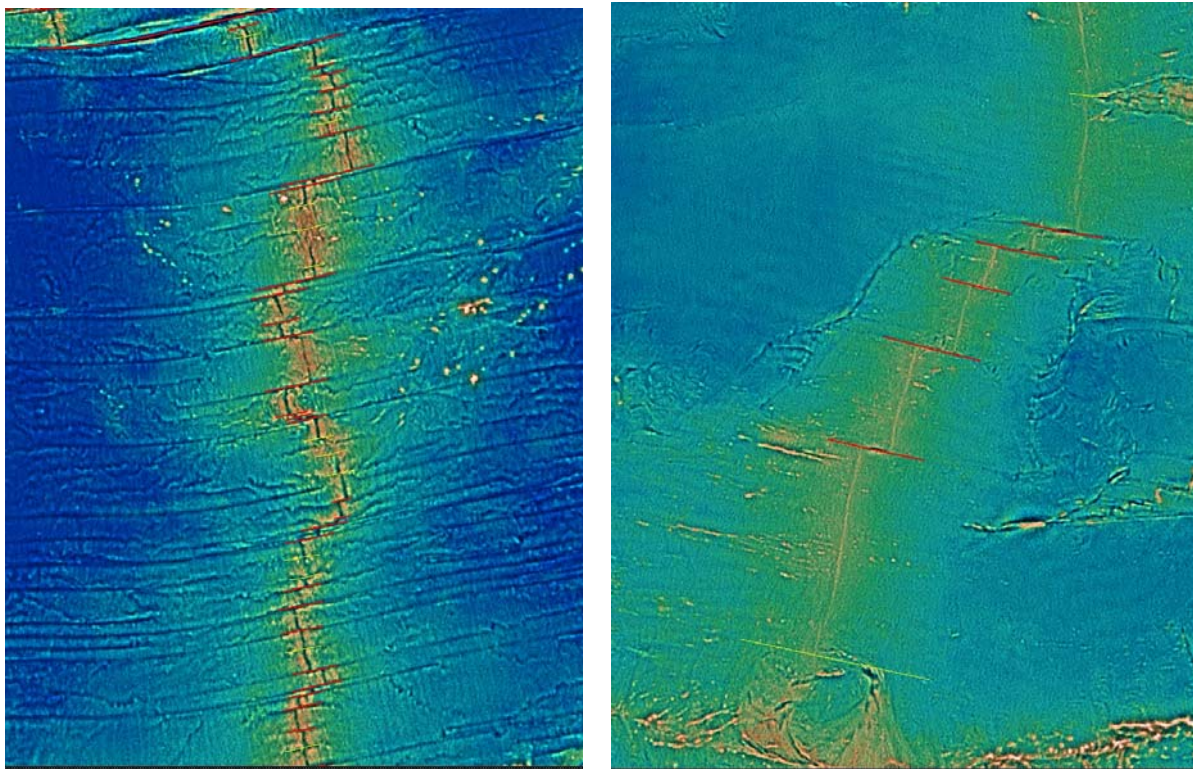


Figure 5. (left) South Atlantic bathymetry (color) with vertical gravity gradient superimposed (shading) from the latest bathymetry and gravity grids reveals the first order (red lines) and second order (yellow lines) segmentation of the ridges. (right) South Pacific bathymetry and vertical gravity gradient at same vertical and horizontal scale as the South Atlantic. Ridge segments are much longer along the faster spreading East Pacific Rise than the slower spreading Mid-Atlantic Ridge.

A more poorly understood phenomenon is the variations in ridge segmentation with spreading rate [Abbott, 1986; Sandwell, 1986]. A variety of models have been proposed [Kastens, 1987] for ridge segmentation including: thermal contraction joints [Collette, 1979; Sandwell, 1986], thermal bending stresses [Turcotte, 1974], segmented mantle upwellings [Lin and Phipps Morgan, 1992; Madge and Sparks, 1997; Parmentier and Phipps Morgan, 1990; Schouten *et al.*, 1985], and minimum energy and damage rheology configurations [Hieronymus, 2004; Lachenbruch, 1973; Oldenburg and Brune, 1975]. After the discovery of transform faults more than 40 years ago, there is still no consensus on why they exist and why the ridge segmentation varies with spreading rate. A leading hypothesis is that transform

faults and fracture zones provide a mechanism for ridge-parallel shrinkage of the lithosphere. However, if this is correct then this mechanism should not be effective on faster spreading ridges where the transform spacing is large. Perhaps other types of cracking and plate bending occur along the fast spreading ridges [Gans *et al.*, 2003; Sandwell and Fialko, 2004]. If the plates do not shrink in the ridge-parallel direction then large cracks may penetrate 30 km deep into the lithosphere as proposed by [Korenaga, 2007]. Another possibility is that plates readily contract in all three dimensions. In this case the lateral shrinkage will appear as significant perturbations to the global plate motion models [Kumar and Gordon, 2008]. We propose a more careful analysis of on-ridge and off-ridge segmentation to help resolve these fundamental issues related to cooling of the oceanic lithosphere.

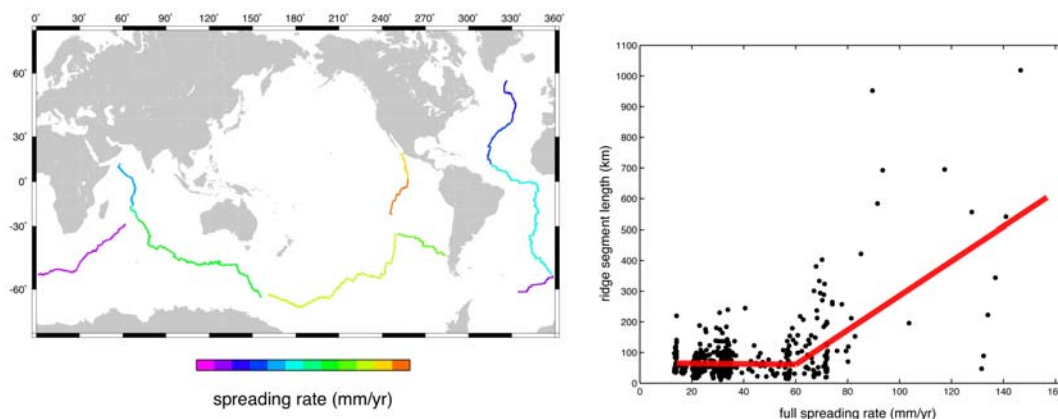


Figure 6. (left) Present-day spreading rate from [DeMets *et al.*, 1994] with segments digitized from latest grids. (right) Preliminary version of ridge segment length versus spreading rate. For rates less than about 70 mm/yr the typical ridge segment length varies from 50–100 km. At higher rates there is a wider variation in segment length with some segments 1000 km long. Note that the Reykjanes ridge was not included and there is a lack of transform fault segmentation around the Easter and Juan Fernandez microplates [Naar and Hey, 1989].

2.2 BROADER IMPACTS

To determine the effectiveness of our web outreach activities, please do a Google search on the following keywords and our web site topex.ucsd.edu will be near the top of the sites listed: *marine gravity* (3rd/253,000), *bathymetry* (6th/837,000), *topography* (6th/8.5 million), *seafloor* (6th/694,000). This “no frills” web site was accessed 4.5 million times this past year. The key to the success of these pages is long-term stability and consistency. The gravity and bathymetry data are distributed at three levels to help fill the needs of expert, intermediate, and novice users. The expert users want global grids of gravity, topography, geoid height, and roughness. These are available by anonymous ftp to topex.ucsd.edu. In addition expert users sometimes want access to the raw xyz files of gravity and topography. These are delivered as ASCII files from geographic searches http://topex.ucsd.edu/cgi-bin/adv_cruise.cgi. The intermediate users usually prefer ascii files of sub areas derived from these grids. The interface is found at http://topex.ucsd.edu/cgi-bin/get_data.cgi. Finally the novice users want fully digested information for education or enjoyment. Images and movies are available at http://topex.ucsd.edu/marine_topo/globe.html. These three delivery mechanisms have gone largely unchanged since 1999. In the past, we have employed undergraduate students to maintain these web pages and we will continue to employ undergraduates in the future.

The section above on human resources documents our use of NSF funds for graduate and undergraduate level education. While there is no specific budget line for outreach activities outside of UCSD/SIO, we will continue to: participate in media activities, give talks at the San Diego Fleet Science Center and Natural History Museum, and give presentations at junior high and elementary schools.

4. REFERENCES

- Abbott, D. (1986), A statistical correlation between ridge crest offsets and spreading rate, *J. Geophys. Res.*, *13*, 157-160.
- Bird, P., Y. Y. Kagan, and D. D. Jackson (Eds.) (2002), Plate tectonics and earthquake potential of spreading ridges and oceanic transform faults, 203-218 pp., American Geophysical Union, Washington, D.C.
- Chandler, M. T., and P. Wessel (2007), The mgd77 supplement to the generic mapping tools, *Computers & Geosciences*, *33*(1), 62-75.
- Collette, B. (1979), Thermal Contraction Joints in Spreading Seafloor as Origin of Fracture Zones, *Nature*, *251*, 299-300.
- DeMets, C., R. G. Gordon, D. F. Argus, and S. Stein (1994), Effect of recent revisions to the geomagnetic reversal timescale on estimates of current plate motions, *Geophys. Res. Lett.*, *21*, 2191-2194.
- DiMarzio, J. P., A. C. Brenner, H. A. Fricker, J. L. Saba, B. E. Schutz, C. A. Shuman, and H. J. Zwally (2007), Digital Elevation Models of the Antarctic and Greenland Ice Sheets Using Data From ICESat, digital file.
- Gans, K. D., D. S. Wilson, and K. C. Macdonald (2003), Pacific plate gravity lineaments: Extension or thermal contraction?, *Geochemistry, Geophysics, Geosystems*, *4*, doi:10.1029.
- Goff, J. A. (1991), A Global and Regional Stochastic-Analysis of near-Ridge Abyssal Hill Morphology, *J. of Geophys. Res.*, *96*(B13), 21713-21737.
- Goff, J. A., W. H. F. Smith, and K. M. Marks (2004), The Contributions of Abyssal Hill Morphology and Noise to Altimetric Gravity Fabric, *Oceanography*, *17*(1), 24-37.
- Gregg, P. C., J. Lin, M. D. Behn, and L. G. J. Montesi (2007), Spreading rate dependence of gravity anomalies along oceanic transform faults, *Nature*, *448* (doi:10.1038), 183-187.
- Hieronimus, C. F. (2004), Control on seafloor spreading geometries by stress- and strain-induced lithospheric weakening, *Earth. Planet. Sci. Lett.*, *222*, 177-189.
- Hofmeister, A. M., and R. E. Criss (2005), Earth's heat flux revised and linked to chemistry, *Earth Planet. Sci. Lett.*, *395*, 159 - 177.
- IBCAO (2003), IOC IHO IASC - International Bathymetric Chart of the Arctic Ocean (IBCAO). <http://www.ngdc.noaa.gov/mgg/bathymetry/arctic/arctic.html>.
- Kastens, K. K. (1987), A compendium of causes and effects of processes at transform faults and fracture zones, *Rev. Geophys. Res.*, *25*(7), 1554-1562.
- Korenaga, J. (2007), Thermal cracking and deep hydration of oceanic lithosphere: A key to generation of plate tectonics?, *J. Geophys. Res.*, *112* (doi:10.1029/2006JB004502), B05408.
- Kumar, R. R., and R. G. Gordon (2008), Horizontal Thermal Contractual Straining of Oceanic Lithosphere: The Ultimate Limit to the Rigid Plate Hypothesis, submitted to *J. Geophys. Res.*
- Lachenbruch, A. H. (1973), A Simple Mechanical Model for Oceanic Spreading Centers, *J. Geophys. Res.*, *78*, 3395-3417.
- Lemoine, F. G., and e. al. (1998), *The development of the joint NASA CSFC and the national Imagery and Mapping Agency (NIMA) Geopotential Model EGM96*, 320 pp, Goddard Space Flight Center, NASA, Greenbelt, Maryland.
- Lin, J., and J. Phipps Morgan (1992), The spreading rate dependence of three-dimensional mid-ocean ridge gravity structure, *Geophys. Res. Lett.*, *19*, 13-16.
- Lyons, S. N., D. T. Sandwell, and W. H. F. Smith (2000), Three-dimensional estimation of elastic thickness under the Louisville Ridge, *J. Geophys. Res.*, *105*, 13239-13252.
- Macdonald, K. C., P. J. Fox, L. J. Perram, M. F. Eisen, R. M. Haymon, S. P. Miller, S. M. Carbotte, M. H. Cormier, and A. N. Shor (1988), A New View of the Mid-Ocean Ridge from the Behavior of Ridge-Axis Discontinuities, *Nature*, *335*(6187), 217-225.

- Madge, L. S., and D. W. Sparks (1997), Three-dimensional mantle upwelling, melt generation, and melt migration beneath segment slow spreading ridge, *J. Geophys. Res.*, 102, 20571-20583.
- Menard, H. W. (1967), Sea Floor Spreading Topography and Second Layer, *Science*, 157(3791), 923-&.
- Naar, D. F., and R. N. Hey (1989), Speed limit for oceanic transform faults, *Geology*, 17(5), 420-422.
- Oldenburg, D. W., and J. N. Brune (1975), An explanation for the orthogonality of ocean ridges and transform faults, *J. Geophys. Res.*, 80(17), 2575-2585.
- Parmentier, E. M., and J. Phipps Morgan (1990), Spreading Rate Dependence of Three-Dimensional Structure in Oceanic Spreading Centres, *Nature*, 348, 325-328.
- Pavlis, N. K., S. A. Holmes, S. C. Kenyon, and J. K. Factor (2007), Earth Gravitational Model to Degree 2160: Status and Progress, paper presented at *IUGG XXIV General Assembly*, Perugia, Italy July 2-13, 2007.
- Pollack, H. N., S. J. Hurter, and J. R. Johnson (1993), Heat flow from the Earth's interior: Analysis of the global data set, *Rev. Geophys.* 31(267 - 280).
- Sandwell, D., and Y. Fialko (2004), Warping and cracking of the Pacific plate by thermal contraction, *J. Geophys. Res.*, 109(B10411), doi:10.1029/2004JB003091.
- Sandwell, D. T. (1986), Thermal Stress and the Spacings of Transform Faults, *J. Geophys. Res.*, 91(B6), 6405-6417.
- Schouten, H., K. D. Klitgord, and J. A. Whitehead (1985), Segmentation of mid-ocean ridges, *Nature*, 317, 225-229.
- Sclater, J. G., C. Jaupart, and D. Galson (1980), The heat flow through oceanic and continental crust and the heat loss of the earth., *Rev. Geophysics and Space Physics*, 18, 269-311.
- Small, C., and D. T. Sandwell (1992), An Analysis of Ridge Axis Gravity Roughness and Spreading Rate, *Journal of Geophysical Research-Solid Earth*, 97(B3), 3235-3245.
- Small, C. (1994), A global analysis of mid-ocean ridge axial topography, *Geophys. J. Int.*, 116, 64-84.
- Smith, W. H. F. (1998), Seafloor tectonic fabric from satellite altimetry, *Annual Review of Earth and Planetary Sciences*, 26(1), 697-747.
- Turcotte, D. L. (1974), Are Transform Faults Thermal Contraction Cracks?, *J. Geophys. Res.*, 79, 2573-2577.
- USGS (1997), Global topography at 30 arc second averages (GTOPO30), edited, U. S. Geological Survey, EROS Data Center.
- Wessel, P., and A. B. Watts (1988), On the accuracy of marine gravity measurements, *J. Geophys. Res.*, 93(B1), 393-413.

David T. Sandwell

Contact Information:

Scripps Institution of Oceanography
La Jolla, CA 92093-0225
<http://topex.ucsd.edu>

dsandwell@ucsd.edu
ph. (858) 534-7109

Present Position: Professor of Geophysics, Scripps Institution of Oceanography

Education:

Ph.D., 1981 University of California at Los Angeles, Geophysics and Space Physics
M.S., 1978 University of California at Los Angeles, Geophysics
B.S., 1975 University of Connecticut, Major Physics, Minor Mathematics

Professional Experience:

1989-93 Scripps Institution of Oceanography, Associate Professor
1985-89 University of Texas at Austin, Research Scientist
1982-85 National Geodetic Survey, Research Geophysicist

Other Experience:

1/08 - President Elect of Geodesy Section of the AGU
1/07 - 1/09 Chair of Western North America InSAR Consortium (WInSAR)
5/05-9/05 Member of committee to review ESA's Earth Observation Envelope Programme
6/03-7/04 Member of NASA Jupiter Orbiter Icy Moons Science Definition Team
6/01-4/04 Associate Editor of *Journal of Geophysical Research*
2/01-12/03 Member of NRC U.S. National Committee to the IUGG
10/99-7/02 Chair of Western North America InSAR Consortium (WInSAR)
9/98 - 6/01 Member of NRC Space Studies Board, Committee on Earth Studies
10/95-12/00 AGU Editor of *Earth Interactions*, Electronic Journal
5/95 - 12/96 Member of NRC, US Committee on Geodynamics
9/94 - 5/96 SIO Representative to UCSD Academic Senate
9/93 - 8/94 Chair of UCSD Academic Senate Committee on Computing
2/92 - 12/95 Office of Technology Assessment panel on Earth Observing Systems
6/90 - 1/95 Member of National Research Council, Committee on Geodesy
12/86 - 1/91 Science steering group member for NASA's satellite gravity program
1/87 - 12/90 Associate Editor, *Reviews of Geophysics and Space Physics*
2/85 - 1/89 Associate Editor, *Journal of Geophysical Research*

Recent Research Funding:

10/05-9/08 ONR Predicted Bathymetry for Naval Operations and Scientific Applications
6/03-6/08 NSF/NASA Marine Gravity, Seafloor Topography and Seafloor Roughness
1/03-9/05 NSF Synthetic Aperture Sonar for High Resolution Mapping and Change Detection
7/01-6/05 NSF Observations of the Earthquake Cycle from ERS and ALOS InSAR

Cruise Participation:

9/03 Co-chief on R/V Revelle to test feasibility of Synthetic Aperture Sonar
2/97 Participant in expedition to Foundation Seamounts, South Pacific
1/94 Co-chief scientist on R/V Melville to map Eltanin and Udintsev Fracture Zones
1/93 Chief scientist on R/V Melville to map Pukapuka En-Echelon Ridges
2/89 Assistant scientist on R/V Surveyor to map the Shackleton Fracture Zone
3/87 Assistant chief scientist on R/V Washington to explore Seasat gravity lineations
5/83 Participating scientist on Bermuda Swell heat flow experiment

Awards and Memberships:

11/04 George P. Woollard Award and Fellow of the Geological Society of America
12/97 Fellow of the American Geophysical Union
12/95 Bowie Lecture American Geophysical Union
9/98- Society for Exploration Geophysics
6/77- American Geophysical Union
6/80- International Association of Geodesy

(5) Related and (5) Significant Publications:

- Sandwell, D. T., and G. Schubert, Lithospheric Flexure at Fracture Zones, *J. Geophys. Res.*, 87, 4657-4667, 1982.
- Sandwell, D. T., Thermal Stress and the Spacings of Transform Faults, *J. Geophys. Res.*, 91, 6405-6418, 1986.
- Winterer, E. L., and D. T. Sandwell, Evidence From En Echelon Cross-grain Ridges for Tensional Cracks in the Pacific Plate, *Nature*, 329, 534-537, 1987.
- Small, C. and D. T. Sandwell, An Abrupt Change in Ridge-Axis Gravity with Spreading Rate, *J. Geophys. Res.*, 94, 17383-17392, 1989.
- Smith, W. H. F. and D. T. Sandwell, Bathymetric Prediction from Dense Satellite Altimetry and Sparse Shipboard Bathymetry, *J. Geophys. Res.*, 99, 21803-21824, 1994.
- Sandwell, D. T. and W. H. F. Smith, Marine Gravity from Geosat and ERS-1 Altimetry, *J. Geophys. Res.*, 102, 10039-10054, 1997.
- Smith, W. H. F. and D. Sandwell, Global Seafloor Topography from Satellite Altimetry and Ship Depth Soundings, *Science*, 277, p.1956-1962, 1997.
- Sandwell, D. T., Y. Fialko, Warping and Cracking of the Pacific Plate by Thermal Contraction, *J. Geophys. Res.*, 109, B10411, doi:10.1029/2004JB003091, 2004.
- Sandwell, D. T., and W.H.F. Smith, Retracking ERS-1 Altimeter Waveforms for Optimal Gravity Field Recovery, *Geophys. J. Int.*, 163, 79-89, 2005.
- Sandwell, D. T., Smith, W. H. F., S. Gille, S., Kappel E., Jayne S., Soofi K. , Coakley B., and L. Geli, Bathymetry from Space: Rationale and requirements for a new, high-resolution altimetric mission, *Comptes Rendus de l'Académie des Sciences*, 338, p. 1049-1062, 2006.

Synergistic Activities:

Teach graduate classes: *Geodynamics; Satellite Remote Sensing; Synthetic Aperture Radar*.
Distribute global gravity and topography data for research and education: <http://topex.ucsd.edu>

Collaborators and other affiliations:

Duncan Agnew	Sarah Gille	Bernard Minster
Gidi Baer	Graham Kent	John Orcutt
Yehuda Bock	Larry Lawver	Paul Rosen
Robert Cheney	Dave McAadoo	Peter Shearer
Yuri Fialko	Rob Mellors	Walter Smith

Graduate and Postdoctoral Advisors:

Bruce Douglas
Gerald Schubert

Students and post docs:

Y. John Chen	Bill Moore	Chris Small
Catherine Johnson	Dietmar Mueller	Mara Yale
Bridget Konter-Smith	Evelyn Price	Bohai Zhang
Dan Levitt	Jean-Yves Royer	
Suzanne Lyons	Lydie Sichoix	

SUMMARY PROPOSAL BUDGET

YEAR 1

ORGANIZATION University of California-San Diego Scripps Inst of Oceanography				FOR NSF USE ONLY			
				PROPOSAL NO.	DURATION (months)		
PRINCIPAL INVESTIGATOR / PROJECT DIRECTOR David T Sandwell				AWARD NO.	Proposed	Granted	
A. SENIOR PERSONNEL: PI/PI, Co-PI's, Faculty and Other Senior Associates (List each separately with title, A.7. show number in brackets)				NSF Funded Person-months		Funds Requested By proposer	Funds granted by NSF (if different)
	CAL	ACAD	SUMR				
1. David T Sandwell - Professor	0.00	0.00	0.00	\$	0	\$	
2.							
3.							
4.							
5.							
6. (0) OTHERS (LIST INDIVIDUALLY ON BUDGET JUSTIFICATION PAGE)	0.00	0.00	0.00		0		
7. (1) TOTAL SENIOR PERSONNEL (1 - 6)	0.00	0.00	0.00		0		
B. OTHER PERSONNEL (SHOW NUMBERS IN BRACKETS)							
1. (0) POST DOCTORAL SCHOLARS	0.00	0.00	0.00		0		
2. (0) OTHER PROFESSIONALS (TECHNICIAN, PROGRAMMER, ETC.)	0.00	0.00	0.00		0		
3. (1) GRADUATE STUDENTS					25,071		
4. (1) UNDERGRADUATE STUDENTS					5,760		
5. (0) SECRETARIAL - CLERICAL (IF CHARGED DIRECTLY)					0		
6. (1) OTHER					6,013		
TOTAL SALARIES AND WAGES (A + B)					36,844		
C. FRINGE BENEFITS (IF CHARGED AS DIRECT COSTS)					13,815		
TOTAL SALARIES, WAGES AND FRINGE BENEFITS (A + B + C)					50,659		
D. EQUIPMENT (LIST ITEM AND DOLLAR AMOUNT FOR EACH ITEM EXCEEDING \$5,000.)							
TOTAL EQUIPMENT					0		
E. TRAVEL 1. DOMESTIC (INCL. CANADA, MEXICO AND U.S. POSSESSIONS)					3,200		
2. FOREIGN					0		
F. PARTICIPANT SUPPORT COSTS							
1. STIPENDS \$ _____					0		
2. TRAVEL _____					0		
3. SUBSISTENCE _____					0		
4. OTHER _____					0		
TOTAL NUMBER OF PARTICIPANTS (0) TOTAL PARTICIPANT COSTS					0		
G. OTHER DIRECT COSTS							
1. MATERIALS AND SUPPLIES					1,000		
2. PUBLICATION COSTS/DOCUMENTATION/DISSEMINATION					0		
3. CONSULTANT SERVICES					0		
4. COMPUTER SERVICES					2,220		
5. SUBAWARDS					0		
6. OTHER					590		
TOTAL OTHER DIRECT COSTS					3,810		
H. TOTAL DIRECT COSTS (A THROUGH G)					57,669		
I. INDIRECT COSTS (F&A)(SPECIFY RATE AND BASE) MTDC (Rate: 54.5000, Base: 43854)							
TOTAL INDIRECT COSTS (F&A)					23,900		
J. TOTAL DIRECT AND INDIRECT COSTS (H + I)					81,569		
K. RESIDUAL FUNDS					0		
L. AMOUNT OF THIS REQUEST (J) OR (J MINUS K)				\$	81,569	\$	
M. COST SHARING PROPOSED LEVEL \$ 0				AGREED LEVEL IF DIFFERENT \$			
PI/PI NAME David T Sandwell				FOR NSF USE ONLY			
ORG. REP. NAME*				INDIRECT COST RATE VERIFICATION			
		Date Checked	Date Of Rate Sheet	Initials - ORG			

SUMMARY PROPOSAL BUDGET

YEAR **2**

ORGANIZATION University of California-San Diego Scripps Inst of Oceanography				FOR NSF USE ONLY			
				PROPOSAL NO.	DURATION (months)		
PRINCIPAL INVESTIGATOR / PROJECT DIRECTOR David T Sandwell				AWARD NO.	Proposed	Granted	
A. SENIOR PERSONNEL: PI/PI, Co-PI's, Faculty and Other Senior Associates (List each separately with title, A.7. show number in brackets)				NSF Funded Person-months		Funds Requested By proposer	Funds granted by NSF (if different)
	CAL	ACAD	SUMR				
1. David T Sandwell - Professor	0.00	0.00	0.00	\$	0	\$	
2.							
3.							
4.							
5.							
6. (0) OTHERS (LIST INDIVIDUALLY ON BUDGET JUSTIFICATION PAGE)	0.00	0.00	0.00		0		
7. (1) TOTAL SENIOR PERSONNEL (1 - 6)	0.00	0.00	0.00		0		
B. OTHER PERSONNEL (SHOW NUMBERS IN BRACKETS)							
1. (0) POST DOCTORAL SCHOLARS	0.00	0.00	0.00		0		
2. (0) OTHER PROFESSIONALS (TECHNICIAN, PROGRAMMER, ETC.)	0.00	0.00	0.00		0		
3. (1) GRADUATE STUDENTS					26,326		
4. (1) UNDERGRADUATE STUDENTS					5,760		
5. (0) SECRETARIAL - CLERICAL (IF CHARGED DIRECTLY)					0		
6. (1) OTHER					6,314		
TOTAL SALARIES AND WAGES (A + B)					38,400		
C. FRINGE BENEFITS (IF CHARGED AS DIRECT COSTS)					14,778		
TOTAL SALARIES, WAGES AND FRINGE BENEFITS (A + B + C)					53,178		
D. EQUIPMENT (LIST ITEM AND DOLLAR AMOUNT FOR EACH ITEM EXCEEDING \$5,000.)							
TOTAL EQUIPMENT					0		
E. TRAVEL					3,200		
1. DOMESTIC (INCL. CANADA, MEXICO AND U.S. POSSESSIONS)							
2. FOREIGN					0		
F. PARTICIPANT SUPPORT COSTS							
1. STIPENDS	\$		0				
2. TRAVEL			0				
3. SUBSISTENCE			0				
4. OTHER			0				
TOTAL NUMBER OF PARTICIPANTS (0)				TOTAL PARTICIPANT COSTS	0		
G. OTHER DIRECT COSTS							
1. MATERIALS AND SUPPLIES					1,000		
2. PUBLICATION COSTS/DOCUMENTATION/DISSEMINATION					0		
3. CONSULTANT SERVICES					0		
4. COMPUTER SERVICES					2,220		
5. SUBAWARDS					0		
6. OTHER					590		
TOTAL OTHER DIRECT COSTS					3,810		
H. TOTAL DIRECT COSTS (A THROUGH G)					60,188		
I. INDIRECT COSTS (F&A)(SPECIFY RATE AND BASE)							
MTDC (Rate: 54.5000, Base: 45410)							
TOTAL INDIRECT COSTS (F&A)					24,748		
J. TOTAL DIRECT AND INDIRECT COSTS (H + I)					84,936		
K. RESIDUAL FUNDS					0		
L. AMOUNT OF THIS REQUEST (J) OR (J MINUS K)				\$	84,936	\$	
M. COST SHARING PROPOSED LEVEL \$ 0				AGREED LEVEL IF DIFFERENT \$			
PI/PI NAME David T Sandwell				FOR NSF USE ONLY			
ORG. REP. NAME*				INDIRECT COST RATE VERIFICATION			
				Date Checked	Date Of Rate Sheet	Initials - ORG	

SUMMARY PROPOSAL BUDGET Cumulative

ORGANIZATION University of California-San Diego Scripps Inst of Oceanography				FOR NSF USE ONLY			
				PROPOSAL NO.	DURATION (months)		
PRINCIPAL INVESTIGATOR / PROJECT DIRECTOR David T Sandwell				AWARD NO.	Proposed	Granted	
A. SENIOR PERSONNEL: PI/PD, Co-PI's, Faculty and Other Senior Associates (List each separately with title, A.7. show number in brackets)				NSF Funded Person-months		Funds Requested By proposer	Funds granted by NSF (if different)
				CAL	ACAD	SUMR	
1. David T Sandwell - Professor				0.00	0.00	0.00	\$ 0 \$
2.							
3.							
4.							
5.							
6. () OTHERS (LIST INDIVIDUALLY ON BUDGET JUSTIFICATION PAGE)				0.00	0.00	0.00	0
7. (1) TOTAL SENIOR PERSONNEL (1 - 6)				0.00	0.00	0.00	0
B. OTHER PERSONNEL (SHOW NUMBERS IN BRACKETS)							
1. (0) POST DOCTORAL SCHOLARS				0.00	0.00	0.00	0
2. (0) OTHER PROFESSIONALS (TECHNICIAN, PROGRAMMER, ETC.)				0.00	0.00	0.00	0
3. (2) GRADUATE STUDENTS							51,397
4. (2) UNDERGRADUATE STUDENTS							11,520
5. (0) SECRETARIAL - CLERICAL (IF CHARGED DIRECTLY)							0
6. (2) OTHER							12,327
TOTAL SALARIES AND WAGES (A + B)							75,244
C. FRINGE BENEFITS (IF CHARGED AS DIRECT COSTS)							28,593
TOTAL SALARIES, WAGES AND FRINGE BENEFITS (A + B + C)							103,837
D. EQUIPMENT (LIST ITEM AND DOLLAR AMOUNT FOR EACH ITEM EXCEEDING \$5,000.)							
TOTAL EQUIPMENT							0
E. TRAVEL 1. DOMESTIC (INCL. CANADA, MEXICO AND U.S. POSSESSIONS)							6,400
2. FOREIGN							0
F. PARTICIPANT SUPPORT COSTS							
1. STIPENDS \$ _____							0
2. TRAVEL _____							0
3. SUBSISTENCE _____							0
4. OTHER _____							0
TOTAL NUMBER OF PARTICIPANTS (0) TOTAL PARTICIPANT COSTS							0
G. OTHER DIRECT COSTS							
1. MATERIALS AND SUPPLIES							2,000
2. PUBLICATION COSTS/DOCUMENTATION/DISSEMINATION							0
3. CONSULTANT SERVICES							0
4. COMPUTER SERVICES							4,440
5. SUBAWARDS							0
6. OTHER							1,180
TOTAL OTHER DIRECT COSTS							7,620
H. TOTAL DIRECT COSTS (A THROUGH G)							117,857
I. INDIRECT COSTS (F&A)(SPECIFY RATE AND BASE)							
TOTAL INDIRECT COSTS (F&A)							48,648
J. TOTAL DIRECT AND INDIRECT COSTS (H + I)							166,505
K. RESIDUAL FUNDS							0
L. AMOUNT OF THIS REQUEST (J) OR (J MINUS K)							\$ 166,505 \$
M. COST SHARING PROPOSED LEVEL \$ 0				AGREED LEVEL IF DIFFERENT \$			
PI/PD NAME David T Sandwell				FOR NSF USE ONLY			
ORG. REP. NAME*				INDIRECT COST RATE VERIFICATION			
		Date Checked		Date Of Rate Sheet		Initials - ORG	

C *ELECTRONIC SIGNATURES REQUIRED FOR REVISED BUDGET

BUDGET JUSTIFICATION

Work will be performed by David Sandwell, Walter Smith (NOAA) and an SIO graduate student Xiaopeng Tong using facilities at SIO. Karen Scott will help organize this effort and coordinate travel, computer purchases, and day-to-day operations. The total budget to NSF is about \$82k/year for 2 years. The major budget items are salary support and tuition for a graduate student, and 1 mo./year salary for a Research Project Assistant to help organize and execute the research effort. We also request ~\$6k/year for an undergraduate student to participate in the research and update the web pages.

Salary recharge rates are calculated for actual productive time only (except for non-faculty academic sick leave, which is charged as direct). The rates include components for employee benefits, provisions for applicable merit increases and range adjustments in accordance with University policy. Domestic travel includes funding for one scientist to present results at Fall AGU Meeting each year and for Sandwell to travel to NOAA to work with Smith for a week each year. Project specific costs include computer network services, telephone equipment, tolls, voice and data communication charges, photocopying, faxing, postage, data tapes, office and computer supplies, and publication costs. Supply and expense items, categorized as project specific, and computer networking services are for expenses that specifically benefit this project and are reasonable and necessary for performance of this project.

Current and Pending Support

(See GPG Section II.D.8 for guidance on information to include on this form.)

The following information should be provided for each investigator and other senior personnel. Failure to provide this information may delay consideration of this proposal.	
Investigator: David Sandwell	Other agencies (including NSF) to which this proposal has been/will be submitted. None
Support: <input checked="" type="checkbox"/> Current <input type="checkbox"/> Pending <input type="checkbox"/> Submission Planned in Near Future <input type="checkbox"/> *Transfer of Support	
Project/Proposal Title: Improvement of Predicted Bathymetry for Naval Operations and Scientific Applications	
Source of Support: ONR N00014610140	
Total Award Amount: \$ 243,265	Total Award Period Covered: 11/01/05-09/30/08
Location of Project: SIO	
Person-Months Per Year Committed to the Project. Cal: 0 Acad: Sumr:	
Support: <input checked="" type="checkbox"/> Current <input type="checkbox"/> Pending <input type="checkbox"/> Submission Planned in Near Future <input type="checkbox"/> *Transfer of Support	
Project/Proposal Title: High Resolution Marine Gravity, Seafloor Topography, and Seafloor Roughness	
Source of Support: NSF OCE 0326707	
Total Award Amount: \$ 367,567	Total Award Period Covered: 07/15/03-06/30/07*
Location of Project: SIO *NCE approved thr 06/30/08	
Person-Months Per Year Committed to the Project. Cal: 0 Acad: Sumr:	
Support: <input checked="" type="checkbox"/> Current <input type="checkbox"/> Pending <input type="checkbox"/> Submission Planned in Near Future <input type="checkbox"/> *Transfer of Support	
Project/Proposal Title: The Geoid, Mean Dynamic Topography and Upper Ocean Variability in the Southern Ocean (w/ Sarah Gille, PI)	
Source of Support: NASA	
Total Award Amount: \$ 428,964	Total Award Period Covered: 07/01/04-06/30/09
Location of Project: SO	
Person-Months Per Year Committed to the Project. Cal: 0 Acad: Sumr:	
Support: <input checked="" type="checkbox"/> Current <input type="checkbox"/> Pending <input type="checkbox"/> Submission Planned in Near Future <input type="checkbox"/> *Transfer of Support	
Project/Proposal Title: Continental Margin Gravity and Bathymetry	
Source of Support: ConocoPhillips	
Total Award Amount: \$ 30,000	Total Award Period Covered: 03/01/07-03/01/08
Location of Project:	
Person-Months Per Year Committed to the Project. Cal: 0 Acad: Sumr:	
Support: <input type="checkbox"/> Current <input checked="" type="checkbox"/> Pending <input type="checkbox"/> Submission Planned in Near Future <input type="checkbox"/> *Transfer of Support	
Project/Proposal Title: Observations and Modeling of Shallow Fault Creep Along the San Andreas Fault Zone UCSD 20081732	
Source of Support: NSF EAR 0811772	
Total Award Amount: \$ 305,676	Total Award Period Covered: 06/01/08-05/31/11
Location of Project:	
Person-Months Per Year Committed to the Project. Cal: 0 Acad: Sumr:	

Current and Pending Support

(See GPG Section II.D.8 for guidance on information to include on this form.)

The following information should be provided for each investigator and other senior personnel. Failure to provide this information may delay consideration of this proposal.	
Investigator: David Sandwell	Other agencies (including NSF) to which this proposal has been/will be submitted. None
Support: <input type="checkbox"/> Current <input checked="" type="checkbox"/> Pending <input type="checkbox"/> Submission Planned in Near Future <input type="checkbox"/> *Transfer of Support	
Project/Proposal Title: Geodetic Imaging and Modeling of the San Andreas Fault System	
UCSD 20081269	
Source of Support: NASA/ROSES	
Total Award Amount: \$ 386,471	Total Award Period Covered: 01/01/08-12/31/10
Location of Project: SIO	
Person-Months Per Year Committed to the Project. Cal: 0 Acad: Sumr:	
Support: <input type="checkbox"/> Current <input checked="" type="checkbox"/> Pending <input type="checkbox"/> Submission Planned in Near Future <input type="checkbox"/> *Transfer of Support	
Project/Proposal Title: Accomplishment-Based Renewal Proposal: High Resolution Gravity, Topography, and Seafloor Roughness - THIS PROPOSAL	
UCSD 20082549	
Source of Support: NSF MGG	
Total Award Amount: \$ 166,505	Total Award Period Covered: 09/01/08-03/31/10
Location of Project: SIO	
Person-Months Per Year Committed to the Project. Cal: 0 Acad: Sumr:	
Support: <input type="checkbox"/> Current <input checked="" type="checkbox"/> Pending <input type="checkbox"/> Submission Planned in Near Future <input type="checkbox"/> *Transfer of Support	
Project/Proposal Title: Continental Margin Gravity and Bathymetry (continuation of award UCSD20080295)	
UCSD 20082643	
Source of Support: Conoco-Phillips	
Total Award Amount: \$ 30,000	Total Award Period Covered: 03/02/08-03/01/09
Location of Project: SIO	
Person-Months Per Year Committed to the Project. Cal: 0 Acad: Sumr:	
Support: <input type="checkbox"/> Current <input type="checkbox"/> Pending <input type="checkbox"/> Submission Planned in Near Future <input type="checkbox"/> *Transfer of Support	
Project/Proposal Title:	
Source of Support:	
Total Award Amount: \$	Total Award Period Covered:
Location of Project:	
Person-Months Per Year Committed to the Project. Cal: Acad: Sumr:	
Support: <input type="checkbox"/> Current <input type="checkbox"/> Pending <input type="checkbox"/> Submission Planned in Near Future <input type="checkbox"/> *Transfer of Support	
Project/Proposal Title:	
Source of Support:	
Total Award Amount: \$	Total Award Period Covered:
Location of Project:	
Person-Months Per Year Committed to the Project. Cal: Acad: Sumr:	

FACILITIES, EQUIPMENT, AND OTHER RESOURCES

Software and Data – Over the past 15 years, Sandwell and Smith have developed specialized software for processing of radar altimeter profiles, computing gravity anomalies from spherical harmonic models and residual sea surface slopes, and predicting seafloor depth from marine gravity and ship soundings. In addition, we have assembled global depth soundings from a variety of sources and have converted all the data to a common format for the construction of global bathymetry models.

General Computing Equipment - Our lab maintains state-of-the-art workstations, tape drives, and disk facilities for processing bathymetry and satellite altimetry data. We have access to a 30-terabyte mass storage system for backup and archival of results. Additionally, IGPP houses the Visualization Center at Scripps that comprises high-end immersive environments and graphics cluster systems, along with commodity graphics systems such as the Geowall-II and the iCluster (see <http://siovizcenter.ucsd.edu>).

SUPPLEMENTARY DOCUMENTATION

This section contains the following subsections:

- A) Letter of commitment from long-term collaborator Walter H. F. Smith at NOAA who is an equal investigator on this research.
- B) Comments and recommendations regarding the gravity and topography grids from peers in a variety of field.

Ridge – Trish Gregg/Mark Behn

Tectonics- Dietmar Mueller and Joann Stock

Seamounts – Paul Wessel

Physical Oceanography –Steve Jayne

Tide Modeling – Laurence Padman

Seismology – Shamita Das

Exploration Geophysics - Khalid Soofi

- C) Six reprints used as documentation for the Accomplishment-Based Renewal Proposal. This is many pages and probably **should not be printed**.



UNITED STATES DEPARTMENT OF COMMERCE
National Oceanic and Atmospheric Administration
NATIONAL ENVIRONMENTAL SATELLITE, DATA
AND INFORMATION SERVICE
Silver Spring, Maryland 20910

Laboratory for Satellite Altimetry
NOAA mail code E/RA-31

11 February 2008

Prof. Dr. David T. Sandwell
IGPF UCSD SIO code 0225
La Jolla CA 92093-0225

Re: NSF Accomplishment-Based Renewal Proposal "High-Resolution Gravity, Topography, and Seafloor Roughness"

Dear David,

I am writing to express my enthusiastic support and commitment to your NSF Accomplishment-Based Renewal Proposal "High-Resolution Gravity, Topography, and Seafloor Roughness". In addition to collaborating on the proposed tasks, I can provide connections to data and leverage a network of further U.S. and international partnerships.

As you know, I am cleared to access classified data held in the geodesy (St. Louis MO) and maritime (Bethesda MD) divisions of the National Geospatial-intelligence Agency, and in the Naval Oceanographic Office (Stennis Space Center MS) of the Naval Meteorology and Oceanography Command. By Memorandum of Agreement between these agencies, NOAA, and UCSD, I am the team lead coordinating this effort. NGA and CNMOC are supporting this project with releasable data and access to classified sources for ground-truthing the improvements in our data editing and assimilation algorithms.

You also know that since 2004 I am Chairman of the scientific and technical sub-committee of "GEBCO", the committee for the General Bathymetric Charts of the Oceans, a UN effort under the International Hydrographic Organization (IHO) and Intergovernmental Oceanographic Commission of UNESCO. In November 2007 GEBCO's Guiding Committee adopted our approach to global ocean mapping by fusion of in situ and satellite data, to be employed in future GEBCO products. New data are now flowing into our project from IHO member agencies via IHB and the British Oceanographic Data Centre. This will have enormous impact on the quality of the product in shallow water. We will furnish a global moderate-resolution (1 mile) bathymetry and topography model that will blend seamlessly with higher resolution local compilations developed for coastal hydrodynamic modeling such as tsunami run-up. Through GEBCO we also have access to international expertise in variable meshed grids, web services, and other useful things.

Our collaboration has spanned nearly two decades now, and has been a great source of pride and pleasure for me. Our papers in *Science* and the *Journal of Geophysical Research* on bathymetry and gravity have been cited more than 700 and 500 times. I will be delighted to continue our data product and human resources development, documentation, outreach, and new scientific investigations into the nature of fundamental seafloor processes.

Highest regards,

Walter H. F. Smith



B) To help focus our two-year research program we sent an e-mail to peers in a variety of subfields who are familiar with this research. The outgoing email request follows:

Dear Colleague,

We are preparing a proposal to obtain 2 additional years of funding from NSF to merge our 1-minute global marine gravity model (V16.1) with a new 5-minute continental gravity model being developed at the National Geospatial Agency called EGM2007. In addition we have just finished a 1-minute bathymetry grid (V9.1) and are in the process of revising the grid by gathering and editing more ship soundings. Finally we will propose to look at the details of ridge segmentation and morphology globally as well as investigate other research topics. The budget will pay for a graduate and undergraduate student, some travel, publications, and computer expenses.

Could you send a short e-mail note on how you have used these data in the past and what specific improvements you would like to see over the next 2-3 years? We will include this response in the supplementary documents section as evidence that additional research is (or is not) needed. The effective deadline is Feb 12. The entire renewal-based proposal is only 4 pages so this documentation will be valuable for the review process.

Title: Accomplishment-Based Renewal Proposal: High-Resolution Gravity, Topography, and Seafloor Roughness

Investigators: David Sandwell and Walter Smith.

Thanks,

David

P.S. Negative comments such as "the grid has been useful but there is a large depth error in the Tasman Sea due to a bad ship track" are valuable to justify additional work.



WOODS HOLE OCEANOGRAPHIC INSTITUTION

February 10, 2007

Dear David,

We are writing in support of your NSF proposal extension: *Accomplishment-Based Renewal Proposal: High-Resolution Gravity, Topography, and Seafloor Roughness*. In 2006, we took advantage of the outstanding advancements made by the Sandwell and Smith version 16, one-minute resolution, global marine gravity model. This new high-resolution model made it possible for us to conduct a global study of the residual mantle Bouguer gravity anomalies at oceanic transform faults. This study showed for the first time a spreading rate dependence of gravity anomalies at oceanic transform faults, which was published in this past year in the journal *Nature* (Gregg, Lin, Behn, & Montési, *Nature*, 2007). Our study and the subsequent results would not have been possible without the increased resolution capabilities in the global marine gravity model through versions 15 and 16. One compelling advantage of using the global marine gravity model data is that ship time to collect ship gravity is costly and sometimes difficult to procure. As such, a well-maintained global marine gravity database is essential for conducting both global studies as well as studies in locations without adequate ship-track gravity coverage.

We note that there remains room for improvement in this data set. Comparison of anomalies calculated from the global marine gravity model and those calculated from ship gravity reveal that limitations remain in the resolution of the satellite gravity in areas of the seafloor characterized by large, short wavelength bathymetric variations. This is particularly apparent at inside corner highs of oceanic transform faults on slow-spreading mid-ocean ridges. These issues may be resolved by incorporating higher resolution ship track bathymetry data in these regions. Because the global satellite-derived gravity dataset is such a heavily utilized tool for marine research, further improvements such as those proposed by Sandwell & Smith will benefit a large portion of the marine community. We will certainly continue to use this data and our research will benefit from advancements made in resolution.

If you have any further questions, please contact us at pgregg@whoi.edu or mbehn@whoi.edu.

Sincerely,

Patricia M. Gregg

Ph.D. Candidate
MIT/WHOI Joint Program
Woods Hole Oceanographic Institution
MS 24
Woods Hole, MA 02543
Office Phone: (508) 289-3371
Email: pgregg@whoi.edu

Dr. Mark D. Behn

Assistant Scientist
Dept. Geology & Geophysics
Woods Hole Oceanographic Institution
MS 22
Woods Hole, MA 02543
Office Phone: (508) 289-3637
Email: mbehn@whoi.edu

From: dietmarmuller@mac.com
Subject: Re: e-mail letter for renewal proposal
Date: February 4, 2008 1:52:06 AM PST

Hi David,

I am glad to hear that you will try to get funding for additional work on the global gravity and bathymetry grids.

For me and several of my collaborators two issues are the largest problems in using the current grids:

1) There are severe ship track artefacts in the previous bathymetry grid, and this makes it virtually impossible to use illuminated plots of this grid for making figures for papers or proposals, especially for tectonically oriented work, because the ship track artifacts look like fracture zones. A particularly bad example can be found in the Norfolk Basin.

2) The current low-resolution continental gravity model also hampers correlation of tectonic features from land to sea.

In addition, we have recently also used a downward-continued 2m version of the recent gravity grid (15.1) for an analysis of seafloor roughness (Walter Smith is a co-author of this work), which has provided some pretty interesting results, illustrating that there are factors which have an effect on roughness at least as large as spreading rate. A higher-resolution downward continued gravity grid would certainly be interesting in this context.

I hope this helps.

Cheers,
Dietmar
R. Dietmar Müller
Associate Professor
School of Geosciences, Building H11
University of Sydney NSW 2006, AUSTRALIA

From: jstock@gps.caltech.edu
Subject: Re: e-mail letter for renewal proposal
Date: January 31, 2008 10:08:06 AM PST

Hi David,
in response to your email, here are some comments, which you can use as you see fit.

I think you are providing an invaluable resource the scientific community with this gravity grid and related work.

We have found your global marine gravity information to be extremely helpful for all sorts of things - one of the biggest uses is for helping us understand what is on the seafloor in places in the southern oceans with no ship surveys (and for planning cruises to locations where we need a ship survey because we see features in the gravity field that are of unknown or uncertain origin). Many of the major advances in recognizing key tectonic features of the seafloor in the western Pacific were also fundamentally started by the observations of the gravity grid (for instance, the dead spreading center of the Osborn trough; the Wishbone Scarp, which may be a paleo-transform fault or an old incipient subduction zone that never progressed to full subduction). The more resolution you can give us with these data, and the better it can be tied to on-land gravity information, the more useful it will be for everybody.

I tend not to use your gravity-derived bathymetry too much, because there are still places where it clearly does not fit new observations, maybe because of the use of bathymetry from old ship tracks that were poorly navigated (I am just guessing). If you can incorporate ship multibeam data into your grid as these data become available, that would be really useful (but I presume you are doing that).

There are some places where the predicted bathymetry (using gravity) does not fit the known bathymetry even though both data sets are high quality and well navigated. These also key places for future investigation because it tells us that something else is contributing to the gravity field in a way that is not well known or easy to model (for example along some of the trench systems you have this problem). So it is not just a question of making a good bathymetry grid, but also of comparing the results to understand why these differences arise and what it can tell us about processes in the earth.

If I can provide any other comments please let me know.

Best regards,

Joann

From: pwessel@hawaii.edu
Subject: Support for renewal proposal
Date: February 6, 2008 8:42:40 AM PST

Dear Dave and Walter-

I strongly support your proposal to continue your excellent work on the global gravity and topography grids. My students and I are heavy users of these products for our research in intraplate volcanism and plate tectonics where regional or global assessments are required. For instance, we use your vertical gravity gradient (VGG) grid to detect and characterize seamounts in the world's oceans; the success or failure of our quest to locate all seamounts with height > 1 km depends critically on the availability of the latest processed grids. We are also very interested in using the free-air gravity grid to track oceanic fracture zones as part of a new global fracture zone initiative with Dietmar Muller. Finally, the predicted bathymetry grid is simply the best available data set for regional-scale bathymetric studies. Our Generic Mapping Tools (GMT) provide support for your file formats, which allows the > 10,000 GMT users worldwide easy access to your gridded data.

So, your work is certainly important and has a truly global impact. Can these products be improved? Yes, I believe so. There are several issues I would like to see you make improvements in. As we are trying to examine features at the threshold of the data resolution it is critical to be aware of the uncertainties in the data. I understand variables such as sea state and tides play significant roles in raising the noise level but this information is not readily available to the users of your gravity grids. While the casual user may not care, experts using your data in trying to do cutting-edge research most certainly care about error sources, so I hope you will consider distributing an error grid which would give your best estimate of the uncertainties in the values. As for the predicted bathymetry one would hope for a similar error product to accompany the data grid. Another issue is the treatment of original soundings in the predicted depth grid. Some tracks are still fairly visible in the grid (e.g, see around Cape Town). Part of that is the higher frequency content of the ship data but some seems to be related to mis-leveling. Hopefully our crossover corrections for the NGDC shiptracks (which should be available later this year) can be incorporated to reduce some of these artifacts.

Best of luck with the proposal.

Prof. Paul Wessel
Dept of Geology & Geophysics
SOEST, U of Hawaii at Manoa

From: sjayne@whoi.edu
Subject: Re: Fwd: e-mail letter for renewal proposal
Date: February 11, 2008 11:07:34 AM PST

Hi David - Here's my little blurb for your renewal proposal, is this along the lines of what you need?

The predicted bathymetry and topographic roughness are crucially important to correctly modeling the ocean. As ocean models achieve higher fidelity with progressively finer resolution, uncertainty in the bathymetry becomes more problematic. It is believed that one of the limiting factors for tidal modeling is errors in the bottom topography. Furthermore, to understand internal wave generation and propagation, the bathymetric roughness is also required, on the finest scales possible.

Steven Jayne
Physical Oceanography Dept., MS 21
Woods Hole Oceanographic Inst.
Woods Hole, MA 02543-1541

From: padman@esr.org
Subject: RE: e-mail letter for renewal proposal
Date: January 31, 2008 9:26:59 AM PST
Hi David,

I will certainly want to encourage further support of your efforts. It might be Wednesday next week before I can get to this, as I have meetings and deadlines beforehand. In the meantime, some random thoughts:

1) 9.1 still seems "lumpy" in places where we don't think it is.

2) I think the grid should go south to at least cover the ice shelves (so, ~85.5 S). And, it should include seabed topography under ice shelves as well as it is known. I have created a 1-km "ice-shelf mask" for the Antarctic and will work towards updated ice surface elevation for the shelves, basically refining BEDMAP. For a lot of modelers, a consistent set of (seabed topography; ice thickness; water column thickness) files would be invaluable. BEDMAP is behind the times with regard to bathymetry and the under-ice-shelf topography, and the 5-km grid is insufficient to resolve some important grounding line features.

I don't know whether you'd like to encompass (2) in your proposed work, but I'd like to see it. It is very easy to make a case for it, especially in climate modeling terms these days and riding the prospects arising from IPY activities. The Antarctic community will support making better maps of ice thickness, but seems uninterested in paying for professional merging of oceanographically-relevant products like bathymetry.

Cheers ... Laurie

Dr Laurence Padman
Senior Scientist
Earth & Space Research

From: Shamita.Das@earth.ox.ac.uk
Subject: e-mail letter for renewal proposal
Date: February 1, 2008 1:25:44 AM PST

Dear Dave,

I have used your data to interpret the earthquake rupture process for large, submarine earthquakes. I think the easiest is for me to give you a list of papers where this is used, so I do so below. Do you still need a letter from me? I could say that I need better quality marine data to better interpret my results, in the letter.

Good luck, and I will be at igpp from March 8 for a month. best wishes shamita

S. Das and AB Watts (2008), Effect of the subducting seafloor topography on the rupture characteristics of great subduction zone earthquakes, Submitted to Special Volume on the Proceedings of SUBCO Conference, June 2007, Montpellier, France, Springer Publications.

Robinson, D. P., S. Das, A. B. Watts (2006), Earthquake rupture stalled by subducting fracture zone, Science, 312(5777), 1203-1205.

Das, S. and C. Henry (2003) Spatial relation between main earthquake slip and its aftershock distribution, Rev. Geophys., 41(3), 1013, doi:10.1029/2002RG000119, 2003.

C. Henry and S. Das, (2002), The Mw 8.2 February 17, 1996 Biak, Indonesia earthquake: Rupture history, aftershocks and fault plane properties, J. Geophys. Res., 107(B11), 2312, doi:10.1029/2001JB000796, 2002.

D. P. Robinson, C. Henry, S. Das and J. H. Woodhouse (2001), Simultaneous Rupture Along Two Conjugate Planes of the Wharton Basin Earthquake, Science, 292, 1145-1148. [See also: Perspectives: "Indian ocean actively deforms", by C. Deplus, 2001, Science, 292(5519), 1850-1851.]

C. Henry, S. Das and J. H. Woodhouse, (2000). The great March 25, 1998 Antarctic Plate earthquake: Moment tensor and rupture history, J. Geophys. Res., 105, 16,097-16,119.

From: Khalid.A.Soofi@conocophillips.com
Subject: RE: e-mail letter of support for renewal proposal
Date: January 31, 2008 9:25:58 AM PST

David,

The Remote Sensing Lab of Technology Department – ConocoPhillips maintains a set of global grids at our corporate headquarters to help Exploration and Production departments of various ConocoPhillips' Business Units around the world. Among others, these global grids include of Free Air Gravity Anomaly and Detailed Bathymetry and Topography. The Free Air Gravity is mainly used by the Exploration Group to look for either new plays in old basins or new basins altogether for potential new resources of Hydrocarbons. More specifically the Free Air Gravity Anomaly can be used to define the outlines of sedimentary basins, model the potential thickness of sedimentary cover and depth to basement. It is also used frequently to verify the interpreted horizons from 3D seismic data. The topography and bathymetry data is mainly used by our Production Department to generate potential routes for pipelines to transport hydrocarbons, look for potential facility sites (when combined with satellite imagery) and in general provide an efficient tool for desktop studies.

The offshore Free Air Gravity Anomaly has been steadily improved from a 10 minute to the current 1

minute grid, however the on shore gravity anomaly has been static at 15 minute grid, which essentially makes that useless for any on shore exploration applications. There is a desperate need to improve that resolution to bring it par to offshore quality/resolution.

We also need to improve the resolution of bathymetry, particular in areas of less than 2000 meters of water. The current grid is extremely smooth near shore and has large errors which makes these data unusable near shore.

Soofi

Retracking ERS-1 altimeter waveforms for optimal gravity field recovery

David T. Sandwell¹ and Walter H. F. Smith²

¹*Scripps Institution of Oceanography, La Jolla, CA 92093-0225, USA*

²*National Oceanic and Atmospheric Administration, Silver Spring, MD 20910, USA*

Accepted 2005 July 27. Received 2005 June 6; in original form 2004 December 8

SUMMARY

We have reprocessed ERS-1 radar altimeter waveforms using an algorithm designed to minimize sea surface slope error and decouple it from significant wave height (SWH) error. Standard waveform retracking estimates three parameters—arrival time, SWH and amplitude. We show that errors in retracked estimates of arrival time and SWH are inherently correlated because of the noise characteristics of the returned waveform. This suggests that some of what is called ‘sea state bias’ in the literature may be caused by correlated errors rather than true electromagnetic or skewness bias. We have developed a retracking algorithm that reduces this error correlation and makes the resolution of sea surface slope signals independent of sea state. The main assumption is that the SWH varies smoothly along the satellite track over wavelengths of 90 km. This approach reduces the rms error in sea surface slope to only 62 per cent of that of standard retracking methods. While our method is optimized for gravity field recovery, it may also improve the resolution of sea surface height signals of interest to physical oceanographers.

Key words: gravity anomaly, radar altimetry.

INTRODUCTION

Satellite radar altimetry has become an important tool for investigating the tectonics of the ocean basins, especially in areas of sparse ship coverage. The ocean surface is nearly an equipotential surface of gravity, so high spatial resolution maps of ocean surface topography can be converted to gravity anomalies and even used to predict regional variations in seafloor depth (Smith & Sandwell 1997). Further improvement in the accuracy and resolution of the marine gravity field will require more precise altimeter measurements and/or a longer duration mission to minimize the various noise sources. For recovery of the static marine gravity field, the critical measurement is the slope of the ocean surface. Laplace’s equation combined with Bruns’ formula shows that one microradian (μrad) of ocean surface slope roughly corresponds to 1 milligal (mGal) of gravity anomaly. Ocean surface slope can be estimated by differencing height measurements along satellite altimeter profiles, so absolute range accuracy is largely irrelevant. Indeed the usual corrections and ancillary data that are needed to recover the temporal variations in ocean surface height associated with currents and eddies are largely unimportant for the recovery of the gravity field because the slope of these corrections is far less than the slope error in the radar altitude measurement.

Consider the recovery of a 1 mGal accuracy gravity anomaly having a wavelength of 28 km. This requires a sea surface slope accuracy of 1 μrad over a 7-km-length scale (1 s of flight along the satellite track), necessitating a height precision of 7 mm in one-

per-second measurements of sea surface height. Current satellite altimeters such as Geosat, ERS-1/2 and Topex have typical 1-s averaged range precision of 30–40 mm resulting in gravity field accuracies of 4–6 mGal. There are three ways to improve the gravity field accuracy. First, one could design and fly a new radar altimeter with inherently better range precision than the current generation of altimeters (Raney *et al.* 2004). Second, one could make multiple measurements of ocean surface slope. The currently available non-repeat ocean altimeter measurements come from 1.5 yr of Geosat during its Geodetic Mission and 1 year of ERS-1 during its geodetic phase. Third, one could improve the range precision of the existing measurements.

Maus *et al.* (1998) took the third approach, developing and implementing a new waveform retracking algorithm that significantly improves the precision and along-track resolution of the ERS-1 altimeter data. Their algorithm operates on multiple waveforms and imposes a smoothness criterion for the multiple arrival times within the group. More important, they use a single rise-time parameter for the group to stabilize the recovery of the arrival times. While their paper provides a recipe for improving range precision with respect to standard retracking methods, they do not fully discuss the assumptions of their method and the physical meaning of constrained parameters in their approach.

In this paper we develop our own retracking approach. Our results confirm the analysis and recommendations of Maus *et al.* (1998), and clarify why that approach works well. However, our approach does not require simultaneous inversion of multiple waveforms, and

we also do not require a smoothness constraint on arrival times; our only constraint is that the rise-time parameter must vary smoothly along the satellite's ground track. Physically this corresponds to the assumption that the sea surface roughness, due to ocean waves and swell, varies smoothly in space. Our approach is easier to implement on a small computer, as the non-linear least-squares inversion operations are done only one waveform at a time. Further, the correlation length scales in the rise-time and amplitude parameters are explicitly adjustable in our technique, giving physical insight and meaning to the tuned parameters.

Here we investigate the general problem of correlated errors and sea state bias, to show the motivation for our retracking scheme. Our strategy for reducing those errors obtains a significantly reduced error variance, but more importantly, the spatial resolution of data processed by our method is independent of sea state. These results may be applied to ocean data from any satellite radar altimeter and should have wide application. Using our method, we have retracked the ERS-1 altimeter waveform data for all of the geodetic phase and part of the 35-day-repeat phase, and we will make these retracked data available to the scientific community. This paper, therefore, also contains an investigation of the expected error distribution in ERS-1 waveforms caused by a unique feature of the ERS-1 hardware. We are also experimenting with retracking all of the Geosat altimeter data using similar methods. Geosat has its own unique peculiarities, which will be the subject of another paper.

A MODEL FOR THE RETURNED OCEAN WAVEFORM AND ITS EXPECTED NOISE

To understand the assumptions and technique for improving the range precision, we start with a simplified discussion of how a radar pulse interacts with the ocean surface. For a more complete treatment of the engineering aspects of radar design and ocean reflection characteristics see the primary references (Brown 1977; Hayne 1980; MacArthur *et al.* 1987; Hayne *et al.* 1994; Rodriguez & Martin 1994; Chelton *et al.* 2001; Amarouche *et al.* 2004). The radar altimeter emits a short pulse, or more precisely, a frequency-modulated chirp that reflects from the ocean surface and returns to the antenna. The recorded power is the double convolution of the system point target response with the ocean surface height distribution and the two-way antenna pattern. The height distribution of ocean waves is well approximated by a Gaussian function (Stewart 1985); if the point target response is also approximated with a Gaussian form then the form of the return power is well approximated by an error function with a slow decay of the trailing edge due to the finite antenna beam width. A model for the expected power versus time is (Brown 1977; Amarouche *et al.* 2004).

$$M(t, t_o, \sigma, A) = \frac{A}{2} [1 + \operatorname{erf}(\eta)] \begin{cases} 1, & t < t_o \\ \exp[-(t - t_o)/\alpha], & t \geq t_o \end{cases} \quad (1)$$

where

$$\eta = \frac{(t - t_o)}{\sqrt{2}\sigma}, \quad (2)$$

and where t is the time since the pulse was transmitted, t_o is the arrival time of the half power point of the returned energy, σ is the arrival rise-time parameter, A is the amplitude of the returned waveform, and α is an exponential decay in the trailing edge due to the finite beam width of the antenna. In addition to these four parameters,

waveforms from some altimeters also show a background noise level.

The pointing accuracy of the ERS spacecraft was generally very good and the antenna mispointing was much less than the antenna beam width, so we set this decay parameter α to a constant (137 nsec). The ERS-1 altimeter hardware truncated small power levels to zero (discussed below), and so we do not need a background noise level parameter. Therefore our retracking model for ERS-1 has only three free parameters, A , t_o and σ . The automatic gain control loop in hardware maintained A at a relatively constant level, and the significantly variable parameters of chief concern in this paper are t_o and σ . In our model fitting, these are treated as non-dimensional parameters in dimensionless units of waveform sample gate widths; the physical time sampled by an ERS-1 waveform gate sample is 3.03 ns of two-way travel time, corresponding to 0.4545 m of range to the sea surface. The rise width of the waveform, σ , is a convolution of the effective width of the point target response and the vertical distribution of ocean surface waves, usually parameterized in terms of a Gaussian standard deviation equal to one-fourth of the significant wave height, SWH. An example model waveform for $\sigma = 6.67$ ns (significant wave height of 3.6 m) is shown in Fig. 1 (upper).

The objective of our analysis is to reduce the error in the estimated arrival time of the pulse, t_o . However, before considering this problem one must understand the signal and noise characteristics of the return waveform. The ERS radar altimeter emits 1020 pulses per second and the returned power P_i is recorded in 64 gates spaced at 3.03 ns. An onboard tracker is used to keep the pulse approximately centred in the traveltime window (gate 32) while 50 returned pulses are averaged. The averaged returned waveforms are available from the European Space Agency in the 'WAP' data product, which also contains the onboard tracker's estimate of the expected range to the ocean surface used to align the waveforms.

An individual radar pulse reflects from numerous random scatterers on the ocean surface so the return power versus time will be noisy—essentially following a Rayleigh scattering distribution. This high noise level is reduced in the 50 waveform average. Assuming the speckle is incoherent from pulse to pulse, this incoherent average will reduce the speckle noise by a factor of $\sqrt{50}$. Ideally, in averaging 50 values one first sums the individual contributions and then divides the sum by 50. However, to avoid overflow in the ERS-1 hardware, each waveform gate sample was first divided by 50, the result truncated downward to an integer, and then the truncated value added to the accumulating sum. Since each waveform contains random fluctuations the effect of this hardware truncation can only be investigated with a Monte Carlo simulation (Appendix A). We have found that expected mean power levels below about 23 will be truncated to zero, so the emergent leading edge of the pulse is lost. The averaging of 50 pulses combined with the truncation issue leads to the following functional form for the uncertainty in the power W_i as a function of the recorded power P_i

$$W_i = \frac{(P_i + P_o)}{\sqrt{K}}, \quad (3)$$

where K is the number of statistically independent waveforms used in the average and P_o is the offset due to the truncation. Our Monte Carlo simulation of the truncation process and our experiments in optimizing the retracking of real ERS waveforms led us to use $K = 44$ and $P_o = 50$, which is essentially the same weighting used by Maus *et al.* (1998). While the results are largely insensitive to the exact numerical values for K and P_o , the functional form of this uncertainty leads to a high correlation between the arrival time

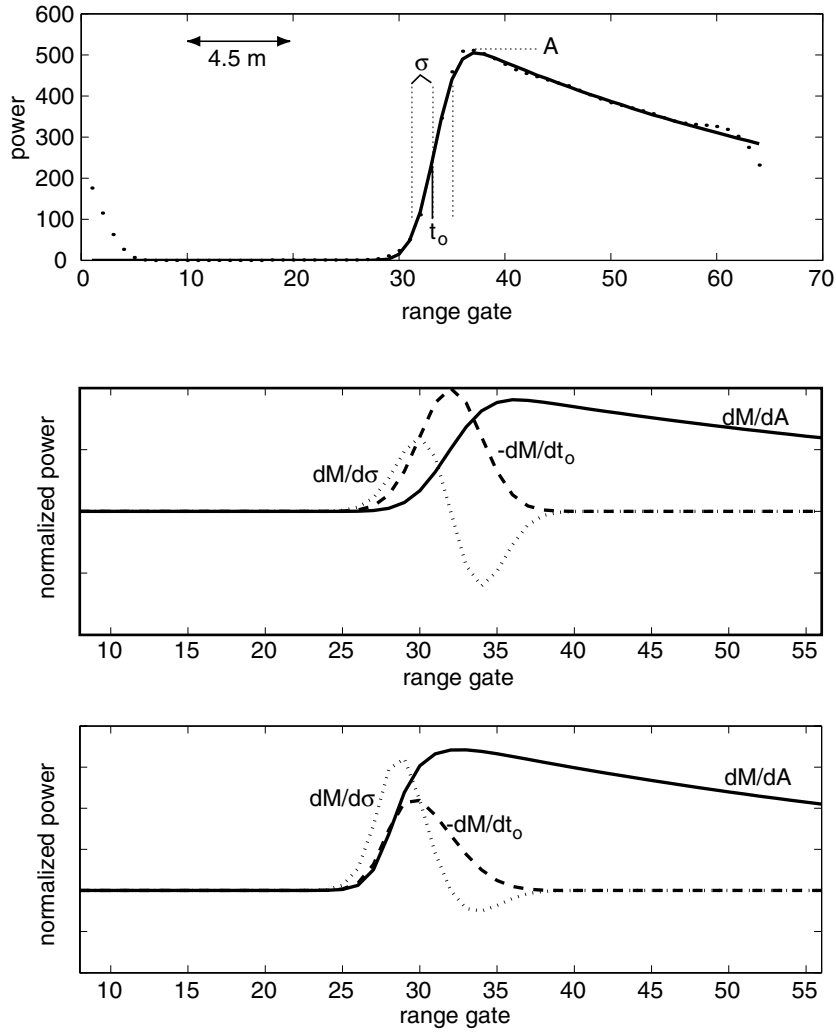


Figure 1. Upper—average of 10 000 ERS-1 radar waveforms (dotted) and a simplified model (solid, equation 1) with three adjustable parameters: A —amplitude, t_o —arrival time, and σ —rise time. Time parameters are measured in dimensionless waveform gate widths equal to 3.03 ns of two-way travel time or 454 mm of range to the sea surface. middle—partial derivatives of model (eq. 1) with respect to A (solid), t_o (dashed) and σ (dotted) versus gate number. Note the functions dM/dt_o and $dM/d\sigma$ are orthogonal. Lower—partial derivatives of the model waveform weighted by the expected uncertainty in the power (eq. 3). Note the functions dM/dt_o and $dM/d\sigma$ appear similar. This leads to a high correlation between arrival time and rise time during the least-squares estimation.

and the rise time when they are estimated using a weighted least-squares approach. Overcoming this correlation is the essence of our study.

LEAST-SQUARES MODEL FITTING: CORRELATED MODEL ERRORS

A standard least-squares approach is used to estimate the three parameters (t_o , σ and A). Because the problem is non-linear in arrival time and SWH, we use an iterative gradient method. The chi-squared measure of misfit is

$$\chi^2 = \sum_{i=1}^N \left[\frac{P_i - M_i(t_o, \sigma, A)}{W_i} \right]^2, \quad (4)$$

where N is the number of gates used for the fit and M_i is the model evaluated at the time of the i th gate. One starts the iteration by subtracting a starting model based on parameters t_o^o , σ^o and A^o . The updated model parameters t_o^1 , σ^1 and A^1 are found by solving the

following linear system of equations

$$\begin{bmatrix} P'_1 \\ P'_2 \\ \vdots \\ P'_N \end{bmatrix} = \begin{bmatrix} \frac{\partial M_1}{\partial t_o} & \frac{\partial M_1}{\partial \sigma} & \frac{\partial M_1}{\partial A} \\ \vdots & \vdots & \vdots \\ \frac{\partial M_N}{\partial t_o} & \frac{\partial M_N}{\partial \sigma} & \frac{\partial M_N}{\partial A} \end{bmatrix} \begin{bmatrix} t_o^1 - t_o^o \\ \sigma^1 - \sigma^o \\ \vdots \\ A^1 - A^o \end{bmatrix}, \quad (5)$$

where P'_i is the waveform power minus the model from the previous iteration. The derivatives of the model with respect to the parameters are

$$\frac{\partial M}{\partial t_o} = \frac{-A}{\sigma\sqrt{2\pi}} e^{-\eta^2}, \quad (6)$$

$$\frac{\partial M}{\partial \sigma} = \frac{-A}{\sigma\sqrt{\pi}} \eta e^{-\eta^2},$$

$$\frac{\partial M}{\partial A} = \frac{M}{A}.$$

We have not included the complications of the exponential decay in the partial derivatives of eq. (1) because this effect is largely removed with the starting model, and because residual misfits in the plateau of the waveform are chiefly random and do not significantly drive the fit of the three important parameters. These partial derivatives are shown in Fig. 1 for the case of an unweighted and weighted least-squares adjustment. A standard Newton iteration algorithm is used

to determine the three model parameters (t_0 , σ , A) that minimize the rms misfit.

An interesting feature of this least-squares problem is an inherent correlation between errors in estimated arrival time and errors in estimated rise time. We explore this with Monte Carlo experiments simulating model fitting to noisy data. In an experiment we generate 2000 realizations of noisy waveforms, each waveform having the

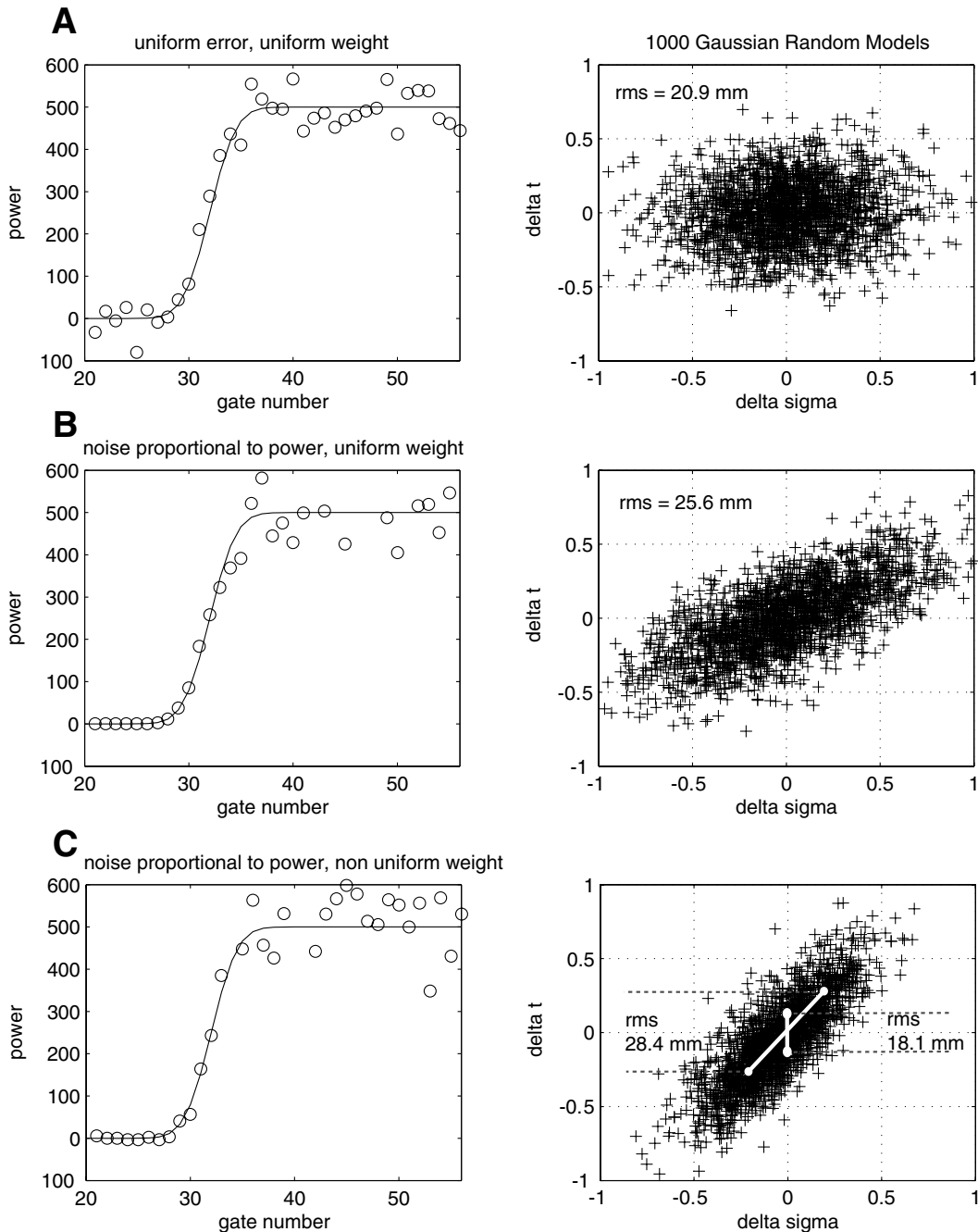


Figure 2. Simulations of least-squares parameter estimation. For each case (A, B, C) 2000 random models were constructed by adding noise to the exact model waveform (solid curve left plots) and a non-linear least-squares approach was used to recover the model parameters. Right plots show errors in estimation of arrival-time (δt) and rise-time ($\delta \sigma$) parameters. Case A with uniform noise and uniform weight has no correlation between arrival time and rise time (rms-arrival-time error equivalent to 20.9 mm in sea surface height). Case B with noise proportional to power and uniform weight has some correlation between arrival time and rise-time (rms-arrival-time error 25.6 mm of height equivalent). Case C with noise proportional to power and weight inversely proportional to power has high correlation between arrival time and rise time (rms-arrival-time error 28.4 mm in height). If the rise-time parameter were known the rms error in arrival time could be reduced to 18.1 mm of height, corresponding to a 36 per cent reduction in noise.

same known true parameters for arrival time, rise time and amplitude, plus an independent realization of random noise. We then do a least squares fit to each waveform, obtaining 2000 noisy estimates of each model parameter, and we examine the error distribution in these estimated parameters. The results of these experiments are shown in Fig. 2, for each of three different cases we examined: experiment 'A' employs constant waveform error and uniform least-squares weighting; experiment 'B' employs waveform error proportional to waveform power but uniform least-squares weighting; and experiment 'C' has waveform error and least-squares weight both proportional to waveform power.

First consider experiment 'A', the physically unrealistic case where the waveform noise is uniform across all gates. Noise in the waveform power introduces an error in all three estimated parameters. The simulation shows that the error in rise time and arrival-time are uncorrelated, and for this case, the rms uncertainty in the arrival-time estimate is equivalent to 20.9 mm of uncertainty in resolved sea surface height (Fig. 2a).

It is physically more realistic to consider cases in which the received waveform noise is proportional to the received power (eq. 3). In this situation we may choose to make a uniformly weighted least-squares fit, setting all W_i equal in eq. (4) (effectively an unweighted fit), or we may choose non-uniform weighting, substituting (3) in (4), (a weighted fit). Our simulations of these two cases are experiments 'B' (unweighted) and 'C' (weighted).

In the unweighted case (Fig. 2b) the simulation shows a correlation between rise time and arrival time and rms uncertainty in the arrival time has increased to 25 mm of height equivalent. More important, the two parameters are now correlated so a positive error in the estimate of rise time will produce a positive error in the estimate of arrival time. Since rise time and arrival time are related to the physical parameters of SWH and sea surface height, the inherent correlation has the same effect as the so-called sea state bias. True electromagnetic (EM) bias occurs because more energy reflects from the troughs of the waves than from the crests so arrival time increases with increasing SWH. The simulation shows the same type of behaviour. Indeed we suggest that the so-called sea state bias (different for each altimeter, Scharroo & Lillibridge 2005) consists of a true EM bias and an artificial bias that is related to the least-squares estimation approach as well the noise response characteristics of the radar instrument.

Finally we consider the case of a weighted least-squares estimate of the three waveform parameters (Fig. 2c). Maus *et al.* (1998) proposed that to obtain an improved estimate of the arrival time one should weight the least-squares adjustment where the gates with higher noise (i.e. higher power) are down weighted (eqs 3 and 4). We remark that in theory, this weighted least-squares approach should yield the maximum likelihood model parameters if there is no gate-to-gate or waveform-to-waveform correlation of the waveform errors. This weighted approach is the basis of the 'SMLE' retracker used by the European Space Agency to make the 'OPR' retracked data product. However, in this case our simulations and previous studies (Dumont 1985; Rodriguez 1988), show even a more severe correlation between rise time and arrival time having a slope of 1, which translates into a sea state bias of nearly 25 per cent. We confirmed this effect by retracking ERS-1 data using the three-parameter weighted least-squares approach and then determining the sea state bias that provides the best rms match between retracked sea surface slopes and slopes of the GFSC00 mean sea surface model (Wang 2000). The analysis of real data requires a 23 per cent SSB for best fit. Note when the sea state bias is estimated for heights rather than slopes, the best SSB is about 8 per cent. This is because the errors in

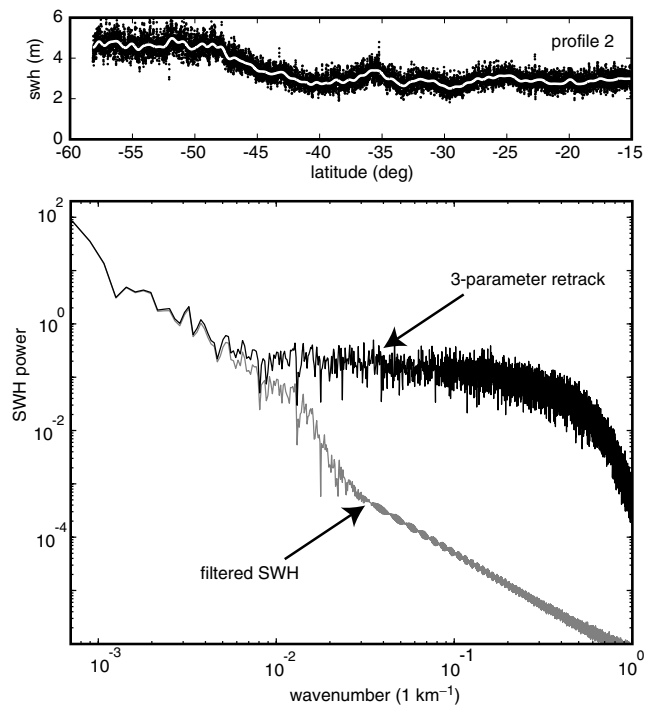


Figure 3. Upper—SWH profile across the South Pacific Ocean derived from the 3-parameter retracking algorithm. Lower—Power spectrum of SWH for six profiles shows a noise floor intersecting the SWH signal at a wavelength of about 100 km. We filter the SWH using a Gaussian filter with a 0.5 gain at 90-km wavelength (grey curves upper and lower) to provide a stable estimate of SWH for the 1-parameter retracking algorithm.

the SWH primarily occur at short wavelengths which are enhanced in the slope profiles. In addition to the adverse correlation of the weighted least-squares approach, the rms error in the arrival time increases to 28.4 mm of height equivalent, which is worse than the case of uniform weight.

APPROACHES TO REDUCE THE SEA SURFACE HEIGHT ERROR

Assume for the moment that the true rise time and amplitude were known *a priori* so that the least-squares model fit could be performed for only one parameter, the arrival time. This case is illustrated in Fig. 2(c) where we have assigned zero error to our rise-time estimate. For this one-parameter model, the rms in the arrival time is reduced to 18.1 mm of height equivalent. This is a 30 per cent improvement over the three-parameter unweighted solution and nearly a 40 per cent improvement over the three-parameter weighted solution. Therefore if the rise time, or equivalently, the SWH was known *a priori*, then the arrival time could be measured more precisely which would lead to an improved estimate of slope and ultimately gravity anomaly.

To achieve this objective, we assume that the SWH varies smoothly along each satellite profile. There is a physical basis for making the assumption—at least in the deep ocean. Spatial variations in SWH will depend on convolution of temporal variations in wind forcing with the wave group velocity (6–12 m s⁻¹). Typically a storm takes a day or so to pass over a fixed point and during this time the surface waves will travel 500–1000 km usually outrunning the storm. Therefore, SWH should be very smooth over length scales less than

a few hundred kilometres. The assumption will break down as the waves approach depths comparable to their wavelength ~ 300 m, since the amplitudes will increase and the wavelength will shorten over distances related to the bathymetric gradient. Therefore, the assumption will not be as good in coastal areas. Monaldo (1988) found correlation scales of order 100 km in the SWH field.

Our overall approach for minimizing error in sea surface slope is to: (1) retrack each waveform (or several waveforms) independently using the full three-parameter model, (2) smooth the rise-time and amplitude parameters in the along-track direction with a low-pass filter and (3) retrack the data again using the smoothed rise time and amplitude as *a priori* constraints in the more precise one-parameter fit for arrival time only. The appropriate low-pass filter wavelength for the rise-time parameter was determined through a power spectral analysis of six altimeter profiles crossing the Pacific basin. An example is shown in Fig. 3 where the SWH power decreases with increasing spatial frequency until 0.01 cyc-km $^{-1}$. At higher wavenumbers the power is relatively flat and we interpret this as white noise caused by errors in our estimate of the rise-time parameter; to suppress this noise we have adopted a Gaussian low-pass filter with a 0.5 gain at 90 km full wavelength. In addition to smoothing the rise-time parameter prior to retracking, we also smooth the amplitude but over a shorter wavelength, using a Gaussian low-pass filter with a 0.5 gain at 14 km full wavelength. This length is slightly less than the characteristic length scale of a noise

resonance in the onboard alpha/beta tracking software that adjusts the tracking parameters and gain onboard the satellite (Rodriguez & Martin 1994).

IMPROVEMENTS IN PRECISION, RESOLUTION, AND COVERAGE

We have implemented this retracking algorithm using the ERS-1 Altimeter Waveform Product (WAP, Infoterra Limited, Farnborough, UK, 2001) provided by the European Space Agency at the full 20 Hz sampling rate. These data include the ocean-mode waveforms sampled at 64 range gates. Phases E and F provide an 8-km track spacing at the equator that is needed for construction of 16-km wavelength resolution gravity models. The six repeat cycles from phase G were used to assess the performance of the retracking algorithm.

Waveform data were pre-processed to add the latest orbits and corrections. Precise ERS-1 orbits (Scharroo *et al.* 1998) were used to recompute the latitude, longitude and height of the spacecraft above the WGS84 reference ellipsoid. The CSR4.0 tide model (Bettadpur & Eanes 1994) was computed at each location while the other environmental corrections available on the WAP record were used. For recovery of the gravity field from altimetry, the only corrections that exceed the 1 μ rad desired error threshold are due to coastal tides and large orbit error (>2 m). The 550 days of waveform data were

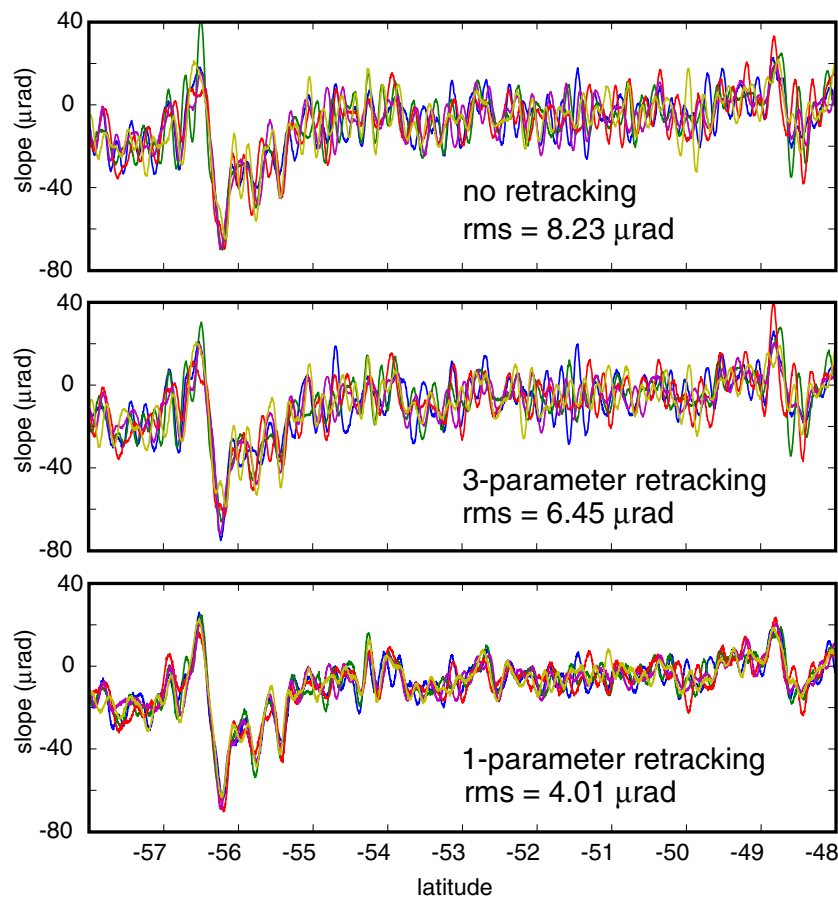


Figure 4. Profiles of along-track sea surface slope for 6 repeat cycles crossing the South Pacific Ocean in a region of generally high SWH. The upper profiles were derived from the onboard tracker available in the waveform data record (rms deviation from model of 8.23 μ rad). The middle profiles were derived using a weighted least-squares 3-parameter retracking algorithm as in Monte Carlo experiment 'C' shown in Fig. 2(c) (rms = 6.45 μ rad). The lower profiles were derived from a 1-parameter retracking algorithm constrained by smoothing the rise-time and amplitude parameters as in the text (rms = 4.01 μ rad).

reformatted into 184-byte records at a 20-Hz sampling rate, which amounts to about 0.5 billion waveforms (95 Gbytes). The three-parameter retracking was performed using a standard non-linear Newton–Raphson iteration where typically five to nine iterations were needed to achieve convergence. The data were segmented into profiles having time gaps no greater than 4 s and low-pass Gaussian filters were applied to the rise-time and amplitude parameters. The data were retracked a second time using the smoothed rise-time and amplitude parameters and solving for the arrival time using a Golden section search in one dimension as implemented in Numerical Recipes (Press *et al.* 1992).

IMPROVEMENTS IN SLOPE ACCURACY AND ALONG-TRACK RESOLUTION

Accuracy and resolution were estimated using the 6 repeat profiles from phase G of the ERS-1 mission. Accuracy was assessed by computing along-track slope for profiles crossing the Pacific ocean over areas of both high and low SWH (Fig. 4). Slope was computed at 20 Hz sampling rate and then low-pass filtered with a 0.5 gain at 18 km to simulate the smoothing filters that are applied when a gravity field is constructed. Slopes based on the arrival-time estimate from the onboard tracker are shown in the top panel and have an rms deviation about the mean profile of $8.23 \mu\text{rad}$. Slopes derived from the three-parameter retracking algorithm (centre panel) have an rms deviation of $6.45 \mu\text{rad}$ while slopes derived from the one-parameter retracking algorithm (lower panel) have an rms deviation of $4.01 \mu\text{rad}$. Further analysis shows the greatest improvement in areas of generally high SWH. Although we have not analysed the comparable Ocean Product (OPR V3) for these ERS-1 data, we expect the noise level is similar to the three-parameter retracking results. Thus this new algorithm reduces the rms error to 62 per cent of the rms error for the standard retracking methods which corresponds to a 38 per cent improvement in range precision.

Improvements in along-track slope accuracy translate into improvements in along-track resolution. To assess the resolution improvement we selected two areas for repeat-track analysis that match the two areas used by Yale *et al.* (1995). The first area is the equatorial Atlantic, which has high gravity signal and low oceanographic noise (Fig. 5, top). Coherence between repeat tracks was computed for the three cases of onboard tracking (dotted), three-parameter retrack (dashed line) and one-parameter retrack (solid line). This area shows an improvement in resolution from 36 to 32 km. A similar analysis in the South Pacific, which is an area of low gravity signal and high oceanographic noise, shows an improvement from 43 to 33 km.

Finally, we demonstrate the improvement in altimeter coverage in coastal areas. The test area is the back-arc region between Indonesia and Borneo. This is a challenging area for gravity field recovery from altimetry because the tracks run mainly N–S and the track spacing is greatest at the equator (~ 8 km). The gravity anomalies have relatively short wavelength and low amplitude in relation to the noise. We plot along-track slope profiles minus EGM96 (Lemoine *et al.* 1998) for two cases—onboard tracking (Fig. 6—left) and retracked (Fig. 6—right). The lower noise level of the retracked data reveals previously unseen gravity signals spanning multiple adjacent tracks; note that both sets of profiles were edited and filtered using the same algorithms. The lower noise level of the retracked data causes fewer data to be edited, especially near the coastline so near-shore coverage is improved.

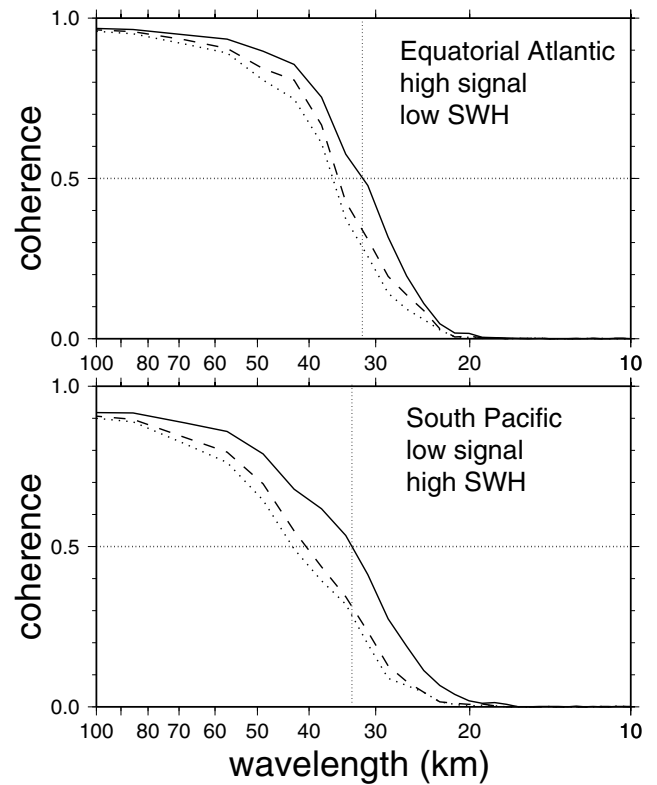


Figure 5. Coherence between repeat altimeter profiles in two areas studied in Yale *et al.* (1995). Dotted curve no retracking, dashed curve 3-parameter retracking, solid curve 1-parameter retracking. Retracking improved the 0.5 coherence from 36 to 32 km in the Equatorial area and from 43 km to 33 km in the South Pacific area. An important result is that the 1-parameter approach yields a wavelength of 0.5 coherence, which is essentially independent of sea state.

Using the retracked ERS-1 data we have also constructed a gravity model and compared the satellite-derived gravity to a ship profile to determine the improvement in accuracy due to retracking (Fig. 7). The comparison with anomalies from gravity model Version 9.1 (no retracking) has a mean difference of 25.3 mGal and an rms difference of 5.62 mGal. Retracking of ERS-1 results in an improved rms of 4.75 mGal. (Non-zero mean differences are expected due to absolute calibration errors in ship gravimetry, Wessel & Watts 1988.) In addition to retracking ERS-1 data we are experimenting with retracking Geosat data and using a least-squares method of bi-harmonic splines (Sandwell 1987; Wessel & Bercovici 1998) to grid the along-track residual slopes. These combined effects improve the rms misfit to 2.98 mGal. We believe that a more careful treatment of all the non-repeat orbit altimeter data will result in significant improvements in the global marine gravity field.

COMPARISON WITH THE METHOD OF MAUS *ET AL.*

To increase the precision of estimated arrival time, Maus *et al.* (1998) invert 408 waveforms simultaneously to recover 408 estimates of arrival time but constrained to share only a single estimate of rise time. In addition, the 408 arrival-time estimates are coupled, as in a smoothing spline, to guarantee that the power spectrum of the resulting sea surface height will have a desired shape. We believe the key to their approach, which was not highlighted in their study,

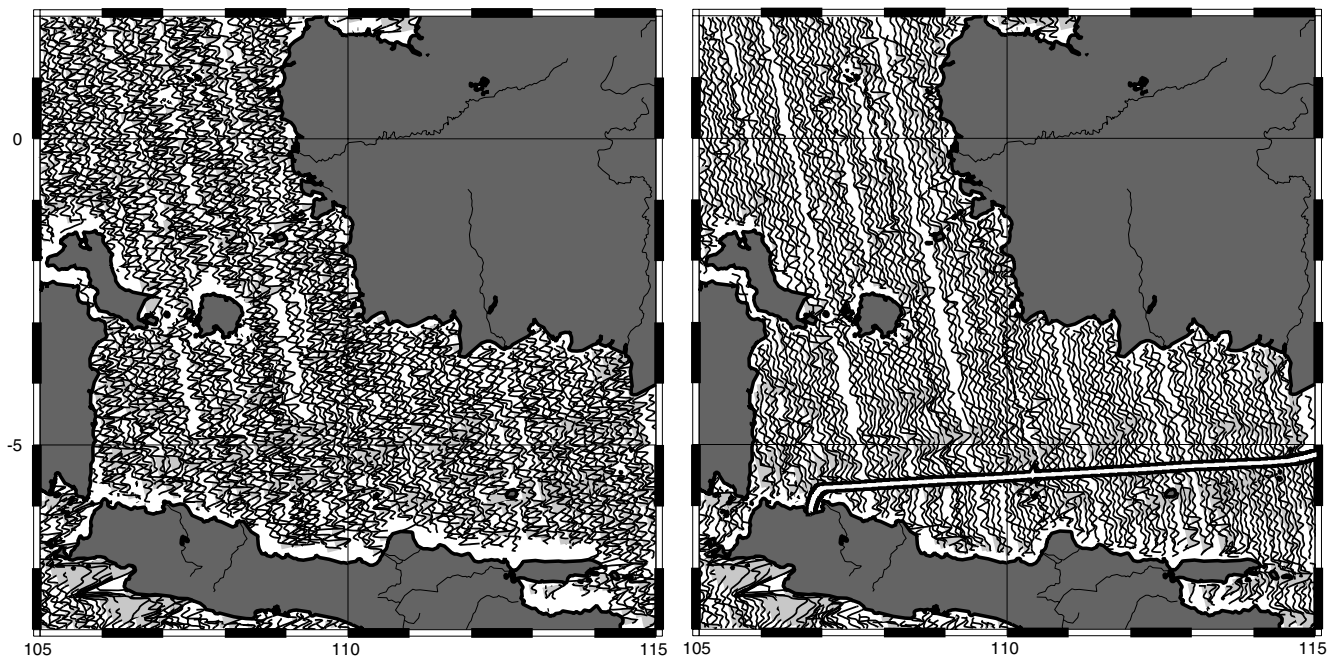


Figure 6. Along-track sea surface slope for ascending profiles from the ERS-1 geodetic phases with the EGM96 model removed. Left—arrival time from onboard tracker, right—arrival time from 1-parameter retracking algorithm. The decrease in noise level reveals gravity lineaments associated with basement structure of this continental margin. Retracking also improves recovery of data near shore. The trackline of the shipboard gravity profile used to assess the accuracy of the satellite-derived gravity is shown in the right panel.

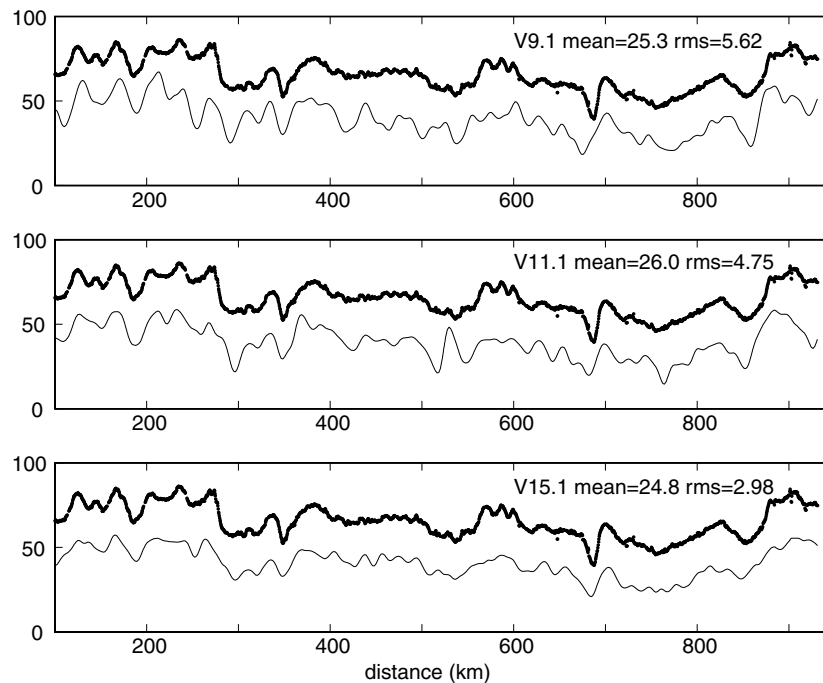


Figure 7. Comparison between satellite-derived gravity models (thin lines) and a shipboard gravity profile (points) across the Java Sea (trackline in Fig. 6). (top) Gravity model version 9.1 does not use retracked altimeter data and has an rms misfit of 5.62 mGal. The mean difference of 25 mGal is due to a mean error commonly found in shipboard gravity (Wessel & Watts 1988). (middle) Gravity model version 11.1 uses retracked ERS-1 altimeter data but the Geosat data were not retracked; the rms misfit is improved by nearly 1 to 4.75 mGal. (bottom) Gravity model version 15.1 is based on both retracked ERS-1 and Geosat altimeter profiles and also used a local least-squares adjustment to simultaneously fit the residual along-track slopes from ERS-1, Geosat, and Topex. The rms is improved further to 2.98 mGal, which is about one-half the rms of the V9.1 gravity field.

is that they force the rise time (i.e. the SWH) to remain constant across a window of 408 points (132 km). Our experiments show that any *a priori* constraint that suppresses freedom for error in rise time will also reduce the error in sea surface height. If the Maus

et al. (1998) approach were implemented in a running window, it would have the effect of applying a boxcar filter to SWH with a filter width of 132 km. This is similar to our use of a Gaussian filter with a characteristic wavelength of 90 km. We did not find that it was

necessary to simultaneously impose a smoothness constraint on the geoid as performed by Maus *et al.* (1998). Instead we perform the along-track filtering after the retracking process. However, we found that the overall results were improved by simultaneously fitting three waveforms in a moving window to effectively reduce the along-track sampling rate from 20 to 10 Hz.

The Maus *et al.* approach is cumbersome to implement because it requires simultaneous inversion of 408 waveforms with an imposed correlation among the arrival-time parameters to ensure sea surface height smoothness. However, it has the advantage that the retracking only needs to be performed once. Our approach, although it requires a three-step process, is easy to understand and trivial to implement, as the inversion operation works on only one waveform (or a few waveforms) at a time. Furthermore, our scheme allows direct estimation of the resolved correlation scale in the SWH field (Fig. 3) and makes explicitly clear the role of the smoothing applied to the SWH and amplitude parameters.

CONCLUSIONS

The Monte Carlo simulation of altimeter waveforms, as well as the analysis of ERS waveform data, demonstrates an inherent correlation between least-squares estimates of arrival time and rise time. The correlation is caused by the noise properties of the return waveform. Noise is low prior to the arrival of the waveform and increases later in the waveform as more energy scatters off the rough ocean surface. This change in noise introduces the inherent correlation that can mimic true sea-state bias. The correlation is greatest over short length scales (<90 km) and can be removed by low-pass filtering SWH along profiles. Most oceanographic studies of repeat altimeter profiles are focused in intermediate and long wavelength variations in height where this correlation is less of a problem. Nevertheless it is likely that some of this correlation is falsely absorbed into the parameterization of the true EM sea state bias.

The noise properties of the return waveform are well understood, so it seems reasonable to perform a weighted least-squares estimate of the waveform parameters. However, simulations show that weighting the fit leads to a more significant correlation between arrival time and rise time with a slope of one (in dimensionless waveform gate width units). This high correlation also increases the error in the arrival time suggesting that a weighted least-squares approach is inferior to the unweighted least-squares approach (Rodriguez 1988). Maus *et al.* (1998) overcome the higher errors introduced by a non-uniform weight function by using a multiple waveform retracking algorithm that solves for a single rise-time parameter and multiple arrival-time parameters. While their approach provides significant improvements in range precision, they left unstated the fundamental assumption of their parameterization: that the rise time (i.e. SWH) varies smoothly along the satellite track. Here we explicitly make this assumption and establish the wavelength of the low-pass filter that is optimal for smoothing the rise time (~90 km). We argue that the rms-height distribution of waves in the deep ocean will vary smoothly in space due to the high group velocity of the wave trains relative to the speed of the storms that generate the waves. This assumption may become invalid across sharp wind fronts and in shallow coastal areas just seaward of the surf zone.

Our retracking algorithm works on individual waveforms, but three steps are involved. First, a standard three-parameter retracking algorithm is used. Second, the rise-time and amplitude parameters obtained at the first step are low-pass filtered along continuous pro-

files. Third, the data are retracked again, using the smoothed values from the second step and solving for only the arrival time. Note that fixing the rise time and amplitude to the smoothed values basically fixes the shape of the waveform to agree with surrounding waveforms; this in turn provides stability to the least-squares estimate. Using this approach we obtain a 38 per cent improvement in range precision between the standard three-parameter approach and the one-parameter approach. Moreover, we find that the precision of the arrival time is less sensitive to the SWH. Maus *et al.* (1998) reached a similar conclusion.

Finally we have used this approach to retrack all ERS-1 data for the geodetic phases (E and F) as well as six repeat cycles of phase G. These data were combined with all available Geosat geodetic mission data, Geosat exact repeat mission data and Topex/Poseidon altimetry data to construct a new marine gravity field. The method of combining the along-track slopes is described in Sandwell & Smith (1997). A 1-min grid is available by ftp (version 11.1 at <http://topex.ucsd.edu>). We have experimented with a similar approach to retrack all of the data from the Geosat Geodetic Mission. Preliminary results are shown in Fig. 7. The value of retracking all of the repeat-track altimetry from Geosat, ERS-1/2 and Topex/Poseidon is unclear. Retracking will certainly improve the short-wavelength precision of the measurements. Moreover, it is possible that this retracking will eliminate the artificial component of the sea state bias and provide a consistent SSB model for all altimeters. However, the long-wavelength accuracy of this retracking approach still needs to be investigated.

ACKNOWLEDGMENTS

The European Space Agency generously provided the raw ERS-1 waveform data through their distributor Infoterra Limited. We thank Helen Fricker for providing software to read the raw ERS waveform data. This research was supported by NASA (NAG5-13673) and the National Science Foundation (NSF OCE-0326707). ConocoPhillips and ExxonMobil provided critical start-up funding the research and continue to support this effort. The contents are solely the opinions of the authors and do not constitute a statement of policy, decision, or position on behalf of NOAA or the US Government.

REFERENCES

- Abramowitz, M. & Stegun, I.A., 1972. *Handbook of Mathematical Functions With Formulas, Graphs, and Mathematical Tables*, US Government Printing Office, Washington, DC, p. 1045.
- Amarouche, L., Thibaut, P., Zanife, O.Z., Dumont, J.-P., Vincent, P. & Steunou, N., 2004. Improving the Jason-1 ground retracking to better account for attitude effects, *Marine Geodesy*, **27**, 171–197.
- Bettadpur, S.V. & Eanes, R.J., 1994. Geographical representation of radial orbit perturbations due to ocean tides: Implications for satellite altimetry, *J. geophys. Res.*, **99**(C12), 24 883–24 898.
- Brown, G.S., 1977. The average impulse response of a rough surface and its application, *IEEE Transactions on Antenna and Propagation*, **AP-25**(1), 67–74.
- Chelton, D.B., Reis, J.C., Haines, B.J., Fu, L.L. & Callahan, P.S., 2001. Satellite altimetry, in *Satellite Altimetry and Earth Sciences*, pp. 1–131, eds. Fu, L.L. & Cazenave, A., Academic Press, San Diego.
- Dumont, J.-P., 1985. Estimation Optimale des Parametres des Signaux Radar Poseidon, Institut National Polytechnique de Toulouse, Toulouse, France.

- Hayne, G.S., 1980. Radar altimeter mean return waveforms from near-normal-incidence ocean surface scattering, *IEEE Transactions on Antennas and Propagation*, AP-28(5), 687–692.
- Hayne, G.S., Hancock, D.W., Purdy, C.L. & Callahan, P.S., 1994. The corrections for significant wave height and altitude effects in the TOPEX radar altimeter, *J. geophys. Res.*, 99(NC12), 24 941–24 955.
- Lemoine, F.G. *et al.*, 1998. The development of the joint NASA CSFC and the national Imagery and Mapping Agency (NIMA) geopotential model EGM96. NASA/TP-1998-206861, Goddard Space Flight Center, NASA, Greenbelt, Maryland.
- MacArthur, J.L., Marth, J.P.C. & Wall, J.G., 1987. The Geosat radar altimeter, *Johns Hopkins APL Technical Digest*, 8(2), 176–181.
- Maus, S., Green, C.M. & Fairhead, J.D., 1998. Improved ocean-geoid resolution from retracked ERS-1 satellite altimeter waveforms, *Geophys. J. Int.*, 134(N1), 243–253.
- Monaldo, F., 1988. Expected differences between buoy and radar altimeter estimates of wind speed and significant wave height and their implications on buoy-altimeter comparisons, *J. geophys. Res.*, 93(C3), 2285–2302.
- Press, W.H., Teukolsky, S.A., Vetterling, W.T. & Flannery, B.P., 1992. *Numerical recipes in C*, 2nd edn, Cambridge University Press, New York, p. 994.
- Raney, R.K., Smith, W.H.F. & Sandwell, D.T., 2004. Abyss-Lite: *A High-Resolution Gravimetric and Bathymetric Mission*. American Institute of Aeronautics and Astronautics, San Diego, pp. 1–5.
- Rodriguez, E., 1988. Altimetry for non-Gaussian oceans: Height biases and estimation of parameters, *J. geophys. Res.*, 93, 14 107–14 120.
- Rodriguez, E. & Martin, J.M., 1994. Assessment of the TOPEX altimeter performance using waveform retracking, *J. geophys. Res.*, 99(C12), 24 957–24 969.
- Sandwell, D.T., 1987. Biharmonic spline interpolation of Geos-3 and Seasat altimeter data, *Geophys. Res. Lett.*, 14(2), 139–142.
- Sandwell, D.T. & Smith, W.H.F., 1997. Marine gravity anomaly from Geosat and ERS-1 satellite altimetry, *J. geophys. Res.*, 102(B5), 10 039–10 054.
- Scharroo, R. & Lillibridge, J., 2005. Non-Parametric sea-state bias models and their relevance to sea level change studies, *Proc. of the 2004 Envisat & ERS Symposium*, Salzburg, Austria.
- Scharroo, R., Visser, P.N.A.M. & Mets, G.J., 1998. Precise orbit determination and gravity field improvement for the ERS satellites, *J. geophys. Res.*, 103(C4), 8113–8127.
- Smith, W.H.F. & Sandwell, D.T., 1997. Global sea floor topography from satellite altimetry and ship depth soundings, *Science*, 277(26 September), 1956–1961.
- Stewart, R.H., 1985. *Methods of Satellite Oceanography*, Univ. of Calif. Press, Berkeley, California, p. 360.
- Wang, Y.M., 2000. The satellite altimeter data mean sea surface GSFC98, *Geophys. Res. Lett.*, 25(5), 701–704.
- Wessel, P. & Bercovici, D., 1998. Interpolation with splines in tension: a Green's function approach, *Mathematical Geology*, 30(1), 77–93.
- Wessel, P. & Watts, A.B., 1988. On the accuracy of marine gravity measurements, *J. geophys. Res.*, 93(B1), 393–413.
- Yale, M.M., Sandwell, D.T. & Smith, W.H.F., 1995. Comparison of along-track resolution of stacked Geosat, ERS-1 and TOPEX satellite altimeters, *J. geophys. Res.*, 100(B8), 15 117–15 127.

APPENDIX A: THE EFFECT OF ERS-1 HARDWARE TRUNCATION ON THE EXPECTED MEAN AND VARIANCE OF WAVEFORM GATE SAMPLES

The ERS-1 spacecraft transmitted radar pulses with a pulse repetition frequency of 1020 Hz. Fifty consecutive waveforms were accumulated on-board in hardware to form a quasi-average waveform, and only these quasi-average waveforms were telemetered to the ground for processing. Unfortunately the reported quasi-average waveform is not precisely the arithmetic mean of the received and

gated values,

$$\bar{P} = \frac{1}{50} \sum_{k=1}^{50} P_k.$$

Instead, to prevent the sum from overflowing the hardware, the following formula was used to accumulate the average waveform power:

$$\tilde{P} = \sum_{k=1}^{50} \text{floor}(P_k/50).$$

where ‘floor(x)’ in the above expression is the greatest integer less than or equal to x . This appendix explores the probability distributions for P , \bar{P} and \tilde{P} .

The probability distribution for the power in a returned radar pulse, P

The radar signal received by an altimeter has contributions from many randomly distributed radar scatterers on the ocean surface. The phase from each scatterer is uniformly and randomly distributed (Brown 1977). The in-phase (C) and quadrature (S) components of the received signal are each the sum of a large number of random variables; therefore C and S have Gaussian distributions with zero mean and equal variance. The relative phase of C and S , that is, $\phi = \text{atan2}(S, C)$, is uniformly and randomly distributed. The altimeter detects the power of the returned waveform: $P = C^2 + S^2$. P is thus a random variable that, apart from a scale factor, is distributed as chi-square with two degrees of freedom, χ_2^2 , that is, it has an exponential distribution, in which the standard deviation is equal to the mean. If the expected value of P is \hat{P} then the variance of P is \hat{P}^2 .

Factors affecting the distribution of a sequence of 50 returned pulses

Traditional radar altimeters such as ERS-1 do not have a high enough sampling rate to operate in a synthetic aperture mode (i.e. along track spacing $< 1/2$ antenna diameter) so each returned waveform may be considered independent realization of the ocean surface. Over 1/20 of a second, the ocean wave height distribution, density of scatterers on the surface, delay and attenuation of energy along the propagation path and antenna pointing should not change appreciably. Therefore during the acquisition of 50 consecutive pulses the expected returned power, \hat{P} , should depend only on the receive time relative to the return onset time: $\hat{P} = \hat{P}(t - t_0)$. Hereafter, we will assume that the radar instrument is tracking correctly, so that each of the waveforms in a sequence of 50 is correctly aligned, meaning that the waveform sample gates are distributed around t_0 with the same distribution as each pulse is sampled by the waveform gates. These conditions will ensure that the expected value of the power in any one waveform gate is a constant during the acquisition of 50 consecutive waveforms. Each of the 50 waveforms then is independently and identically distributed, by virtue of the short decorrelation time and the proper tracking.

The distribution of the arithmetic mean of 50 returned values, \bar{P}

The arithmetic mean \bar{P} is a linear combination of 50 random variables and so should have an approximately Gaussian distribution,

by the central limit theorem. More precisely, the distribution of \bar{P} is, apart from a scale factor again, that of chi-square with 100 degrees of freedom; however, the distribution of χ_{100}^2 is very well approximated by a Gaussian distribution (Abramowitz & Stegun 1972, section 26.4.11 and following). \bar{P} is an unbiased estimator; its expected value is \hat{P} . This can be found directly by taking the expectation of the equation for \bar{P} , or by appropriately scaling the χ_{100}^2 distribution, or simply making use of the fact that the arithmetic mean is unbiased. The variance of \bar{P} obtained by scaling the χ_{100}^2 distribution is the same as would be found by the Gaussian approximation: $\text{Var}\{\bar{P}\} \approx \text{Var}\{P\}/50 = \hat{P}^2/50$. This means that the expected standard deviation in a mean waveform \bar{P} is roughly $1/7$ of \hat{P} .

The properties of the quasi-average, \bar{P}

Applying again the assumptions that each P_k is independent and identically distributed one reasons that the distribution for \bar{P} must have a Gaussian form for any \hat{P} . This justifies the use of least-squares fitting techniques in retracking. However, the ‘floor’ operation effectively applies an unpredictable scale factor to each P_k in the quasi-average \bar{P} , and it is not immediately obvious how this will affect the expectation (mean) $\mu = E\{\bar{P}\}$ and variance $\sigma^2 = \text{Var}\{\bar{P}\}$.

We estimated the mean and variance of \bar{P} as functions of the expected true power, \hat{P} , by Monte Carlo experiments as follows. We generated pseudo-random deviates X_k uniformly distributed in the interval (0, 1). From these we obtained exponentially distributed, unit mean deviates Y_k by the logarithmic transformation $Y_k = -\log(X_k)$ (Press *et al.* 1992, Section 7.2). By simply scaling $P_k = \hat{P}Y_k$ we generated quasi-random numbers P_k having the correct distribution for realizations of a single waveform pulse gate sample with expected power level \hat{P} . It is then straightforward to form many realizations of \bar{P} and compute the sample mean and standard deviation of these realizations. Graphs of the bias $E\{\bar{P}\} - \hat{P}$ and the standard deviation $\sigma(\bar{P})$ are shown as Fig. A1. The bias is zero when \hat{P} is zero, of course, but quickly approaches a steady value of -23 . Note that this is slightly less than half of the truncation factor of 50, probably reflecting the asymmetry in the exponential distribution of

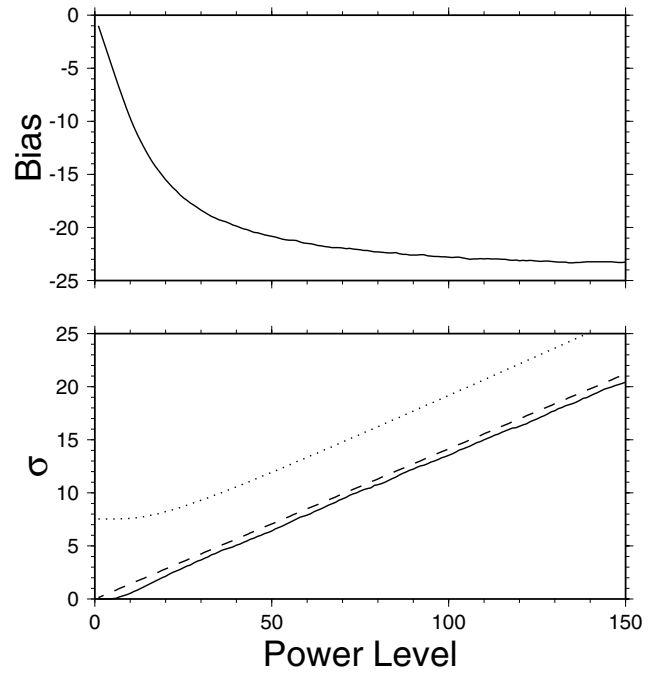


Figure A1. Top: The bias (expected value of the quasi-mean power level, \bar{P} , minus the correct true mean power level, \hat{P}) as a function of the true mean power level, \hat{P} . The asymptotic value of the bias is -23 . Bottom: The standard deviation of the quasi-mean power level (solid line) is slightly less than the standard deviation of the true theoretical population (dashed line, equal to $\hat{P}/\sqrt{50}$). The dotted line shows the least-squares weight used in this paper, $(\hat{P} + 50)/\sqrt{44}$ as a function of \hat{P} . Experimentation showed that this weight gave the best results. It is somewhat higher than the actual standard deviation to avoid overweighting the lowest power levels and to account for a background thermal noise level that is missing from the waveforms because of their truncation at low amplitude.

the P_k ; the expected difference between rounding and truncating a symmetric distribution would be half the truncation factor. The standard deviation is slightly less than the theoretical value of $\hat{P}/\sqrt{50}$, perhaps also due to the exponential distribution.

Warping and cracking of the Pacific plate by thermal contraction

David Sandwell and Yuri Fialko

Scripps Institution of Oceanography, University of California, San Diego, La Jolla, California, USA

Received 16 March 2004; revised 15 July 2004; accepted 2 August 2004; published 26 October 2004.

[1] Lineaments in the gravity field and associated chains of volcanic ridges are widespread on the Pacific plate but are not yet explained by plate tectonics. Recent studies have proposed that they are warps and cracks in the plate caused by uneven thermal contraction of the cooling lithosphere. We show that the large thermoelastic stress produced by top-down cooling is optimally released by lithospheric flexure between regularly spaced parallel cracks. Both the crack spacing and approximate gravity amplitude are predicted by elastic plate theory and variational principle. Cracks along the troughs of the gravity lineaments provide conduits for the generation of volcanic ridges in agreement with new observations from satellite-derived gravity. Our model suggests that gravity lineaments are a natural consequence of lithospheric cooling so that convective rolls or mantle plumes are not required. *INDEX TERMS*: 1208 Geodesy and Gravity: Crustal movements—intraplate (8110); 1236 Geodesy and Gravity: Rheology of the lithosphere and mantle (8160); 1219 Geodesy and Gravity: Local gravity anomalies and crustal structure; 3045 Marine Geology and Geophysics: Seafloor morphology and bottom photography; 8159 Tectonophysics: Rheology—crust and lithosphere; *KEYWORDS*: thermal contraction, Pacific plate, gravity anomalies

Citation: Sandwell, D., and Y. Fialko (2004), Warping and cracking of the Pacific plate by thermal contraction, *J. Geophys. Res.*, 109, B10411, doi:10.1029/2004JB003091.

1. Introduction

[2] Plate tectonics explains most of the topography of the deep ocean basins, but there is still debate regarding the origin of off-ridge features that are younger than the ambient lithosphere, and especially those that are not aligned with the autochthonic seafloor spreading fabric. The Pacific basin contains three main types of the young off-ridge lineaments (Figure 1). (1) Chains of shield volcanoes such as the Hawaiian-Emperor seamounts are well explained by the mantle plume model [Morgan, 1971; Sleep, 1992]. (2) Gravity lineaments are prominent at 140–200 km wavelength and are aligned in the direction of absolute plate motion [Haxby and Weissel, 1986] (Figure 1b). (3) En echelon volcanic ridges appear to be related to the gravity lineaments (Figure 2) and have morphology consistent with the ridge-parallel extensional stress [Lynch, 1999; Sandwell et al., 1995; Winterer and Sandwell, 1987] (Figure 3). The origin of both the gravity lineaments and the linear volcanic ridges has been the subject of many studies and field experiments [Dunbar and Sandwell, 1988; Fleitout et al., 1989; Forsyth et al., 2002; Gans et al., 2003; Haxby and Weissel, 1986].

[3] Several mechanisms have been proposed to explain the gravity lineaments (Figure 4), including small-scale convective rolls [Haxby and Weissel, 1986]; mini hot spots [Fleitout et al., 1989]; extension of the lithosphere or boudinage [Dunbar and Sandwell, 1988]; and thermal

bending stress caused by top-down cooling of the lithosphere [Gans et al., 2003]. Radiometric ages of the Puka-puka ridges in the central Pacific are inconsistent with the mini hot spot model [Sandwell et al., 1995]. The morphology of these volcanic ridges indicates that magma is extruded along cracks that are parallel to the absolute plate motion direction. Also, the chemistry of the dredged basalts is inconsistent with deep melting of plume material [Janney et al., 2000]. The small-scale convection model predicts extension and volcanism on the crests of the gravity lineaments but qualitative observations show that the volcanic ridges preferentially occur in the troughs [Forsyth et al., 2002; Sandwell et al., 1995; Searle et al., 1995; Winterer and Sandwell, 1987]. The boudinage model correctly predicts the characteristic wavelength of the gravity lineaments and the location of the volcanic ridges but at least 10% extension is needed to explain their observed amplitude [Dunbar and Sandwell, 1988]. Plate tectonic measurements of fracture zone spacing show that this amount of relative extension did not occur [Goodwillie and Parsons, 1992] and a recent study limits the extension to less than 2% [Gans et al., 2003]. Thus the alternative explanations are certainly warranted. Here we provide new observational evidence and theoretical arguments indicating that both the gravity lineaments and volcanic ridges result from cooling and thermal contraction of the oceanic lithosphere, and are a natural consequence of plate tectonics.

[4] Cooling and shrinkage of the oceanic lithosphere is a well-understood phenomenon that is responsible for the increase in seafloor depth with age [Parsons and Sclater, 1977]. Nonuniform shrinkage of the plate, mostly driven by

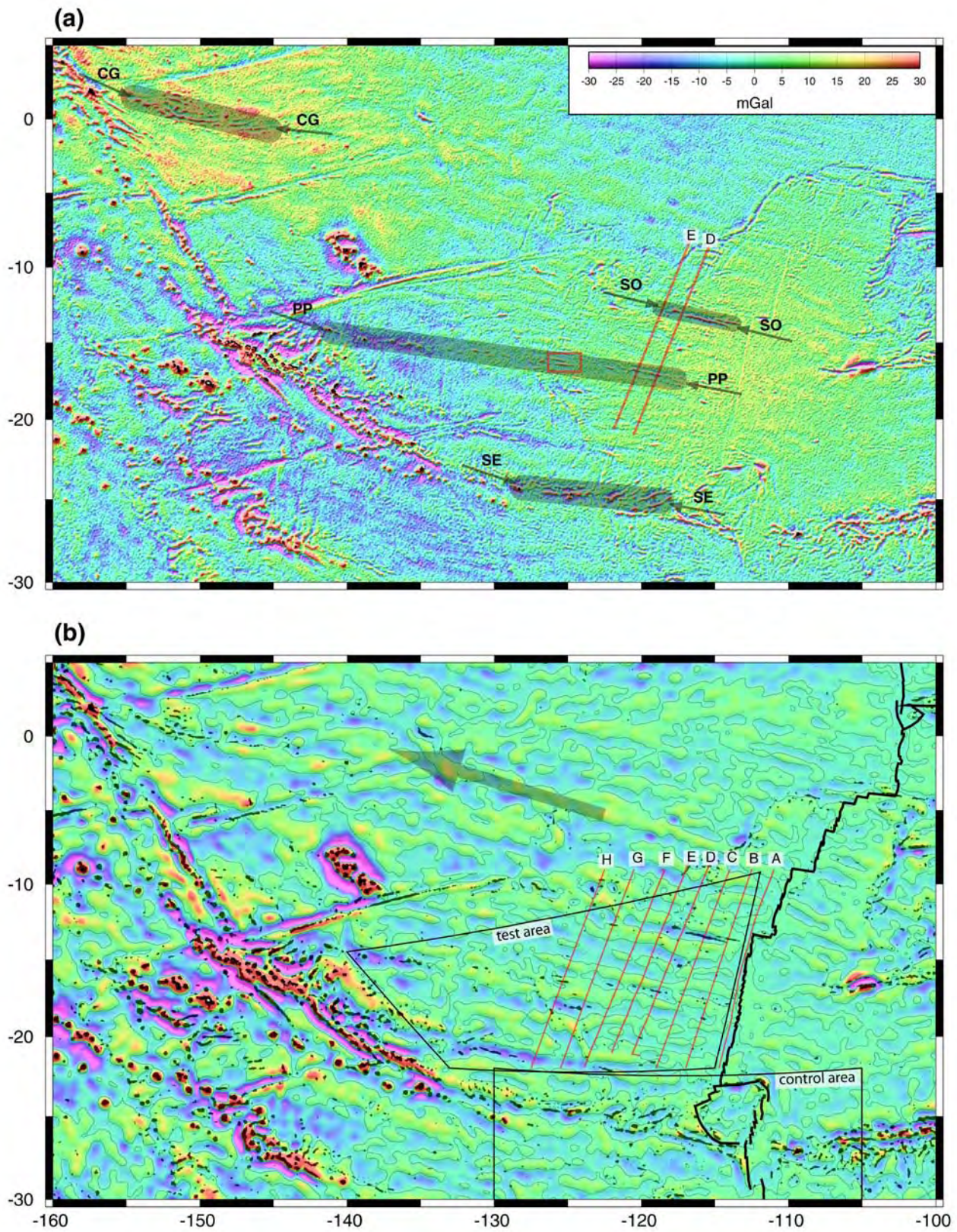


Figure 1

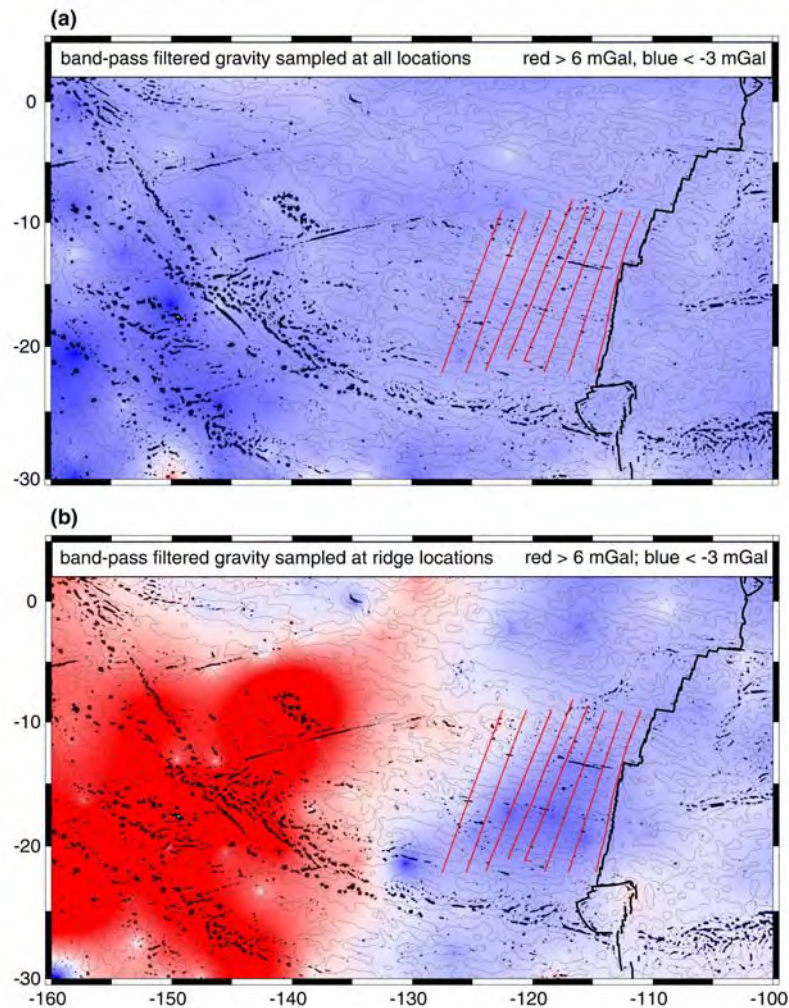


Figure 2. (a) Band-pass filtered gravity anomaly ($80 < \lambda < 600$ km) sampled at all locations and median filtered over a diameter of 450 km (red > 6 mGal; blue < -3 mGal). Because the band-pass filtered data are evenly sampled they have nearly zero mean and median everywhere. (b) Band-pass filtered gravity anomaly ($80 < \lambda < 600$ km) sampled at locations of volcanic ridges and seamounts and median filtered over a diameter of 450 km (red > 6 mGal; blue < -3 mGal). Airy and flexural compensation models predict the band-pass filtered gravity should be >1.5 mGal at volcanic loads. Areas of pronounced gravity lineaments have negative band-pass filtered gravity at volcanic ridges.

Figure 1. (a) Gravity anomaly derived from retracked ERS-1 radar altimeter data, Geosat altimeter data, and Topex altimeter data provides improved accuracy and resolution to reveal the close association between the gravity lineaments and the volcanic ridges. Red lines are track lines of R/V *Conrad* where bathymetry and gravity profiles were collected (see Figures 5 and 6). Red box outlines a part of the Pukapuka ridges that was surveyed by R/V *Melville* (see Figure 3) [Sandwell *et al.*, 1995]. Prominent volcanic ridges in the area include cross-grain ridges [Winterer and Sandwell, 1987] CG; Pukapuka ridges [Sandwell *et al.*, 1995] PP; the ridges of Searle *et al.* [1995] SE; and most recently the Sojourn Ridges [Forsyth *et al.*, 2002] SO. (b) Band-pass filtered gravity anomaly ($80 < \lambda < 600$ km) derived from retracked satellite altimeter data. Color scale saturates at ± 15 mGal. Gravity lineaments with 140-km wavelength develop between the ridge axis and 6 Ma (Profile C) and are oriented in the direction of absolute plate motion (large arrow). Lineaments on older seafloor have somewhat longer wavelength (~ 180 km) and cross the grain of the seafloor spreading fabric. Gravity lineaments also occur on the Nazca plate to the east of the East Pacific Rise. Seamounts and volcanic ridges are marked as black areas. Many of these volcanic chains are geometrically associated with the gravity lineaments. The morphology of three sets of these ridges indicates that they formed by N-S tension of the Pacific plate [Lynch, 1999]. The longest of these ridge groups, the Pukapuka ridges, extends for over 2600 km from 5 Ma old seafloor near the East Pacific Rise to 45 Ma old seafloor near the Tuamotu Archipelago.

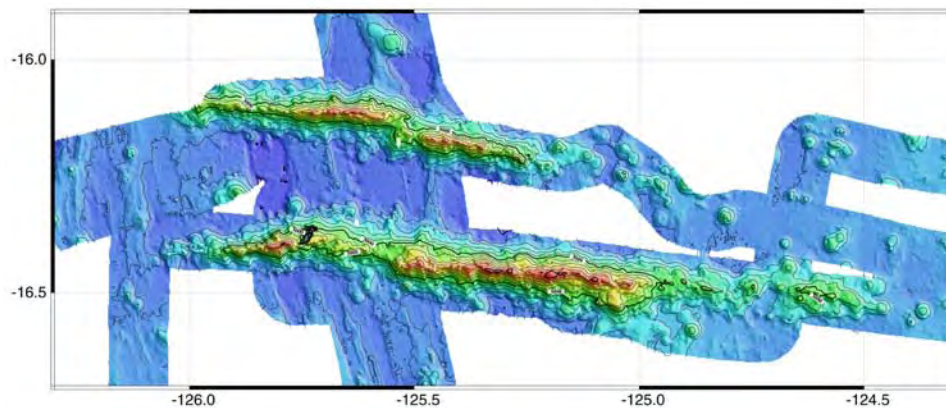


Figure 3. Detailed bathymetry (200-m contour interval) of a pair of volcanic ridges along the Pukapuka chain [Sandwell *et al.*, 1995]. The ridges are about 2 km tall, 10 km wide and 75/150 km long. These ridges formed 9 Ma ago and are on seafloor that is 19 Ma. Notice that the ridges are not perpendicular to the abyssal hill fabric.

the temperature gradients in the top part of the lithosphere, results in the development of thermoelastic stresses that are large enough to fracture the plate [Bratt *et al.*, 1985; Parmentier and Haxby, 1986; Sandwell, 1986; Turcotte, 1974; Wessel, 1992]. Because the thickness of the lithosphere is small compared to its horizontal dimensions, and the seafloor is a stress-free boundary, the vertical component of the deviatoric stress is small and can be neglected. Under the thin plate approximation, the horizontal components of thermoelastic stress can be decomposed into a thermal end load and a thermal bending moment [Boley and Weiner, 1960]. The thermal end loads can be partially relieved by plate-wide shrinkage, especially near the ridge axis, which is unable to support large deviatoric stresses [Fialko, 2001; Parsons and Thompson, 1991]. However, even a plate with free ends may experience large thermoelastic stress, with compressional stress near the surface and tensional stress at depth [Parmentier and Haxby, 1986; Wessel, 1992]. The same physics describes tempering of glass sheets, whereby the residual compression at the surface inhibits the development of tensile fractures [Woo, 1968]. The predicted pattern of thermoelastic deformation is consistent with the focal mechanisms of intraplate earthquakes [Bergman and Solomon, 1984; Shen *et al.*, 1997; Wiens and Stein, 1984]. Recently, Gans *et al.* [2003] proposed that the gravity lineaments are caused by convex upward flexure of the plate between regularly spaced lithospheric cracks where the flexure is driven by thermoelastic bending moments. While their model shows fair agreement with the observations, it does not explain why cracks develop with a particular spacing; Gans *et al.* [2003] assume a 150-km spacing to match the observed spacing.

[5] Here we test and refine the thermal contraction model to explain the origin of both the volcanic ridges and the gravity lineaments through a quantitative analysis of gravity data, as well as by developing a numerical model of thermoelastic flexure. We address the following questions. (1) How do the gravity lineaments develop in amplitude and wavelength as a function of seafloor age? (2) Does the intraplate volcanism indeed preferentially occur in the troughs of the gravity lineaments? These first two questions

are addressed using the gravity anomalies derived from reprocessing of the raw radar waveforms of ERS-1 satellite altimeter data. (3) Is there sufficient thermal bending moment to explain the amplitudes of both the gravity

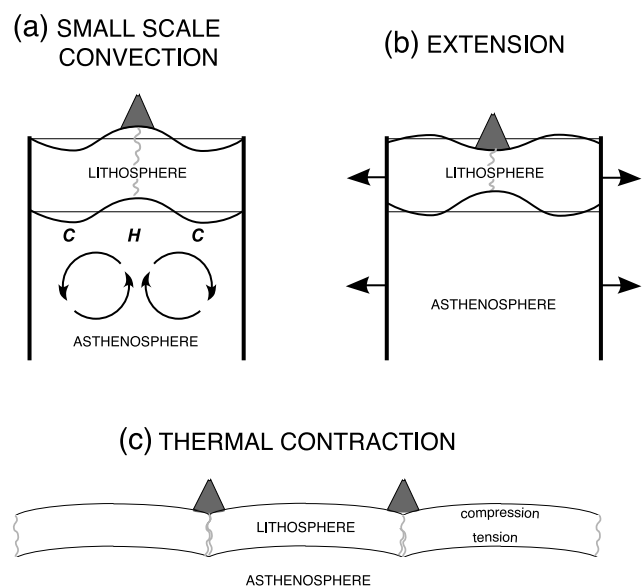


Figure 4. Models for the formation of the gravity lineaments and en echelon volcanic ridges. (a) Small-scale convection cells develop beneath cooled lithosphere and align in the direction of absolute plate motion by shear in the asthenosphere [Buck and Parmentier, 1986; Richter and Parsons, 1975]. Volcanoes develop above the hot upwelling axis of the cell. (b) Slow and diffuse extension creates lithospheric boudinage structures [Ricard and Froidevaux, 1986]. Volcanoes develop in the troughs (maximum strain) if partially melted mantle is available beneath the plate [Sandwell *et al.*, 1995]. (c) Thermoelastic flexure will develop if the lithosphere is cracked at a regular intervals [Gans *et al.*, 2003]. Volcanoes will develop above the cracks if partially melted mantle is available beneath the plate.

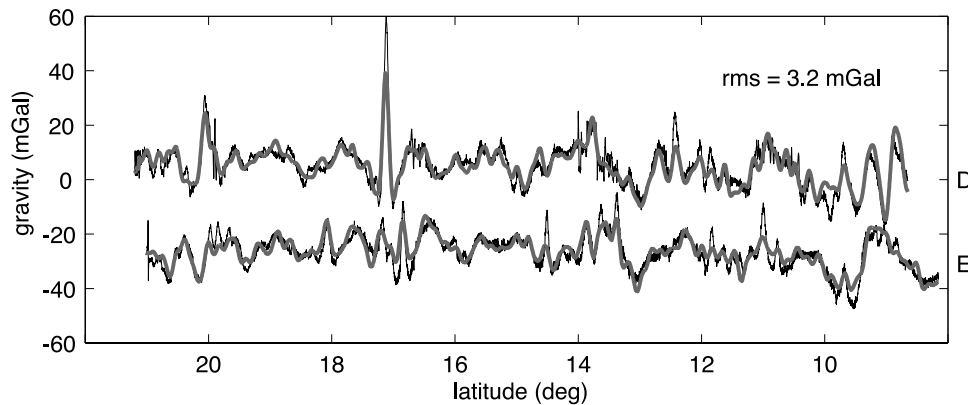


Figure 5. Comparison between shipboard (black) and satellite-derived (gray) gravity anomalies along profiles D and E (Figure 1) [Abers *et al.*, 1988] has 3.2 mGal RMS deviation. The improved resolution and accuracy of the retracked ERS-1 altimeter data is used to better delineate the volcanic ridges.

lineaments and the associated topography? (4) Finally, what mechanism controls the regular spacing of cracks of the order of the flexural wavelength? One of the most important aspects of the thermoelastic model is that both the amplitude and spacing of the gravity lineaments are predicted from quantifying a process that is fundamental to plate tectonics, namely, the thermal contraction of the oceanic lithosphere.

2. Gravity Lineaments and Volcanic Ridges From Satellite Altimetry

[6] The central Pacific gravity lineaments were first discovered from the analysis of Seasat altimeter data [Haxby and Weissel, 1986]. While the track spacing and resolution of the Seasat data was sufficient to reveal the 140–200 km gravity lineaments, the discovery of volcanic ridges required better coverage and higher precision. The ERS-1 satellite altimeter increased the coverage during its geodetic phase (1994–95) and the higher quality Geosat altimeter data were declassified in 1995 [Sandwell and Smith, 1997]. Since the volcanic ridges are typically only 20 km wide and usually less than 1000 m tall, most were not visible above the 5–7 mGal noise level in the altimeter-derived gravity anomaly maps. Guided by these noisy gravity maps, several sets of ridges were surveyed by multibeam sonar (Figure 1a, shaded areas): cross-grain ridges [Winterer and Sandwell, 1987]; Pukapuka ridges [Sandwell *et al.*, 1995]; the ridges of Searle *et al.* [1995]; and most recently the Sojourn Ridges [Forsyth *et al.*, 2002]. These sets of ridges appear to be preferentially located in the troughs of the gravity lineaments although there has been no quantitative confirmation of this observation.

[7] To confirm the spatial correlation between the ridges and the gravity lineaments, we improve the resolution of the ERS-1 altimeter data by retracking the raw altimeter waveforms [Maus *et al.*, 1998] (Figure 1a). The retracking increases the short-wavelength precision by nearly a factor of 2, so the quality of the ERS-1 data is now superior to the Geosat data (not retracked yet). A new gravity model was constructed using all available altimeter profiles (see version 11 at <http://topex.ucsd.edu>). The RMS deviation between two shipboard profiles and the new gravity model is 3.2 mGal in this area (Figure 5).

[8] The gravity field of the small-scale ridges was separated from the larger scale gravity lineaments using isotropic the filters in Generic Mapping Tools [Wessel and Smith, 1991] (Figure 1b). A two-step, low-pass filter was used to remove features with wavelength shorter than about 80 km. First a median filter was applied to remove the sharp gravity highs associated with seamounts and ridges. This filter replaced each gravity value with the median of all of the values in a 65-km diameter circle. The second filter (applied in the wave number domain) passed wavelengths greater than 108 km and cut wavelengths less than 54 km using a cosine taper to attain a 0.5 gain at 80 km. The high-pass filtered gravity (total minus low-pass gravity) was clipped at 10 mGal to identify volcanic features (black areas in Figures 1b and 2). The clipping amplitude was selected to best match the outline of the volcanic edifices that have been mapped during multibeam bathymetry surveys [Forsyth *et al.*, 2002; Lynch, 1999] without introducing spurious features. To further isolate the gravity lineaments, the low-pass filtered part of the gravity field was high-pass filtered for wavelengths greater than 600 km (cosine taper 1200–600 km). Note that the passband of the filter (108–600 km) was selected to be outside the wavelength band of the gravity lineaments 120–300 km. Also note that while isotropic filters were used, the residual fields are highly anisotropic; both the gravity lineaments and ridges are oriented in approximately the direction of the absolute motion of the Pacific plate over the Hawaiian hot spot (Figure 1b).

[9] Profiles of band-pass filtered gravity reveal the development of the gravity lineaments on young seafloor (Figure 6). The profile closest to the East Pacific Rise (EPR) has very low amplitude and little, if any, periodic variations in the gravity field. The next profile to the west (3.2 Ma) reveals partially developed gravity lineaments (5 mGal peak-to-trough amplitude and 120 km wavelength). The amplitude and wavelength of the gravity lineaments increases with increasing seafloor age; by 8.2 Ma they are fully developed (10 mGal amplitude and 160-km wavelength). There is an indication that the wavelength increases to about 200 km on older seafloor. The gravity lineaments cut across the grain of the older seafloor (>20 Ma) indicating they are younger than the ambient lithosphere.

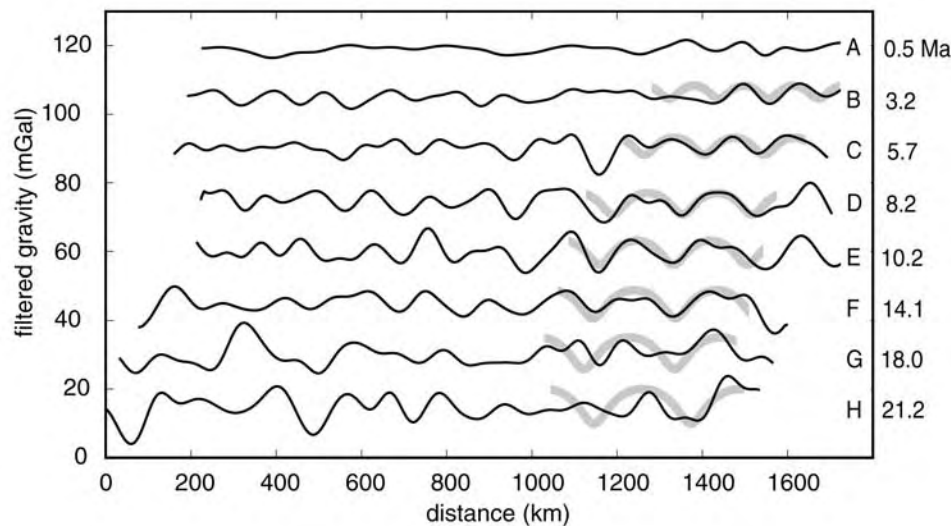


Figure 6. Satellite-derived gravity profiles parallel to the East Pacific Rise crest reveal the development of the gravity lineaments. Two-dimensional filtering of the satellite-derived gravity reveals the development of the seafloor undulations. Undulations are not apparent at the ridge axis (profile A) but develop rapidly on 3.2 Ma seafloor (Profile B) and are fully developed on 7–12 Ma seafloor. Model predictions (gray lines) match the wavelength of the observed seafloor undulations between 0 and 12 Ma. A good amplitude match is obtained by reducing the model amplitude by a factor of 0.75. On older seafloor (>14 Ma), the model overpredicts both the amplitude and wavelength of gravity lineaments.

[10] A visual examination of the area of most intense gravity lineaments suggests that the volcanic ridges are preferentially located in the troughs (Figure 1b, test area). Here we provide a quantitative confirmation of this observation. However, before investigating this relationship between volcanic ridges and gravity lineaments, it is instructive to consider the expected gravity field of a ridge in the absence of gravity lineaments. All models for the gravity field above seafloor topography (e.g., Airy, Pratt, flexural, and thermal isostasy models) have a positive gravity-to-topography ratio at all wavelengths. Therefore no matter how the data are band-pass filtered, the gravity anomaly should always be positive above the crest of a volcanic ridge. To further confirm and quantify this statement, we performed a simulation of flexural loading of a 5-km thick elastic plate [Goodwillie and Watts, 1993] using our identified distribution of volcanic ridges in the test area. The height of each volcano was derived from the predicted bathymetry map [Smith and Sandwell, 1997]. In the absence of gravity lineaments, the model predicts a 1.57 mGal shift in the ridge-sampled, band-pass filtered gravity.

[11] We use two approaches to show that the volcanic ridges in the area of most intense gravity lineaments (test area in Figure 1) are not randomly dispersed with respect to the gravity lineaments. First we sample the band-pass filtered gravity at every location and median-filter the data over a 450-km diameter area. As expected the mean and median of the band-pass filtered gravity is close to zero everywhere (Figure 2a). However, if we sample only at the locations of the volcanic features, distinct patterns emerge (Figure 2b). Areas of large volcanoes and islands, west of -135° longitude, are preferentially associated with positive,

band-pass filtered gravity anomalies as expected. Smaller volcanoes (~ 1000 m tall), east of 135° longitude, are preferentially associated with moderately positive, band-pass filtered gravity except in the areas of intense gravity lineaments where they preferentially associated with valleys of the gravity lineaments (blue are in Figure 2b).

[12] To further quantify this analysis, we examine the statistics of these samples by selecting three areas (Figure 7). The test area was selected to contain the most prominent gravity lineaments. The control area was selected to be on similar age seafloor as the test area and have numerous small volcanic features. We also provide statistics for the entire area. First we make histograms of the area covered by volcanic ridges as a function of the band-pass filtered gravity and compute the mean and standard deviation of the histograms (Figure 7). For the entire area, the mean is 6.85 mGal and the standard deviation is 16.18 mGal. The positive mean confirms the discussion above that band-pass filtered gravity is expected to be positive above volcanic ridges. The large standard deviation is also expected because of the wide range of volcano sizes that populate the entire area. Volcanic ridges in the control area have a positive mean value of 1.39 mGal in agreement with the flexure model simulation above and a standard deviation of 4.10 mGal reflecting a smaller range of volcano sizes. Volcanic ridges in the test area have mean of -0.98 mGal and a standard deviation of 3.88 mGal. The negative mean value is unexpected and in discordance with the compensation models discussed above. Could the difference in mean value, between the test area and the control area (-2.37 mGal), be a statistical fluke? To calculate the probability of this occurring by chance, one needs to

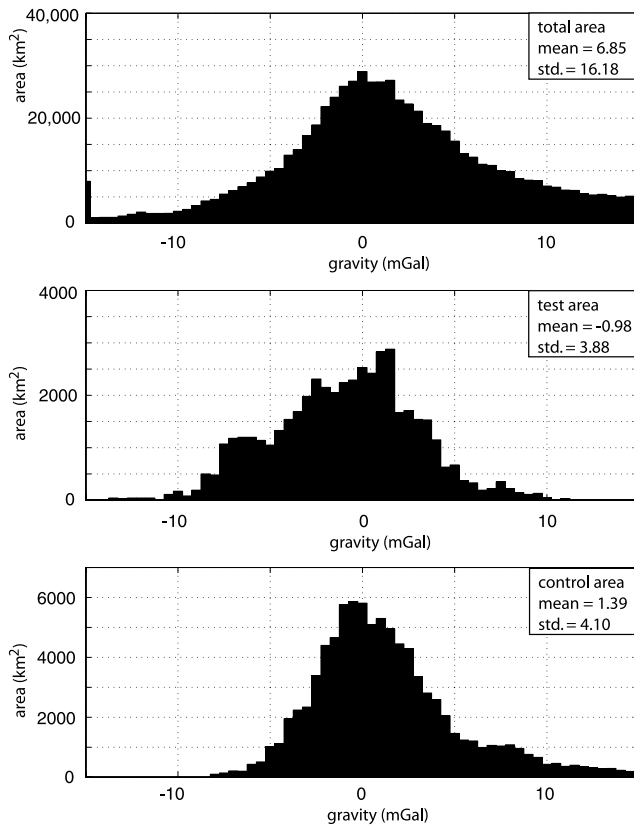


Figure 7. Histograms of the area of volcanic ridge seafloor versus band-pass filtered gravity. (top) The histogram of the part of the total area that is covered by volcanoes has a mean of 6.85 and a standard deviation of 16.18. (middle) The histogram of the test area covered by prominent volcanoes (see Figure 1) has a mean of -0.98 and a standard deviation of 3.88. (bottom) The histogram of the portion of the control area covered by prominent volcanoes has a mean of 1.39 and a standard deviation of 4.10. This difference in mean gravity between the test area and the control area (-2.38 mGal) is consistent with the hypothesis that volcanic ridges in the test area preferentially occur in the troughs of the gravity anomalies.

calculate the uncertainty in the mean of the test area, which is equal to the standard deviation divided by the square root of the number of independent samples (volcanoes). We count 224 independent volcanoes (30-km diameter circle) in the test area so uncertainty in the mean is 0.26 mGal. Therefore the difference of the means of the two populations is 9 times the uncertainty in the mean clearly ruling out a random coincidence. Even if we overestimated the volcano count by a factor of 10 (so there are only 22 independent volcanoes) then the mean difference is still 2.9 times the uncertainty in the mean resulting in a probability of 1 in 535 of this occurring by chance. This demonstrates that the volcanic ridges are indeed preferentially located in the troughs of the gravity lineaments.

[13] On the basis of this analysis, one could propose that volcanic ridges occur in the troughs because they preferentially create or intensify the gravity lineaments. There are two arguments against this proposition. First the

troughs of most gravity lineaments do not contain volcanic ridges. Second, as shown by *Goodwillie and Watts* [1993], the flexural response from even the largest volcanic loads are insufficient to create the gravity signatures of the gravity lineaments. We are left with the hypothesis that gravity lineaments reflect the primary physical process and the volcanic ridges are a possible consequence of this process. Moreover, this process preferentially produces volcanic ridges in the troughs of the gravity lineaments. We believe these observations rule out a small-scale convective origin for the gravity lineaments and ridges.

3. Thermoelastic Cracking of the Lithosphere

[14] *Turcotte* [1974] proposed that thermal stresses caused by cooling of the lithosphere may be responsible for transform faults which act to relieve the stress. He provided an analytic solution for the plate flexure that will develop when the plate is subjected to bending moments at its edges. More recent studies [*Parmentier and Haxby*, 1986; *Wessel*, 1992] have noted that if the plate is free to contract while it is cooling, a downward bending moment will increase almost linearly with the age of the plate. The upper third of the plate will be in compression while the lower two thirds will be in tension. These calculations consider the finite yield strength of the lithosphere which becomes especially important in limiting the near surface stress. *Gans et al.* [2003] use these estimates of increasing thermal bending moment and *Turcotte's* analytic flexure solution to explain the amplitude of the gravity lineaments in the Pacific plate. For a crack spacing of 150 km their calculations shows the development of 100 m of peak-to-trough plate flexure at an age of 3 Ma. However, their model does not explain the observed crack spacing and it also underestimates the amplitudes of the gravity lineaments. Here we present a theoretical model of yielding of the thermoelastically deformed lithosphere that is based on the variational principle. In particular, we postulate that the lithosphere will deform in a way that will minimize the overall mechanical energy stored in a plate. We search for the crack spacing that liberates the maximum mechanical energy, and show that the optimal crack spacing is of the order of the flexural wavelength.

[15] Consider a plate of length L with ends subjected to a bending moment M_T due to accumulation of thermoelastic stress. *Turcotte* [1974] provides an analytic solution for the deflection of a thin elastic plate floating on a fluid half space of density ρ (3300 kg m^{-3}). The plate deflection w , and curvature w'' , are

$$\begin{aligned} w(x) &= A \cos \frac{x}{\alpha} \cosh \frac{x}{\alpha} + B \sin \frac{x}{\alpha} \sinh \frac{x}{\alpha} \\ w''(x) &= \frac{-2A}{\alpha^2} \sin \frac{x}{\alpha} \sinh \frac{x}{\alpha} + \frac{2B}{\alpha^2} \cos \frac{x}{\alpha} \cosh \frac{x}{\alpha} \end{aligned} \quad (1)$$

where $\alpha = \left(\frac{4D}{\Delta\rho g}\right)^{1/4}$ is the flexural parameter, $D = \frac{EH^3}{12(1-\nu^2)}$ is the flexural rigidity, E is the Young's modulus (65 GPa), H is the plate thickness, ν is the Poisson's ratio (0.25), $\Delta\rho$ is the density difference between mantle and seawater, and g is

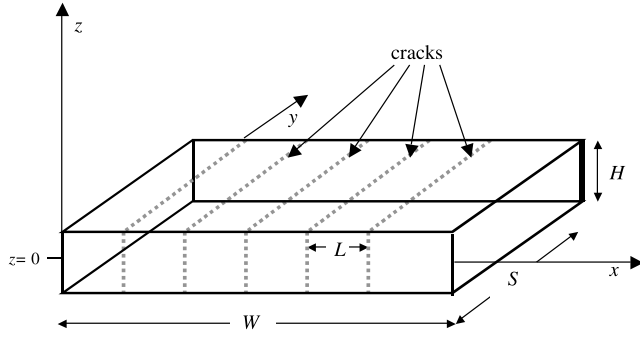


Figure 8. Thin elastic plate of thickness H , length S , and width W , contains N cracks with spacing of L .

the acceleration of gravity (9.8 m s^{-2}). The coefficients A and B are given by

$$A = \frac{\cos \theta \sinh \theta - \sin \theta \cosh \theta M_T \alpha^2}{\sin \theta \cos \theta + \sinh \theta \cosh \theta 2D} \quad (2)$$

$$B = \frac{\cos \theta \sinh \theta + \sin \theta \cosh \theta M_T \alpha^2}{\sin \theta \cos \theta + \sinh \theta \cosh \theta 2D}$$

where $\theta = \frac{L}{2\alpha}$.

4. Energy Released by Flexure

[16] To predict the optimal crack spacing we calculate the energy released by the flexure. The change in the potential energy of elastic deformation stored in a plate is $F = \int_V \sigma(\mathbf{x})\varepsilon(\mathbf{x})dV$, where σ is the stress perturbation, and ε is the strain perturbation about some reference (e.g., lithostatic) state of deformation, and the integration is performed over the entire plate volume V [Boley and Weiner, 1960, p. 262]. Prior to the onset of flexure, the stress σ equals the thermoelastic stress $\sigma_T(z)$ induced by the plate cooling, and the strain ε is zero. After cracking, individual segments of the plate will experience elastic flexure such that the change in stress and strain components may be written as

$$\begin{array}{ll} \text{initial} & \text{final} \\ \varepsilon(z) = 0 & \varepsilon(z) \end{array} \quad (3)$$

$$\sigma(z) = \sigma_T(z) \quad \sigma(z) = \sigma_T(z) + \frac{E}{(1-\nu^2)}\varepsilon(z)$$

For a quasistatic deformation, the change in energy Δf from the initial state to the final state is independent of path and equals

$$\Delta f = \frac{E(\Delta\varepsilon)^2}{(1-\nu^2)} + \sigma_T \Delta\varepsilon \quad (4)$$

The first term in equation (4) is the energy needed (consumed) to flex the plate while the second term is the thermoelastic energy released. Now consider the net energy released when equally spaced cracks are introduced in a cooled plate subject to thermoelastic prestress σ_T (Figure 8).

The plate has length S and width W and contains N longitudinal cracks with spacing L . The total elastic energy released, normalized by the area of the plate, is the energy density Q and it is given by

$$Q = \frac{F}{SW} = \frac{1}{SW} \iiint_V \sigma(\mathbf{x})\varepsilon(\mathbf{x})dzdxdy \quad (5)$$

Noting that the problem is plane strain (there is no deformation along the y axis), and $L = W/N$, one can rewrite the energy density as

$$Q = \frac{1}{L} \int_{-L/2}^{L/2} \int_{-H/2}^{H/2} \sigma(x,z)\varepsilon(x,z)dzdx \quad (6)$$

We expand the integrand in equation (6) using the expressions for energy change (4). For a thin plate flexure, $\varepsilon(z) = -zw''$, where z is the distance from the center of the plate and w'' is the plate curvature given in equation (1). The integral (6) becomes

$$Q = \frac{1}{L} \left\{ \int_{-L/2}^{L/2} [w''(x)]^2 \int_{-H/2}^{H/2} \frac{E}{(1-\nu^2)} z^2 dz dx - \int_{-L/2}^{L/2} w''(x) \cdot \int_{-H/2}^{H/2} \sigma_T(z) z dz dx \right\} \quad (7)$$

The first term on the right-hand side of equation (7) is the energy consumed by flexure of the plate. The second term is the thermoelastic energy released during the flexure. Note that the integral over z in the first term is the flexural rigidity D while the integral over z in the second term is the thermal bending moment M_T . Thus expression (7) can be written as

$$Q = \frac{D}{L} \int_{-L/2}^{L/2} [w''(x)]^2 dx - \frac{M_T}{L} \int_{-L/2}^{L/2} w''(x) dx \quad (8)$$

For both terms, the energy depends on the curvature of the plate, but note that the energy consumed by plate flexure is always positive since it depends on the curvature squared while the thermoelastic energy released by flexure depends on the sign of the curvature. Concave downward flexure releases thermoelastic energy. By differentiating the expression (7) with respect to the crack spacing L , we find that Q has a global minimum at $L_c \approx 3.389\alpha$ (Figure 9), corresponding to the maximum energy release.

[17] It is reasonable to assume that in the presence of random variations in the lithospheric strength and initial yielding induced by thermoelastic stresses, the subsequent deformation will be eventually localized on the optimally spaced macroscopic fracture zones. The occurrence of volcanic ridges along the presumed translithospheric cracks suggests that the crack formation is caused (or assisted by) the magma fracture, whereby the ascending dikes relieve the deviatoric stress in the lithosphere. This mechanism implies

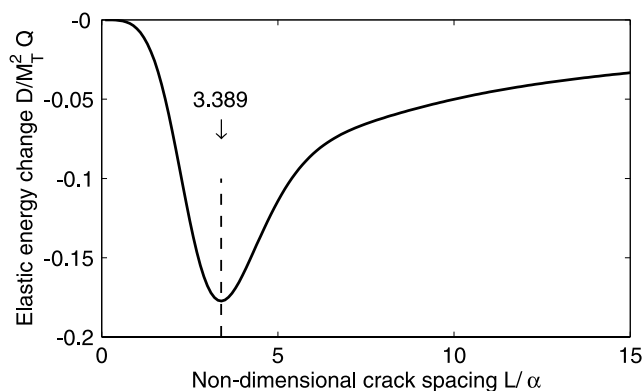


Figure 9. Model prediction for the thermoelastic energy release as a function nondimensional crack spacing L/α . Minimum in the potential energy of elastic deformation of the plate occurs when $L \approx 3.389 \alpha$.

that the crack zone is “weak” only during the dike emplacement; after the stress is reset and the magmatic activity ceases, the mechanical properties of a “cracked” plate do not differ substantially from those of an “intact” plate. Alternatively, the thermoelastic stresses might be relieved primarily by thrust and normal faulting in the shallow and deep sections of the plate, respectively. Even in this case the subsequent magma intrusions are likely to substantially reduce the deviatoric stresses in the lithosphere along the crack zones, as dikes won’t be able to deliver magma to the surface due to the negative dike buoyancy under the normal faulting conditions, and the unfavorable magma fracture orientation under the thrust faulting conditions. The dike intrusions will first relax the extensional stresses at the bottom of the plate, transferring the extension to shallower levels, and allowing the subvertical magma transport in the upper section of the plate. Regardless of whether the lithospheric crack zones are “hot” (magma induced) or “cool” (amagmatic), the crack spacing predicted by our model is controlled only by the flexural wavelength of the lithosphere, and is in excellent agreement with observations (Figure 6). Note that the volcanic activity associated with the inferred crack zones implies the presence of partial melt in the sublithospheric mantle. This melt may represent remnant magma not extracted from the mantle at the ridge axis, or reheating of the asthenosphere by plumes of the Superswell area [Janney *et al.*, 2000]. The orientation of cracks induced by the thermoelastic deformation is controlled by intraplate stresses. In particular, the cracks are predicted to align perpendicular to the least compressive stress.

5. Amplitude and Wavelength of Gravity Lineaments

[18] We use the method of Wessel [1992] to incrementally compute the evolution of thermoelastic stress as a function of depth. At each time step we allow the end load to relax to zero and then check that the stress does not exceed the yield strength envelope for dry olivine and pore water content of 0.5 [Goetze and Evans, 1979]. Our estimates of thermo-

elastic bending moment are 1.6 times greater than the estimates given by Gans *et al.* [2003] but are in agreement with Wessel’s calculations. The difference in the amplitudes is related to the assumption about the strength of the lower part of the thickening lithosphere. Gans *et al.* [2003] assume a sharp cutoff in strength at a temperature of 600°C, while Wessel [1992] used the full ductile flow law to define the strength. This difference results in small variations in strength at the base of the thickening plate which are amplified by the long moment arm to produce a 1.6 increase in thermoelastic moment.

[19] The results of our calculations are shown in Figure 10 where we allow thermoelastic bending moment M_T to develop for some period of time before the cracks with spacing L are introduced (the onset time). The flexural rigidity D at the onset time is computed using the portion of the plate where the yield strength exceeds 20 MPa which roughly corresponds to the depth to the 600°C isotherm. The corresponding values of D and M_T are then used in equation (1) to calculate the flexural topography. For this case of 130-km crack spacing, and 6 Ma onset time the peak-to-trough flexural amplitude is about 200 m and the filtered gravity amplitude is 5 mGal (Figure 10a). We also calculate the flexural energy consumed and the thermoelastic energy released as a function of distance perpendicular to the cracks for an onset time of 6 Ma (Figure 10b). The net energy released is zero near the ends of the flexure. This illustrates why the model discourages the small crack spacing as being unable to efficiently relieve the thermoelastic stress (although the thin plate approximation obviously becomes inapplicable when the crack spacing L is not large compared to the plate thickness H). Toward the center of the flexure the thermoelastic energy released is greater than the flexural energy consumed because the thermal prestress exceeds the flexural stress. Note that if the curvature of the plate becomes concave upward, the stress must increase in magnitude resulting in energy consumption. Therefore there is also an energy penalty when the crack spacing exceeds the critical wavelength L_c .

[20] Because the flexural parameter scales with the plate thickness, $\alpha \propto H^{3/4}$, the optimal crack spacing increases with the increasing age of the lithosphere (Figure 10c). So far we have assumed that the fracture energy required for the crack formation is negligible compared to the energy balance (8). Our dimensional estimates of the thermoelastic energy release seem to justify this assumption (Figure 10c). Although the in situ fracture energy E_F is not well known, and may be scale-dependent, we use values derived from the laboratory measurements (10^2 – 10^3 Jm $^{-2}$ for the tensile fracture energy [Atkinson, 1987; Fialko and Rubin, 1997]) and earthquake data (10^4 – 10^7 Jm $^{-2}$ for the shear fracture energy [Husseini, 1977; Scholz, 2002]) to place an upper bound on work spent on inelastic deformation. For the model shown in Figure 4c, the work spent on creating the cracks per unit area of the seafloor is $E_F H/L$. Thus the fracture energy enhances a penalty for the small crack spacing. Assuming $E_F = 10^7$ Jm $^{-2}$, $H = 15$ km, and $L = 150$ km, we obtain $E_F H/L \sim O(10^6)$ Jm $^{-2}$, i.e., small compared to the thermoelastic energy density Q for the lithosphere older than 1–2 Ma (10^7 – 10^8 Jm $^{-2}$, Figure 10c). However, the fracture energy might not be negligible in the lithosphere younger than 1 Ma. If the apparent absence of

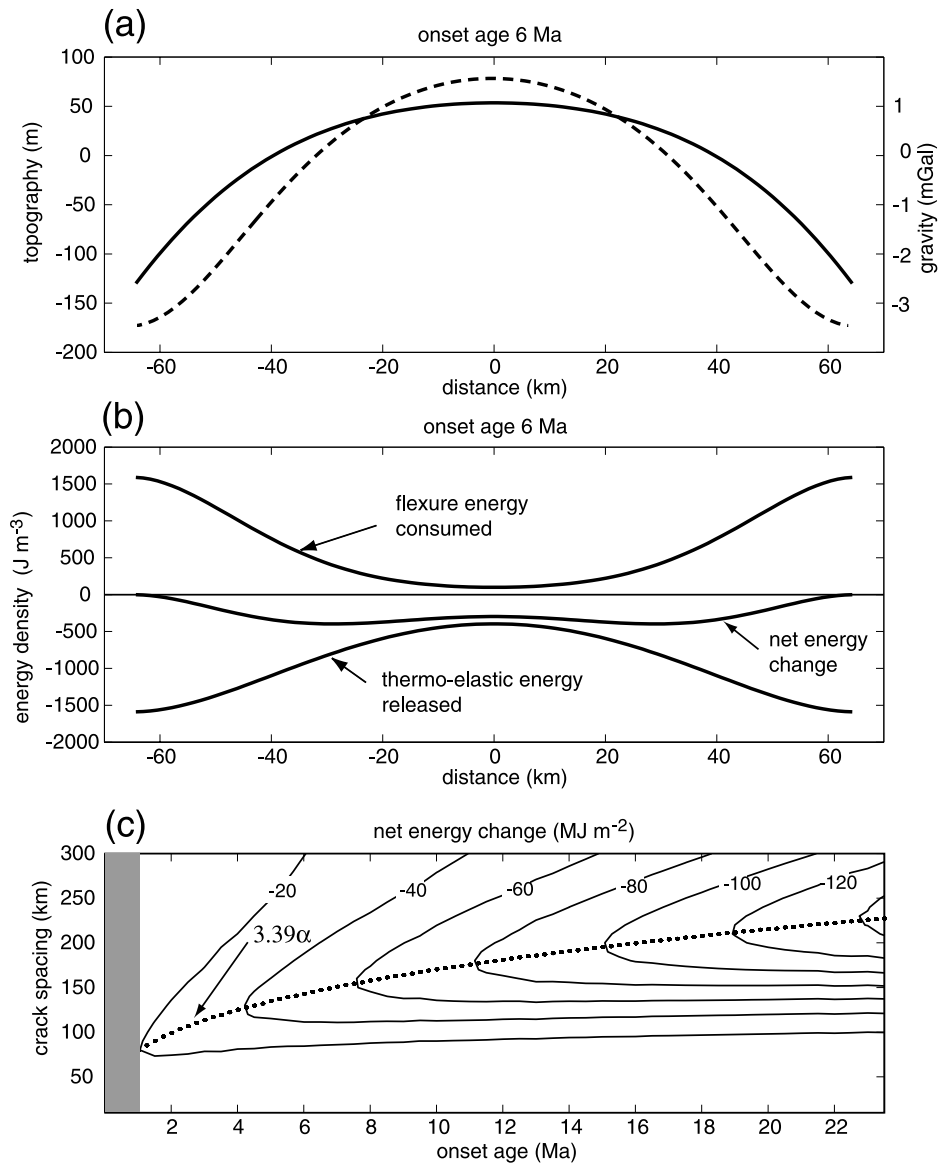


Figure 10. (a) Model of thermoelastic flexure where 130-km spaced cracks are introduced at 6 Ma (solid curve -230 m amplitude topography, dashed curve -5 mGal amplitude gravity anomaly). (b) Thermoelastic energy released by concave down bending exceeds energy consumed by flexing the plate. (c) Net energy versus crack spacing and crack onset age shows a minimum at 3.39 times the flexural parameter α .

the gravity lineaments near the ridge axis (Figure 1b) is interpreted as indicating a fracture resistance of the lithosphere to developing thermoelastic stress, our modeling results may be used to put an upper bound on the effective fracture energy of the lithosphere. For the parameters used in Figure 10, the corresponding energy is of the order of $QL/H \sim 10^7 - 10^8 \text{ Jm}^{-2}$.

[21] Our simple model explains both the wavelength and amplitude of the gravity lineaments observed on young seafloor (Figure 6). The solid curves in Figure 6 are the band-pass filtered gravity profiles at eight ages. The more regular gray curves are the predictions of the model using an onset age corresponding to the present seafloor age. These were computed by assuming uncompensated seafloor topography with uniform crustal thickness ($\rho_c =$

2800 kg m^{-3} ; $\rho_m = 3300 \text{ kg m}^{-3}$; 6 km crustal thickness). The model gravity profiles were low-pass filtered at 80-km wavelength to match the processing of the observed profiles and they were also scaled by 0.75 to provide a better match. This reduced amplitude may reflect incomplete cracking of the plate or an overestimate of Young's modulus used in the model calculation. The crack spacing is not perfectly regular so the model is unable to match the phase for more than about 2 undulations. We align a small section of the model profile to the data profile to illustrate the match in wavelength and amplitude. Note the agreement in amplitude and wavelength at ages of 0.5, 3.2, 5.7, and 8.2 Ma. At greater ages the model slightly overpredicts both the amplitude and the wavelength of the gravity anomalies. Of course, for the real oceanic lithosphere that ages continuously away from

the ridge axis, there is a third dimension that we have not considered. The gravity data alone are insufficient to answer the question of whether the lineaments developed suddenly in the past few million years in response to a plate-wide change in the stress field or whether the process has been continuous in time.

6. Conclusions

[22] Our improved gravity model derived from the ERS satellite altimeter data allows us to robustly resolve both the gravity lineaments and volcanic ridges on the central Pacific seafloor, as confirmed by comparisons with more limited shipboard surveys. We find that volcanic ridges preferentially occur in the troughs of the gravity lineaments. Modeling of the effects of the volcano-induced flexure on the gravity field demonstrates that the gravity lows cannot be explained by the volcanic loads, which essentially rules out a convective origin of the observed gravity lineaments. The satellite altimetry data indicate that lineaments are absent at the EPR axis but develop rapidly on young seafloor on both sides of the spreading ridge. On the Pacific plate they cross the grain of the older seafloor spreading fabric, suggesting that the gravity lineaments manifest an ongoing tectonic process. We develop a model for thermoelastic flexure of a cracked plate using well-constrained parameters of the plate cooling model and the yield strength envelope model. Elastic energy released by thermoelastic flexure has a pronounced maximum at a crack spacing of 3.4 times the flexural parameter of the cooling plate. Our model matches the wavelength and slightly over predicts the amplitude of the observed gravity lineaments. The thermoelastic cracking provides conduits for the escape of available magma to the surface resulting in volcanic ridge formation. The cracks are predicted to align perpendicular to the least compressive stress within the plate. The apparent obliqueness of the gravity lineaments to the older seafloor fabric implies a change in the stress orientation since the old fabric formation. This uniform orientation of the gravity lineaments combined with their increasing wavelength with increasing seafloor age, suggest they were initiated sometime during the past 5–7 Ma and their development continues today. Because the thermoelastic deformation is an intrinsic feature of the plate spreading, our model predicts that the seafloor corrugations and volcanic ridges should be ubiquitous features of the ocean basins. However, the more closely spaced transform faults on the slow spreading ridges (e.g., due to nonuniform magma supply to the ridge axis [Lin and Phipps Morgan, 1992; Fialko and Rubin, 1998]) may prevent the development of significant thermoelastic stress. Moreover, because the flexures have low amplitude (~200 m) they may only be observable on the flanks of the fastest spreading ridges where the sediment cover is minimal, and the ambient topography is smooth.

[23] **Acknowledgments.** We thank the Associate Editor Fredrik Simons and reviewers Doug Wilson and Ken MacDonald for their careful reviews and suggestions for improving the seamount analysis. We also thank David Naar for his critical comments. David Sandwell was supported by grants NSF OCE03-26707 and NASA NAG5-13673. Yuri Fialko was supported by grants OCE 0137226 and EAR 0208165. Correspondence and requests for materials should be addressed to David T. Sandwell (e-mail: dsandwell@ucsd.edu).

References

- Abers, G. A., B. Parsons, and J. K. Weisell (1988), Seamount abundances and distributions in the southeast Pacific, *Earth Planet. Sci. Lett.*, *87*, 137–151.
- Atkinson, B. K. (1987), *Fracture Mechanics of Rock*, pp. 1–23, Academic, San Diego, Calif.
- Bergman, E. A., and S. C. Solomon (1984), Source mechanisms of earthquakes near mid-ocean ridges from body waveform inversion, implications for the early evolution of oceanic lithosphere, *J. Geophys. Res.*, *89*, 11,415–11,444.
- Boley, B., and J. H. Weiner (1960), *Theory of Thermal Stress*, 586 pp., John Wiley, Hoboken, N. J.
- Bratt, S. R., E. A. Bergman, and S. C. Solomon (1985), Thermoelastic stress: How important as a cause of earthquakes in young lithosphere?, *J. Geophys. Res.*, *90*, 10,249–10,260.
- Buck, W. R., and E. M. Parmentier (1986), Convection beneath young oceanic lithosphere: Implications for thermal structure and gravity, *J. Geophys. Res.*, *91*, 1961–1974.
- Dunbar, J., and D. T. Sandwell (1988), A boudinage model for crossgrain lineations, *Eos Trans. AGU*, *69*, 1429.
- Fialko, Y. A. (2001), On origin of near-axis volcanism and faulting at fast spreading mid-ocean ridges, *Earth Planet. Sci. Lett.*, *190*, 31–39.
- Fialko, Y. A., and A. M. Rubin (1997), Numerical simulation of high pressure rock tensile fracture experiments: Evidence of an increase in fracture energy with pressure?, *J. Geophys. Res.*, *102*, 5231–5242.
- Fialko, Y. A., and A. M. Rubin (1998), Thermodynamics of lateral dike propagation: Implications for crustal accretion at slow-spreading mid-ocean ridges, *J. Geophys. Res.*, *103*, 2502–2514.
- Fleitout, L., C. Dalloubeix, and C. Moriceau (1989), Small-wavelength geoid and topography anomalies in the South Atlantic Ocean—A clue to new hot-spot tracks and lithospheric deformation, *Geophys. Res. Lett.*, *16*, 637–640.
- Forsyth, D., S. Webb, D. Scheirer, C. Langmuir, R. Duncan, and K. Donnelly (2002), COOK16MV Cruise Report R/V *Melville*: Tahiti-Easter I., 8 November–24 November, 2001, report, 20 pp., Brown Univ., Providence, R. I.
- Gans, K. D., D. S. Wilson, and K. C. Macdonald (2003), Pacific plate gravity lineaments: Diffuse extension or thermal contraction?, *Geochem. Geophys. Geosyst.*, *4*, 1074, doi:10.1029/2002GC000465.
- Goetze, C., and B. Evans (1979), Stress and temperature in the bending lithosphere as constrained by experimental rock mechanics, *Geophys. J. R. Astron. Soc.*, *59*, 463–478.
- Goodwillie, A. M., and B. Parsons (1992), Placing bounds on lithospheric deformation in the central Pacific Ocean, *Earth Planet. Sci. Lett.*, *111*, 123–139.
- Goodwillie, A. M., and A. B. Watts (1993), An altimetric and bathymetric study of elastic thickness in the central Pacific Ocean, *Earth Planet. Sci. Lett.*, *118*, 311–326.
- Haxby, W. F., and J. K. Weisell (1986), Evidence for small-scale mantle convection from Seasat altimeter data, *J. Geophys. Res.*, *91*, 3507–3520.
- Hussein, M. I. (1977), Energy balance for formation along a fault, *Geophys. J. R. Astron. Soc.*, *49*, 699–714.
- Janney, P. E., J. D. Macdougall, J. H. Natland, and M. A. Lynch (2000), Geochemical evidence from Pukapuka volcanic ridge system for a shallow enriched mantle domain beneath the South Pacific Superswell, *Earth Planet. Sci. Lett.*, *181*, 47–60.
- Lin, J., and J. Phipps Morgan (1992), The spreading rate dependence of three-dimensional mid-ocean ridge gravity structure, *Geophys. Res. Lett.*, *19*, 13–16.
- Lynch, M. A. (1999), Linear ridge groups: Evidence for tensional cracking in the Pacific plate, *J. Geophys. Res.*, *104*, 29,321–29,333.
- Maus, S., C. M. Green, and J. D. Fairhead (1998), Improved ocean-geoid resolution from retracked ERS-1 satellite altimeter waveforms, *Geophys. J. Int.*, *134*(N1), 243–253.
- Morgan, W. J. (1971), Convection plumes in the lower mantle, *Nature*, *230*, 42–43.
- Parmentier, E. M., and W. F. Haxby (1986), Thermal stress in the oceanic lithosphere: Evidence from geoid anomalies at fracture zones, *J. Geophys. Res.*, *91*, 7193–7204.
- Parsons, B., and J. G. Sclater (1977), An analysis of the variation of the ocean floor bathymetry and heat flow with age, *J. Geophys. Res.*, *82*, 803–827.
- Parsons, T., and G. A. Thompson (1991), The role of magma overpressure in suppressing earthquakes and topography: Worldwide examples, *Science*, *253*, 1300–1302.
- Ricard, Y., and C. Froidevaux (1986), Stretching instabilities and lithospheric boudinage, *J. Geophys. Res.*, *91*, 8314–8324.
- Richter, F. M., and B. Parsons (1975), On the interaction of two scales of convection in the mantle, *J. Geophys. Res.*, *80*, 2529–2541.

- Sandwell, D. T. (1986), Thermal stress and the spacings of transform faults, *J. Geophys. Res.*, *91*, 6405–6417.
- Sandwell, D. T., and W. H. F. Smith (1997), Marine gravity anomaly from Geosat and ERS-1 satellite altimetry, *J. Geophys. Res.*, *102*, 10,039–10,054.
- Sandwell, D. T., E. L. Winterer, J. Mammerickx, R. A. Duncan, M. A. Lynch, D. A. Levitt, and C. L. Johnson (1995), Evidence for diffuse extension of the Pacific plate from Pukapuka ridges and cross-grain gravity lineations, *J. Geophys. Res.*, *100*, 15,087–15,099.
- Scholz, C. H. (2002), *The Mechanics of Earthquakes and Faulting*, 496 pp., Cambridge Univ. Press, New York.
- Searle, R. C., J. Francheteau, and B. Cornaglia (1995), New Observations on mid-plate volcanism and the tectonic history of the Pacific plate, Tahiti to Easter Microplate, *Earth. Planet. Sci. Lett.*, *131*, 395–421.
- Shen, Y., D. W. Forsyth, J. Conder, and L. M. Dorman (1997), Investigation of microearthquake activity following an intraplate teleseismic swarm on the flank of the Southern East Pacific Rise, *J. Geophys. Res.*, *102*, 459–475.
- Sleep, N. H. (1992), Hotspot volcanism and mantle plumes, *Annu. Rev. Earth Planet. Sci.*, *20*, 19–43.
- Smith, W. H. F., and D. Sandwell (1997), Global seafloor topography from satellite altimetry and ship depth soundings, *Science*, *277*, 1956–1962.
- Turcotte, D. L. (1974), Are transform faults thermal contraction cracks?, *J. Geophys. Res.*, *79*, 2573–2577.
- Wessel, P. (1992), Thermal stress and the bimodal distribution of elastic thickness estimates of the oceanic lithosphere, *J. Geophys. Res.*, *97*, 14,177–14,193.
- Wessel, P., and W. H. F. Smith (1991), Free software helps map and display data, *Eos Trans. AGU*, *72*, 441, 445–446.
- Wiens, D. A., and S. Stein (1984), Intraplate seismicity and stress in young oceanic lithosphere, *J. Geophys. Res.*, *89*, 11,442–11,464.
- Winterer, E. L., and D. T. Sandwell (1987), Evidence from en-echelon cross-grain ridges for tensional cracks in the Pacific plate, *Nature*, *329*(6139), 534–537.
- Woo, T. C. (1968), Thermal stress problems in glass, *J. Appl. Phys.*, *39*(4), 2082–2087.
-
- Y. Fialko and D. Sandwell, Scripps Institution of Oceanography, University of California, San Diego, IGPP 0225, La Jolla, CA 92093-0225, USA. (dsandwell@ucsd.edu)

20 YEARS OF IMPROVEMENTS TO GEOSAT ALTIMETRY

John LillibrIDGE⁽¹⁾, Walter H.F. Smith⁽¹⁾, David Sandwell⁽²⁾, Remko Scharroo⁽³⁾, Frank Lemoine⁽⁴⁾, and Nikita Zelensky⁽⁵⁾

⁽¹⁾ NOAA Lab. for Satellite Altimetry, 1335 East-West Hwy. E/RA31, Silver Spring, MD, 20910, USA

⁽²⁾ University of California San Diego, 9500 Gilman Drive, La Jolla, CA 92093, USA

⁽³⁾ Altimetrics LLC, 330a South Parsonage Rd., Cornish, NH 03745 USA

⁽⁴⁾ NASA, Space Geodesy Branch, Code 926, Greenbelt, MD 20771, USA

⁽⁵⁾ SGT, Inc., 7701 Greenbelt Road Suite 400, Greenbelt, MD 20770, USA

ABSTRACT

The U.S. Navy GEOSAT mission provided the first long-term altimetric record for studies of ocean circulation, marine gravity/bathymetry and continental ice. The Geodetic Mission (GM) data were declassified by the Navy in 1995 and released by NOAA together with the Exact Repeat Mission data in the 1997 JGM-3 Geophysical Data Records (GDRs).

We have now completed a major upgrade of the GM data by reprocessing the original Sensor Data Records (SDRs) and Waveform Data Records (WDRs). This has allowed us to retrack all the over-ocean waveforms from the GM to improve measurements of sea surface height and its slope and thereby produce better models of marine gravity and bathymetry. A unique two-pass retracking algorithm is used to reduce the noise in along-track sea surface slope, and to reduce the correlation in errors between range and SWH from the waveform fitting.

The precise orbit determination uses the full set of 45 Doppler TRANET tracking stations and is based on a GRACE gravity model. The improved corrections and retracking improve marine gravity and bathymetry resolution, while the new orbits yield better estimates of sea level rise from the GEOSAT time period.

1. INTRODUCTION

The U.S. Navy's GEOSAT mission was comprised of a classified Geodetic Mission (GM) phase, from 31-Mar-1985 to 30-Sep-1986, followed by a 17.05-day cycle Exact Repeat Mission phase, from 8-Nov-1986 to 30-Dec-1989. The GM data were declassified by the Navy on 28-Jun-1995. This allowed NOAA to produce the first complete set of Geophysical Data Records (GDRs) for the entire GEOSAT mission, with the release of the JGM-3 GDR data set in 1997.

The Johns Hopkins University Applied Physics Laboratory operated the GEOSAT ground segment for the entire mission [1]. The raw altimetry data were segmented into two products which were written to separate 9-track

tapes: Sensor Data Records (SDRs), containing 10-Hz measurements of range, AGC, and SWH along with instrumental corrections; and the Waveform Data Records (WDRs) which contained only the 10-Hz (binary) waveform data, representing the radar return power in each of 63 'gates', each 3.125 nanosec wide [2]. The WDRs alone are insufficient to provide range information since they are relative to the absolute range provided in the SDR, and hence were never classified. The SDRs contain all the information necessary to compute sea surface heights, but without the accompanying waveform data, the ranges cannot be retracked.

The SDRs and WDRs were essentially 'separated at birth', and no consolidated product containing both range and waveform information existed for the GEOSAT mission. Previously the waveform data were used for continental ice studies over Greenland and Antarctica, [3], but no global over-ocean retracking of the GEOSAT data had previously been performed.

After a lengthy data rescue operation of SDR data from the NOAA/NODC archives, and WDR data from the NASA/GSFC ice altimetry archive, we have produced a merged GEOSAT GM data set containing all the data. The merger is based upon the unique 'frame count' information common to the WDR and SDR files.

The following sections of this paper describe in more detail how the '20th Anniversary GEOSAT Geodetic Mission Product' data set was constructed, and present preliminary results on improved marine gravity and bathymetry determination based on this data.

2. PRECISE ORBIT DETERMINATION

The original SDR data contain only a very crude orbit state vector. In order to obtain accurate height information, the range must be subtracted from an independently calculated precise satellite orbit, based on Doppler tracking information. The full complement of 45 Navy Opnet and global TRANET Doppler tracking stations, Fig. 1, were used to compute new GEOSAT orbits [4].

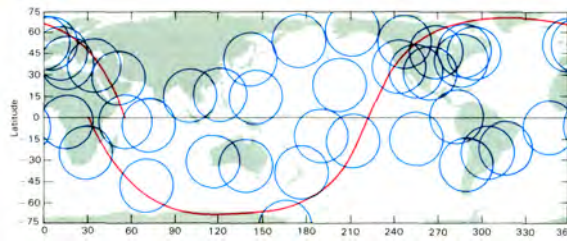


Figure 1. Global network of Doppler tracking stations used for GEOSAT precise orbit determination.

The main improvement in the new GEOSAT orbits is from the use of the GRACE mission’s GGM02C [5] gravity model, which is far superior to the JGM-3 gravity model used in the 1997 GDR release. The Doppler station coordinates are now based on a post-EGM96 gravity and station coordinate solution. Several other aspects of the modeling that goes into the orbit determination system have also been updated, as shown in Table 1. Altimeter crossovers from the retracked data themselves have also been used to help constrain the orbital solution.

Table 1. Models used in the GEOSAT Precise Orbit Determination: JGM-3 GDRs vs. 20th Anniversary Product

Version	JGM-3 GDR	20 th Anniversary
Gravity (static)	JGM3 (70x70)	GGM02C (120x120)
Gravity(time-variable)	C20dot, C21dot, S21dot	C20dot, C21dot, S21dot + 20x20 annual terms from GRACE
Atmospheric gravity	Not applied	NCEP, 50x50 @6 hrs
Ocean Tides	Schwiderski + GEMT3X	(T/P-derived) GOT00.2 (20x20)
Solid Earth Tides	$k_2=0.300$; $k_3=0.093$ + special handling for FCN	IERS2003
Albedo/IR	Knocke & Ries, 1988	Same
Atmospheric drag	MSIS86	MSIS86
Data	Doppler-only	Doppler + Altimeter Crossovers
Parameterization	$C_d/day + C_r + once-per-rev/arc$	$C_d/8 \text{ hrs} + C_r + once-per-rev \text{ along+cross-track/day}$
Doppler station coordinates	JGM2	pgs7727 (post-EGM96: used all ERM & GM Doppler data)

One-day overlaps of the 110 successive 6-day long orbital arcs during the GM, Fig. 2, yield an RMS height difference of 7.5 cm, consistent with a radial orbit error on the order of only 5 cm.

The mean crossover differences in the JGM-3 GDRs, Fig. 3, exhibited significant geographically correlated orbit

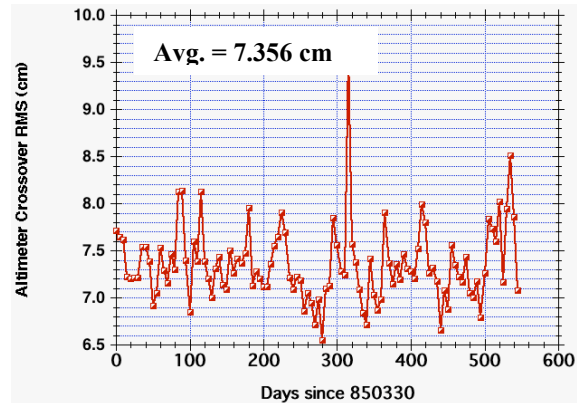


Figure 2. RMS difference in 1-day overlaps between 110 successive 6-day orbital arcs using GGM02C.

error. The new GGM02C orbits have greatly reduced this error, as is particularly evident in areas of “quiet” mesoscale variability, Fig. 4.

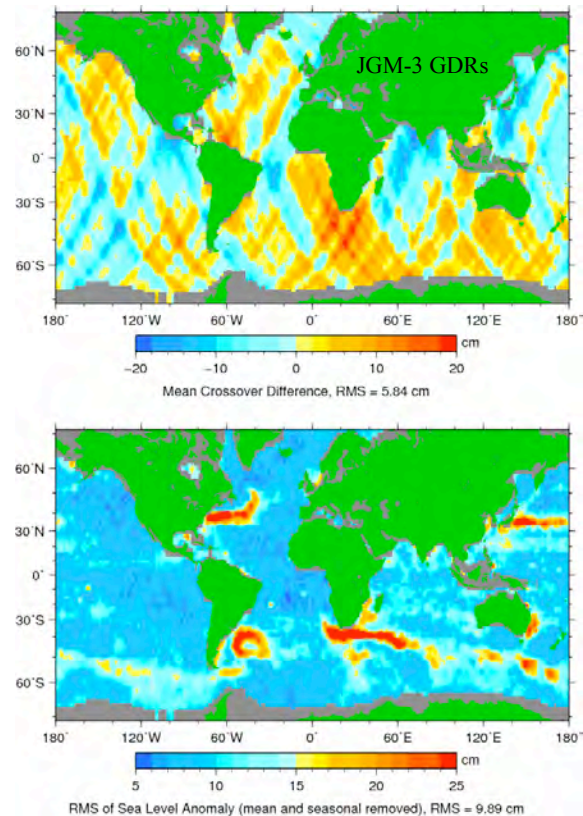


Figure 3. Mean crossover differences (top) and rms sea level variability (bottom) for JGM-3 GDRs.

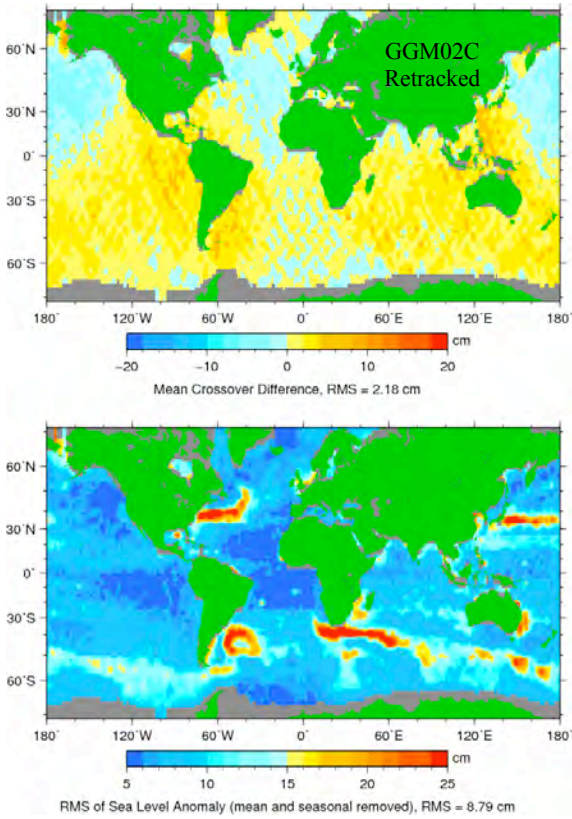


Figure 4 Mean crossover differences (top) and rms sea level variability (bottom) for GGM02C retracked data.

3. ENHANCED PRODUCT & CORRECTIONS

Previous editions of the GEOSAT data were merely upgrades built on prior GDRs, and therefore inherited limitations of the old GDR format: orbits, AGC and SWH were given only once per second, and sea surface height was limited to cm precision. The 20th Anniversary product is generated directly from the original SDR and WDR data, allowing us to store all data at the 10 Hz sampling rate and to mm precision in a new data format.

Through careful reanalysis of the relationship between frame count (onboard satellite clock counts) and UTC, a refined ultra-stable-oscillator height correction is derived, and the “bounce-time” delay in the timing budget is improved by using actual vs. nominal range, to better time-tag the data records. We also used atomic clock time to ensure that no data was lost during the leap second that occurred on June 30, 1985.

3.1 Doppler Correction

We have developed an improved Doppler instrumental range correction. Typically one must choose between a Doppler correction based on the orbital height’s rate of change (which is too smooth) and one based on the actual range’s rate of change (which suffers from noise,

especially over or near non-ocean surfaces). An effective compromise can be reached by employing the along-track derivative of a mean sea surface model:

$$\begin{aligned} \text{Doppler Correction} &\propto \delta(\text{Range})/\delta t \\ &= \delta(\text{Orbit-SSH})/\delta t \\ &\sim \delta(\text{Orbit})/\delta t - \delta(\text{MSS})/\delta t \end{aligned} \quad (1)$$

As shown in Fig. 5, variations in the Doppler correction of several mm occur in regions of large along-track geoid gradients, captured in the mean sea surface. GEOSAT’s long radar ‘chirp’ leads to a proportionality constant of 4.32 mm per m/s of height change in Eq. 1. Along-track variations of several microradians can therefore lead to mm of Doppler correction at the nominal along-track speed of 7 km/s.

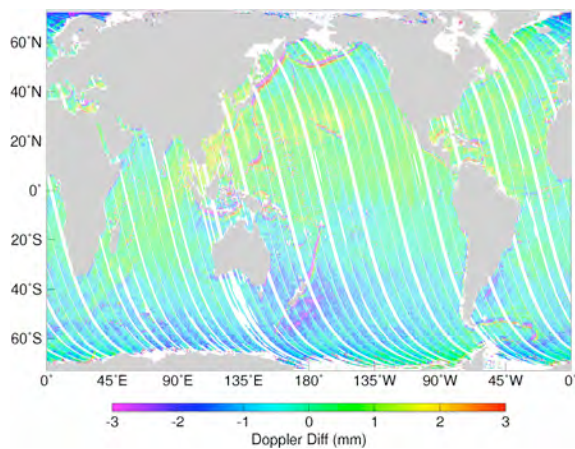


Figure 5. GEOSAT Doppler correction component due to along-track variations in the geoid/mean sea surface

3.2 TOVS Wet Troposphere Correction

Unfortunately GEOSAT did not fly with a radiometer to provide a measured wet troposphere correction. During the GM the only coincident satellite water vapor measurements come from the NOAA polar-orbiter’s TOVS instrument.

In addition to providing a high-quality wet troposphere correction based on the NCEP/NCAR reanalysis model, we also want an independently measured wet troposphere correction based on TOVS. The TOVS correction provided in previous GDRs was based on weekly composited data at 1° spatial resolution. In the intervening years an improved TOVS Pathfinder version of the data [6], with significantly fewer data dropouts, has become available. Using grids of time of day and coincident total precipitable water values, Fig. 6, we are able to do a much better job of filtering the data in space and time than the previous 1° weekly grids.

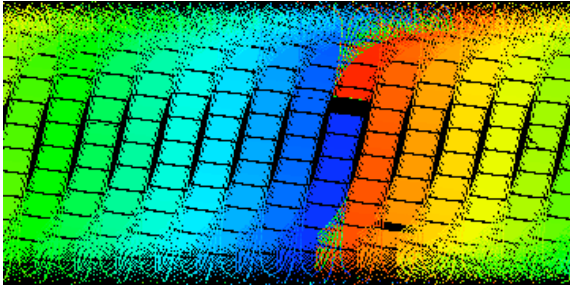
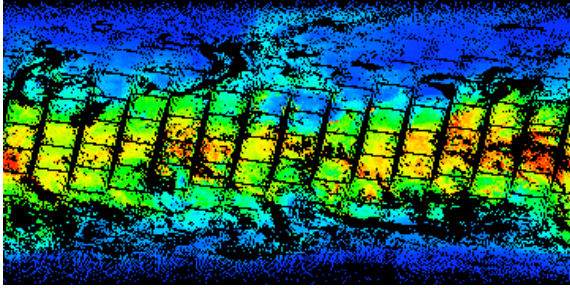


Figure 6. TOVS wet grids of total precipitable water (top) and time, in hour of day (bottom) from Pathfinder.

An autocorrelation analysis of the raw TOVS grids suggested that space and time scales of 2° and $\frac{1}{2}$ day yield optimally interpolated grids.

An example of the interpolated TOVS grid, compared to the NCEP reanalysis model grid provided with this dataset, is shown in Fig. 7.

3.3 Hybrid Sea State Bias Model

A ‘hybrid’ method for estimating the sea state bias correction [7] is applied to the retracked sea surface height anomalies (with no SSB correction applied) to estimate the correction in wave-height/backscatter space. The resulting sea state bias correction grid, which can be interpolated to provide the correction based on each record’s SWH/sigma-0 value, is shown in Fig. 8. Unlike a similar analysis based on the original JGM-3 GDRs (not shown) the retracked Geosat data have a SSB correction more similar to other modern altimetry data sets which have also been retracked. In terms of a simple percentage of waveheight, the correction has a mean value of approximately $4\% \cdot \text{SWH}$.

4. WAVEFORM RETRACKING

Retracking of the GEOSAT waveforms reduces two distinct types of range errors, allowing higher precision gravity and bathymetry fields to be computed from the corrected sea surface height measurements. Range errors associated with the tracker window not being centered on the waveform tend to be more random in nature, and occur when the waveform shape is not well modeled by the classical Brown model. This often happens near coasts

or islands, or when rain or sea-ice distort the radar echo. Retracking corrects for the mis-centering of the waveform from the onboard tracker.

The second type of error is systematic and pervasive, as it is due to the alpha-beta tracker’s causal filter loop in the on-board system. The on-board tracker acts as a critically damped oscillator with a resonance around 0.4 Hz and a group delay of about 0.25 seconds. Sea surface heights computed from the on-board tracker’s range estimates thus have amplified noise in a band centered around 18 km wavelength, while local extrema in height are displaced about 1.7 km down-track of their true position. Retracking eliminates the resonance and the delay, placing features at the proper location along the ground track and sharpening the focus on small-scale features.

The retracking method employed here is two step: first a 5-parameter waveform model is fit to each 10-Hz waveform, solving for amplitude (sigma-0), leading edge slope (SWH), half-power point (range), pre-arrival noise floor, and trailing-edge plateau decay (attitude), Fig. 9.

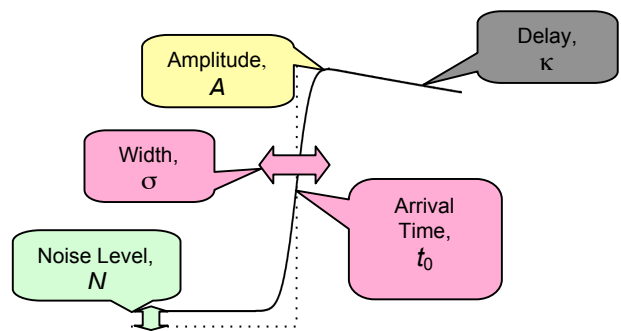


Figure 9. Model waveform used for first pass of 5-parameter retracked fitting.

In the second pass of retracking, along-track smoothed values of all the parameters *except* the range arrival time, t_0 , are formed and a one-parameter fit of the arrival time is made with the other 4 parameters set to their smoothed values. This has the desirable affect of decoupling noise in the estimation of range from noise in the estimation of the leading edge slope, σ , proportional to SWH [8].

The improvement due to retracking is seen in Fig. 10, where power spectra of both signal and noise in sea surface height are shown, before and after retracking. The noise power is cut nearly 50%, resulting in an increase in spatial resolution of nearly 5 km.

These improvements result in a noticeable sharpening of sea floor tectonic signals, as well as a reduction in false sea surface height variability associated with increased SWH variability (e.g. in the Southern Ocean). This is shown in Fig. 11, which compares global maps of sea

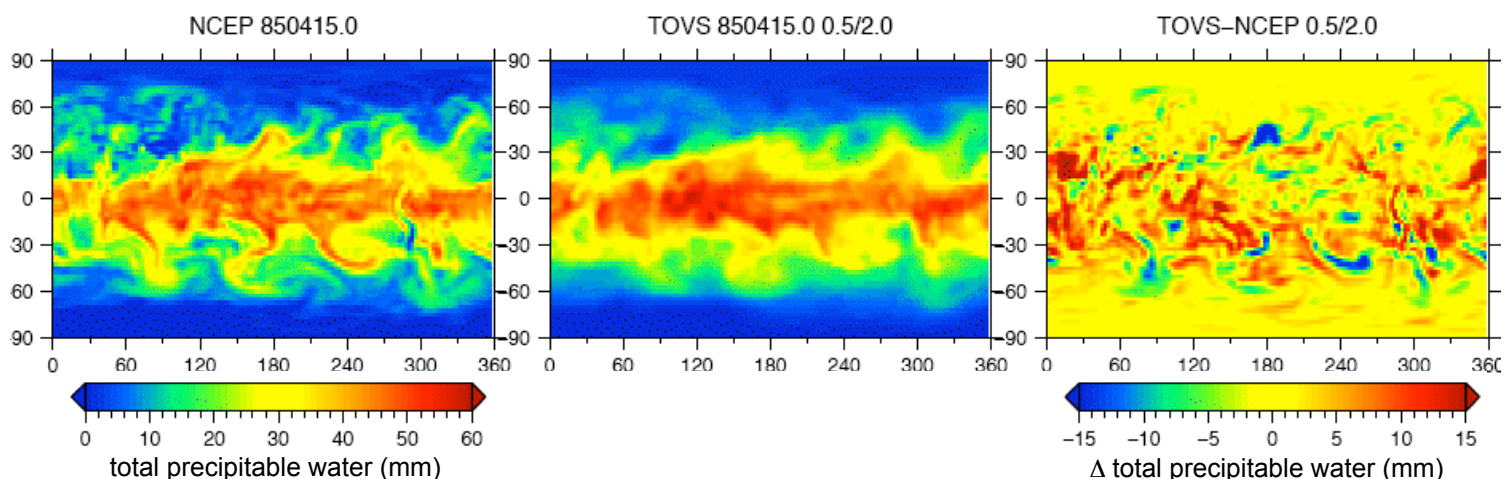


Figure 7. Comparison of total precipitable water grids from NCEP reanalysis (6-hourly, 2.5° grid, left) with new interpolated TOVS pathfinder grids (12-hourly, 2° grid, middle). Difference between TOVS and NCEP grids (right). Units are mm of water.

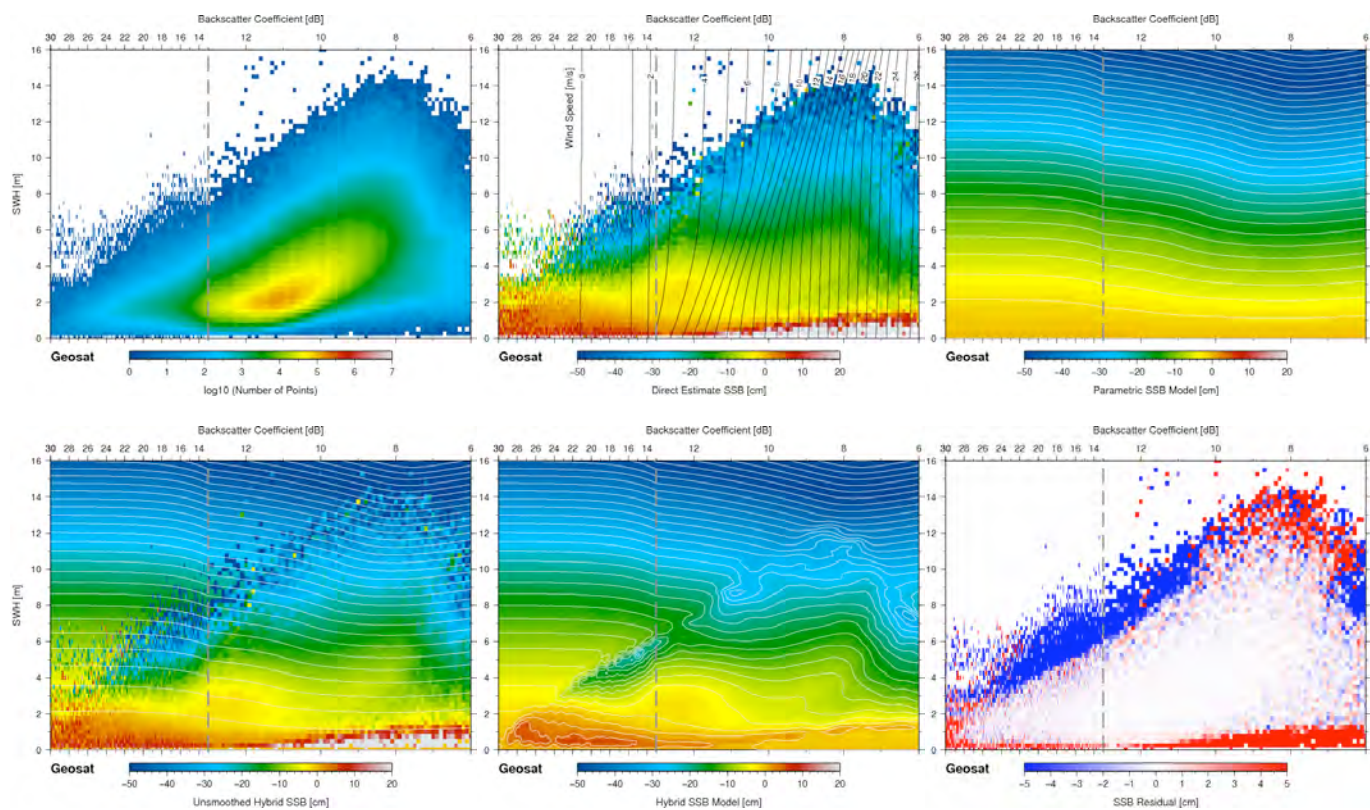


Figure 8. Hybrid sea state bias model analysis based on retracked Geosat GM sea surface height anomalies, in SWH/backscatter space. Upper left: number of points in each .25m/.25dB bin; upper middle: residual SSH anomaly = direct method SSB correction; upper right: smoothed BM4 parametric model; lower left: combined direct+parametric model from upper middle+upper right; lower middle: final smoothed hybrid SSB model; lower right: residual differences between hybrid model (lower middle) and direct estimate itself (upper middle). All SSB correction values in cm.

surface slope filtered with an 18 km high-pass filter, before and after retracking.

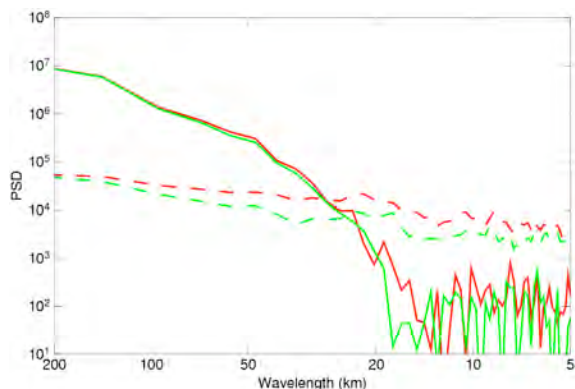


Figure 10. Power spectrum of sea surface height before (red) and after (green) retracking. Noise spectra are dashed while signal spectra are solid. Retracking cuts noise power by 50% at mesoscale and shorter wavelengths. The spatial resolution is also increased, since the signal power remains above the noise power to shorter wavelengths.

5. CONCLUSIONS

GEOSAT was the first multi-year high-precision altimetry mission, and its height measurements have made valuable contributions in the fields of physical oceanography, geodesy, geophysics, and glaciology. It remains unique in terms of the dense spatial sampling of the Geodetic Mission, as well as being the only altimeter operating in the 1980s.

We have produced a new and improved version of the GM dataset by starting with, and merging, the original SDR and WDR records so that waveform retracking can be performed. Better time tagging and new environmental corrections have been applied. The precise orbit determination, based on all available Doppler tracking data, benefits from the latest Grace GGM02C gravity model and inclusion of retracked crossover data from the altimetry. A reduction of several cm rms in radial orbit error is achieved, along with reduced geographically-correlated orbit error. A two-step retracking procedure has been applied to further refine the sea surface heights, reducing correlated noise between SWH and range as well as eliminating an along-track lag in the heights. This has resulted in better spatial resolution for geophysical studies and altimetric bathymetry products.

The GEOSAT GM reanalysis is an excellent example of why altimetric mission data must be preserved. One can never know what improvements in algorithms, retracking techniques, gravity models, and correction fields will be available in the future. Over the 20 years since the GEOSAT mission flew, we have continued to reduce

errors from the orbits and environmental corrections, and have increased the details of spatial resolution in gravity and bathymetry from the sea surface topography.

6. REFERENCES

1. JHU APL, 1987. The Navy Geosat Mission, JHU APL Technical Digest, 8 (2), 169-271.
2. JHU APL, 1985: GEOSAT-A Data Users/Ground System Interface Control Document (ICD), JHU APL, 7292-9510 Rev. 1, Laurel, MD, 122 pp.
3. Zwally, H. J., A. C. Brenner, J. A. Major, R. A. Bindenschadler, and J. G. Marsh, 1989: Growth of Greenland ice sheet - Measurement, *Science* 246, 1587.
4. Haines, B. J., G. H. Born, G. W. Rosborough, J. G. Marsh, and R. G. Williamson, 1990: Precise orbit computation for the Geosat exact repeat mission, *J. Geophys. Res.*, 95 (C3), 2871-2886.
5. Tapley, B., Ries, J., Bettadpur, S., Chambers, D., Cheng, M., Condi, F., Gunter, B., Kang, Z., Nagel, P., Pastor, R., Pekker, T., Poole, S., and Wang, F., 2005: GGM02 - An improved Earth gravity model from GRACE, *J. Geodesy*, 79 (8), 467-478.
6. <http://disc.gsfc.nasa.gov/data/datapool/TOVS/index.html>
7. Scharroo, R. S., J. L. LillibrIDGE, W. H. F. Smith, D. Vandemark, and B. Beckley, 2002: A Hybrid Method of Direct Estimation Sea State Bias Models, 2002 OSTST Meeting, New Orleans, LA.
8. Sandwell, D. T., and W. H. F. Smith, 2005: Retracking ERS-1 Altimeter Waveforms for Optimal Gravity Field Recovery, *Geophys. J. Int.*, 163, 79-89.

7. DISCLAIMER

The views, opinions, and findings contained in this report are those of the authors and should not be construed as an official National Oceanic and Atmospheric Administration or U.S. Government position, policy, or decision.

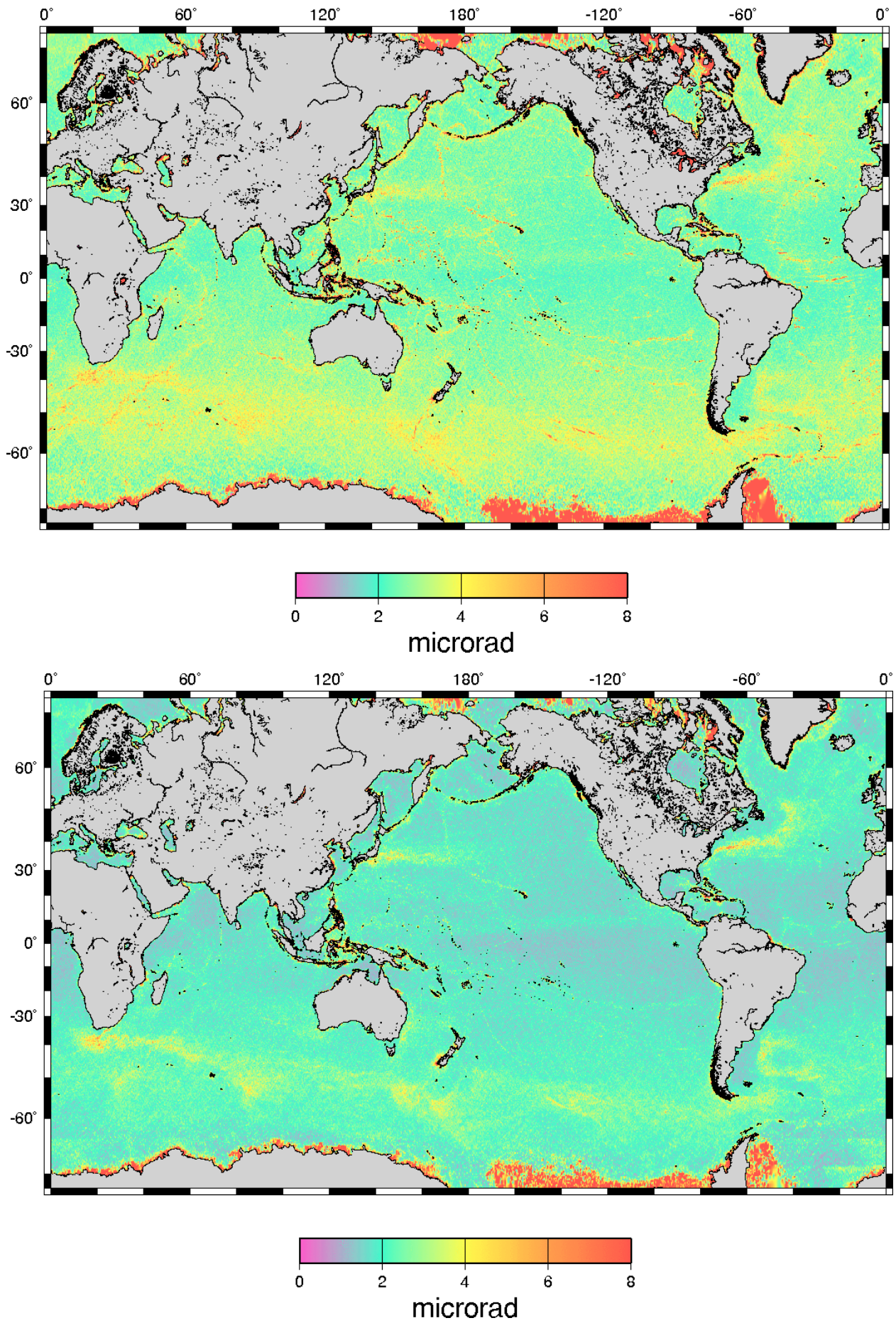


Figure 11. Sea surface slope variability after application of 18 km high-pass filter, before (upper, JGM-3 GDRs) and after (below) two-pass retracking of the waveforms. Note overall reduction in noise after retracking, as well as lack of correlation between high wave height regions, such as Southern Ocean, and surface slope variability. Elimination of the second down-track delay removes seamount and ridge geoid anomalies from the apparent sea surface variability



Global gravity, bathymetry, and the distribution of submarine volcanism through space and time

A. B. Watts,¹ D. T. Sandwell,² W. H. F. Smith,³ and P. Wessel⁴

Received 1 October 2005; revised 25 April 2006; accepted 4 May 2006; published 31 August 2006.

[1] The seafloor is characterized by numerous seamounts and oceanic islands which are mainly volcanic in origin. Relatively few of these features ($< \sim 0.1\%$), however, have been dated, and so little is known about their tectonic setting. One parameter that is sensitive to whether a seamount formed on, near, or far from a mid-ocean ridge is the elastic thickness, T_e , which is a proxy for the long-term strength of the lithosphere. Most previous studies are based on using the bathymetry to calculate the gravity anomaly for different values of T_e and then comparing the calculated and observed gravity anomaly. The problem with such an approach is that bathymetry data are usually limited to single-beam echo sounder data acquired along a ship track and these data are too sparse to define seamount shape. We therefore use the satellite-derived gravity anomaly to predict the bathymetry for different values of T_e . By comparing the predicted bathymetry to actual shipboard soundings in the vicinity of each locality in the Wessel global seamount database, we have obtained 9758 T_e estimates from a wide range of submarine volcanic features in the Pacific, Indian, and Atlantic oceans. Comparisons where there are previous estimates show that bathymetric prediction is a robust way to estimate T_e and its upper and lower bounds. T_e at sites where there is both a sample and crustal age show considerable scatter, however, and there is no simple relationship between T_e and age. Nevertheless, we are able to tentatively assign a tectonic setting to each T_e estimate. The most striking results are in the Pacific Ocean where a broad swath of “on-ridge” volcanism extends from the Foundation seamounts and Ducie Island/Easter Island ridge in the southeast, across the equator, to the Shatsky and Hess rises in the northwest. Interspersed among the on-ridge volcanism are “flank ridge” and “off-ridge” features. The Indian and Atlantic oceans also show a mix of tectonic settings. Off-ridge volcanism dominates in the eastern North Atlantic and northeast Indian oceans, while flank ridge volcanism dominates the northeastern Indian and western south Atlantic oceans. We have been unable to assign the flank ridge and off-ridge estimates an age, but the on-ridge estimates generally reflect, we believe, the age of the underlying oceanic crust. We estimate the volume of on-ridge volcanism to be $\sim 1.1 \times 10^6 \text{ km}^3$ which implies a mean seamount addition rate of $\sim 0.007 \text{ km}^3 \text{ yr}^{-1}$. Rates appear to have varied through geological time, reaching their peak during the Late/Early Cretaceous and then declining to the present-day.

Citation: Watts, A. B., D. T. Sandwell, W. H. F. Smith, and P. Wessel (2006), Global gravity, bathymetry, and the distribution of submarine volcanism through space and time, *J. Geophys. Res.*, *111*, B08408, doi:10.1029/2005JB004083.

1. Introduction

[2] The seafloor is characterized by numerous oceanic islands and seamounts, yet little is known about their tectonic setting. There are many age estimates from field

mapping on ocean islands, dredging on the flanks of seamounts, and scientific drill sites in guyot tops and nearby moat areas. However, the number of sample ages is small (a few hundred) compared to the total number of seamounts, which by some accounts [Menard, 1964] exceed a few hundreds of thousands.

[3] One parameter that may be sensitive to the tectonic setting of a seafloor bathymetric feature is the elastic thickness of the lithosphere, T_e , which is a proxy for its long-term strength. Watts [1978] suggested that oceanic T_e depends on the thermal age of the lithosphere at the time of load emplacement and is given approximately by the depth to the 450°C isotherm based on the plate cooling model, a result that has generally been confirmed in subsequent

¹Department of Earth Sciences, University of Oxford, Oxford, UK.

²Scripps Institution of Oceanography, La Jolla, California, USA.

³Laboratory for Satellite Altimetry, NOAA, Silver Spring, Maryland, USA.

⁴Department of Geology and Geophysics, School of Ocean and Earth Science and Technology, University of Hawaii, Honolulu, Hawaii, USA.

papers [e.g., *Caldwell and Turcotte*, 1979; *Calmant et al.*, 1990; *Lago and Cazenave*, 1981; *Wessel*, 1992; *Watts and Zhong*, 2000].

[4] *Watts et al.* [1980] used the dependence of T_e on age to estimate the tectonic setting of ~ 100 seamounts in the Pacific, a number of which had not been previously sampled. Subsequent studies used T_e to determine tectonic setting not only in the Pacific [*Manea et al.*, 2005], but in the Indian [*Krishna*, 2003] and Atlantic oceans [*Zheng and Arkani-Hamed*, 2002]. However, the total number of such estimates is small compared to the number of seamounts in the world's oceans.

[5] A number of different methods have been used to estimate T_e . These include seismic studies to measure the surfaces of flexure [e.g., *Watts and ten Brink*, 1989] and geomorphic studies of the vertical motions associated with flexure [e.g., *McNutt and Menard*, 1978]. The largest number of estimates, however, has come from forward modeling of the geoid and gravity anomaly. By using a transfer function technique to calculate the anomaly due to the bathymetry and its isostatic compensation and comparing them to the observed anomalies, it has been possible to estimate T_e at a number of oceanic islands and seamounts in each of the world's main ocean basins [*Calmant et al.*, 1990].

[6] The problem with previous gravity modeling approaches is that they have often been applied to ship track sounding data or grids of data that are usually too sparse to fully define the shape of a seamount. As a result, certain assumptions have had to be made in the modeling about the shape of a seamount and whether it is two-dimensional (2-D) or 3-D, which as *Filmer et al.* [1993] have shown may significantly bias T_e .

[7] An alternative approach is to use the global satellite-derived geoid or gravity anomaly, which contains information on the shape of seamounts, to predict the bathymetry for different values of T_e and compare it to observations [e.g., *Goodwillie and Watts*, 1993]. Bathymetric prediction requires, however, implementation of an inverse transfer function. This function grows rapidly at long wavelengths because of isostasy and at short wavelengths because of the attenuation in the geoid or gravity anomaly with increase in water depth. Hence a small error in the gravity anomaly will map into a large error in predicted bathymetry at these wavelengths.

[8] *Dixon et al.* [1983], *Watts et al.* [1985], and *Goodwillie and Watts* [1993] therefore shaped the function in such a way so as to suppress the shortest and longest wavelengths before applying it. By using the geoid derived from satellite altimetry to predict bathymetry they were able to estimate T_e in a range of tectonic settings in the Indian and Pacific oceans.

[9] A different application of the inverse technique is the one by *Smith and Sandwell* [1994a], who used it as a basis to predict bathymetry from satellite gravity anomaly data. They used specially designed filters to shape that part of the inverse transfer function wave band in the range 15–160 km, which was only weakly dependent on T_e . Single ship track echo sounder and multibeam swath bathymetry data were then used to define the bathymetry outside of this wave band.

[10] *Smith and Sandwell* [1994b] extended the prediction wave band so as to calculate bathymetry for different values of T_e . They used a wave band in the range 15–1000 km. This range was sufficiently long to overlap the “diagnostic wave band” of lithospheric flexure, as defined by *Watts* [1983]. By comparing observed and predicted bathymetry in the Atlantic and Pacific oceans south of 30°S (where dense satellite-derived gravity data were then available), they were able to constrain T_e at a number of bathymetric features, including the Louisville Ridge, Walvis Ridge, and Foundation seamounts.

[11] The first detailed application of the inverse technique was the one by *Lyons et al.* [2000] to satellite gravity anomaly data over the Louisville Ridge. They selected the ridge because previous modeling authors [e.g., *Cazenave and Dominh*, 1984; *Watts et al.*, 1988] had made different assumptions about its shape and, as a result, yielded conflicting results. *Lyons et al.* [2000] showed that the inverse technique helped reconcile the previously published results and that T_e was generally low (8–15 km) along the southeastern ridge, south of the Wishbone scarp, and high (23–27 km) to the northwest of it.

[12] The purpose of this paper is to use the global satellite gravity anomaly, together with the inverse transfer function technique of predicting bathymetry, to estimate T_e at selected oceanic islands, seamounts, banks, and rises in each of the world's main ocean basins. Our main aim is to estimate T_e at a greater number of bathymetric features than has been possible in the past and then to use these estimates as a constraint on the distribution of submarine volcanism through space and time.

2. Theory

[13] The gravity anomaly, $G(\mathbf{k})$, associated with seafloor topography, $B(\mathbf{k})$ can be written [e.g., *McKenzie and Bowin*, 1976]

$$G(\mathbf{k}) = Z(k) * B(\mathbf{k})$$

where k is the magnitude of the wave vector \mathbf{k} ($k = (k_x^2 + k_y^2)^{1/2}$), $k = 1/\lambda$, where λ is wavelength, and $Z(k)$ is the transfer function that modifies the topography so as to produce the gravity anomaly.

[14] $Z(k)$ contains information on the state of isostasy and can either be estimated from the free-air gravity anomaly and bathymetry data or calculated for different models of isostasy. For example, $Z(k)$ for the elastic plate (flexure) model of isostasy is given [*Watts*, 2001] by

$$Z(k) = 2\pi G(\rho_c - \rho_w)e^{-kd} \cdot \left\{ 1 - \Phi(k) \frac{((\rho_2 - \rho_i) + (\rho_3 - \rho_2)e^{-kt_2} + (\rho_m - \rho_3)e^{-k(t_2+t_3)})}{(\rho_m - \rho_i)} \right\}$$

where G is gravitational constant, d is mean water depth, ρ_c is density of the seafloor topography, ρ_w is density of seawater, ρ_i is density of the material that infills the flexure, ρ_2 is density of the upper crustal layer, ρ_3 is density of the lower crustal layer, ρ_m is density of the mantle, t_2 is

thickness of upper crustal layer, t_3 is thickness of lower crustal layer, and $\Phi(k)$ is given by

$$\Phi(k) = \left[\frac{Dk^4}{(\rho_m - \rho_i)g} + 1 \right]^{-1}$$

where g is acceleration due to gravity and D is flexural rigidity. D is related to the elastic thickness of the plate, T_e , by

$$D = \frac{ET_e^3}{12(1 - \nu^2)}$$

where E is Young's modulus and ν is Poisson's ratio.

[15] Usually in T_e estimation, the gravity anomaly is computed from the observed bathymetry and compared to the free-air gravity anomaly. T_e is found as the value that best explains the amplitude and wavelength of the gravity anomaly. However, as *Dixon et al.* [1983], *Watts et al.* [1985], *Smith and Sandwell* [1994b], *Lyons et al.* [2000] and *Goodwillie and Watts* [1993] have all demonstrated, T_e may also be estimated by predicting the bathymetry from the gravity (or geoid) anomaly and comparing it to the observed bathymetry. This can be accomplished using

$$B(\mathbf{k}) = Z^{-1}(k) * G(\mathbf{k})$$

where $Z^{-1}(k)$ is the inverse transfer function that modifies the gravity (or geoid) anomaly so as to produce the bathymetry.

[16] Figure 1 shows the functional form of $Z(k)$ and $Z^{-1}(k)$ for $0.001 < k < 0.100$ and a range of assumed T_e , d , and ρ_c values. Other parameters are given in Table 1. Figure 1 shows a strong dependence of $Z(k)$ and $Z^{-1}(k)$ on T_e . $Z(k)$ increases in amplitude and shifts to longer wavelengths as T_e increases while $Z^{-1}(k)$ decreases in amplitude and shifts to longer wavelengths; ρ_c and d have a smaller overall effect and their main influence is on the amplitude of the transfer functions.

[17] $Z(k)$ and $Z^{-1}(k)$ are distinguished by their behavior at long and short wavelengths. $Z(k) \rightarrow 0$ at long wavelengths because of isostatic compensation and at short wavelengths because of upward continuation from the source at the seafloor to the observation point on the sea surface: an effect that increases as $k \rightarrow 1/d$. This behavior causes $Z^{-1}(k)$ to grow rapidly at these wavelengths. Before applying $Z^{-1}(k)$, it is therefore necessary to first shape the function in such a way so as to suppress the longest and shortest wavelengths.

[18] We follow here the "window carpentry" method of *Smith and Sandwell* [1994b, 1997]. They intentionally excluded the diagnostic wave band of flexure: predicting the bathymetry using only the portion of the gravity anomaly spectrum that is shorter than the diagnostic wave band. *Smith and Sandwell* [1994b] chose not to honor actual shipboard soundings, but to use them to calibrate the predictions based on the inverse technique. The reason for this was that they were working with satellite-derived gravity anomaly data south of 30°S where there was little shipboard data. *Smith and Sandwell* [1997] later revised the method to include shipboard data because they were able to

obtain more data, better edit the data they had, and extend the coverage to 72°N and 72°S. Thus their bathymetric predictions since 1997 specifically include shipboard data where available.

[19] Our aim in this paper is to estimate T_e by including the flexural wave band that was intentionally excluded by *Smith and Sandwell* [1994b, 1997]. We will determine T_e by minimizing the root-mean-square (RMS) difference between the predicted bathymetry based on different values of T_e and actual shipboard soundings, omitting all locations that have no soundings. In other words, bathymetric predictions including T_e are fit to actual shipboard sounding data, not to predictions that do not include T_e .

[20] We chose two filters for our analysis, $W_1(k)$ and $W_2(k)$. $W_1(k)$ is a high-pass filter designed to reduce $Z^{-1}(k)$ to zero at long wavelengths. *Smith and Sandwell* [1994a] chose $W_1(k)$ to remove the flexure wave band, and so we use here a different $W_1(k)$, with a high and low cut wavelength of 571 and 804 km, respectively, to retain that band. With these values, $W_1(k) = 0.5$ when $k^{-1} = 675$ km. $W_2(k)$ is a low-pass filter designed to reduce $Z^{-1}(k)$ to zero at short wavelengths. *Smith and Sandwell* [1994a] chose a Wiener filter since such a filter is most effective in the high wave number band where there is an exponential growth in $Z^{-1}(k)$ due to water depth. We chose a value of A , the filter constant, of 3900 km⁴ which is a smaller than the 9500 km⁴ assumed by *Smith and Sandwell* [1994a] because of lower noise levels in the more recent altimeter data [*Sandwell and Smith*, 1997]. With this value, $W_2(k) = 0.5$ when $k^{-1} = 12.5$ km, for water depths of 3 km. The inverse transfer function after it has been modified by the combined filter $W(k) = W_1(k) \times W_2(k)$ is shown in Figure 1 as a solid line in the upper profiles of each panel.

3. Nonlinear Terms

[21] The functions discussed so far are based on a linear admittance theory and so ignore the effect in the expansion of the gravity anomaly of high-order terms in the seafloor topography and its isostatic compensation [*Parker*, 1972]. As a number of workers have pointed out [e.g., *McNutt*, 1979; *Ribe*, 1982; *Smith et al.*, 1989; *Lyons et al.*, 2000], such terms may contribute significantly to the gravity anomaly. *Lyons et al.* [2000], for example, showed that while high-order terms in the topography of the top and bottom of the flexed crust contribute in a negligible way to the gravity anomaly, the contribution to the gravity anomaly of high-order terms in seafloor topography is significant, especially on the crests of tall, steep-sided, low T_e , seamounts where it can exceed 60 mGal.

[22] In order to better understand the effect, we computed the gravity anomaly associated with a synthetic, Gaussian-shaped, seamount in two ways, one using only the first (linear) term ($n = 1$) and the other including higher-order effects. We then used $Z^{-1}(k)$ to estimate T_e from both the linear and higher-order versions of the gravity anomaly. Figures 2a and 2c shows that if $n = 1$ then window carpentry recovers the shape of the input seamount well. However, if $n = 4$ the amplitude of the gravity anomaly increases and the amplitude of the predicted bathymetry exceeds the input bathymetry (Figures 2a and 2b). The effect on the recovery of T_e is shown in Figure 2d. Figure 2 shows that while the

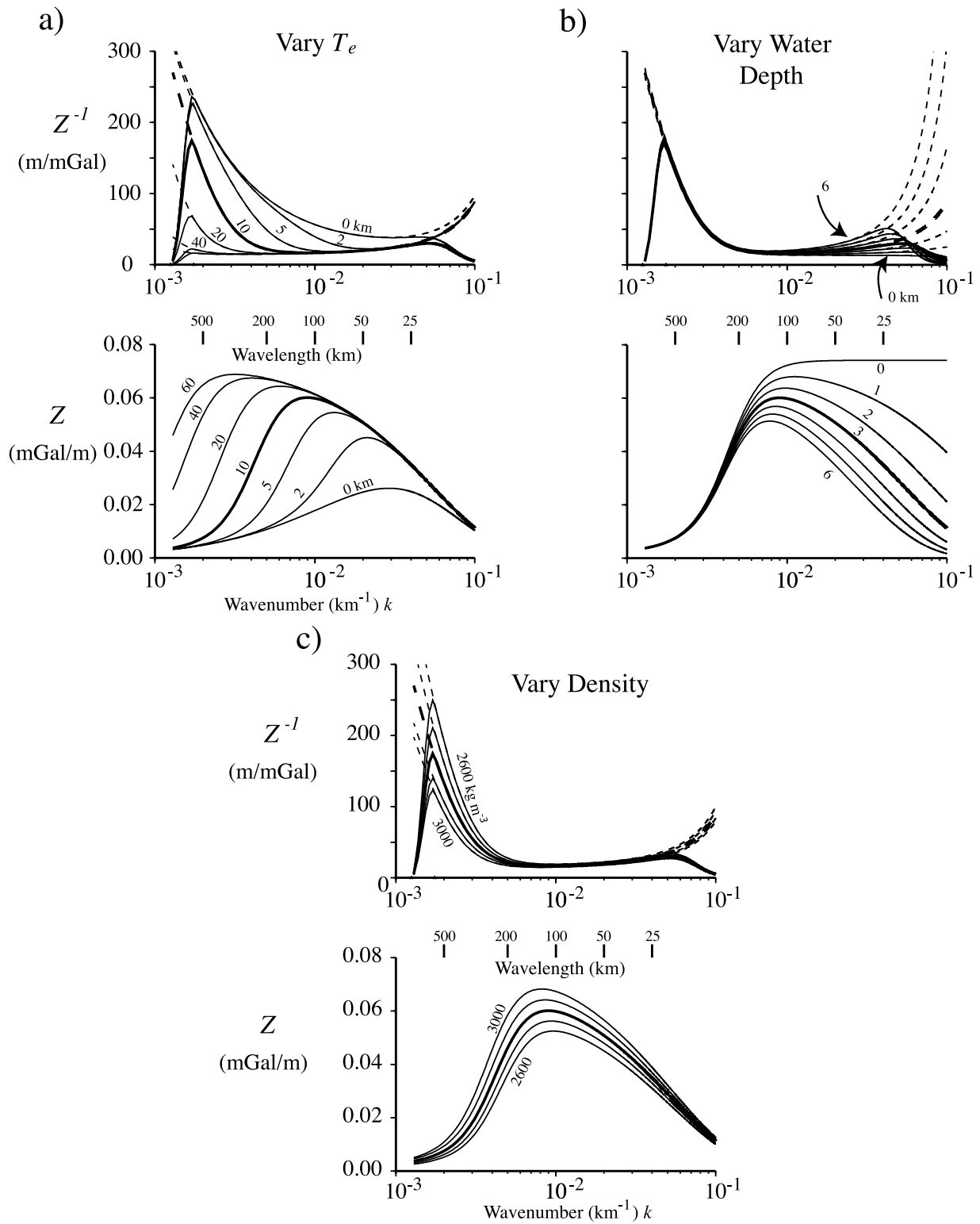


Figure 1. Gravitational admittance for the flexure model of isostasy. The standard model (thick line) is based on an elastic thickness, T_e , of 10 km; water depth, d , of 3 km; and a density of the seafloor topography, ρ_c , of 2800 kg m⁻³. Other model parameters are as defined in Table 1. Bottom profiles show the admittance, $Z(k)$. Top profiles show the inverse admittance, $Z(k)^{-1}$. The inverse admittance has been tapered at long wavelengths using a cosine filter and at short wavelengths by a Weiner filter [Smith and Sandwell, 1994a]. (a) $Z(k)$ and $Z(k)^{-1}$ for a fixed d and ρ_c and T_e in the range 0–60 km. (b) $Z(k)$ and $Z(k)^{-1}$ for a fixed ρ_c and T_e and d in the range 0–6 km. (c) $Z(k)$ and $Z(k)^{-1}$ for a fixed T_e and d and ρ_c in the range 2600–3000 kg m⁻³.

Table 1. Summary of Parameters Assumed in the Gravity Modeling and Bathymetric Prediction

Parameter	Notation in Equations	Value
Density of seawater	ρ_w	1030 kg m ⁻³
Density of seafloor topography	ρ_c	2800 kg m ⁻³
Density of mantle	ρ_m	3330 kg m ⁻³
Density of oceanic “layer 2”	ρ_2	2800 kg m ⁻³
Density of oceanic “layer 3”	ρ_3	2900 kg m ⁻³
Thickness of oceanic “layer 2”	t_2	1.5 km
Thickness of oceanic “layer 3”	t_3	5 km
Density of material that infills the flexure	ρ_i	2800 kg m ⁻³
Young’s modulus	E	100 GPa
Poisson’s ratio	ν	0.25
Wavelength of inverse admittance high pass (high cut)		571 km (harmonic degree, 70)
Wavelength of inverse admittance high pass (low cut)		806 km (harmonic degree, 50)

predicted bathymetry for $n = 1$ recovers the input T_e , well, if $n = 4$ a higher T_e is needed in order for the predicted and input bathymetry to match.

[23] These considerations suggest that the linear inverse transfer function technique may overestimate T_e . However,

this depends on whether the satellite-derived gravity anomaly field used to predict bathymetry recovers the high-order terms. Closely spaced ship surveys using GPS navigation and modern shipboard gravimeters would be expected to fully recover the gravity anomaly over the crest (and flank)

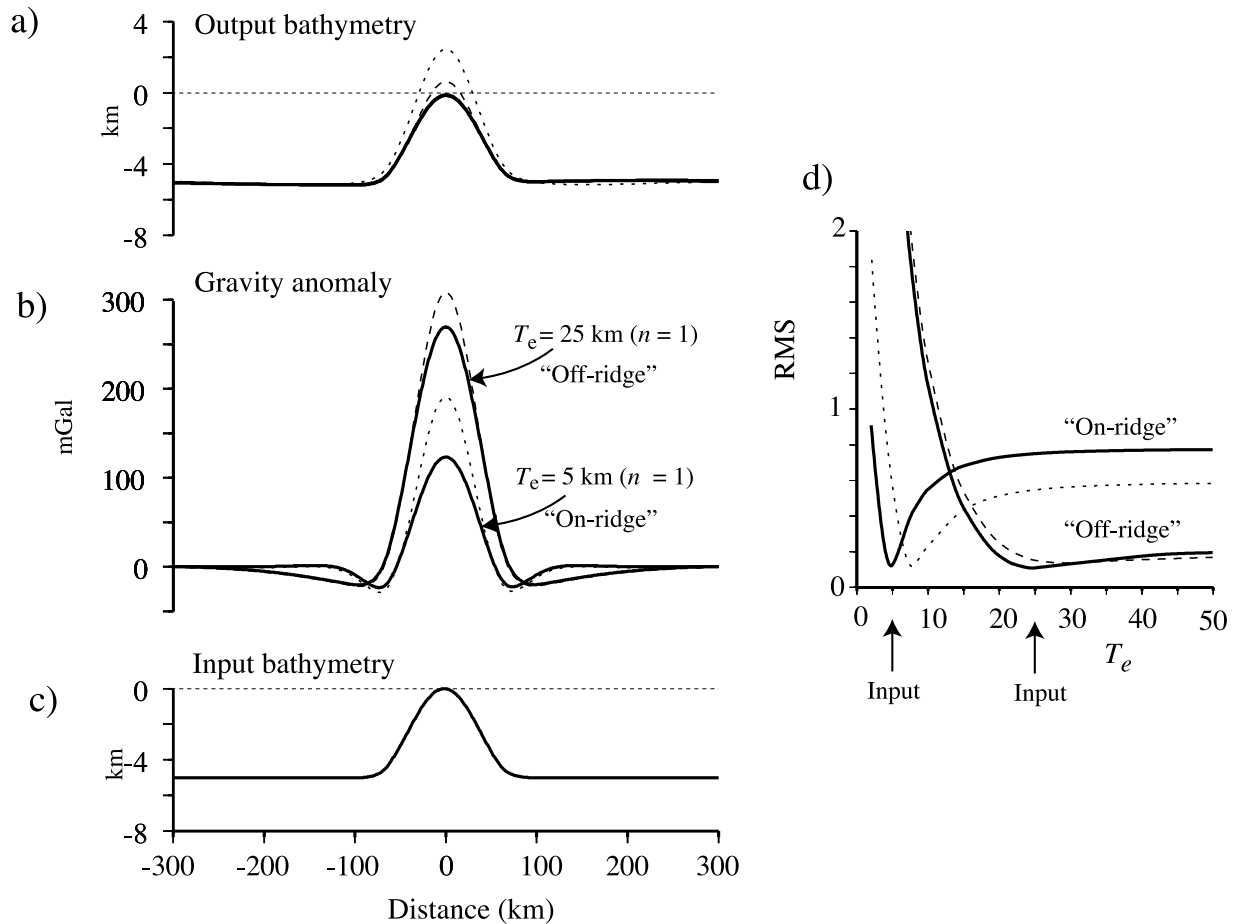


Figure 2. Synthetic tests that use the admittance functions in Figure 1 to calculate the gravity anomaly and predict the bathymetry at a flexurally compensated Gaussian-shaped seamount. (a) “Output” bathymetry based on $Z(k)^{-1}$ and the gravity anomaly in Figure 2b. The output bathymetry for $n = 1$ is the same as the input bathymetry. The output bathymetry for $n = 4$ differs, however, from the input bathymetry. This is because $Z(k)^{-1}$ is based on a linear, first-order, theory. (b) Gravity anomaly based on $T_e = 5$ km (i.e., on ridge) and $T_e = 25$ km (i.e., off ridge) and n in the Parker [1972] expansion of 1 (solid lines) and 4 (dashed lines). (c) “Input” bathymetry used to calculate the gravity anomaly. (d) The root-mean-square (RMS) difference between input and output bathymetry for T_e of 5 and 25 km and n of 1 and 4. The effect of the higher-order terms is to overestimate T_e by up to 2.5–5.2 km.

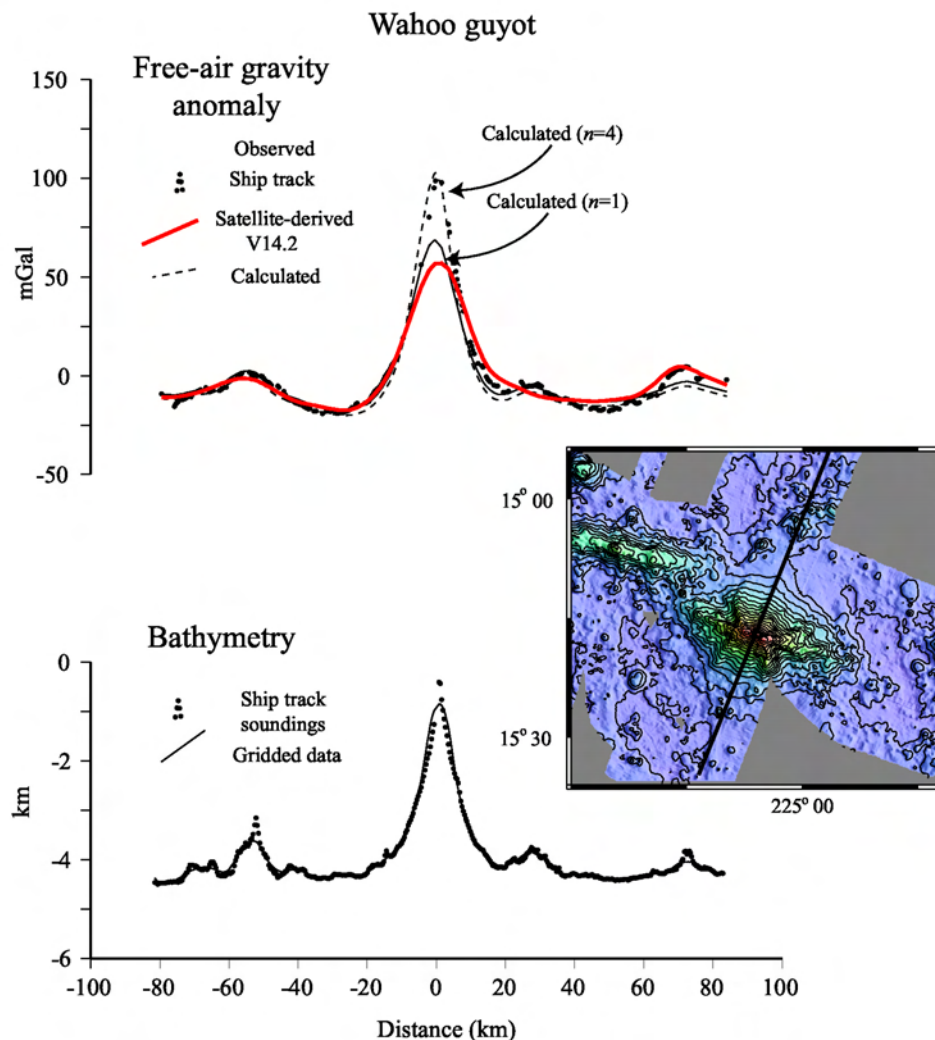


Figure 3. Comparison of the “observed” gravity anomaly recovered from satellite altimeter data to the calculated anomaly based on a grid of shipboard measurements over Wahoo Guyot, Puka Puka Ridge. The inset shows a bathymetry map (contour interval 200 m) based on Figure 3c of *Sandwell et al.* [1995]. (bottom) Shipboard bathymetry measurements (solid circles) and the bathymetry derived from a grid of the measurements (solid line). (top) Observed gravity anomaly based on the satellite-derived V14.2 gravity field of *Sandwell and Smith* [1997] (thick red solid line) and shipboard measurements (solid circles), and the calculated gravity anomaly based on the shipboard grid, $T_e = 1.9$ km and higher-order terms of 1 (thin solid line) and 4 (dashed line). The calculated gravity anomaly for $n = 4$ agrees well with the shipboard measurements but poorly with the satellite-derived gravity data. This, in turn, suggests that V14.2 [*Sandwell and Smith*, 1997] may not have sufficient resolution to resolve the higher-order terms.

of a seamount. However, the satellite-derived gravity anomaly is based on altimetry that may not be of sufficient resolution to recover the high-order terms.

[24] That this may be the case is seen at Wahoo guyot (Puka Puka Ridge) in the central Pacific Ocean (Figure 3). The guyot has been extensively surveyed with multibeam bathymetry [*Sandwell et al.*, 1995]. We used the multibeam data to construct a 2×2 minute bathymetry grid and then used the grid to calculate the gravity anomaly due to the seafloor topography and its compensation. We assumed a $T_e = 1.9$ km which is similar to the value estimated by *Goodwillie* [1995]. Figure 3 shows that while the calculated gravity anomaly with $n = 1$ explains well the amplitude and

wavelength of the satellite-derived gravity anomaly it fits poorly the shipboard gravity anomaly data. These data are fit well, however, by the calculated gravity anomaly with $n = 4$, suggesting that even the most recent satellite-derived gravity fields may not be able to fully recover the higher-order terms.

[25] Wahoo guyot, with its high pedestal height and narrow edifice, is probably a worse case situation as regards the high-order terms. Most other seamounts in the Pacific are smaller and so the contribution to the gravity anomaly of these terms would be expected to be smaller. We have therefore not removed the higher terms in the satellite-

derived gravity field before inverting it for bathymetry as Lyons *et al.* [2000] did, for example, in their study.

4. Method

[26] In their study, Lyons *et al.* [2000] used rectangular 1000×1000 km analysis regions centered on the crest of the Louisville Ridge. They estimated T_e in each region from the RMS difference between the observed and predicted bathymetry, selecting the best fit T_e as that value at the RMS minimum. Since we are concerned in this paper with global T_e estimation, we have modified their technique so that it may be used more efficiently.

[27] We first separated the satellite-derived gravity anomaly (V14.2) and the predicted bathymetry (V8.2) grids of Smith and Sandwell [1997] into their low-pass and high-pass components using a cosine taper between spherical harmonics 50 and 70, corresponding to wavelengths of 571 and 806 km, respectively. These wavelengths were selected in order to isolate that part of the gravity anomaly and bathymetry spectrum that is dominated by lithospheric flexure from the part that is associated with deep processes, such as those associated with mantle convection.

[28] The main computational steps have been described by Smith and Sandwell [1994a, 1997] and so will only be briefly outlined here. The first step is to downward continue the high-pass satellite-derived gravity grid in constant water depth increments of 1 km from 0–6 km. Then, the gravity anomaly at a particular grid cell depth is found from the mean depth (which we estimate from the low-pass predicted bathymetry) and the linear interpolation of the filtered high-pass gravity. The second step is to use the interpolated high-pass gravity, together with the inverse transfer functions, to predict the high-pass bathymetry for different assumed values for the density structure of the crust and T_e . The final step is to sum the low-pass and high-pass predicted bathymetry and compare it to observations based on actual shipboard sounding data.

[29] In order to compare predicted and observed bathymetry at a particular location, we used a cosine “bell” taper, centered at the locality, to define a weighting function and then calculated the RMS difference between the predicted bathymetry based on different assumed values of T_e and the observed bathymetry.

[30] Figure 4 shows an example of the weighting function at two localities in the Line and Hawaiian Islands. We describe the function in terms of a radius, R . With $R = 200$ km the function has a value of 0.5 at a radius of 100 km. The number of points used in the RMS difference calculation between the predicted and observed bathymetry depends on R , the proximity of the locality to land areas (land areas were excluded), and the available ship track bathymetry coverage. The Line Islands are crossed by relatively few ship tracks and have a small land area while the Hawaiian Islands are crossed by a relatively large number of ship tracks and have a large land area. There is therefore a significantly larger number of comparison points for the locality in the Hawaiian Islands than there is for the Line Islands. Despite this, Figure 4 shows good agreement within both weighted regions (RMS difference between predicted and observed bathymetry of 466.5 m and 467.7 m and correlation coefficient of 0.991 and 0.992 for

the Line and Hawaiian islands, respectively). However, the agreement is not perfect. In particular, the predicted bathymetry at the Line Islands locality generally plots below a line with a slope, m , of 1 (i.e., complete agreement between observed and predicted bathymetry) while the predicted bathymetry at the Hawaiian Islands generally plots above it.

[31] The predicted bathymetry shown in Figure 4 is based on an assumed density of the seafloor topography. As was first demonstrated by Nettleton [1939] plots of the free-air gravity anomaly against topography should lie on a straight line with a slope that is related to the density of the topography. Plots of the predicted bathymetry (which has been derived from the free-air gravity anomaly) against the observed bathymetry within the weighted region should therefore also lie on a straight line. A slope of $m = 1$ would indicate a density of seafloor topography of 2800 kg m^{-3} , which is the one assumed in the prediction. Other slopes reflect a different density of the seafloor topography. We can calculate this density from

$$\rho'_c = (\rho_c - \rho_w) * m + \rho_w$$

where ρ_c is the assumed density of the seafloor topography, ρ'_c is the adjusted density, and ρ_w is the density of water. Figure 1 shows that $\rho'_c < \rho_c$ increases $Z^{-1}(k)$ and hence the predicted bathymetry for a particular gravity anomaly while a higher density would decrease it. The adjusted density required at the Line and Hawaiian Islands locality is therefore less (2649 kg m^{-3}) and more (2965 kg m^{-3}), respectively, than the density assumed in the prediction.

[32] Figure 5 shows the RMS difference between predicted and observed bathymetry at the localities in the Line and Hawaiian Islands for different values of R . Both localities show a well-defined RMS difference minimum, although it is better developed in the low T_e Line Islands case than in the high T_e Hawaiian Ridge case. The reason for this is that as T_e increases there is less difference in the flexure and hence a smaller contribution to the gravity anomaly and predicted bathymetry.

[33] We have used the RMS difference minimum, RMS_{\min} , to estimate the best fit T_e and the value of $\text{RMS}_{\min} * (1 + x)$ to estimate its lower and higher bounds, where x is a tolerance parameter. Figure 5 shows that decreasing R sharpens the minimum while increasing R broadens it. T_e decreases with R , but the bias downward is small. The best fit T_e at the Line Islands, for example, decreases from $9.4^{1.6}_{7.4}$ to $6.7^{7.3}_{6.2}$ km ($x = 0.05$) as R is reduced from 400 to 50 km, respectively (see also Table 2). The choice of R is inevitably a compromise. It should not be so small that only a few points in the region of a volcanic edifice are used or so large that the flexural effects of nearby seamounts are included. We choose in this study $R = 200$ km, but we consider the effect of a smaller R , especially at those seamounts that are superimposed on rises, such as those associated with the flexural bulge seaward of deep-sea trenches and midplate topographic swells.

[34] Figure 6 compares the RMS difference between predicted and observed bathymetry at the Line and Hawaiian Islands with other localities in the Emperor seamount chain and the Marquesas Islands. We show two

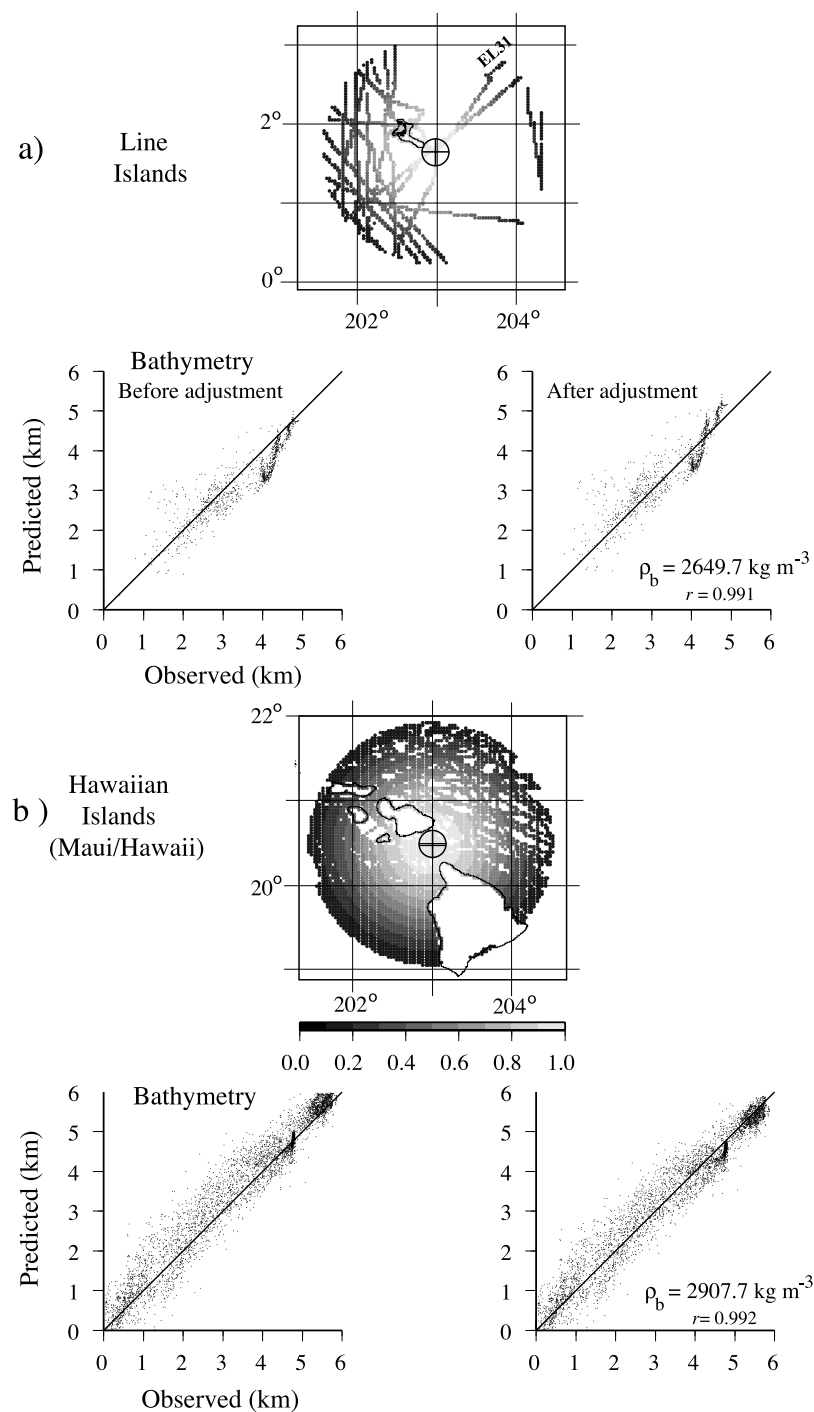


Figure 4. Comparison of observed and predicted bathymetry in a circular region (radius, R , of 200 km) centered on a station (circled cross) in the vicinity of the Hawaiian (longitude 204.0 and latitude 20.5) and Line Islands (longitude 203.0 and latitude 1.6). The observed bathymetry is based on shipboard soundings. The predicted bathymetry has been recovered from the satellite-derived gravity anomaly using the tapered inverse admittance functions in Figure 1 and a T_e that best explains the RMS difference between observed and predicted bathymetry. The thick line in the before adjustment plots shows the expected relationship between the observed and predicted bathymetry if the density of the seafloor topography was 2800 kg m^{-3} . The thick line in the after adjustment plots shows the relationship after adjustment of the seafloor density. (a) Line Islands. (b) Hawaiian Ridge.

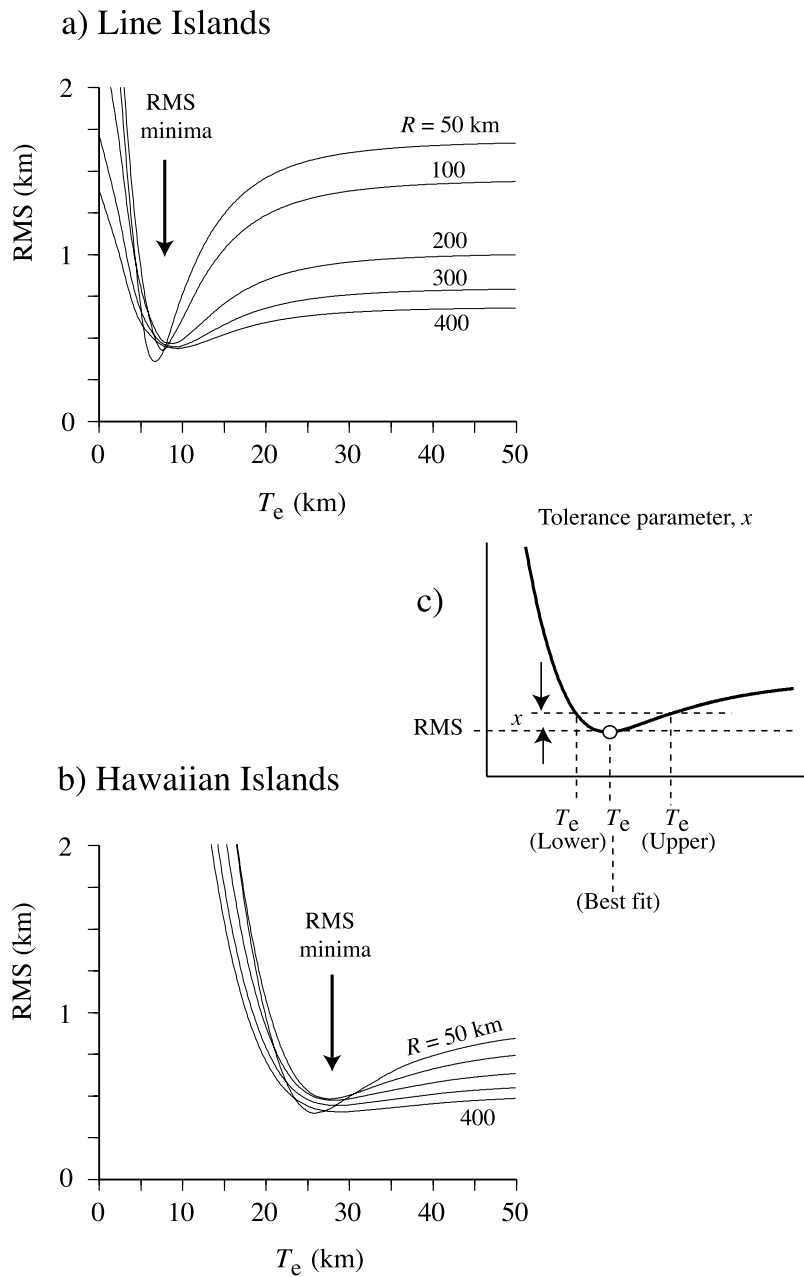


Figure 5. Comparison of the RMS difference between observed and predicted bathymetry for a range of T_e and R values at a station in the region of the (a) Line Islands and (b) Hawaiian Ridge. (c) The best fit and lower and higher bound of T_e . The best fit T_e is defined by the RMS minima. The lower and higher bounds of T_e are defined by the points of intersection where the RMS at the minima has increased by x , the tolerance parameter. The best fit T_e decreases with R . The decrease, assuming $x = 0.05$, is 3.4 km for the Hawaiian Ridge and 2.7 km for the Line Islands.

cases: one where the RMS difference has been computed using a constant density and the other where the density is allowed to vary between the limits 2600 to 3000 kg m⁻³. Figure 6 shows that while a density adjustment reduces the magnitude of the RMS difference, it also broadens the minimum making it less prominent. The effect on T_e varies with different localities. At the Hawaiian and Line Islands, for example, the best fit T_e is reduced by 0.2 and 1.1 km, respectively, while at the Marquesas Islands and Emperor

seamounts it increases by 0.4 and 1.1 km, respectively (see also Table 3).

5. Validation

5.1. Ship Track Data

[35] We first validated the bathymetric prediction technique of recovering T_e using data along ship tracks in the Hawaiian Islands region. This is a well-surveyed area with

Table 2. Dependence of T_e on Radius of the Weighted Points

Longitude	Latitude	Radius, km	Number of Points	Best Fit T_e^a km	RMS, m
<i>Hawaiian Ridge</i>					
204.000	20.500	50	587	25.8 _{24.7} ^{27.4}	390.0
		100	2395	27.6 _{25.6} ^{30.2}	475.4
		200	10495	27.9 _{25.5} ^{31.6}	467.7
		300	21527	28.8 _{25.6} ^{33.0}	436.6
		400	33707	29.2 _{25.7} ^{34.1}	398.0
<i>Line Islands</i>					
202.981	1.640	50	182	6.7 _{6.2} ^{7.3}	357.9
		100	605	7.6 _{7.1} ^{8.1}	424.2
		200	2341	8.8 _{7.4} ^{10.1}	466.5
		300	5658	9.2 _{7.8} ^{10.8}	444.9
		400	9682	9.4 _{7.4} ^{11.6}	435.8

^aBest fit T_e together with its lower bound (subscript) and upper bound (superscript). The lower and upper bounds have been computed assuming a tolerance parameter, x , of 0.05.

nearly complete bathymetric coverage so our new inverse approach can be compared with the standard forward approach in which the gravity anomaly is estimated from the bathymetry in order to determine if the two approaches provide consistent estimates of T_e .

[36] Figure 7 shows the calculated gravity anomaly and predicted bathymetry along two ship tracks that intersect the Hawaiian Ridge between Oahu and Molokai. As has been shown previously [Watts, 1978], the gravity anomaly in the vicinity of the Hawaiian Islands is a strong function of T_e . This is well seen in Figure 7a which compares the observed free-air gravity anomaly along the ship tracks to calculated gravity anomalies based on the GEBCO 1 minute topographic grid and $T_e = 10, 25,$ and 50 km. (We used the GEBCO grid rather than the predicted topography grid because it is based only on shipboard data). The best fit based on the RMS difference between observed and calculated gravity anomalies is for $T_e = 25$ km. Figure 7a shows that a lower T_e predicts a gravity anomaly that is of too short wavelength and low amplitude compared to the observed anomaly, while a higher value predicts an anomaly that has too long a wavelength and high amplitude.

[37] Figure 7b shows that the dependence of the calculated gravity anomaly on T_e extends to the predicted bathymetry. The best fit is again for $T_e = 25$ km. Figure 7b shows that a lower T_e predicts a bathymetry that is of too long wavelength and has too large amplitude compared to the observed, while the higher T_e predicts a bathymetry that is generally of too short wavelength and has too low amplitude. The difference between the best fit T_e and $T_e = 50$ km is not as large in the predicted bathymetry case, however, as it is in the calculated gravity anomaly case.

[38] Figure 8 compares the predicted bathymetry at Hawaii to the Line Islands, Marquesas Islands, and Emperor seamounts. These features also show a strong dependence of the predicted bathymetry on T_e . This is best seen with reference to the predicted bathymetry for $T_e = 16$ km (thick solid line). The predicted bathymetry based on this T_e at the Line Islands is too short in wavelength and too low in amplitude compared to the observed suggesting $T_e < 16$ km. The predicted bathymetry based on this T_e at Hawaii, however, has too long a wavelength and too high an amplitude suggesting $T_e > 16$ km. Only at the Emperor seamounts and Marquesas Islands does $T_e = 16$ km gener-

ally account for the observations. These results confirm earlier suggestions that T_e must vary spatially in the Pacific.

5.2. Previous T_e Estimates

[39] During the past three decades, there have been some 25 studies of flexure at oceanic islands and seamounts that have yielded >80 estimates of T_e [see Watts, 2001, and references therein]. There is therefore an extensive database with which to compare our estimates based on bathymetric prediction.

[40] Figure 9 compares the T_e from previous estimates with the estimates derived from bathymetric prediction. The previous T_e estimates are based on the work by Watts [2001, Table 6.2]. The T_e estimates derived from bathymetric prediction are based on $R = 100, 200,$ and 300 km. We only consider estimates where the difference between the best fit T_e and the lower bound is <15 km. This criterion retains a sharp, well-defined, RMS difference between observed and predicted bathymetry minimum and eliminates broad, poorly defined, minimum. The total number of previous estimates is 94, which reduces to 83 ($R = 200$ km) and 72 ($R = 200$ km and adjusted density) after application of the criteria. Horizontal bars on the previous T_e estimates reflect the published uncertainties. Vertical bars on the T_e estimates have been derived from RMS_{\min} , assuming $x = 0.025$. Figure 9 shows generally good agreement

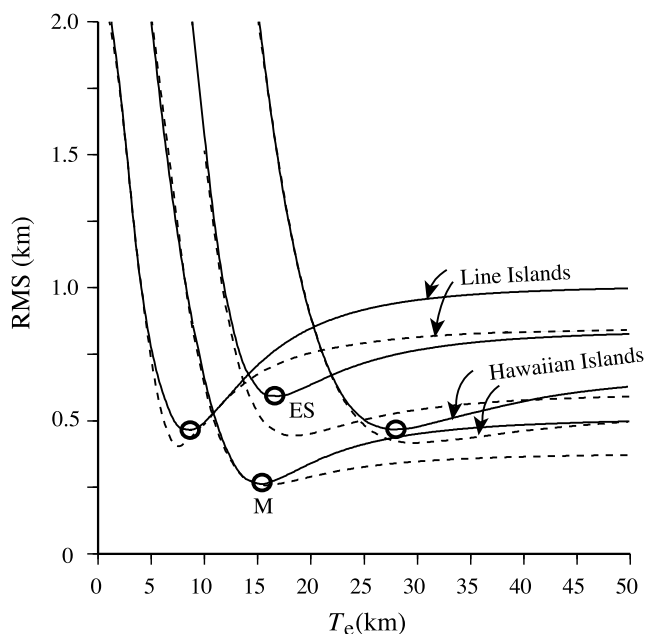


Figure 6. Comparison of the RMS difference between observed and predicted bathymetry for a station in the region of the Line Islands, Emperor Seamounts (ES) (longitude 171.6, latitude 35.0), Marquesas Islands (M) (longitude 220.0, latitude -9.0), and the Hawaiian Ridge. The differences assume $R = 200$ km and either no adjustment to the density (solid lines) or adjustment (dashed lines). The best fit T_e increases for the Line Islands and decreases for the Marquesas Islands, Emperor Seamounts, and Hawaiian Ridge after application of the density adjustment. The difference (Table 2) is largest for the Hawaiian Ridge (1.8 km) and smallest for the Marquesas Islands (0.4 km).

Table 3. Dependence of T_e on Density Adjustment^a

	Unadjusted Density				Adjusted Density				Density kg m ⁻³
	T_e			RMS, m	T_e			RMS, m	
	Lower	Best Fit	Upper		Lower	Best Fit	Upper		
Line Islands	7.4	8.8	10.1	466.5	7.0	7.7	8.5	404.1	2689.9 2649.7
Marquesas Islands	14.1	15.4	16.6	262.6	14.4	15.8	18.0	257.7	2821.1 2829.8
Emperor Seamounts	15.0	16.9	19.3	593.4	16.4	18.0	21.5	444.6	2974.2 2988.7
Hawaiian Ridge	25.5	27.9	31.6	467.7	27.0	29.7	35.4	416.2	2890.5 2907.7

^a $R = 200$ km. Bold values indicate the adjusted density of the seafloor topography (e.g., Figure 4).

between the two sets of estimates. This is despite the fact that the previous T_e estimates are based on a wide range of assumptions concerning seamount shape, elastic plate parameters, and the structure of oceanic crust. We found the highest correlation coefficient ($r = 0.63$) is for $R = 200$ km and an adjusted density.

[41] One seamount that has been a focus for new T_e estimation methods is Great Meteor in the central Atlantic Ocean. This seamount has a smooth flat top, rises ~ 4 km above the surrounding seafloor and is ~ 150 km across at its base. *Watts et al.* [1975] used an analytical solution of the general flexure equation and ship track gravity data to estimate $T_e = 18.9$ km which compares with the ~ 20.0 km estimate of *Verhoef* [1984] and the $19.0_{17.0}^{21.0}$ km estimate of *Calmant et al.* [1990], who used the geoid anomaly derived from Seasat altimeter data and a transfer function technique. More recent estimates have been based on improved geoid data (e.g., GEOSAT, ERS-1) and have yielded estimates of $14.5_{12.0}^{17.0}$ km [*Goodwillie and Watts*, 1993] and 18.2 km and 15.9 km [*Ramillien and Mazzege*, 1999]. These latter estimates compare well to our estimate based on bathymetric prediction of $15.5_{13.4}^{18.1}$ km ($R = 200$ km). However, Great Meteor is located ~ 20 km from another Cruiser seamount which as *Verhoef* [1984] demonstrated has a lower T_e than Great Meteor. Therefore a better estimate for the Great Meteor seamount might be one that is based on $R < 200$ km. We found, for example, that T_e increases to $16.0_{14.6}^{21.2}$ km for $R = 100$ km. Irrespective, the agreement with previous estimates is close, especially when account is taken of the different assumptions that have been made in these studies concerning the elastic parameters, infill density, and density of seafloor topography.

[42] Probably the most direct comparison that we can make between our estimates and previous ones is with those of *Lyons et al.* [2000]. This study used a similar inverse transfer function method and filter design to the one used here. The main differences are that *Lyons et al.* [2000] used satellite-derived gravity V9.2 and predicted bathymetry V6.2 and they calculated the RMS difference between the observed and calculated bathymetry in a rectangular window. Figure 9 and Table 4 show that there is a good agreement between our estimates and those of *Lyons et al.* [2000].

5.3. Seamount Age Data

[43] Previous studies suggest that oceanic T_e depends on the age of the lithosphere at the time of loading [e.g., *Watts and Zhong*, 2000]. Hence there should be some relationship

between the T_e estimates derived from bathymetric prediction and age at those localities where there is both a sample age and an age for the underlying oceanic crust.

[44] We therefore constructed a sample age database from the compilations of *McDougall and Duncan* [1988], *Clouard and Bonneville* [2001], *Davis et al.* [2002], *Koppers et al.* [2003], and *Koppers and Staudigel* [2005] in the Pacific Ocean and *O'Connor et al.* [1999] and *Watts* [2001] in the Atlantic and Indian oceans. We then used bathymetric prediction to estimate T_e at each locality in the database, retaining only those estimates that met the RMS difference shape criteria discussed earlier. The number of estimates obtained was 291, the large majority of which (92%) were from the Pacific Ocean.

[45] Figure 10 shows a plot of T_e against age of the oceanic crust at each sample site. Although there is considerable scatter, the data show an upper envelope, which is given approximately by the depth to the 450°C oceanic isotherm, based on the cooling plate model of *Parsons and Sclater* [1977]. The envelope is indicative of a dependence of T_e on age. This is because the T_e of a seamount on oceanic crust of a particular age will be equal or less than that of the youngest seamount: older features will have a lower T_e because they formed on younger lithosphere. A similar reasoning was used by *Wessel* [1997, 2001] to explain scatterplots of the free-air gravity anomaly against age.

[46] Figure 11a shows a plot of T_e against age of the oceanic crust at the time of loading. Again, the plot shows considerable scatter. Many T_e estimates plot outside the expected $300\text{--}600^\circ\text{C}$ isotherm range and there is clearly no single controlling isotherm that describes all the T_e data. There is evidence, however, of an increase in the minimum and maximum T_e values over the first approximately 60 Ma and a weak positive correlation ($r = 0.36$) between T_e and the square root of age.

[47] In an attempt to understand the cause of the scatter in Figure 11a, we have examined the effect on T_e of plate age uncertainties and load-induced stress relaxation. Figure 11b shows all the sample sites, except those from the Cretaceous and Jurassic magnetic quiet zones where the age of the oceanic crust is uncertain. Figure 11c shows all the data, except sites with load ages > 50 Ma where significant stress relaxation may have occurred. Figure 11 shows that while r decreases to 0.24 in Figure 11b, it increases to 0.44 in Figure 11c. Therefore uncertainties in magnetic quiet zone age are probably not a major contributing factor to the scatter, but load-induced stress relaxation might be.

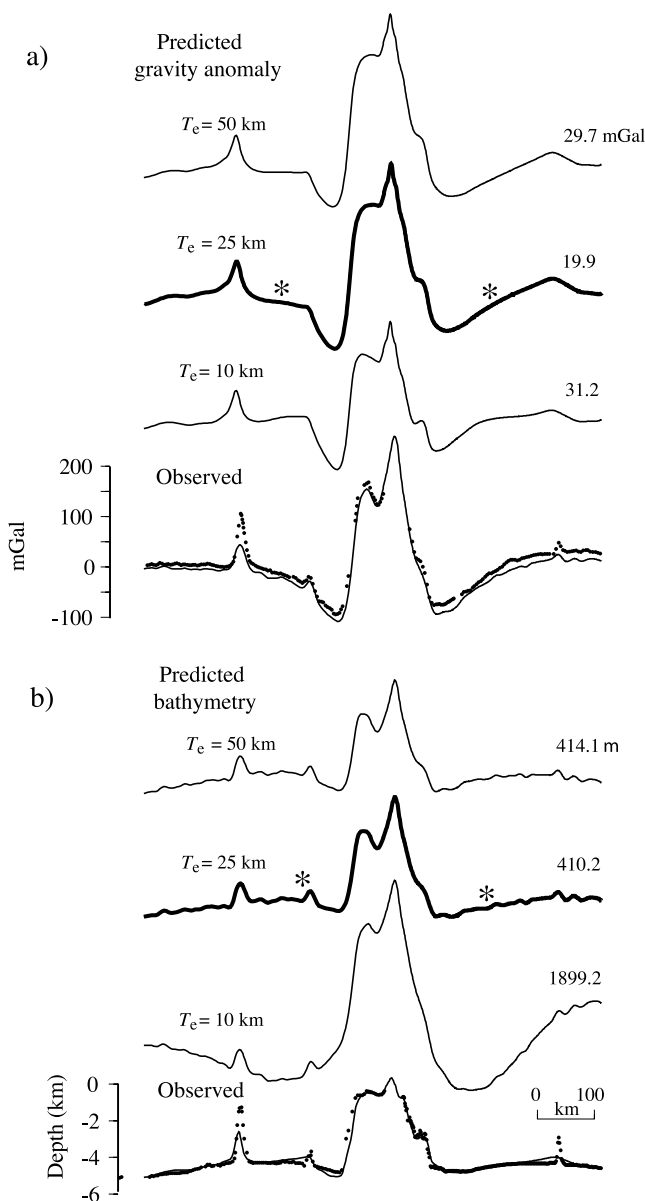


Figure 7. Comparison of observed and calculated gravity anomaly and bathymetry data along a ship track that intersects the Hawaiian Ridge between Oahu and Molokai. The numbers to the right of each profile indicate the RMS difference between observed and calculated gravity and bathymetry data. (a) Observed and calculated gravity anomaly profiles. The observed gravity anomaly data are based on shipboard free-air gravity anomaly data acquired during cruises of V2105 and C1220 (solid circles) and the satellite-derived V14.2 gravity field (solid line). The calculated gravity anomalies are based on a GEBCO 1 minute grid of topography [British Oceanographic Data Centre, 2003] and T_e of 10, 25, and 50 km. The asterisks indicate features in the observed data that are particularly well explained by the calculated profiles. (b) Observed and calculated bathymetry profiles. The observed bathymetry is based on shipboard bathymetry data acquired during cruises of V2105 and C1220 (solid circles) and the GEBCO grid (solid line). The calculated bathymetry is based on the inverse admittance functions in Figure 1 and a T_e of 10, 25 and 50 km.

[48] Another possibility are regional variations in, for example, the controlling isotherm. Figures 12a and 12b shows a plot of T_e against age for the Pacific oceanic crust at the time of loading for the *Koppers et al.* [2003], *Davis et al.* [2002], *Koppers and Staudigel* [2005], and *Clouard and Bonneville* [2001] databases. Figure 12 shows that the French Polynesia, Line Islands, Marshall Islands, Gilbert Ridge, and Foundation seamounts (open squares) have a T_e that is lower than the expected 300–600°C isotherm range while the Japanese and Cobb/Kodiak seamounts (open triangles) have a T_e that is higher. T_e at most other sample sites plot within the expected range.

[49] The maps in Figure 12 show the distribution of the sample localities that fall within the expected range, together with the sites that generally have a lower and higher than expected T_e . Sites with low T_e fall in two main regions. The first is French Polynesia and the Foundation seamounts where previous studies [*McNutt and Menard*, 1978; *Calmant*, 1987; *Calmant and Cazenave*, 1987; *Goodwillie and Watts*, 1993; *Clouard et al.*, 2003; *Maia and Arkani-Hamed*, 2002] have already shown that T_e is often smaller than expected. The second is northwest of French Polynesia and includes the Line Islands, Gilbert Ridge, and Marshall Islands. There have, unfortunately, been relatively few previous T_e studies in these regions. However, *Watts et al.* [1980] and *Smith et al.* [1989] also found unusually low T_e at various sites in the Mid-Pacific Mountains and Magellan seamounts. The Magellan seamounts are of interest because they backtrack into the Society Island region of French Polynesia [*Smith et al.*, 1989]. Furthermore, they have some of the same geochemical affinities (e.g., Sr-Nd-Pb isotopic signatures) as the South Pacific Isotopic and Thermal Anomaly (SOPITA) [*Smith et al.*, 1989; *Staudigel et al.*, 1991], as do the Line Islands [*Koppers et al.*, 1998; *Davis et al.*, 2002]. The low T_e sites may therefore reflect the anomalous mantle temperatures associated with the SOPITA that persisted for at least 100 Myr.

[50] In contrast, sites with high T_e are concentrated around the rim of the Pacific (e.g., the Cobb/Kodiak and Japanese seamounts). There are a number of possible explanations for this. One is that our T_e estimates do not reflect the seamounts, but the topographic rise on which they are superimposed. The Cobb/Kodiak and the Japanese seamounts are located, for example, on the flexural bulge seaward of a deep-sea trenches. The width of the bulge is up to 400–600 km and so its associated gravity effect may not have been removed from the high-pass gravity anomaly that was to predict the bathymetry.

[51] That this may be the case is suggested by our T_e estimates at the Cobb/Kodiak seamounts. These seamounts are superimposed on a flexural bulge seaward of the eastern Aleutian deep-sea trench and the Queen Charlotte Trough. Our estimates range from $17.0_{14.8}^{19.9}$ to $27.1_{23.7}^{32.6}$ km ($R = 200$ km) and are closer to the estimates of *Harris and Chapman* [1994] for the bulge (12–25 km) than they are to their seamount estimates (2–5 km). Indeed, when we assume $R = 50$ km which focuses the comparison more on the seamounts than the bulge, T_e decreases to $9.9_{8.6}^{15.6}$ to $16.8_{12.7}^{30.6}$ km. These estimates are still not as low as those of *Harris and Chapman* [1994], who used a disc shaped load approximation to the

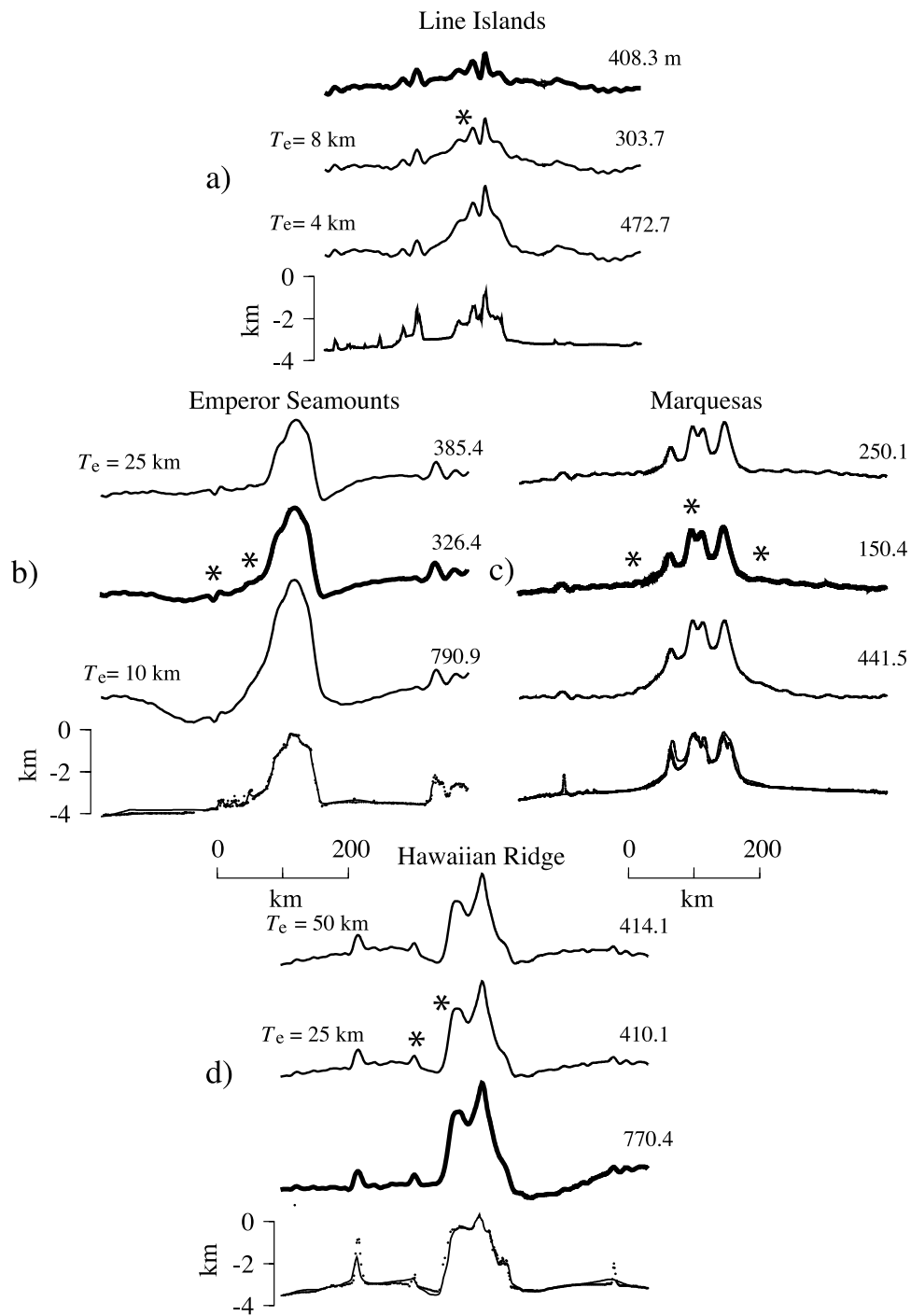


Figure 8. Comparison of observed and calculated bathymetry data along ship track profiles that intersect the Line Islands, Marquesas Islands, Emperor Seamounts, and Hawaiian Ridge. The observed bathymetry (solid circles) is based on data acquired during cruises EL31 (Line Islands), CRGN02 (Marquesas Islands), KK730 and KK750 (Emperor Seamounts) and V2105 and C1220 (Hawaiian Ridge) and the GEBCO grid (thin lines). The calculated bathymetry is based on the tapered inverse admittance functions in Figure 1 and $T_e = 10$ km (thin line), 8 km (thin line), 16 km (thick line), 25 km (thin line), and 50 km (thick line). (a) Line Islands. (b) Emperor seamounts. (c) Marquesas Islands. (d) Hawaiian Ridge.

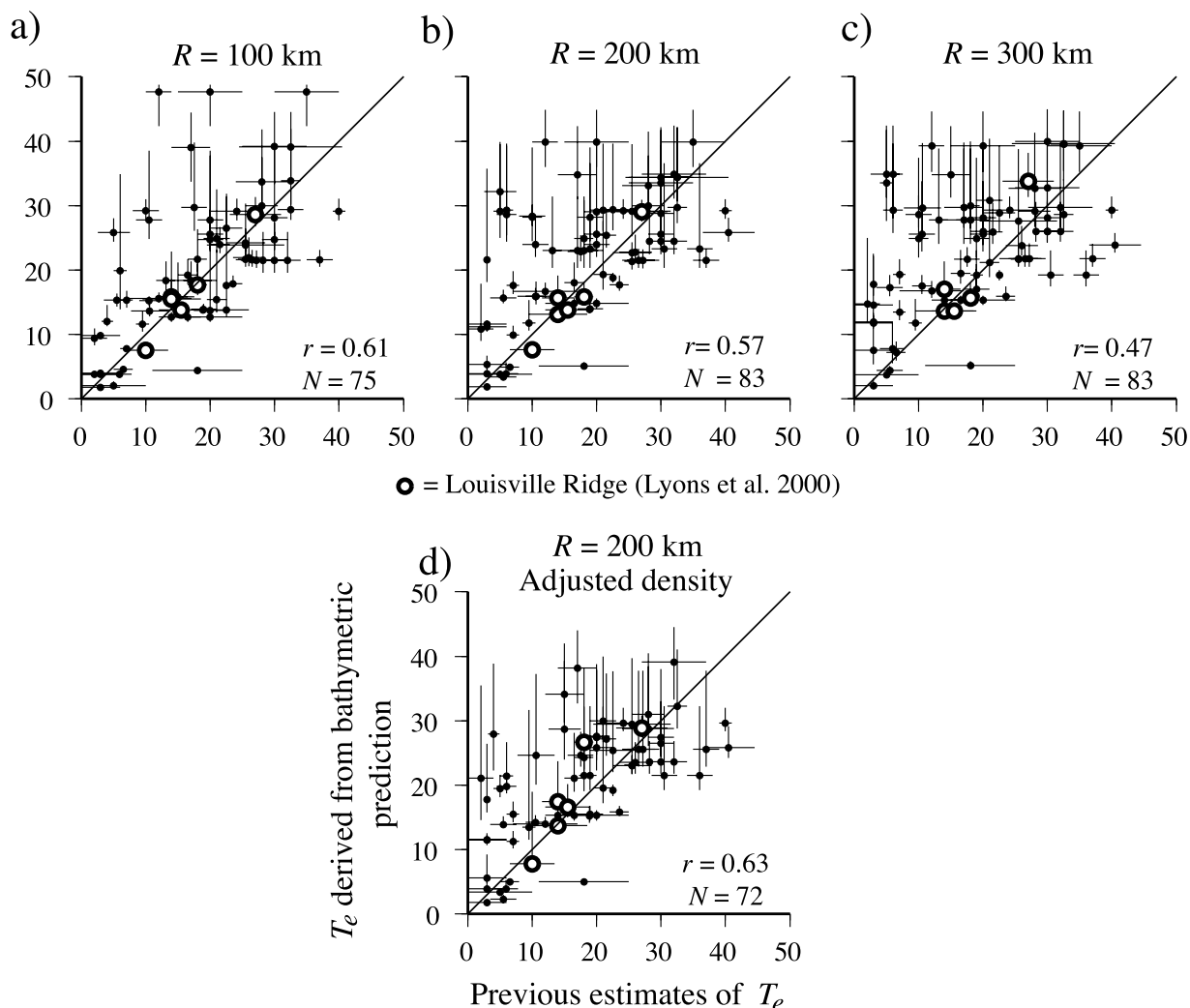


Figure 9. Comparison of previous estimates of T_e to the best fit T_e derived from bathymetric prediction. The previous estimates are based on Table 6.2 of *Watts* [2001]. The “best fit” T_e is shown for different values of R and both unadjusted and adjusted density. (a) $R = 100$ km and unadjusted density. (b) $R = 200$ km and unadjusted density. (c) $R = 300$ km and unadjusted density. (d) $R = 200$ km and adjusted density. The horizontal bars are based on the observed T_e error range in Table 6.2 of *Watts* [2001]. The vertical bars are based on the lower and higher bounds of T_e and $x = 0.025$. The open circles compares our estimates of T_e at the Louisville Ridge with those of *Lyons et al.* [2000], who used a similar method to the one used here. N is number of comparison points. The correlation coefficient, r , measures how strong a linear correlation exists between the previous estimate and best fit T_e .

bathymetry in their flexure models, but they are more compatible with a near ridge origin for the seamount chain, as suggested by *Cousens et al.* [1999].

6. Results

[52] We have used the satellite-derived gravity anomaly and shipboard bathymetry measurements to estimate T_e at each locality in the *Wessel* [2001] global seamount database. This database was selected because it contains not only locations, but also size information (i.e., height, base radius) that may be used to estimate the volume of individual seamounts.

[53] The *Wessel* [2001] database yielded a total of 9758 T_e estimates (Figure 13). Not all these estimates are indepen-

dent since we may have sampled the same bathymetric feature more than once. The average density and T_e of the sampled features is $2810.6 \pm 148.5 \text{ kg m}^{-3}$ and 18.4 ± 11.0 km, respectively. The symmetry in the lower and upper

Table 4. Comparison of the Results in This Paper With Those of *Lyons et al.* [2000] at the Louisville Ridge

Region of <i>Lyons et al.</i> [2000]	Longitude of Center Point	Latitude of Center Point	<i>Lyons et al.</i> [2000]	This Paper
A	186.00	-28.00	27.0 _{23.0} —	28.9 _{25.8} ^{32.8}
F	188.10	-40.70	15.5 _{12.0} —	17.4 _{13.1} ^{30.0}
G	199.83	-43.00	14.0 _{9.5} ^{22.5}	13.7 _{11.6} ^{17.1}
H	201.80	-45.20	15.5 _{12.0} —	16.6 _{13.4} ^{23.7}
J	211.80	-47.50	10.0 _{6.5} —	7.8 _{6.9} ^{30.1}

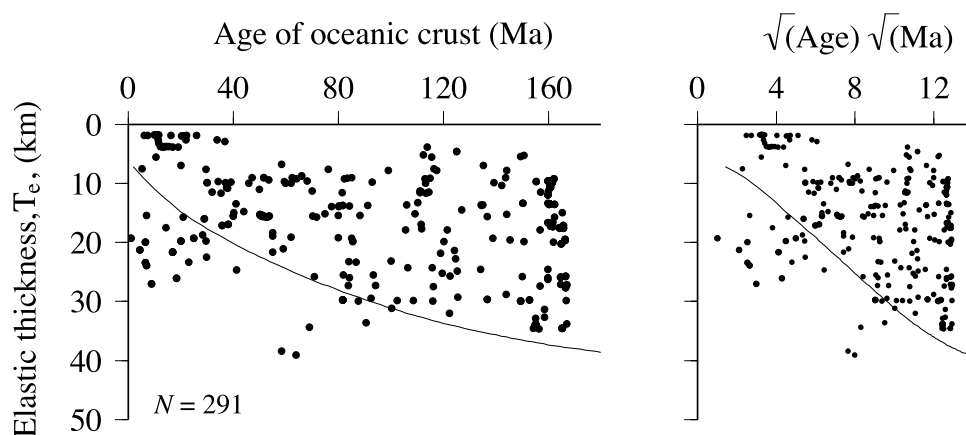


Figure 10. Scatterplot of the best fit T_e derived from bathymetric prediction against age of the oceanic crust at sample sites in the Pacific, Indian, and Atlantic oceans. The best fit T_e is based on $R = 200$ km and an adjusted density. The sample sites are based on the work by *McDougall and Duncan* [1988], *Koppers et al.* [2003], *Davis et al.* [2002], *Koppers and Staudigel* [2005], and *Clouard and Bonneville* [2001] in the Pacific and *O'Connor et al.* [1999] and *Watts* [2001] in the Indian and Atlantic oceans. The age of the oceanic crust is from *Müeller et al.* [1997]. (left) T_e against age of oceanic crust. (right) T_e against the square root of age of oceanic crust. The upper envelope in each plot corresponds approximately to the depth to the 450°C isotherm, based on the plate cooling model of *Parsons and Sclater* [1977]. N is as defined in Figure 9.

bounds (Figure 13b) suggest that the RMS difference between observed and predicted bathymetry is generally well defined and that T_e is well resolved. We attribute this to the high number of bathymetry points (average is 2709.3) used to compute the RMS difference and the relatively low RMS difference (average is 336.9 m) at the minimum.

[54] The remaining 2098 localities in the *Wessel* [2001] database did not yield a T_e estimate. The main reason for this is probably the small size of some of the features. For example, there is a factor of 3 higher proportion of small features (i.e., features with a base radius <8 km and height <1.8 km) among the group that did not yield a T_e estimate than in the rest of the database. A base radius of <8 km corresponds to a wavelength of <~16 km and most bathymetric features will appear uncompensated and, hence yield no RMS difference minima, at these wavelengths.

[55] Figure 14 shows the global T_e estimates which have been color-coded according to their magnitude. Red dots indicate seamounts where $0 < T_e < 12$ km. This range is similar to that obtained by *Cochran* [1979] and *McNutt* [1979] from spectral studies of seafloor topography at slow spreading and fast spreading ridges in the Atlantic and Pacific oceans and is consistent with the results of more recent studies on intermediate spreading ridges in the Indian Ocean [e.g., *Krishna*, 1997]. We therefore assign seamounts with this T_e range an “on-ridge” setting, although as Figure 11 suggests, “near-ridge” might be a more appropriate description. Blue dots indicate seamounts with $T_e > 20$ km. This lower limit is similar to that obtained by *Watts* [1978] from spectral studies of seafloor topography along the Hawaiian-Emperor seamount chain. We therefore assign such seamounts an off-ridge setting. The remaining (green) dots correspond to intermediate estimates ($12 \leq T_e \leq 20$ km) and so these seamounts are assigned a “flank ridge” setting.

[56] We recognize that such a separation of seamounts into their different settings is arbitrary. This is because each T_e estimate has a lower and higher bound and therefore some estimates may overlap between different tectonic settings. Nevertheless, we believe Figure 14 to be a useful guide. Interestingly, the settings change over small horizontal scales, such that an on-ridge or flank ridge seamount maybe located within a few km of an off-ridge one. Furthermore, the same bathymetric feature (e.g., the Ninetyeast and Chagos Laccadive ridges) may be associated with more than one setting.

[57] The Pacific shows the most striking patterns. Of particular note is a broad swath of on-ridge volcanism that extends for >7000 km from the south central Pacific, across the equator, and into the western Pacific. The swath includes (from southeast to northwest) the Easter/Salas y Gomez ridge, the Ducie Island/Easter ridge, the Foundation Seamounts; the Tuamotu Plateau and Austral Islands; the Line Islands, the Gilbert Ridge and the Mid-Pacific Mountains; and the Shatsky and Hess rises. An on-ridge setting is generally consistent with what is known about the age of these features and the underlying crust. The Easter/Salas y Gomez ridge and Foundation Seamounts, for example, are 0–22 Ma and appear to have been emplaced on 2–10 Myr oceanic crust [*O'Connor et al.*, 1998]. *Maia and Arkani-Hamed* [2002] suggested these features formed at the intersection of the Pacific-Antarctic ridge with a hot spot. The Ducie Island/Easter ridge, which is conjugate to the Easter/Salas y Gomez ridge, probably formed in a similar tectonic setting. There is, however, no clear hot spot age progression along these ridges. It has been proposed that the ridges may have formed by magma leaking either along preexisting lines of weakness [*Bonatti et al.*, 1977; *Searle et al.*, 1995] or subduction-induced tensile cracks [*Sandwell et al.*, 1995]. The Tuamotu Plateau has few sample ages, but *Patriat et al.* [2002] concur with the earlier suggestions of

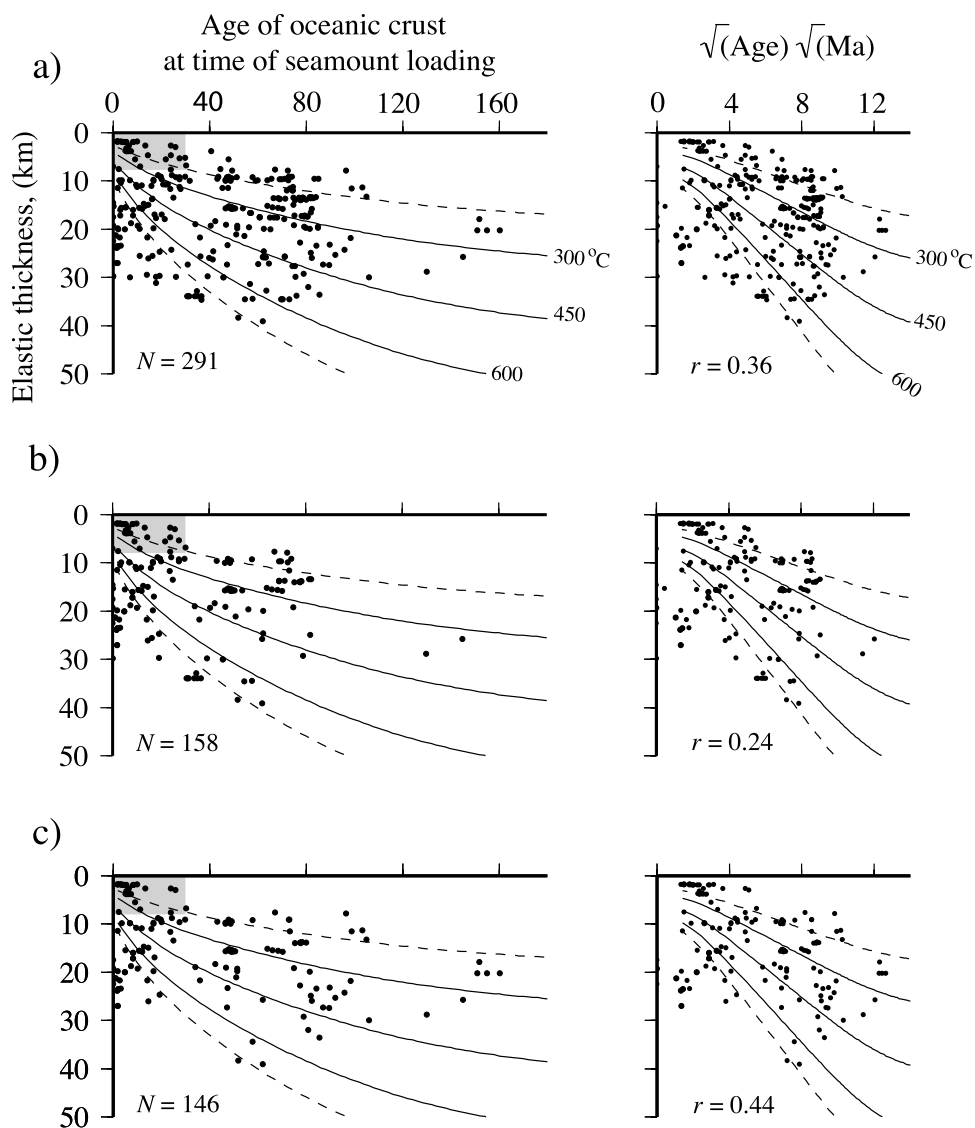


Figure 11. Plot of the best fit T_e derived from bathymetric prediction against age of the oceanic crust at the time of loading at sample sites in the Pacific, Indian, and Atlantic oceans. The sample sites are the same as those used in Figure 10. (left) T_e against age of oceanic crust at the time of loading. (right) T_e against the square root of age of oceanic crust at the time of loading. Thin solid lines show the 300, 450, and 600°C isotherms. Thin dashed lines show the 200°C (uppermost curve) and 700°C (lowermost curve) isotherms. N and r are as defined in Figure 9. Grey shading outlines the region where $0 < T_e < 8$ km and the age of the oceanic crust at the time of loading is 0–30 Ma. (a) All data. (b) All data except sample sites from the Cretaceous and Jurassic magnetic quiet zones. (c) All data except sites where the sample age is >50 Ma.

Watts *et al.* [1980] that the plateau formed at or near the paleo-East Pacific Rise. The Austral Islands range in age from 3.7 to 39.6 Ma, but most ages cluster in the range 26–32 Ma, suggesting that the bulk of the islands formed on 8–24 Myr seafloor on or near a ridge crest [McNutt *et al.*, 1997]. However, the range of sample ages suggests a less voluminous veneer of volcanism at the Austral islands that may be off ridge [McNutt *et al.*, 1997]. An on-ridge setting is also suggested for the Gilbert Ridge which ranges in age from 64–72 Ma and was emplaced on 63–81 Myr crust [Koppers and Staudigel, 2005]. More difficult to reconcile are the Line Islands which range in age from

68 to 86 Ma and so were emplaced on 14–52 Myr oceanic crust [Davis *et al.*, 2002]. These ages are more indicative of a flank ridge, or even off-ridge, tectonic setting than an on-ridge one. One possibility is that the Line Islands, like the Austral Islands, have experienced a prolonged history of volcanism, such that T_e reflects a large-volume early event while the sample ages reflect a small-volume later event. An on-ridge setting for the Shatsky Rise and Hess Rise, however, is in better agreement. The Shatsky Rise ranges in age from 132–146 Ma and formed on or near an Early Cretaceous RRR triple junction [Sager and Han, 1993] while the Hess Rise ranges in age from 89–97 Ma and

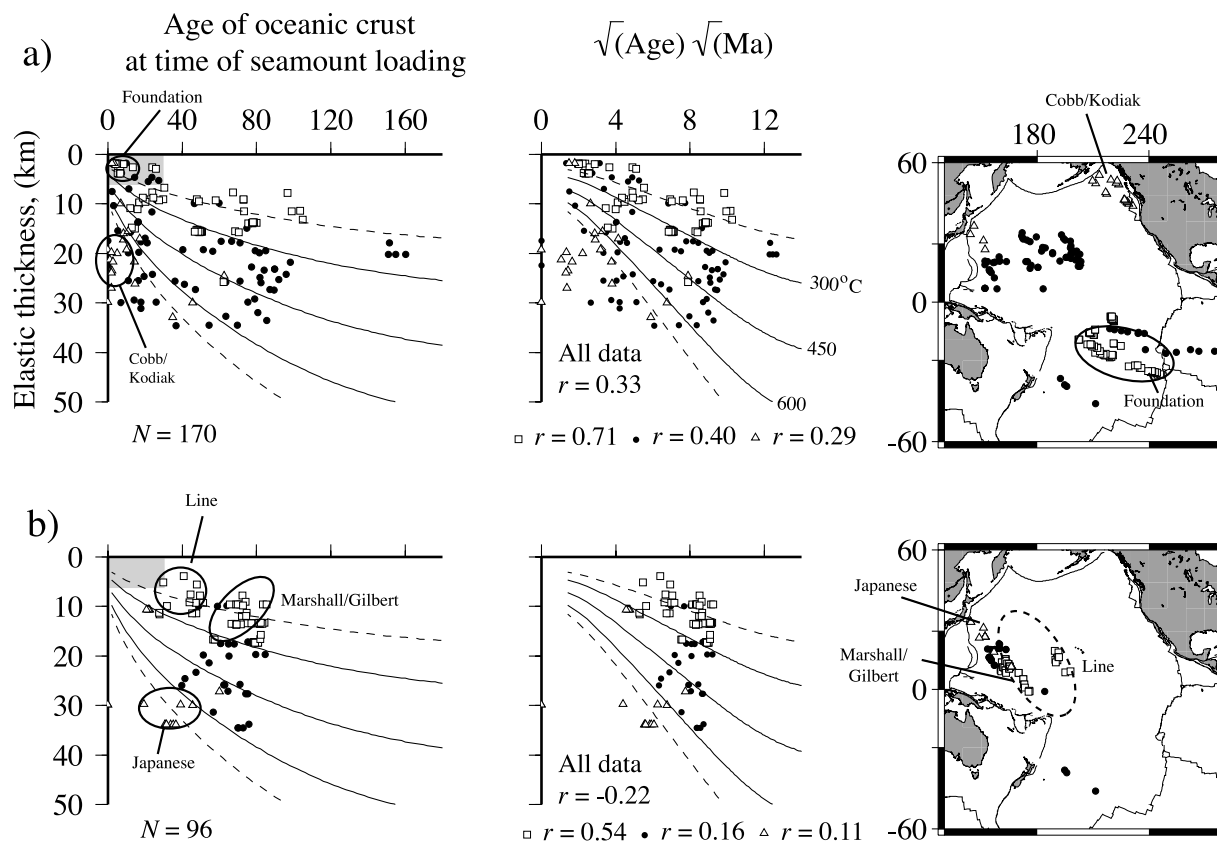


Figure 12. Plot of the best fit T_e derived from bathymetric prediction against age at sample sites in the Pacific Ocean. (left) Plot of T_e against age of the oceanic crust at the time of loading, (middle) plot of T_e against the square root of age of the oceanic crust at the time of loading, and (right) the distribution of the sample sites. Open squares, sites from the French Polynesia, Foundation Seamounts, Marshall/Gilbert Islands, and the Line Islands. Open triangles, sites from the Cobb/Kodiak seamount chain and the Japanese seamounts. Solid circles, all other data. Grey shading, N and r are as defined in Figures 9 and 11. The ellipses show clusters of sample sites where T_e is lower than expected for the 300–600°C isotherm range. (a) *Clouard and Bonneville* [2001] sample sites. (b) *Koppers et al.* [2003], *Davis et al.* [2002], and *Koppers and Staudigel* [2005] sample sites.

formed on or near a Middle Cretaceous R-R-R triple junction [*Clouard and Bonneville*, 2001].

[58] Interspersed among the on-ridge seamounts in the Pacific are off-ridge and flank ridge features (Figure 14). The most prominent off-ridge feature is the Hawaiian Ridge, which ranges in age from ~0–43 Ma and was emplaced on 47–90 Myr oceanic crust [*Clague and Dahymlpe*, 1987]. Other off-ridge features are found in the Magellan seamounts and Marcus Wake guyots. The Magellan seamounts range in age from 80 to 100 Ma and were emplaced on 50–70 Myr oceanic crust [*Koppers et al.*, 1998] while the Marcus Wake guyots range in age from 78–126 Ma and were emplaced on 29–77 Myr oceanic crust. These ages are compatible with an off-ridge setting.

[59] The most prominent flank ridge features are the Marquesas Islands, the Cross-Line trend, and the Society Islands. The Marquesas Islands range in age from 1 to 5 Ma and were emplaced on 49–54 Ma oceanic crust. The age of the Cross-Line trend is uncertain, but the late Eocene (36–40 Ma) age of *Schlanger et al.* [1984] suggest they were emplaced on 26–59 Ma oceanic crust. The Cross-Line trend is therefore younger than the Line Islands ridge and so a flank ridge setting is reasonable, given that the Line Islands

are mostly on ridge. The Society Islands are 0–4 Ma and were emplaced on 61–85 Myr oceanic crust [*White and Duncan*, 1996] suggestive of an off-ridge rather than a flank ridge setting. However, as *Natland and Winterer* [2005] have pointed out, the Society Islands, like the Marquesas Islands, show some of the same “cross-grain ridges” as the Cross-Line trend. The sample ages may therefore reflect small-volume recent volcanism while the T_e reflects a large-volume early event (in this case, late Eocene) along preexisting lines of weakness.

[60] A special feature of the Pacific is that the same geological province may be characterized by one or more settings. For example, the Musician seamounts yield on-ridge and flank ridge settings while the Tasmantid seamounts show flank ridge and off-ridge settings. The Musician seamounts range in age from 82 to 96 Ma and were emplaced on ~0–30 Myr oceanic crust [*Kopp et al.*, 2003] while the Tasmantid seamounts range in age from 6.4 to 24.0 Ma and were emplaced on ~36–64 Myr oceanic crust [*McDougall and Duncan*, 1988]. Both sets of observations are consistent with a mixed setting. Probably the most striking example of a mixed setting is the Mid-Pacific Mountains. Here, off-ridge and particularly flank ridge and

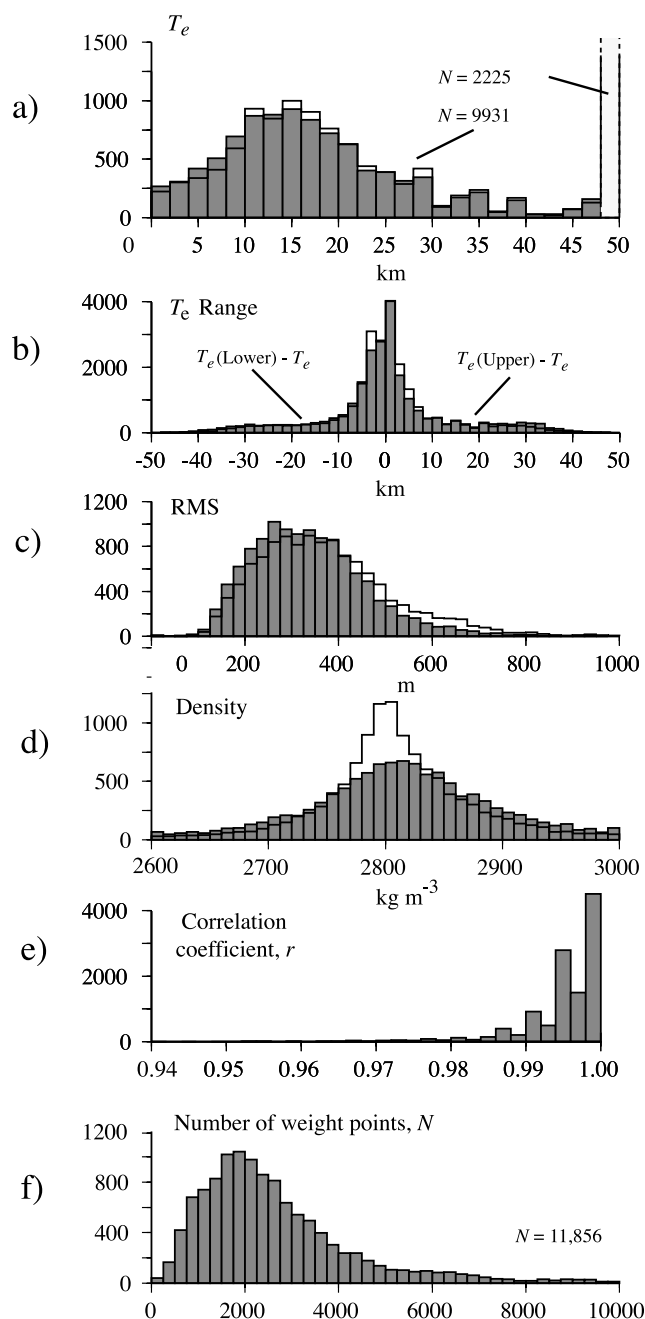


Figure 13. Histograms of parameters derived from bathymetric prediction at all the sites in the Wessel [2001] global seamount database. (a) Best fit T_e . (b) High and low bounds of T_e . (c) RMS difference between observed and predicted bathymetry. (d) Density. (e) Correlation coefficient. (f) Number of points used the RMS and correlation coefficient calculations. The stair step lines show the parameters if the density is permitted to vary at each site.

on-ridge settings are juxtaposed. The age of the seafloor in the region is in the range 160–170 Ma which implies volcanism over a long time interval, as indeed appears to have been the case from the few sample ages that are available.

[61] When compared to the Pacific, the Indian Ocean has a small number of T_e estimates. Nevertheless, it shows

examples of all three types of tectonic setting. The most prominent on-ridge features are the Ninetyeast and Chagos-Laccadive ridges. The Ninetyeast ridge ranges in age from ~ 80 –38 Ma [Duncan, 1991] and is generally considered to have formed when the Kerguelen hot spot was centered on the paleo-Southeast Indian Ridge. The Chagos-Laccadive ridge ranges in age from ~ 45 to 57 Ma [Duncan and Hargaves, 1990] and is believed to have formed when the Reunion hot spot was centered on the paleo-Southwest Indian Ridge. The segmentation of the on-ridge estimates (Figure 14) suggests, however, asymmetry in the thermal properties of the paleo-Indian ridge or, more likely, temporal shifts in the relative location of the ridge crest and hot spot.

[62] Other, more persistent, on-ridge features in the Indian Ocean include the Mascarene Plateau, Madingley Rise, Amsterdam–St. Paul Plateau, Rodriguez Island, Marion Dufresne Rise, and Conrad Rise. The Mascarene Plateau and Madingley Rise are conjugate to the northern part of the Chagos-Laccadive ridge and so together may have formed a large volcanic plateau before seafloor spreading between the Seychelles and western India separated them. The Amsterdam–St. Paul Plateau is located on young seafloor (~ 10 Ma) at a transform offset of the Southeast Indian Ridge and is historically active [Johnson *et al.*, 2000]. Rodriguez Island is 8–10 Ma and was emplaced on 10–12 Myr oceanic crust, although probably not on a transform. Both sets of ages are therefore consistent with an on-ridge setting. More enigmatic is the on-ridge setting for the Marion Dufresne and Conrad Rise. These features are located south of Crozet Island on 75–90 Ma oceanic crust, but little is known about their age. An on-ridge setting suggests an age that is a little older than the Afansay-Nikitin rise (~ 80 Ma) which is believed to have formed [Curry and Munasinghe, 1991] when the Crozet hot spot was centered on the paleo-Southwest Indian Ridge.

[63] The Indian Ocean is characterized by a number of off-ridge features. Most of these features, however, are located on the crest of the flexural bulge seaward of the Java-Sumatra trench. Christmas Island, for example, is Late Cretaceous to Eocene [Woodroffe, 1988] in age and formed on 25–50 Myr oceanic crust [Exon *et al.*, 2002]. We obtained $29.8_{25.7}^{42.4}$ ($R = 200$ km) for Christmas Island, which is higher than expected based on these age data. When we decreased R to focus more on the island than the bulge, we did not obtain a RMS minimum. However, a nearby seamount (longitude 104.283, latitude -11.517) yielded $28.4_{23.8}^{40.2}$ km ($R = 200$ km) and $19.1_{16.7}^{21.2}$ km ($R = 50$ km). This lower value is more compatible with the sample and crustal age data. The Afansay Nikitin seamount is located at the southern terminus of the 85°E ridge [Curry and Munasinghe, 1991] and so should not have been influenced by the bulge. According to Krishna [2003] the seamount formed during the Late Cretaceous, on ~ 35 Myr oceanic crust, suggesting a flank ridge rather than an off-ridge setting. We obtained seven T_e estimates at Afansay Nikitin seamount, one of which was flank ridge. Of the remainder, four decreased and two increased when we used a smaller R . The maximum decrease in T_e , however, was only 5–7 km. Our result of a flank ridge setting is therefore robust and suggests that at least part of the seamount and its superimposed rise is younger than Late Cretaceous. More clearly

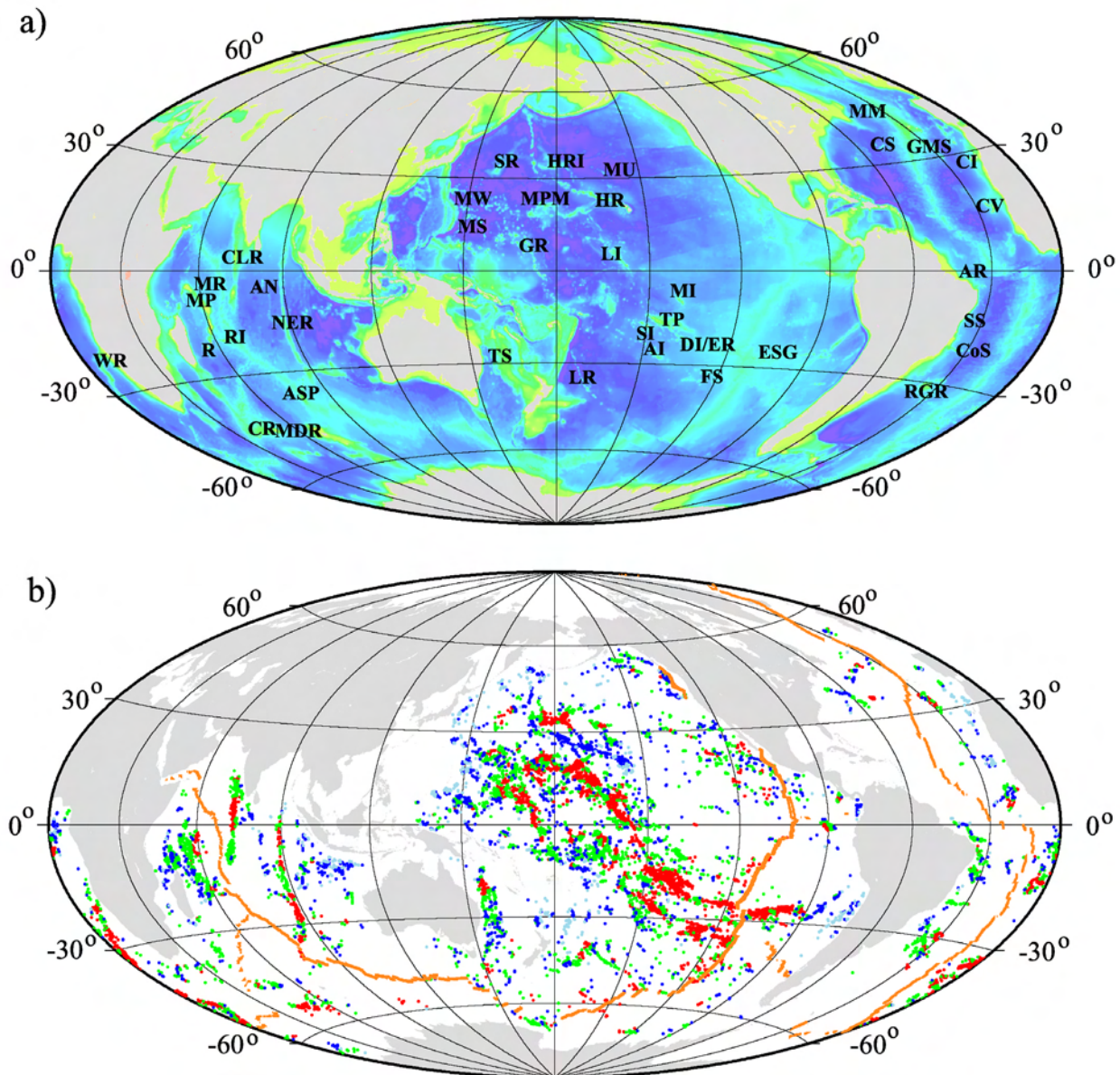


Figure 14. Distribution of on-ridge ($0 < T_e < 12$ km), flank ridge ($12 \leq T_e \leq 20$ km), and off-ridge ($T_e > 20$ km) seamounts in the *Wessel* [2001] global seamount database. (a) Bathymetry map based on the GEBCO 1 min grid showing selected features referred to in the text. AI, Austral Islands; AR, Atol das Rocas seamount; ASP, Amsterdam–St. Paul Plateau; AN, Afansay-Nikitin seamount; CLR, Chagos-Laccodive Ridge; CV, Cape Verde Islands; CI, Canary Islands; CR, Conrad Rise; CS, Cruiser seamount; CoS, Columbia seamounts; DI/ER, Ducie Island–Easter Island ridge; ESG, Easter Island–Salas y Gomez ridge; HR, Hawaiian Islands; HRI, Hess Rise; FS, Foundation Seamounts; GR, Gilbert Ridge; GMS, Great Meteor Seamount; LI, Line Islands; LR, Louisville Ridge; MDR, Marion Dufresne Rise; MPM, Mid-Pacific Mountains; MI, Marquesas Islands; MW, Marcus-Wake Guyots; MR, Madingley Rise; MM, Milne mounds; MP, Mascarene Plateau; MS, Magellan Seamounts; MU, Musician Seamounts; NER, Ninetyeast Ridge; R, Reunion; Rodrigues Island; RGR, Rio Grande Rise; SI, Society Islands; SR, Shatsky Rise; SS, Stocka Seamount; TS, Tasmantid Seamounts; TP, Tuamotu Plateau; WR, Walvis Ridge. (b) Map showing the tectonic setting of seamounts, banks, and rises. Red solid circles, on-ridge. Green solid circles, flank ridge. Blue solid circles, off-ridge. Note that only those estimates where the difference between the best fit and lower bound T_e is < 15 km have been plotted. Orange line indicates zero age oceanic crust.

off ridge is Reunion which is <2 Ma [McDougall, 1971] and was emplaced on 56–58 Myr oceanic crust [Charvis *et al.*, 1999]. We obtained $34.9_{26.7}^{49.9}$ km at Reunion, consistent with the sample and crustal ages. Also off ridge, although less clearly so, are Mauritius and Crozet Island. Mauritius is 8–10 Ma [McDougall, 1971] and was formed on 40–42 Myr oceanic crust while Crozet Island is a Pleistocene shield volcano [Gunn *et al.*, 1970] that was emplaced on 70 Myr oceanic crust. We obtained $20.0_{16.8}^{30.4}$ km and $21.9_{20.0}^{25.9}$ km at Mauritius and Crozet Island, respectively, which is generally consistent with the sample and crustal ages.

[64] A feature of the Indian Ocean is the large number of flank ridge settings. The Nazareth Bank, Seychelles Bank, Maldives/Bombay Ridge, and Chagos Bank in the western Indian Ocean, for example, all yield flank ridge settings. The Seychelles Bank is a granitic “microcontinent”, but Nazareth Bank (along with the intervening Mascarene Plateau and Saya de Malha Bank) was probably formed during the Eocene/Oligocene by volcanism along the Reunion hot spot track [Duncan and Hargaves, 1990]. Therefore the flank ridge setting reflects the movement of the Carlsberg Ridge, which began separating Seychelles and west India ~ 40 Ma, off the hot spot due to the northward motion of the Indian-Australian plate.

[65] The Atlantic, like the Indian Ocean, is characterized by a mix of settings. In the south Atlantic, most of the seamounts, banks and rises that compose the Walvis Ridge and the northern part of the Rio Grande Rise are on-ridge. These features formed at the intersection of the south Atlantic ridge with a hot spot that is now centered on Tristan da Cunha and Gough Island [O'Connor and Duncan, 1990], compatible with an on-ridge setting. Other on-ridge features include the St. Helena seamounts, Discovery seamount, Meteor Rise and the Shona Ridge. The St. Helena seamount chain, like the Rio Grande Rise and Walvis Ridge, probably formed at a hot spot influenced ridge [O'Connor *et al.*, 1999], compatible with an on-ridge origin. The origins of Discovery seamount [Kempe and Schilling, 1974], Meteor Rise and the Shona Ridge [Moreira *et al.*, 1995] are unclear, but their close proximity to the R-R-R Bouvet triple junction is consistent with an on-ridge setting. The western South Atlantic is dominated by flank ridge estimates. These include the Columbia, Stocka, Perembuco and Atol das Rocas seamount groups offshore the eastern Brazil continental margin. Unfortunately, few of these features have been dated.

[66] In the North Atlantic, the Cruiser seamounts, the conjugate Corner Rise, and the Milne Mounds are all on ridge. These features are believed to have formed at the interaction of the Mid-Atlantic Ridge with a hot spot that is now centered just to the east of the ridge crest at the Azores [Gente *et al.*, 2003] and so are compatible with an on-ridge setting. The Great Meteor seamount is flank ridge, confirming the earlier suggestion of Verhoef [1984] that it formed further from the ridge crest than its immediate neighbor, the Cruiser seamount. The eastern North Atlantic is dominated by off-ridge settings. They include Madeira, Canary, and Cape Verde, all of which are associated with Neogene and younger volcanism [Carracedo *et al.*, 1998; Stillman *et al.*, 1982]. Although there is evidence of older volcanism in both the Canary and Cape Verde islands, most workers consider that the bulk of the islands are <20 Ma and that

they were emplaced on old (>120 Myr) oceanic crust, compatible with an off-ridge setting.

7. Discussion

7.1. Distribution of Volcanism Through Space and Time

[67] Previous studies at individual seamounts and oceanic islands [e.g., Watts, 1978; Caldwell and Turcotte, 1979; Lago and Cazenave, 1981; Calmant *et al.*, 1990; Wessel, 1992; Watts and Zhong, 2000] suggest that T_e is dependent on the age of the oceanic lithosphere at the time of loading and is given approximately by the depth to the 300–600°C oceanic isotherm. Our estimates of T_e at the sample sites where age is known (e.g., Figure 11) suggest, however, that there is no single controlling isotherm that describes all the data. Therefore it may not be possible to use the global T_e data set to estimate age.

[68] We can, however, consider the on-ridge estimates since their age should reflect the age of the underlying oceanic crust. The entire on-ridge database could be used, that is, estimates in the range $0 < T_e < 12$ km. However, Figure 11a suggests that some of these estimates have formed on oceanic crust as old as 100 Ma and therefore maybe more off ridge than on ridge. A better range might therefore be a more limited one. We therefore chose a range of $0 < T_e < 8$ km since Figure 11a shows that a majority of these estimates formed on young oceanic crust, in the range 0–30 Ma.

[69] Figure 15 shows histograms of the age of the on-ridge estimates. Two histograms are shown: one of the entire data set (Figure 15a) and one of a limited data set (Figure 15b). Both histograms show similar patterns. On-ridge volcanism is widely distributed throughout the Cenozoic and Mesozoic. There is a prominent peak at ~ 90 –125 Ma (Albian-Aptian). Other peaks in volcanism occur at ~ 10 Ma (late Miocene) and ~ 50 Ma (early Eocene). The timing of the prominent peak is similar to the one deduced by Wessel [2001] from free-air gravity anomaly amplitudes and seamount limiting heights.

[70] Figure 15c shows the temporal distribution of the limited on-ridge data set. The solid triangles show on-ridge estimates in time slices of 120–160, 80–120, and 40–80 Ma. The crosses show those sample ages in the Koppers *et al.* [2003], Davis *et al.* [2002], Koppers and Staudigel [2005], and Clouard and Bonneville [2001] databases that fall within each time slice. Figure 15c shows that on-ridge volcanism was usually accompanied by flank ridge and off-ridge volcanism in the plate interior. The activity was most intense during 80–120 Ma when much of the paleo-East Pacific Ridge crest was active and there was significant off-ridge volcanism as expressed in what now comprises the Magellan, Geologists, Marcus-Wake, and Japanese seamounts.

7.2. Testing the Fixed Hot Spot Hypothesis

[71] There has been much debate recently concerning the fixed hot spot hypothesis and its ability to explain the distribution of submarine volcanism through space and time. The focus of the debate has been on the Pacific Ocean where it has been clear for some time [Bonatti and Harrison, 1976; Epp, 1984; Jackson and Shaw, 1975] that

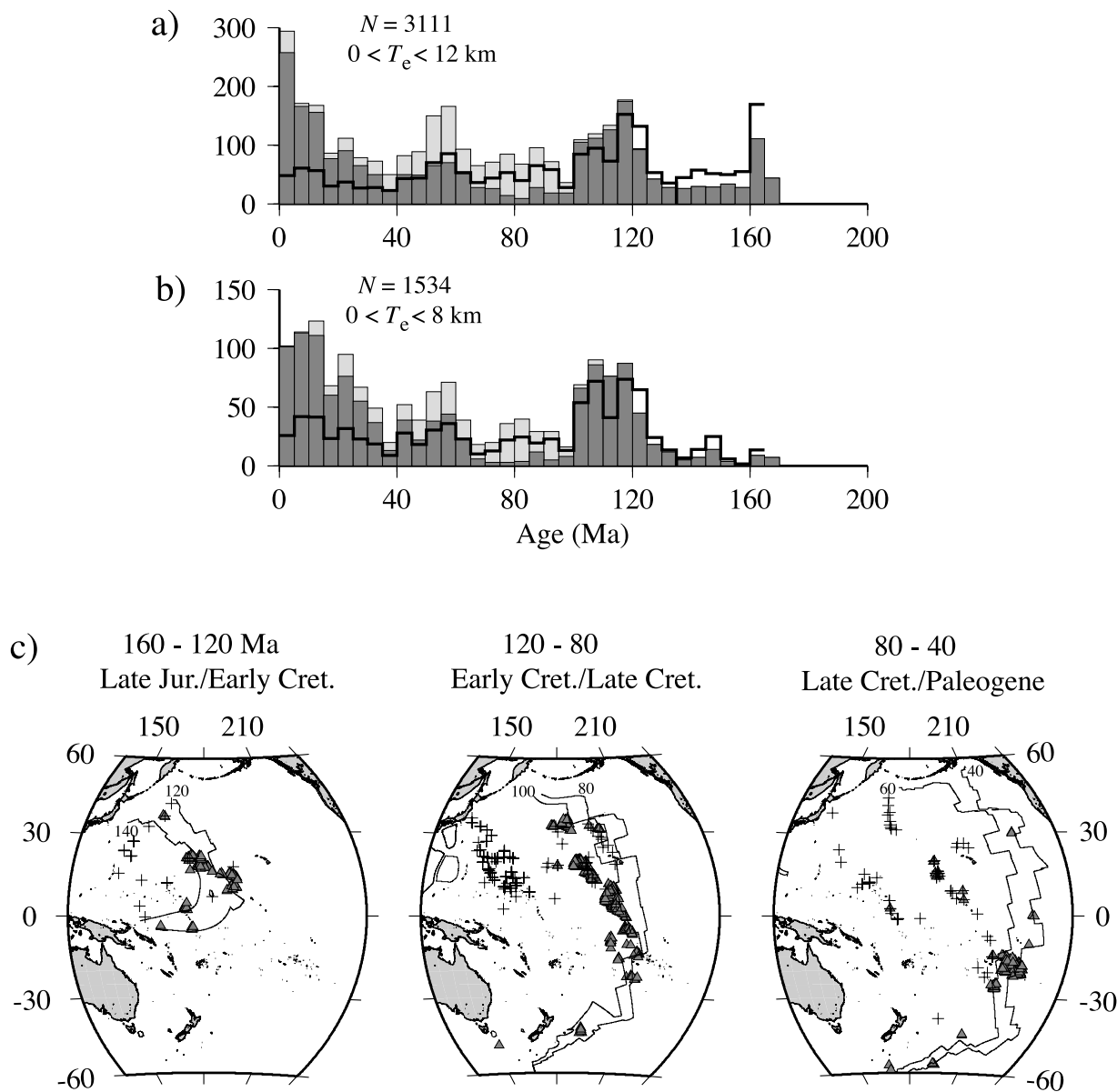


Figure 15. Distribution of on-ridge volcanism through space and time. (a) Histogram of ages based on the estimates where $0 < T_e < 12$ km. N , number of estimates. (b) Histogram of ages based on the estimates where $0 < T_e < 8$ km. (c) Maps showing the distribution of volcanism in Figure 15b for three time slices: 160–120 Ma, 120–80 Ma, and 80–40 Ma. Thin lines show selected isochrons (in 20 Myr intervals) based on work by Müller *et al.* [1997]. Crosses show where samples from the Clouard and Bonneville [2001], Koppers *et al.* [2003], and Davis *et al.* [2002] databases have ages that fall within the time slices. Solid triangles show the distribution of the estimates where $0 < T_e < 8$ km that fall within the time slices.

the fixed hot spot hypothesis, while it elegantly explains the progressive increase in age along the Hawaiian Ridge, is unable to explain all the patterns of volcanism that are observed. Since T_e is a proxy for tectonic setting, it may therefore provide an independent way to test the hypothesis.

[72] To examine this further, we have used bathymetric prediction to estimate T_e along the Foundation seamount chain in the south central Pacific. Existing age [O'Connor *et al.*, 1998, 2002], T_e [Maia and Arkani-Hamed, 2002], and submarine morphology data are consistent with the formation of these seamounts at a hot spot-influenced paleo-Pacific-Antarctica ridge crest. If this is correct, then the

younger eastern end of the chain should have formed on young seafloor while the older western end should have formed on old seafloor.

[73] Figure 16 compares the estimated T_e based on bathymetric prediction to the expected T_e based on the fixed hot spot hypothesis. Figure 16 shows a plot of the estimated and expected T_e against distance from the inferred position of the hot spot that generated the Foundation seamount chain. T_e has been estimated at each seamount digitized from the predicted bathymetry maps of Smith and Sandwell [1994a] by Koppers *et al.* [2001]. We show the RMS difference between observed and predicted bathymetry at

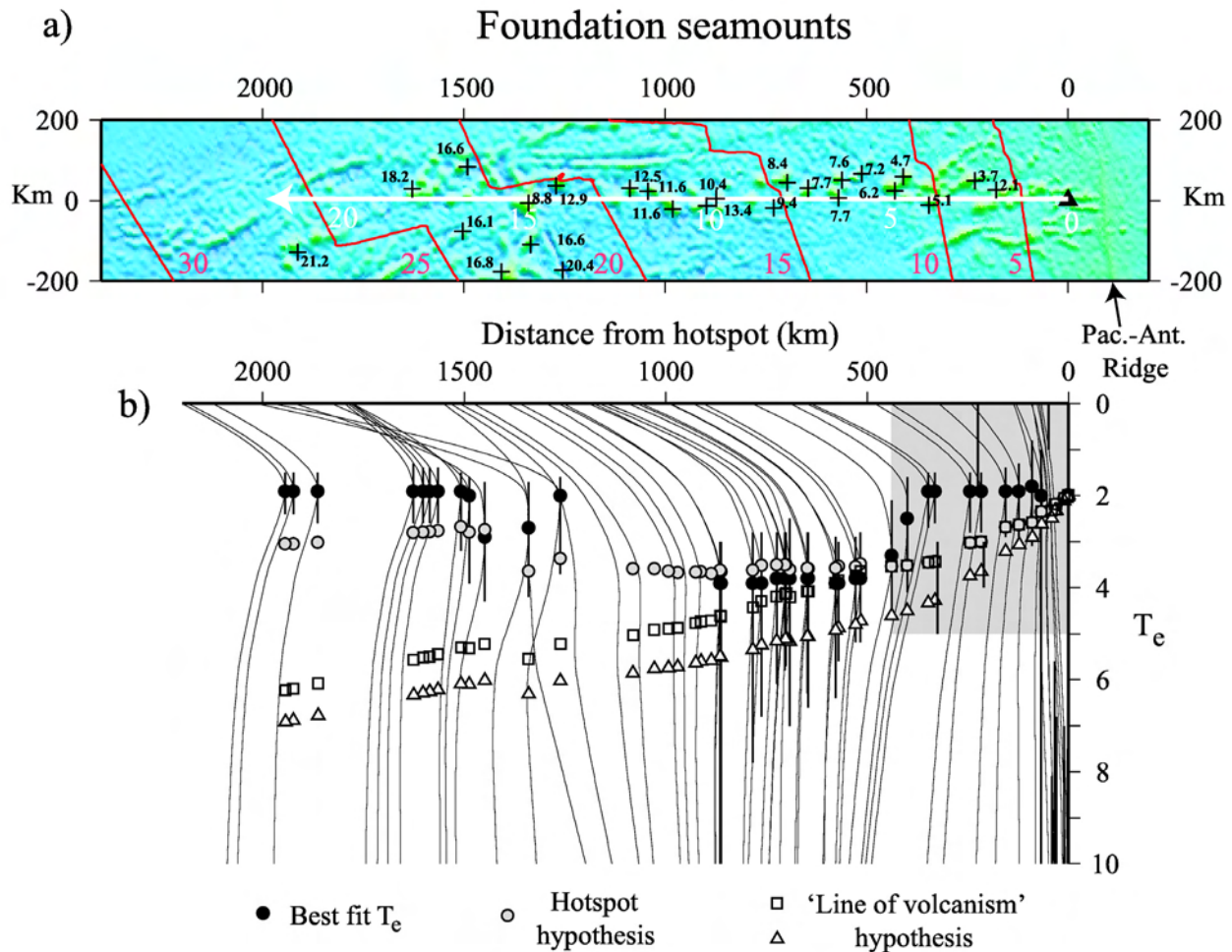


Figure 16. Test of the fixed hot spot hypothesis at the Foundation seamount chain. (a) Predicted bathymetry projected into the frame of the Hawaiian stage pole between 43 and 0 Ma (longitude 294.67, latitude 67.01). The white arrow and white numbers show the predicted age progression in Myr of the Foundation Seamounts for a hot spot located at longitude 248.25, latitude -37.32 , just to the west of the Pacific-Antarctica ridge crest. Crosses and bold numbers show radiometric age dates based on *O'Connor et al.* [2002]. (b) RMS difference between observed and predicted bathymetry plotted as a function of distance from the hot spot. Solid circles show the best fit T_e and vertical bars show upper and lower bounds. Gray circles show the expected T_e based on the fixed hot spot hypothesis and a 200°C controlling oceanic isotherm. Open squares and triangles show the expected T_e based on the “line of volcanism” hypothesis. Triangles assume that the entire seamount chain was emplaced on the seafloor today. Squares assume that the first 5 Myr formed according to the hot spot hypothesis and then >5 Ma was formed according to the line of volcanism hot spot hypothesis. The gray shaded region shows the region of the *Maia and Arkani-Hamed* [2002] study whose T_e estimates in the first 5 Myr along the chain (0–5 km) are in general accord with our results.

each seamount, together with the best fit T_e and its lower and upper bounds. The expected T_e is based on a controlling isotherm of 200°C which is lower than normally assumed in flexure studies. However, it is the same controlling isotherm as was deduced by *Maia and Arkani-Hamed* [2002] at the young (<5 Ma) end of the chain. The distance has been computed by projection along a small circle about the Hawaiian stage pole (latitude 67.017, longitude 294.467). Figure 16 shows that the expected T_e should increase away from the Pacific-Antarctica ridge crest as the age difference between the age of the seamount and the underlying oceanic

crust increases, and then decreases as the seamounts cross from the older to the younger side of an unnamed fracture zone between the Resolution and Mocha fracture zones [*Maia and Arkani-Hamed*, 2002]. This pattern in the expected T_e is repeated in the estimated T_e . We conclude therefore that our estimates of T_e derived from bathymetric prediction are in accord with the hot spot hypothesis, at least along the Foundation seamount chain.

[74] Of interest is to determine whether it might be possible to use our T_e estimates to resolve between the hot spot hypothesis and the competing “line of volcanism”

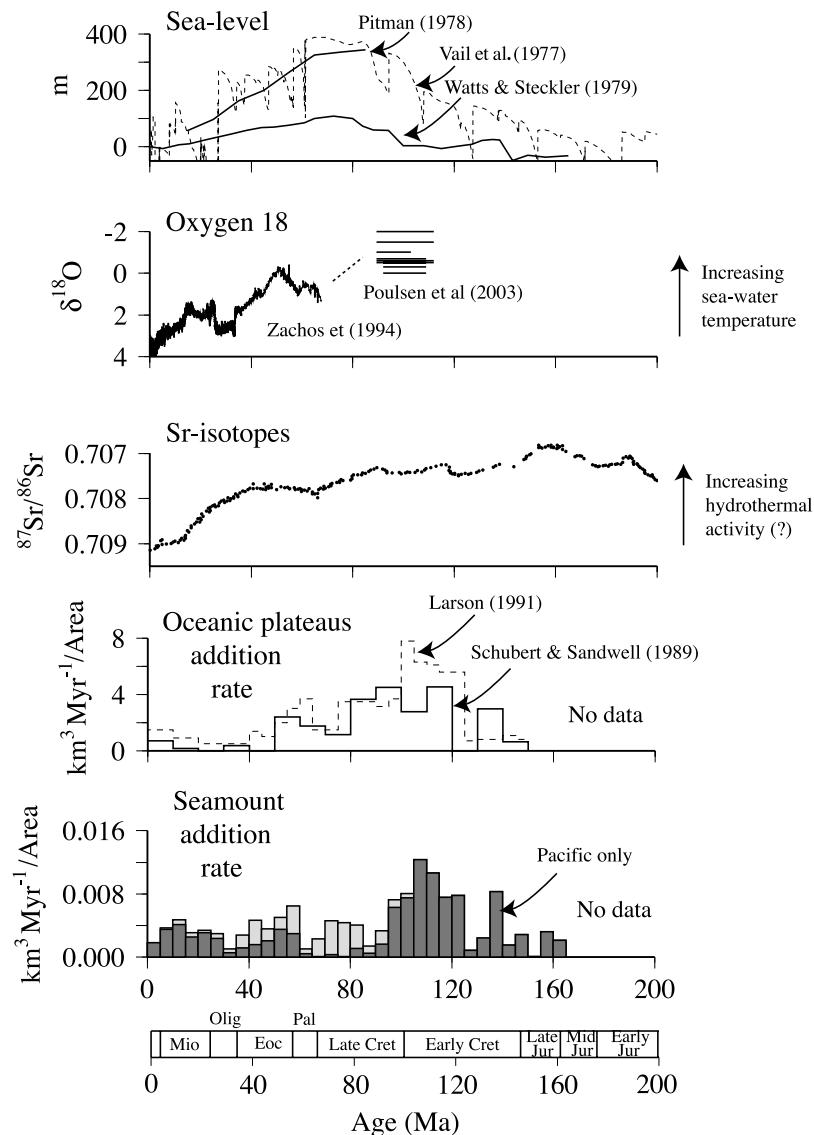


Figure 17. Global seamount and oceanic plateau addition rate through time and its relationship to changes in the seawater strontium and foraminiferal oxygen 18 isotope record and sea level. The global seamount addition rate is based on volume and age estimates at those sites where $0 < T_e < 12$ km. The oceanic plateau addition rate is based on the work by *Schubert and Sandwell* [1989] and *Larson* [1991]. Note that the *Schubert and Sandwell* [1989] rate is based on volumes of oceanic plateaus above normal seafloor depth (i.e., their V1 and V2) while the *Larson* [1991] rate is based on volumes of *Schubert and Sandwell* [1989] with the addition of the crustal root and potential symmetric twin plateaus. The strontium isotope record is based on the work by *Jones and Jenkyns* [2001], and the oxygen 18 isotope record is based on the work by *Zachos et al.* [1994] and *Poulsen et al.* [2003].

hypothesis. We show in Figure 16, for example, the T_e expected for two cases: one where the volcanism is the same age (0 Ma) along the entire length of the chain and the other where the age increases from 0 to 5 Ma and is then constant with age. In both cases, T_e increases with age because loading occurs on progressively older seafloor. Figure 16 shows, however, that neither case can account for the T_e derived from bathymetric prediction. Only the hot spot hypothesis can explain the predicted T_e . Therefore bathymetric prediction has the potential to discriminate between the two competing hypotheses, especially at seamount

chains that are emplaced on young oceanic lithosphere where the change T_e is expected to be the greatest.

7.3. Addition Rate of Seamounts Through Time

[75] The *Wessel* [2001] global database includes information on the size of seamounts, banks and rises and so can be used, together with our new T_e estimates, to calculate the volume and, possibly, the rate of addition of submarine volcanism through space and time.

[76] We calculated the volume using estimates of seamount base radius and height from *Wessel* [2001] and the formula for the volume of a frustum. The total volume of

the 9758 seamounts that yielded a T_e estimate is $7.8 \times 10^6 \text{ km}^3$, the largest contribution to which (71%) comes from the Pacific. This compares to the volume of $10.0 \times 10^6 \text{ km}^3$ that would have been obtained if we had used all the seamounts in the database. This volume does not include any material that may infill the flexural depression or that may have underplated the flexed oceanic crust.

[77] While these volumes are significant, they are small when compared to the magmatic material that is produced at mid-ocean ridges and oceanic plateaus. The volume of oceanic crust that has been created at mid-oceanic ridges is $1448 \times 10^6 \text{ km}^3$ [Cogne and Humler, 2004] while the volume of material that has been added to the surface and base of the oceanic crust at the oceanic plateaus is $33.1 \times 10^6 \text{ km}^3$ [Schubert and Sandwell, 1989].

[78] Nevertheless, the rate at which seamounts have been added to the top of the oceanic crust might be significant. Figure 17 shows the addition rate as a function of time for the limited on-ridge data set and compares it to other geophysical and geochemical proxies. Figure 17 shows a general agreement between the seamount addition rate and the oceanic plateau addition rate, as computed by Schubert and Sandwell [1989] and Larson [1991]. Both rate calculations show an increase at $\sim 120 \text{ Ma}$ and then a decrease to the present-day. The main difference is that the seamount addition rate is higher prior to $\sim 120 \text{ Ma}$ than it is subsequently, while the oceanic plateau rate is less. However, this may be a result of the lack of information on past oceanic plateaus and seamounts, such as those associated with Tethys and other oceans that have long since closed.

[79] The general decrease in seamount and oceanic plateau addition rate since $\sim 80 \text{ Ma}$ correlates with a decrease in global sea level and, interestingly, an increase in seawater strontium and foraminiferal oxygen stable isotopes. The increase in seawater $^{87}\text{Sr}/^{86}\text{Sr}$ has been interpreted in terms of a decrease in hydrothermal activity [Jones and Jenkyns, 2001] while the increase in foraminiferal $\delta^{18}\text{O}$ ratios has been interpreted in terms of a decrease in sea surface water temperature [Zachos et al., 2001]. These correlations suggest some link between submarine volcanism, hydrothermal activity, and sea surface water temperatures. Despite their small volumes, compared to oceanic plateaus, seamounts are important because of their wide distribution, tall pedestal heights and steep, unstable, slopes. Indeed, there is evidence that seamounts might influence such diverse phenomena as hydrothermal circulation [Harris et al., 2004], mesoscale eddies [Hogg, 1980], and biological activity [Rogers, 1994]. Therefore any attempt to seek links between tectonic activity (e.g., rifting) and the history of the Earth's climate should, we believe, also take into account seamounts and their distribution through space and time.

8. Conclusions

[80] We draw the following conclusions from this study:

[81] 1. The gravity field derived from satellite altimeter data can be used to predict global bathymetry for different values of the elastic thickness of the oceanic lithosphere, T_e .

[82] 2. By comparing the predicted bathymetry to shipboard bathymetry measurements we have obtained 9758 estimates of T_e at seamounts, banks and rises in the Pacific, Indian, and Atlantic oceans.

[83] 3. Estimation of T_e at the same localities as previous studies shows that bathymetric prediction is a robust way to estimate T_e and its lower and upper bounds.

[84] 4. Estimation of T_e at 291 sites of known sample and crustal age, however, shows that there is no simple relationship between T_e and age, and no single controlling isotherm that describes all the data.

[85] 5. The average density and T_e of the 9758 estimates is $2810.6 \pm 148.5 \text{ kg m}^{-3}$ and $18.4 \pm 11.0 \text{ km}$, respectively. We attribute the high standard deviations to the wide range rock types and tectonic settings associated with submarine volcanism.

[86] 6. The Pacific, Atlantic, and Indian oceans are characterized by a mix of tectonic settings such that seamounts that formed on ridge are in close proximity to flank ridge and off-ridge seamounts.

[87] 7. The highest concentration of on-ridge seamounts is in the south central and western Pacific. Interspersed among the on-ridge estimates are flank ridge and off-ridge estimates. Off-ridge settings dominate in the eastern North Atlantic, while flank ridge settings dominate the northwestern Indian and western South Atlantic oceans.

[88] 8. By assuming that T_e at the on-ridge estimates reflect the age of their underlying oceanic crust, we have estimated the age of >1500 seamounts.

[89] 9. The volcanism shows peaks in activity during the Early/Late Cretaceous, early Eocene, and Miocene.

[90] 10. The rate of on-ridge seamount addition appears to have decreased with time, from a peak of $0.012 \text{ km}^3 \text{ yr}^{-1}$ during the Late/Early Cretaceous to only $\sim 0.002 \text{ km}^3 \text{ yr}^{-1}$ at the present-day. These rates are small, however, when compared to the rate of addition of oceanic plateaus ($2.3 \text{ km}^3 \text{ yr}^{-1}$) and oceanic crust at mid-ocean ridges ($18.1 \text{ km}^3 \text{ yr}^{-1}$).

[91] **Acknowledgments.** This work was completed while one of us (A.B.W.) was a Visiting Professor at the Scripps Institution of Oceanography. We thank A. Koppers, H. Staudigel, and J. Winterer for discussions on the tectonics of the Pacific Ocean basin; D. Forsyth, M. McNutt, and an anonymous reviewer for their critical comments; and the Green Scholar Programme for support. This work was also supported by a NASA (NAG5-13673) and NSF (OCE03-26707) grant to D.T.S. for retracking of the radar altimeter waveforms for gravity field improvement and a NSF grant OCE99-06773 to P.W. W.H.F.S. acknowledges NOAA. The contents of this paper, however, are solely the opinions of the authors and do not constitute a statement of policy, decision, or position on behalf of NOAA or the U.S. Government.

References

- Bonatti, E., and C. G. A. Harrison (1976), Hot lines in the Earth's mantle, *Nature*, **263**, 402–404.
- Bonatti, E., C. G. A. Harrison, D. E. Fisher, J. Honnorez, J.-G. Schilling, J. J. Stipp, and M. Zentilli (1977), Easter volcanic chain (southeast Pacific): A mantle hot line, *J. Geophys. Res.*, **82**, 2457–2478.
- British Oceanographic Data Centre (2003), The GEBCO digital atlas, Centenary edition [CD-ROM], Liverpool, U.K.
- Caldwell, J. G., and D. L. Turcotte (1979), Dependence of the elastic thickness of the oceanic lithosphere on age, *J. Geophys. Res.*, **84**, 7572–7576.
- Calmant, S. (1987), The elastic thickness of the lithosphere in the Pacific Ocean, *Earth Planet. Sci. Lett.*, **85**, 277–288.
- Calmant, S., and A. Cazenave (1987), Anomalous elastic thickness of the oceanic lithosphere in the south-central Pacific, *Nature*, **32**, 236–238.
- Calmant, S., J. Francheteau, and A. Cazenave (1990), Elastic layer thickening with age of the oceanic lithosphere, *Geophys. J. Int.*, **100**, 59–67.
- Carracedo, J. C., S. Day, H. Guillou, E. R. Rodriguez Badiola, J. A. Canas, and F. J. Perez Torrado (1998), Hotspot volcanism close to a passive continental margin: The Canary Islands, *Geol. Mag.*, **135**, 591–604.

- Cazenave, A., and K. Dominh (1984), Geoid heights over the Louisville Ridge (South Pacific), *J. Geophys. Res.*, *89*, 11,171–11,179.
- Charvis, P., A. Laesanpura, J. Gallart, A. Hirn, J.-C. Lepine, B. de Voogd, T. A. Minshull, Y. Hello, and B. Pontoise (1999), Spatial distribution of hotspot material added to the lithosphere under La Reunion, from wide-angle seismic data, *J. Geophys. Res.*, *104*, 2875–2893.
- Clague, D. A., and G. B. Dalrymple (1987), The Hawaiian-Emperor volcanic chain. part I. Geologic evolution, in *Volcanism in Hawaii*, edited by R. W. Decker, T. L. Wright, and P. H. Stauffer, *U.S. Geol. Surv. Prof. Pap.*, *1350*, 5–54.
- Clouard, V., and A. Bonneville (2001), How many Pacific hotspots are fed by deep-mantle plumes?, *Geology*, *29*, 695–698.
- Clouard, V., A. Bonneville, and P.-Y. Gillot (2003), The Tarava seamounts: A newly characterized hotspot chain on the South Pacific Superswell, *Earth Planet. Sci. Lett.*, *207*, 117–130.
- Cochran, J. R. (1979), An analysis of isostasy in the world's oceans: 2. Mid-ocean ridge crests, *J. Geophys. Res.*, *84*, 4713–4729.
- Cogne, J.-P., and E. Humler (2004), Temporal variation of oceanic spreading and crustal production rates during the last 180 Myr, *Earth Planet. Sci. Lett.*, *227*, 427–439.
- Cousens, B., J. Dostal, and T. S. Hamilton (1999), A near-ridge origin for seamounts at the southern terminus of the Pratt-Welker Seamount Chain, northeast Pacific Ocean, *Can. J. Earth Sci.*, *36*, 1021–1031.
- Curry, J. R., and T. Munasinghe (1991), Origin of the Rajmahal Traps and the 85°E Ridge: Preliminary reconstructions of the trace of the Crozet hotspot, *Geology*, *19*, 1237–1240.
- Davis, A. S., L. B. Gray, D. A. Clague, and J. R. Hein (2002), The Line Islands revisited: New ⁴⁰Ar/³⁹Ar geochronologic evidence for episodes of volcanism due to lithospheric extension, *Geochem. Geophys. Geosyst.*, *3*(3), 1018, doi:10.1029/2001GC000190.
- Dixon, T. H., M. Naraghi, M. K. McNutt, and S. M. Smith (1983), Bathymetric prediction from Seasat altimeter data, *J. Geophys. Res.*, *88*, 1563–1571.
- Duncan, R. A. (1991), Age distribution of volcanism along aseismic ridges in the eastern Indian Ocean, *Proc. Ocean Drill. Program Sci. Results*, *121*, 507–517.
- Duncan, R. A., and R. B. Hargaves (1990), ⁴⁰Ar/³⁹Ar geochronology of basement rocks from the Mascarene Plateau, the Chagos bank, and the Maldives Ridge, *Proc. Ocean Drill. Program Sci. Results*, *115*, 43–51.
- Epp, D. (1984), Possible perturbations to hotspot traces and implications for the origin and structure of the Line Islands, *J. Geophys. Res.*, *89*, 11,273–11,286.
- Exon, N. F., M. D. Raven, and E. H. De Carlo (2002), Ferromanganese nodules and crusts from the Christmas Island region, Indian Ocean, *Mar. Georesour. Geotechnol.*, *20*, 275–297, doi:10.1080/0360886029005195.
- Filmer, P. E., M. K. McNutt, and C. J. Wolfe (1993), Elastic thickness of the lithosphere in the Marquesas and Society Islands, *J. Geophys. Res.*, *98*, 19,565–19,577.
- Gente, P., J. Dymant, M. Maia, and J. Goslin (2003), Interaction between the Mid-Atlantic Ridge and the Azores hot spot during the last 85 Myr: Emplacement and rifting of the hot spot-derived plateaus, *Geochem. Geophys. Geosyst.*, *4*(10), 8514, doi:10.1029/2003GC000527.
- Goodwillie, A. M. (1995), Short-wavelength gravity lineations and unusual flexure results at the Puka Puka volcanic ridge system, *Earth Planet. Sci. Lett.*, *136*, 297–314.
- Goodwillie, A. M., and A. B. Watts (1993), An altimetric and bathymetric study of elastic thickness in the central Pacific Ocean, *Earth Planet. Sci. Lett.*, *118*, 311–326.
- Gunn, B. M., C.-Y. Ramon, N. Watkins, C. E. Abranson, and J. Nougier (1970), Geochemistry of an oceanite-Ankaramite-Basalt suite from East Island, Crozet Archipelago, *Contrib. Mineral. Petrol.*, *28*, 319–339.
- Harris, R. N., and D. S. Chapman (1994), A comparison of mechanical thickness estimates from trough and seamount loading in the southeastern Gulf of Alaska, *J. Geophys. Res.*, *99*, 9297–9317.
- Harris, R. N., A. T. Fisher, and D. S. Chapman (2004), Fluid flow through seamounts and implications for global mass fluxes, *Geology*, *32*, 725–728.
- Haxby, W. F., and J. K. Weissel (1986), Evidence for small-scale mantle convection from Seasat altimeter data, *J. Geophys. Res.*, *91*, 3507–3520.
- Hogg, N. G. (1980), Effects of bottom topography on ocean currents, in *Orographic Effects in Planetary Flows*, *GARP Publ.*, vol. 23, edited by R. Hide and P. W. White, pp. 167–205, World Meteorol. Org., Geneva.
- Jackson, E. D., and H. R. Shaw (1975), Stress fields in the Pacific plate: Delineated in time by linear volcanic chains, *J. Geophys. Res.*, *80*, 1861–1874.
- Johnson, K. T. M., D. W. Graham, K. H. Rubin, K. Nicolaysen, D. S. Scheirer, D. W. Forsyth, E. T. Baker, and L. M. Douglas-Priebe (2000), Boomerang seamount: The active expression of the Amsterdam–St. Paul hotspot, Southeast Indian Ridge, *Earth Planet. Sci. Lett.*, *183*, 245–259.
- Jones, C. E., and H. C. Jenkyns (2001), Seawater strontium isotopes, oceanic anoxic events, and seafloor hydrothermal activity in the Jurassic and Cretaceous, *Am. J. Sci.*, *301*, 112–149.
- Kempe, D. R. C., and J.-G. Schilling (1974), Discovery Tablemount basalt: Petrology and geochemistry, *Contrib. Mineral. Petrol.*, *44*, 101–115.
- Kopp, H., C. Kopp, J. Phipps Morgan, E. R. Flueh, W. Weinrebe, and W. J. Morgan (2003), Fossil hot spot-ridge interaction in the Musicians Seamount Province: Geophysical investigations of hot spot volcanism at volcanic elongated ridges, *J. Geophys. Res.*, *108*(B3), 2160, doi:10.1029/2002JB002015.
- Koppers, A. A. P., and H. Staudigel (2005), Asynchronous bends in Pacific seamount trails: A case for extensional volcanism?, *Science*, *307*, 904–907.
- Koppers, A. A. P., H. Staudigel, J. R. Wijbrans, and M. S. Pringle (1998), The Magellan seamount trail: Implications for Cretaceous hotspot volcanism and absolute Pacific plate motion, *Earth Planet. Sci. Lett.*, *163*, 53–68.
- Koppers, A. A. P., J. Phipps Morgan, J. W. Morgan, and H. Staudigel (2001), Testing the fixed hotspot hypothesis using ⁴⁰Ar/³⁹Ar age progressions along seamount trails, *Earth Planet. Sci. Lett.*, *185*, 237–252.
- Koppers, A. A. P., H. Staudigel, M. S. Pringle, and J. R. Wijbrans (2003), Short-lived and discontinuous intraplate volcanism in the South Pacific: Hot spots or extensional volcanism?, *Geochem. Geophys. Geosyst.*, *4*(10), 1089, doi:10.1029/2003GC000533.
- Krishna, K. S. (1997), Isostatic response of the Central Indian Ridge (western Indian Ocean) based on transfer function analysis of gravity and bathymetry data, *Tectonophysics*, *257*, 137–148.
- Krishna, K. S. (2003), Structure and evolution of the Afanasy Nikitin seamount, buried hills and 85°E Ridge in the northeastern Indian Ocean, *Earth Planet. Sci. Lett.*, *209*, 379–394.
- Lago, B., and A. Cazenave (1981), State of stress in the oceanic lithosphere in response to loading, *Geophys. J. R. Astron. Soc.*, *64*, 785–799.
- Larson, R. L. (1991), Latest pulse of Earth: Evidence for a mid-Cretaceous superplume, *Geology*, *19*, 547–550.
- Lyons, S. N., D. T. Sandwell, and W. H. F. Smith (2000), Three-dimensional estimation of elastic thickness under the Louisville Ridge, *J. Geophys. Res.*, *105*, 13,239–13,252.
- Maia, M., and J. Arkani-Hamed (2002), The support mechanism of the young Foundation Seamounts inferred from bathymetry and gravity, *Geophys. J. Int.*, *149*, 190–210.
- Manea, M., V. C. Manea, V. Kostoglodov, and M. Guzman-Speziale (2005), Elastic thickness of the oceanic lithosphere beneath the Tehuantepec Ridge, *Geofis. Int.*, *44*, 157–168.
- McDougall, I. (1971), The geochronology and evolution of the young oceanic island of Reunion, Indian Ocean, *Geochem. Cosmochim. Acta*, *35*, 261–270.
- McDougall, I., and R. A. Duncan (1988), Age progressive volcanism in the Tasmanid Seamounts, *Earth Planet. Sci. Lett.*, *89*, 207–220.
- McKenzie, D. P., and C. O. Bowin (1976), The relationship between bathymetry and gravity in the Atlantic Ocean, *J. Geophys. Res.*, *81*, 1903–1915.
- McNutt, M. K. (1979), Compensation of oceanic topography: An application of the response function technique to the Surveyor area, *J. Geophys. Res.*, *84*, 7589–7598.
- McNutt, M. K., and H. W. Menard (1978), Lithospheric flexure and uplifted atolls, *J. Geophys. Res.*, *83*, 1206–1212.
- McNutt, M., D. Caress, J. Reynolds, K. A. Jordahl, and R. A. Duncan (1997), Failure of plume theory to explain midplate volcanism in the southern Austral Islands, *Nature*, *389*, 479–482.
- Menard, H. W. (1964), *Marine Geology of the Pacific*, 271 pp., McGraw-Hill, New York.
- Moreira, M., T. Staudacher, P. Sarda, J. G. Schilling, and C. J. Allegre (1995), A primitive plume neon component in MORB: The Shona ridge-anomaly, South Atlantic (51–52°S), *Earth Planet. Sci. Lett.*, *133*, 367–377.
- Mueller, R. D., W. R. Roest, J.-Y. Royer, L. M. Gahagan, and J. G. Sclater (1997), Digital isochrons of the world's ocean floor, *J. Geophys. Res.*, *102*, 3211–3214.
- Natland, J. H., and E. L. Winterer (2005), Fissure control on volcanic action in the Pacific, in *Plumes, Plates and Paradigms*, edited by G. R. Foulger et al., *Spec. Pap. Geol. Soc. Am.*, *388*, 687–710.
- Nettleton, L. L. (1939), Determination of density for reduction of gravity observations, *Geophysics*, *4*, 176–183.
- O'Connor, J. M., and R. A. Duncan (1990), Evolution of the Walvis Ridge–Rio Grande Rise hot spot system: Implications for African and South American plate motions over plumes, *J. Geophys. Res.*, *95*, 17,475–17,502.
- O'Connor, J. M., P. Stoffers, and J. R. Wijbrans (1998), Migration rate of volcanism along the Foundation Chain, SE Pacific, *Earth Planet. Sci. Lett.*, *164*, 41–59.

- O'Connor, J. M., P. Stoffers, P. van den Bogaard, and M. McWilliams (1999), First seamount age evidence for significantly slower African plate motion since 19 to 30 Ma, *Earth Planet. Sci. Lett.*, *171*, 575–589.
- O'Connor, J. M., P. Stoffers, and J. R. Wijbrans (2002), Pulsing of a focused mantle plume: Evidence from the distribution of foundation chain hotspot volcanism, *Geophys. Res. Lett.*, *29*(9), 1350, doi:10.1029/2002GL014681.
- Parker, R. L. (1972), The rapid calculation of potential anomalies, *Geophys. J. R. Astron. Soc.*, *31*, 447–455.
- Parsons, B. (1982), Causes and consequences of the relation between area and age of the ocean floor, *J. Geophys. Res.*, *87*, 289–302.
- Parsons, B., and J. G. Sclater (1977), Ocean floor bathymetry and heat flow, *J. Geophys. Res.*, *82*, 803–827.
- Patriat, M., F. Klingelhoefer, D. Aslanian, I. Contrucci, M. Gutscher, J. Talandier, F. Avedik, J. Francheteau, and W. Weigel (2002), Deep crustal structure of the Tuamotu plateau and Tahiti (French Polynesia) based on seismic refraction data, *Geophys. Res. Lett.*, *29*(14), 1656, doi:10.1029/2001GL013913.
- Pitman, W. C. (1978), The relationship between eustasy and stratigraphic sequences of passive margins, *Geol. Soc. Am. Bull.*, *89*, 1389–1403.
- Poulsen, C. J., A. S. Gendaszek, and R. L. Jacob (2003), Did the rifting of the Atlantic Ocean cause the Cretaceous thermal maximum?, *Geology*, *31*, 115–118.
- Ramillien, G., and P. Mazzega (1999), Non-linear altimetric geoid inversion for lithospheric elastic thickness and crustal density, *Geophys. J. Int.*, *138*, 667–678.
- Ribe, N. M. (1982), On the interpretation of frequency response functions for oceanic gravity and bathymetry, *Geophys. J. R. Astron. Soc.*, *70*, 273–287.
- Rogers, A. D. (1994), The biology of seamounts, *Adv. Mar. Biol.*, *30*, 305–350.
- Sager, W. W., and H.-C. Han (1993), Rapid formation of the Shatsky Rise oceanic plateau inferred from its magnetic anomaly, *Nature*, *364*, 610–613.
- Sandwell, D. T., and W. H. F. Smith (1997), Marine gravity anomaly from Geosat and ERS-1 satellite altimetry, *J. Geophys. Res.*, *102*, 10,039–10,054.
- Sandwell, D. T., E. L. Winterer, J. Mammerickx, R. A. Duncan, M. A. Lynch, D. A. Levitt, and C. L. Johnson (1995), Evidence for diffuse extension of the Pacific plate from Pukapuka ridges and cross-grain gravity lineations, *J. Geophys. Res.*, *100*, 15,087–15,099.
- Schlanger, S. O., M. Garcia, B. H. Keating, J. J. Naughton, W. W. Sager, J. A. Haggerty, J. A. Philpott, and R. A. Duncan (1984), Geology and geochronology of the Line Islands, *J. Geophys. Res.*, *89*, 11,261–11,272.
- Schubert, J., and D. T. Sandwell (1989), Crustal volumes of the continents and of oceanic and continental submarine plateaus, *Earth Planet. Sci. Lett.*, *92*, 234–246.
- Searle, R. C., J. Francheteau, and B. Cornaglia (1995), New observations on mid-plate volcanism and the tectonic history of the Pacific plate, Tahiti to Easter microplate, *Earth Planet. Sci. Lett.*, *131*, 395–421.
- Smith, W. H. F., and D. T. Sandwell (1994a), Bathymetric prediction from dense satellite altimetry and sparse shipboard bathymetry, *J. Geophys. Res.*, *99*, 21,803–21,824.
- Smith, W. H. F., and D. T. Sandwell (1994b), Elastic lithosphere thickness estimated from dense satellite altimetry and sparse shipboard bathymetry, *Eos Trans. AGU*, *75*, 154.
- Smith, W. H. F., and D. T. Sandwell (1997), Global sea floor topography from satellite altimetry and ship depth soundings, *Science*, *277*, 1956–1962.
- Smith, W. H. F., H. Staudigel, A. B. Watts, and M. S. Pringle (1989), The Magellan Seamounts: Early Cretaceous record of the South Pacific isotopic and thermal anomaly, *J. Geophys. Res.*, *94*, 10,501–10,523.
- Staudigel, H., K. H. Park, M. S. Pringle, J. L. Rubenstone, W. H. F. Smith, and A. Zindler (1991), The longevity of the South Pacific isotopic and thermal anomaly, *Earth Planet. Sci. Lett.*, *102*, 24–44.
- Stillman, C. J., H. Furnes, M. J. Le Bas, A. H. F. Robertson, and J. Zielonka (1982), The geological history of Maio, Cape Verde Islands, *J. Geol. Soc. London*, *139*, 347–361.
- Vail, P. R., R. M. Mitchum, and S. Thompson (1977), Relative sea-level from coastal onlap, in *Seismic Stratigraphy: Applications to Hydrocarbon Exploration*, edited by C. E. Payton, AAPG Mem., *26*, 63–82.
- Verhoef, J. (1984), A geophysical study of the Atlantis-Meteor seamount complex, Ph.D. thesis, Univ. of Utrecht, Utrecht.
- Watts, A. B. (1978), An analysis of isostasy in the world's oceans: 1, Hawaiian-Emperor Seamount Chain, *J. Geophys. Res.*, *83*, 5989–6004.
- Watts, A. B. (1983), The strength of the Earth's crust, *J. Mar. Technol.*, *17*, 12.
- Watts, A. B. (2001), *Isostasy and Flexure of the Lithosphere*, 458 pp., Cambridge Univ. Press, New York.
- Watts, A. B., and M. S. Steckler (1979), Subsidence and eustasy at the continental margin of eastern North America, in *Deep Drilling Results in the Atlantic Ocean: Continental Margins and Paleoenvironment, Maurice Ewing Ser.*, vol. 3, edited by M. Talwani, et al, pp. 218–234, AGU, Washington, D. C.
- Watts, A. B., and U. S. ten Brink (1989), Crustal structure, flexure and subsidence history of the Hawaiian Islands, *J. Geophys. Res.*, *94*, 10,473–10,500.
- Watts, A. B., and S. Zhong (2000), Observations of flexure and the rheology of oceanic lithosphere, *Geophys. J. Int.*, *142*, 855–875.
- Watts, A. B., J. R. Cochran, and G. Selzer (1975), Gravity anomalies and flexure of the lithosphere: A three-dimensional study of the Great Meteor Seamount, N.E. Atlantic, *J. Geophys. Res.*, *80*, 1391–1398.
- Watts, A. B., J. H. Bodine, and N. M. Ribe (1980), Observations of flexure and the geological evolution of the Pacific Ocean basin, *Nature*, *283*, 532–537.
- Watts, A. B., J. R. Cochran, P. Patriat, and M. Doucoure (1985), A bathymetry and altimetry profile of the Southwest Indian Ridge at 31°S, *Earth Planet. Sci. Lett.*, *73*, 129–139.
- Watts, A. B., J. K. Weissel, R. A. Duncan, and R. L. Larson (1988), Origin of the Louisville Ridge and its relationship to the Eltanin Fracture Zone system, *J. Geophys. Res.*, *93*, 3051–3077.
- Wessel, P. (1992), Thermal stresses and the bimodal distribution of elastic thickness estimates of the oceanic lithosphere, *J. Geophys. Res.*, *97*, 14,177–14,193.
- Wessel, P. (1997), Sizes and ages of seamounts using remote sensing: Implications for intraplate volcanism, *Science*, *277*, 802–805.
- Wessel, P. (2001), Global distribution of seamounts inferred from gridded Geosat/ERS-1 altimetry, *J. Geophys. Res.*, *106*, 19,431–19,442.
- White, W. M., and R. A. Duncan (1996), Geochemistry and geochronology of the Society Islands: New evidence for deep mantle recycling, in *Earth Processes: Reading the Isotopic Code, Geophys. Monogr. Ser.*, vol. 95, edited by A. Basu and S. Hart, pp. 183–206, AGU, Washington, D. C.
- Woodroffe, C. D. (1988), Vertical movement of isolated oceanic islands at plate margins: Evidence from emergent reefs in Tonga (Pacific Ocean) Cayman Islands (Caribbean Sea) and Christmas Island (Indian Ocean), *Z. Geomorphol., Suppl.* *69*, 17–37.
- Zachos, J. C., L. D. Scott, and K. C. Lohmann (1994), Evolution of early Cenozoic marine temperatures, *Paleoceanography*, *9*, 353–387.
- Zachos, J., M. Pagani, L. Sloan, E. Thomas, and K. Billups (2001), Trends, rhythms, and aberrations in global climate, 65 Ma to present, *Science*, *292*, 686–693.
- Zheng, Y., and J. Arkani-Hamed (2002), Rigidity of the Atlantic oceanic lithosphere beneath New England seamounts, *Tectonophysics*, *359*, 359–369.

D. T. Sandwell, Scripps Institution of Oceanography, MC 0225, University of California, San Diego, La Jolla, CA 92093-0225, USA.

W. H. F. Smith, Laboratory for Satellite Altimetry, NOAA, MC E/RA31, 1335 East-West Highway, Room 5408, Silver Spring, MD 20910-3282, USA.

A. B. Watts, Department of Earth Sciences, University of Oxford, Parks Road, Oxford OX1 3PR, UK. (tony@earth.ox.ac.uk)

P. Wessel, Department of Geology and Geophysics, SOEST, University of Hawaii, 1680 East-West Road, Honolulu, HI 96822, USA.

Bathymetry from Space: Rationale and requirements for a new, high-resolution altimetric mission

Bathymétrie spatiale : arguments en faveur d'une nouvelle mission altimétrique "haute résolution"

David T. Sandwell¹, Walter H. F. Smith², Sarah Gille¹, Ellen Kappel³, Steven Jayne⁴, Khalid Soofi⁵, Bernard Coakley⁶ and Louis Géli⁷

¹Scripps Institution of Oceanography, La Jolla, CA, 92093-0225

²Laboratory for Satellite Altimetry, NOAA, Silver Spring Maryland, 20910-3282

³Geoscience Professional Services, Bethesda, Maryland,

⁴Dept. of Physical Oceanography, Woods Hole Oceanographic Inst., Woods Hole, MA 02543

⁵Conoco Inc., 600 North Dairy Ashford, Houston, TX, 77252-2197

⁶Geophysical Institute, University of Alaska, Fairbanks, Alaska 99775

⁷Ifremer, Marine Geosciences Department, BP 70, 29280 Plouzané, France

Citation: Sandwell, DT; Smith, WHF; Gille, S; Kappel, E; Jayne, S; Soofi, K; Coakley, B; Geli, L. 2006. Bathymetry from space: Rationale and requirements for a new, high-resolution altimetric mission. *Comptes Rendus Geoscience*. 338 (14-15) : 1049-1062.

March 31, 2005

Revised April 26, 2006

Résumé

La profondeur des fonds marins est une donnée essentielle pour un grand nombre de domaines d'activité : scientifique, économique, politique. La bathymétrie – la science de la mesure des profondeurs de l'océan – a des applications aussi diverses que la gestion des ressources minérales et vivantes, l'aménagement des habitats sous-marins, l'implantation des câbles sous-marins et autres pipe-lines, l'extension des juridictions des pays riverains dans le cadre de l'article 76 de la convention des Nations Unies sur le droit de la mer, etc. Sur le plan scientifique, des questions d'ordre fondamental - telles que la formation des fonds océaniques ou le rôle du relief sous-marin sur l'évolution du climat – passent par une connaissance globale et homogène de la topographie du plancher océanique.

Les cartes globales de bathymétrie actuellement disponibles sont inadaptées pour bon nombre de ces applications, car de vastes zones océaniques demeurent inexplorées. Les sondeurs acoustiques multi-faisceaux offrent la résolution adéquate, mais il faudrait plus de 200 années-navire pour couvrir l'ensemble des grands fonds, à un coût de l'ordre de plusieurs milliards d'euros. En revanche, l'altimétrie satellitaire permettrait d'obtenir un modèle global de bathymétrie satisfaisant pour de nombreuses applications, en moins de six ans, à un coût inférieur à la centaine de millions d'euros. En effet, dans l'océan, les masses d'eau ont tendance à s'accumuler au dessus des montagnes sous-marines à cause de l'attraction causée par les reliefs. La surface de l'océan au repos (en l'absence de toute perturbation océanique) correspond au géoïde, une surface équipotentielle en tous points perpendiculaire à la force de pesanteur locale.

Les satellites altimétriques mesurent les variations de hauteur de la surface des océans, donc les ondulations du géoïde associées aux variations de la topographie sous-marine. Les données altimétriques actuelles, combinées aux données existantes de bateaux, permettent ainsi d'estimer, de manière indirecte, les variations de topographie dans les longueurs d'ondes comprises entre 16 et 160 km. Une nouvelle mission altimétrique, spécifiquement dédiée à la collecte de données gravimétriques « haute résolution », permettrait d'accéder à des longueurs d'onde plus courtes, jusqu'à ~ 6 km environ. Cet article détaille les objectifs pour lesquels ce gain en résolution est essentiel :

- Déterminer le rôle de la topographie sous-marine et de la rugosité des fonds sur la circulation globale, les échanges à l'intérieur de la masse d'eau, le climat, les habitats benthiques.
- Comprendre les processus géologiques à l'origine des structures intra-plaques telles que les collines abyssales, les micro-plaques, les propagateurs et les volcans sous-marins.
- Cartographier le champ de gravité et améliorer les systèmes de navigation inertielle.
- Fournir une couverture gravimétrique « haute résolution », homogène et globale, des marges continentales.
- Asseoir les revendications de juridiction dans le cadre de la convention des Nations Unies sur le Droit de la Mer.

La résolution de la gravimétrie satellitaire se heurte à des limitations d'ordre physique (liées à la loi de gravité) et non instrumental. La technologie actuelle permet d'accéder à la résolution ultime de la méthode. Les spécifications techniques d'une mission spécifiquement dédiée à la gravimétrie « haute résolution » et à la bathymétrie sont beaucoup moins contraignantes et moins coûteuses que celles des missions océanographiques. La donnée fondamentale à acquérir est la pente du géoïde, à une précision de l'ordre du microradian (1 mm par km) ; la détermination ultra-précise de la hauteur de la surface de l'océan n'est pas nécessaire.

Pour atteindre la résolution ultime, il est proposé ici :

- d'améliorer la précision de l'altimètre d'un facteur 2 par rapport à ceux qui ont été embarqués sur ERS-1 et GeoSat, ce qui est faisable actuellement, de manière à réduire le bruit dû aux vagues
- de densifier les traces, pour porter à 6 km l'espacement à l'équateur
- de porter à 6 ans la durée de la mission afin de pouvoir réduire le bruit par sommation sur les traces répétitives
- d'incliner les orbites à 60° (ou 120°) de façon à avoir la même précision sur les composantes nord-sud et est-ouest de la déflexion de la verticale.
- d'améliorer les performances de l'altimètre près des côtes (celui-ci doit « décrocher » et « raccrocher » au plus près de la terre).

Summary

Bathymetry is foundational data, providing basic infrastructure for scientific, economic, educational, managerial, and political work. Applications as diverse as tsunami hazard assessment, communications cable and pipeline route planning, resource exploration, habitat management, and territorial claims under the Law of the Sea all require reliable bathymetric maps to be available on demand. Fundamental Earth science questions, such as what controls seafloor shape and how seafloor shape influences global climate, also cannot be answered without bathymetric maps having globally uniform detail.

Current bathymetric charts are inadequate for many of these applications because only a small

fraction of the seafloor has been surveyed. Modern multibeam echosounders provide the best resolution, but it would take more than 200 ship-years and billions of dollars to complete the job. The seafloor topography can be charted globally, in five years, and at a cost under \$100M. A radar altimeter mounted on an orbiting spacecraft can measure slight variations in ocean surface height, which reflect variations in the pull of gravity caused by seafloor topography. A new satellite altimeter mission, optimized to map the deep ocean bathymetry and gravity field, will provide a global map of the world's deep oceans at a resolution of 6-9 km. This resolution threshold is critical for a large number of basic science and practical applications, including:

- Determining the effects of bathymetry and seafloor roughness on ocean circulation, mixing, climate, and biological communities, habitats, and mobility.
- Understanding the geologic processes responsible for ocean floor features unexplained by simple plate tectonics, such as abyssal hills, seamounts, microplates, and propagating rifts.
- Improving tsunami hazard forecast accuracy by mapping the deep ocean topography that steers tsunami wave energy.
- Mapping the marine gravity field to improve inertial navigation and provide homogeneous coverage of continental margins.
- Providing bathymetric maps for numerous other practical applications, including reconnaissance for submarine cable and pipeline routes, improving tide models, and assessing potential territorial claims to the seabed under the United Nations Convention on the Law of the Sea.

Because ocean bathymetry is a fundamental measurement of our planet, there is a broad spectrum of interest from government, the research community, industry, and the general public.

Mission Requirements

The resolution of the altimetry technique is limited by physical law, not instrument capability. Everything that can be mapped from space can be achieved now, and there is no gain in waiting for technological advances. Mission requirements for Bathymetry from Space are much less stringent and less costly than typical physical oceanography missions. Long-term sea-surface height accuracy is not needed; the fundamental measurement is the slope of the ocean surface to an accuracy of ~1 microradian (1 mm per km). The main mission requirements are:

Improved range precision. A factor of two or more improvement in altimeter range precision with respect to current altimeters is needed to reduce the noise due to ocean waves.

Fine cross-track spacing and long mission duration. A ground track spacing of 6 km or less is required. A six-year mission would reduce the error by another factor of two.

Moderate inclination. Existing satellite altimeters have relatively high orbital inclinations, thus their resolution of east-west components of ocean slope is poor at low latitudes. The new mission should have an orbital inclination close to 60° or 120° so as to resolve north-south and eastwest components almost equally while still covering nearly all the world's ocean area.

Near-shore tracking. For applications near coastlines, the ability of the instrument to track the ocean surface close to shore, and acquire the surface soon after leaving land, is desirable.

Mapping the Ocean Floor

The depth to the ocean floor and the roughness of the bottom vary throughout the oceans as a result of numerous geologic processes [Brown, *et al.*, 1998]. This seafloor topography influences the ocean circulation and mixing that moderate Earth's climate [Kunze and Llewellyn Smith, 2004; Munk and Wunsch, 1998], and the biological diversity and food resources of the sea. The ocean floor records the geologic history and activity of the ocean basins [Mueller, *et al.*, 1997], revealing areas that may store resources such as oil and gas [Fairhead, *et al.*, 2001], and generate earthquakes and tsunamis [Moffeld, *et al.*, 2004]. Despite the importance of Earth's ocean floor to our quality of life, we have made much better maps of the surfaces of other planets, moons, and asteroids.

After five decades of surveying by ships carrying echosounders, most of the ocean floor remains unexplored and there are vast gaps between survey lines (Figure 1). The primary reason for this lack of data is that ships are slow and expensive to operate. For example, a systematic mapping of the deep oceans by ships would take more than 120 years of survey time. Moreover, because the swath width of a multibeam echo sounder is proportional to depth, it takes much longer (750 ship-years) to survey the shallow (< 500 m) continental margins [Carron, *et al.*, 2001]. While shipboard surveys offer the only means for high-resolution seafloor mapping, moderate accuracy and resolution (12-17 km full wavelength) can be achieved using satellite radar altimetry at a fraction of the time and cost (Figure 2). Radar altimeters aboard the ERS-1 and Geosat spacecraft have surveyed the marine gravity field over nearly all of the world's oceans to a high accuracy and moderate spatial resolution of 25-45 km; [Cazenave, *et al.*, 1996; Sandwell and Smith, 1997; Tapley and Kim, 2001]. In the wavelength band 10 to 160 km, variations in gravity anomaly are highly correlated with seafloor topography (Figure 3) and thus, in principle, can be used to recover topography [Baudry and Calmant, 1991; Dixon, *et al.*, 1983; Jung and Vogt, 1992; Ramillien and Cazenave, 1997; Smith and Sandwell, 1994]. The sparse ship soundings constrain the long wavelength (> 160 km) variations in seafloor depth and are also used to calibrate the local variations in topography to gravity ratio associated with varying tectonics and sedimentation.

Satellites have another advantage in comparison to the present database of echosoundings, namely globally uniform resolution. By carrying the same sensor all over the globe, a satellite makes measurements of the same quality everywhere, a requirement for mapping the global distribution patterns of bathymetric features. Ships have not done this. The era of frontier exploration, when scientists could take ships into remote areas merely for curiosity's sake, was an era of single-beam echosounders and relatively poor navigation. The last two decades have seen great technical advances in echosounding (multi-beam swath mapping systems, Figure 2) and navigation (Global Positioning System), but these have been deployed over only a few percent of the ocean's area. The focus has been on coastal regions and Exclusive Economic Zones, and research emphasizing "hypothesis testing," which requires ships to revisit previously surveyed areas. The result is that even today, most of the data available in the remote oceans are the old-style, low-tech data.

Sensing Gravity and Bathymetry from Space

The ocean's surface has broad bumps and dips that reflect variations in the pull of gravity. In the deep ocean where sediments are thin, seafloor features such as seamounts produce minor variations in gravity, which in turn produce tiny variations in ocean surface height (Figure 3). On the shallow continental margins, where sediments are thick and the seafloor is relatively flat, gravity anomalies reflect the structure of the sedimentary basins. Gravity can be measured at orbital altitude using spacecraft such as CHAMP, GRACE, and GOCE [Tapley and Kim, 2001]. However, because these spacecraft measure gravity at altitudes higher than 250 km, they are unable to recover wavelengths shorter than about 160 km. In contrast, satellite altimeters offer much higher spatial resolution gravity measurements because they sense the gravity field at the ocean surface, which is typically only 4 km above the seafloor. In the deep ocean basins, where sediments are thin and seabed geology is simple, satellite altimeter data may be used to predict bathymetry at a half-wavelength scale of 6-9 km (Figure 3). Existing satellite altimeter data have proved the feasibility of the technique and revealed the overall, large-scale tectonic features of the ocean basins. A properly designed mission using existing technology could bring significant new resolution (Figure 4), capturing a critical scale of features, and facilitating new science and applications.

The radar altimeter measures sea surface bumps and dips by measuring the travel time of microwave pulses. These pulses reflect from an area of ocean surface (footprint) that grows with increasing sea state. For gravity field recovery and bathymetric estimation, along track sea surface height differences (slopes) are needed, instead of absolute heights. The major error source is the roughness of the ocean surface due to ocean waves. This means that a new mission optimized for recovery of gravity and bathymetry can be simpler and cheaper than other altimeter missions such as Topex/Poseidon used to measure ocean dynamics and sea-level rise. This is because the absolute height, and any component of height which changes only over wavelengths much longer than a few hundred km, is irrelevant, as it contributes to negligible slope. For example, most of the standard altimeter corrections such as radial orbit error, ionosphere and troposphere delays, and deep ocean tides have slopes less than 1 microradian, which corresponds to a 1-milligal gravity accuracy. Besides having less stringent accuracy requirements, an altimeter optimized for gravity field recovery must have dense ground track coverage. Current altimeters optimized for physical oceanography all have repeating orbits with sparse track coverage and thus do not contribute to the recovery of high-resolution gravity and bathymetry.

New Science

A new space bathymetry mission would furnish—for the first time—a global view of the ocean floor at the proper scale to enable important progress in basic and applied science. Ocean and climate modelers and forecasters would be able to account for how the ocean bottom steers currents and how bottom roughness controls the mixing of heat, greenhouse gases, and nutrients. The details of the tectonic and volcanic processes that shape the ocean floor could be studied in their full complexity, beyond the over-simplified view given in the plate tectonic theory. The hazards to coastal communities posed by tsunamis could be more realistically assessed, as deep ocean bathymetry focuses and defocuses tsunami wave energy to the extent that coastal wave height can vary by factors of 2-3.

Ocean Circulation, Mixing, and Climate

Bathymetry defines the bottom boundary of the ocean. At large scales it determines basic flow patterns of ocean circulation. At small scales it controls the transport of water between ocean basins, and seafloor roughness converts energy from horizontal flows to mix the ocean vertically. Both ocean circulation and mixing play major roles in climate.

The sun fuels Earth's climate system, supplying most of its energy near the equator. The tropics would be painfully hot and high latitudes uninhabitably cold were it not for the atmosphere and ocean, which spread the sun's energy poleward. Both the atmosphere and the ocean contribute roughly equally to the poleward transfer of heat, but the ocean has vastly greater heat storage capacity. The energy required to heat the entire atmosphere by 1°C would warm the ocean by less than 0.001°C. Because the ocean is slow to heat and cool, it moderates climate change.

To evaluate how the ocean influences climate, oceanographers try to understand how the ocean transports and stores climatologically important properties such as heat and carbon dioxide. This requires identifying the routes that water follows as it flows in deep currents along the seafloor, as well as how it mixes with other waters as it moves along. The deepest, densest water in ocean basins results from sinking at high latitudes. Water that has sunk recently contains the most recent signature of the current state of the climate: high concentrations of carbon dioxide, for example, or slightly warmer temperatures than less-recently ventilated water. State-of-the-art ocean models investigate the impact of mixing from overflows over sills and in deep ocean basins through direct simulation and parameterization. Because ocean currents interact with the bottom of the ocean, detailed knowledge of seafloor bathymetry will help improve predictions of the global ocean circulation and heat transport, and thus their effect on climate.

Predicting Ocean Circulation

Numerical models of the ocean's circulation forecast currents for shipping and military operations, predict climate, provide early warnings for natural disasters, and help us understand the fundamental physics that governs ocean circulation, which in turn helps develop improved forecast models. Bathymetry provides the bottom boundary condition for all types of ocean models [Gille, *et al.*, 2004]. Ocean circulation models are remarkably sensitive to small perturbations in bathymetry. In high-resolution models used to predict oceanic flows, small (25 km) topographic features can steer major currents (Figure 5). Other ocean models run for climate prediction show how changes in bathymetry influence poleward heat transport. Ocean climate modelers looked at the impact of changing the depth of the ridge separating the high-latitude Norwegian Sea from the North Atlantic Ocean. In their model, the ocean transports nearly twice as much heat northward when the ridge contains deep passageways. This difference implies significantly different climate regimes. These results show that accurate representation of ridges and canyons is important even for low-resolution climate models, and that topographic features in the deep ocean can steer upper ocean and surface level flows, even when the flow does not intersect topography.

In the future, accurate high-resolution bathymetry is expected to become a more pressing requirement, as other modeling challenges are solved. In the next ten years, projected increases in computer power will permit global models to simulate eddies and currents with scales of 10 km or less. New satellite-derived bathymetry will then be needed to give modelers the ocean bottom boundary at the same resolution as the currents and eddies they want to model. This will help to make ocean circulation models that better predict how heat and other water properties move through the ocean to influence climate.

Understanding Ocean Mixing

Small-scale bathymetry has a large impact on ocean circulation because it influences how water mixes [Polzin, *et al.*, 1997]. Understanding how the ocean mixes is crucial for understanding Earth's climate because vertical mixing determines how quickly heat and carbon dioxide can penetrate into the deep ocean [Jayne, *et al.*, 2004]. Predictions of global sea level rise over the next century differ by 25% or more depending on the rate of vertical mixing. Most deep-ocean mixing can be attributed to two processes, both of which depend on bathymetry. As water flows through tightly constrained passageways and over sills it rapidly mixes with surrounding water. This mixing affects the concentrations of heat and dissolved gases in seawater and the total quantities that can be stored in the ocean. As a result, in models containing these passageways, small changes to the topography can lead to significant changes in ocean circulation and in the way that heat is transported through the ocean.

Vertical mixing in the deep ocean also controls aspects of the horizontal circulation. Both wind-driven and tidal currents generate internal waves when they flow over abyssal topography. These waves subsequently mix the ocean vertically through wave breaking or other mechanisms. Measurements of vertical mixing in the Brazil Basin indicate that mixing rates vary with geographic location and depth, and the energetics of dissipation depend on fine-scale topography in the deep ocean (Figure 6). Models that predict future climate will require accurate bathymetry in order to predict spatially varying mixing rates. Unfortunately, the best global bathymetry that is currently available does not resolve seafloor topography at all length scales. Theoretical studies suggest that bathymetric features as small as 1 km may influence mixing. A new mission could map the length scales constraining 50% to 70% of the tidally driven mixing. Some features that generate internal waves are too small to be visible from space, but they may be predicted statistically, provided that bathymetry is resolved down to lengths where the statistics of roughness may be extrapolated from fractal models (8 km, Figure 4).

There are still unknown circulation pathways in the ocean, and the best bathymetry cannot yet determine where critical mixing is happening. A factor of two increase in the horizontal scales resolved and a factor of five increase in the signal-to-noise ratio, possible with the proposed satellite mission, will permit many of these currently unknown pathways to be mapped, and areas with topographically enhanced mixing to be found.

Beyond Plate Tectonics

The broad architecture and geologic history of the ocean basins can be elegantly explained by plate tectonic theory, which states that Earth's outer rocky layer is divided into a number of rigid blocks called plates. These plates move slowly over Earth's surface. The plate's interiors should be geologically stable and inactive, and earthquakes, volcanoes, and mountain building occur only near plate boundaries. This theory grew up in the 1960s when seafloor bathymetry was relatively crude; evidence came primarily from the geographical pattern of seafloor magnetic anomalies, and the global distribution of earthquakes, volcanoes, and fossils.

In the mid-1990s, satellite altimeter measurements of the marine gravity field provided the first globally uniform and detailed view of ocean floor architecture [Sandwell and Smith, 1997]. This new view seemed to both confirm and complicate plate tectonic theory. The satellite perspective displayed a globally continuous pattern of mid-ocean ridges and fracture zones, as the theory predicted. However, the data also revealed many features that the theory did not anticipate—mid-ocean ridges that propagated into old, thick oceanic lithosphere; spreading centers that overlapped (sometimes forming microplates that rotate rapidly between larger plates for a few million years); and a very complex pattern of volcanic seamounts in the interiors of plates [Wessel and Lyons, 1997]. These new features provide clues to the changing forces applied to the tectonic plates and the geologic history of our planet.

The improved resolution of a new space bathymetry mission will reveal hundreds of small structures on a global basis, and patterns of volcanism and fracturing that are not currently mapped. A more detailed view of the global mid-ocean ridge spreading system will permit a better understanding of what causes ridges to periodically break into segments, what causes the topographic variability displayed at mid-ocean ridges [Smith, 1998] (Figure 4), and whether there is a limit to how fast seafloor can be created at spreading centers [Naar and Hey, 1989]. A clearer view of plate motion over the past 180 million years recorded in the patterns of ocean floor structures [Mueller, *et al.*, 1997] will shed light on the synchronicity of plate reorganizations and plate motion changes, and hence on the strength of plates, an important question in earthquake physics. Plate location through time is linked to the opening and closing of seaways, which may have influenced climate by dramatically changing global ocean circulation patterns.

Origin of Undersea Volcanoes

Seamounts are active or extinct undersea volcanoes. They sustain important ecological communities, determine habitats for fish, and act as obstacles to water currents, enhancing tidal energy dissipation and ocean mixing. For all these reasons, it is important to map them. Seamounts come in a range of sizes, and the smaller ones are much more common than the larger ones [Wessel, 2001]. Analysis of the size distribution suggests that a new space-based mapping should increase the number of charted seamounts 18-fold, from roughly 3000 to nearly 60,000 (Figure 7).

Patterns in the geographical distribution of seamounts may settle a debate about the fundamental relationship between volcanism and plate tectonics [Natland and Winterer, 2005]. In basic plate

theory, plate interiors are geologically inactive, and a “hot spot” theory was added to explain linear volcanic chains in the middles of plates, such as at Hawaii. Although this theory is now enshrined in all introductory textbooks, many scientists are questioning its validity. Some believe it cannot explain all seamount chains, and a few scientists do not believe hotspots exist at all. Alternative explanations include excess magma supply spilling beyond mid-ocean ridges, stretching and cracking of plates, or small-scale convection under plates. A space-based mapping will be required to address the issue, as the seamount distribution pattern can only be revealed by a systematic mapping with a globally uniform resolution of seamount sizes.

Forecasting Tsunamis

Tsunamis are waves triggered by earthquakes and landslides or, rarely, an unusually large seafloor volcanic eruption [Moffeld, et al., 2004]. A large tsunami can drive huge waves against the coastlines, endangering people and damaging property in low-lying areas. The tragic Indonesian Tsunami of December 26, 2004 killed more than 200,000 people and left millions homeless. Early warning systems for tsunamis can save lives by allowing people to evacuate, but tsunami forecasts have to be done quickly because tsunamis can traverse the entire ocean basins in just a few hours. Tsunami simulations [Moffeld, et al., 2001] have shown that relatively small-scale details of deep-ocean bathymetry have a significant impact on tsunami heights because of the cumulative effect of refraction (Figure 8). In many parts of the North Pacific, the predicted maximum tsunami height differs dramatically depending on the resolution of the bathymetry. Further improvements in bathymetry are expected to produce significant improvements in tsunami forecasts, facilitating mitigation in shoreline regions that are frequently endangered and allowing targeted evacuations of at-risk populations. The bathymetry of the Indian Ocean is very poorly sampled by ships and thus a systematic mapping at 10-km resolution is needed to compile a library of tsunami scenarios for rapid consultation in case of another major event. This effort should be completed as soon as possible because major earthquakes are sometimes clustered in time.

Other Applications of Improved Bathymetry

Continental Margins and Hydrocarbon Exploration

Geologists call the outermost layer of rocky earth the “crust.” Continental crust is much thicker and older than oceanic crust. The margin of the continental crust, which is formed by rifting, is structurally complex and often obscured by thick layers of sediment. Understanding the margins and their sedimentary basins is important because most of the world’s oil and gas wealth is formed in basins at the continental margins, and because new international law allows new territorial claims in this area.

In the deep ocean, where the crust is young and the overlying sediments are thin, ocean surface gravity anomalies observable from space are easily correlated with bathymetry. The situation is

different at the continental margins where sediments are thick and the underlying rocks are of variable density and thickness. Here, gravity anomalies are often poorly correlated with bathymetry. Despite the lack of direct correlation between bathymetry and gravity at a margin, the gravity data obtained from a new space bathymetry mission would dramatically improve our understanding of the variety of continental margins in several ways. Gravity anomalies reveal mass anomalies and their compensation; these can be interpreted to reveal sediment types and basin locations [Fairhead, et al., 2001]. A uniform, high-resolution gravity mapping continuous from the deep ocean to the shallow shelf will make it possible to follow fracture zones and other structures out of the ocean basin onto the adjacent continent, to define and compare segmentation of margins along their length, and to indicate the position of the continent-ocean boundary. Rifted, fault-bounded blocks of continental crust often have dimensions of 5-25 km by 20-100 km. The shapes of these blocks must be seen in three dimensions to understand rifting tectonics. These individual blocks are not resolved in current data but would be mapped by the proposed space bathymetry mission. While current altimeter data delineate the large offshore basins and major structures, they do not resolve some of the smaller geomorphic features, including the smaller basins. Spatial scales shorter than 20 km in the presently available data cannot be interpreted with confidence close to shore, as the raw altimeter data are often missing or unreliable near the coast. The exploration industry would benefit from altimeter data with as much resolution as possible and extending as near-shore as possible.

Law of the Sea Definition of the Continental Shelf

One of the many objectives of the United Nations Convention on the Law of the Sea is to subdivide ocean space into zones under the jurisdiction of a Coastal State or of the International Seabed Authority. Coastal States may claim territorial rights to the seabed and its resources beyond their traditional Exclusive Economic Zones by submitting a claim to a Juridical Continental Shelf. This shelf represents a seaward prolongation of a State's territory and must be delineated according to a complex legal formula prescribed in Article 76 of the Convention. Bathymetry from Space can potentially contribute to resolving one element of the formula, the 2500 m isobath [Monahan, 2004]. Altimetry can also contribute to the problem of determining the location of the foot of the slope. Such uses of altimetric data are consistent with the view expressed by the Commission on the Limits of the Continental Shelf that altimetric data will be considered admissible as supporting information in a submission.

Although publications on space bathymetry caution that the technique may not be most accurate in continental slope and rise areas, it seems to be accurate enough for the purpose of determining a Juridical Continental Shelf under Article 76. A joint U.S.-Canadian study compared the location of the 2500 m isobath as measured by acoustic swath bathymetry from a GPS-navigated ship survey, and as estimated from the space bathymetry technique using existing satellite data. The study found that the location discrepancies between the two techniques were small enough to be within International Hydrographic Organization guidelines for errors in bathymetric surveys. To maximize the territory claimed, the Convention allows Coastal States to select data emphasizing seaward protrusions of their shelves. Thus, it is likely that space bathymetry will be used for reconnaissance of areas where a State might profitably invest in more detailed ship surveys.

Inertial Navigation

A passenger in a moving vehicle can perceive changes in the vehicle's velocity (direction or speed), because they cause the passenger's body to lean in the direction opposite the change. Inertial navigation systems work the same way, computing the motion of a vehicle by sensing accelerations on it. Precise inertial navigation systems require knowledge of gravity anomalies; otherwise a tilt of the direction of gravity (Figure 3) is mistaken for a turn of the vehicle.

Advanced integrated navigation systems now in use on some ships and aircraft require knowledge of anomalies in the direction of gravity at the 0.5 arc-second (2 microradians) level for optimum performance. Military data supporting this requirement were collected over limited areas of Earth during the Cold War. A systematic global data set of this quality does not yet exist. The measurements that a new bathymetry from space mission would obtain—sea surface slopes to 1 microradian— will allow computation of the gravity de-flection angles at sufficient precision to support precise inertial navigation at sea over nearly the entire globe.

Implementation

Current space bathymetry can resolve 12 km on rough seafloor and only 20 km on smooth seafloor. A new mission with sufficient accuracy to resolve 6-9 km would capture most of the interesting geophysics of seafloor spreading and the statistical properties of the finer-scale roughness.

Current Limitations and Future Requirements

The laws of physics impose a fundamental limit on the resolution of the topography that can be inferred from sea surface gravity to about twice the regional ocean depth, which is 6-9 km in the deep ocean. This physical limit has not yet been achieved from satellite altimetry because the ocean surface is roughened by waves that are typically 2-4 m tall. Conventional radar altimeters illuminate a spot on the ocean surface that is large enough to average out some of the local irregularities due to ocean waves. The noise is further reduced by averaging a thousand pulses over a 6 km distance along the satellite track. Attaining the physical limit will require a factor of five improvement in the accuracy of the global sea surface slope, which can be achieved through a combination of improved radar technology and multiple mappings. We envision a new mission with the following characteristics:

Altimeter precision. The most important requirement is improvement in ranging technology to achieve at least a factor of two enhancement in range precision (with respect to older altimeters such as GEOSAT and TOPEX) in a typical sea state of 3 m. In shallow water, where upward continuation is minor, and in calm seas where waves are not significant, it will also be important to have an along-track footprint that is much less than one-half of the resolution. This footprint is smaller than the standard pulse-limited footprint of GEOSAT or TOPEX, so new technology must be used.

Mission duration. The GEOSAT Geodetic Mission (1.5 years), which has superior range precision to the ERS-1 Geodetic Mission [Yale, et al., 1995] (1 year), provided a single mapping of the oceans at ~5 km track spacing. Since the measurement noise scales as the square root of the number of measurements, a six-year mission could reduce the error by an additional factor of two.

Moderate inclination. The short, non-repeat orbit phases of the Geosat and ERS-1 altimeters had relatively high inclination (72° GEOSAT, 82° ERS) and thus poor accuracy of the eastwest slope at the equator. A new mission should have an inclination of ~60° to improve east-west slope recovery. This, combined with the other improvements, will meet the factor of five requirement.

Near-shore tracking. For applications near coastlines, the ability of the instrument to track the ocean surface close to shore, and acquire the surface soon after leaving land, is desirable.

It should be stressed that the basic measurement is not the height of the ocean surface but the slope of the ocean surface to an accuracy of better than 1 microradian (1 mm height change over 1 km horizontal distance). The need to resolve height differences, and not heights, means that the mission can be much cheaper than other altimeter missions and can take advantage of a spacecraft platform that is less stable than other missions require. The 1 microradian slope precision can be achieved without measuring radar propagation delays in the ionosphere and troposphere, as the slopes of these corrections are negligible. These factors reduce the cost and complexity of the spacecraft with respect to a typical altimeter optimized for recovery of ocean currents.

Delay-Doppler altimeter technology. A delay-Doppler radar altimeter such as planned for CryoSat II can deliver the required height precision and spatial resolution. This innovative satellite altimeter uses signal processing strategies borrowed from synthetic aperture radar to improve height measurement precision by a factor of two, and to reduce along-track footprint size by a factor of five or more, in marked contrast to a conventional radar altimeter. Unfortunately the CryoSat ground segment cannot capture the full SAR waveforms globally so it will be operated as a conventional altimeter over the oceans. Onboard processing, to reduce the data transmission requirements, has been demonstrated in a delay-Doppler altimeter built by the Johns Hopkins University Applied Physics Laboratory (JHU APL) and flight-tested on Naval Research Laboratory (NRL) and National Aeronautics and Space Administration (NASA) P-3 aircraft. A preliminary design study by JHU APL for the National Oceanic and Atmospheric Administration (NOAA) suggests that a delay-Doppler space bathymetry mission could be completed for approximately \$60 M, plus launch costs.

Acknowledgements. This material is based upon work supported by the National Science Foundation under Grant No. 0326707

Figure captions

Légendes des figures

Figure 1. The Pacific-Antarctic rise, which has an area about equal to North America, is a broad rise of the ocean floor caused by sea floor spreading between two major tectonic plates. To the west of the ridge lies the Louisville seamount chain which is a chain of large undersea volcanoes having a length equal to the distance between New York and Los Angeles. These features are unfamiliar because they were unknown 30 years ago [Menard and Smith, 1966]. The Louisville seamount chain was first detected in 1972 using depth soundings collected along random ship crossings of the South Pacific. Six years later the full extent of this chain was revealed by a radar altimeter aboard the Seasat (NASA) spacecraft [Haxby, et al., 1983]. Recently, high density data collected by the Geosat (US Navy) and ERS-1 (European Space Agency) spacecraft data show the Pacific-Antarctic Rise and the Louisville Ridge in unprecedented detail [Smith and Sandwell, 1997].

Figure 1. La dorsale Pacifique-Antarctique - un vaste relief de la taille de l'Amérique du Nord - est produite par accréation de croûte océanique entre les plaques Pacifique et Antarctique. Sur le flanc ouest de la dorsale, s'étend une chaîne de volcans sous-marins - dite *chaîne de Louisville* - sur une distance équivalente à la largeur (Est-Ouest) des Etats-Unis. Découvertes relativement récemment (voir en haut à gauche, la carte de [Menard et Smith, 1965]), ces structures sont peu connues des non-spécialistes. La chaîne de Louisville a été détectée en 1972, à partir de levés bathymétriques exploratoires épars la recoupant. L'étendue de la chaîne a été vue dans son ensemble six plus tard, grâce aux données altimétriques de *SeaSat* de la NASA [Haxby et al, 1983]. Les données altimétriques acquises par les satellites *GeoSat* (US Navy) et *ERS-1* (Agence Spatiale Européenne) révèlent des détails des structures dans des zones vierges de tout levé bathymétrique.

Figure 2. Modern tools for mapping the deep ocean floor. A) A shipboard multibeam echo sounders uses sound waves to map 10-20 km wide swaths at ~200 horizontal resolution. B) An Earth-orbiting radar cannot see the ocean bottom, but it can measure ocean surface height variations induced by ocean floor topography. While the resolution of the echo sounder technique is far superior to the ultimate resolution of the satellite altimeter technique (~ 8 km), complete mapping of the deep oceans using ships would take 200 ship-years at a cost of billions of dollars [Carron, et al., 2001]. Indeed, the shipboard and altimeter methods are highly complementary. The current distribution of ship soundings provides the long-wavelength (> 160 km) information that cannot be obtained from gravity because of spatial variations in isostasy (Figure 3). Satellite altimeters provide the global uniform coverage in the 16 to 160 km wavelength band. When interesting features are discovered in satellite gravity, they can be surveyed in fine detail by ships.

Figure 2 : Outils modernes de cartographie du plancher océanique. A) Les sondeurs acoustiques multifaisceaux permettent de couvrir, à chaque passage du navire, une bande de plancher océanique de 10 à 20 km de large, avec une résolution horizontale de l'ordre de 200 m. B) Les ondes des altimètres-radar ne pénètrent pas à l'intérieur de la masse d'eau, mais peuvent mesurer les variations de la surface moyenne des océans engendrées par la topographie sous-marine. La résolution des sondages acoustiques est très largement supérieure à celle que l'on peut espérer atteindre avec les modèles déduits de l'altimétrie (~ 8 km dans le meilleur des cas). Il faudrait cependant l'équivalent de 200 années de temps-navire pour couvrir l'ensemble des grands fonds océaniques, ce qui représente des coûts de plusieurs milliards de dollars [Carron, et al., 2001]. L'altimétrie et l'acoustique sont complémentaires à plusieurs titres. En effet, sur le plan global, les données bathymétriques actuelles fournissent les grandes longueurs d'onde (> 160 km) de la topographie du plancher océanique, qui ne peuvent pas être obtenues de la gravimétrie satellitaire, du fait des variations latérales du mode de compensation isostatique. Les satellites altimétriques fournissent une couverture globale de la topographie aux longueurs d'onde comprises entre 16 et 160 km. Les structures intéressantes détectées par satellite peuvent ensuite être étudiées en détail avec des navires équipés de sondeurs acoustiques.

Figure 3. Satellite-derived bathymetry. A) A mountain on the ocean floor adds to the pull of Earth's gravity and changes its direction subtly, causing extra water to pile up around the mountain. The tilt in the direction of gravity, called a "deflection of the vertical," is equal to the slope of the sea surface, and is measured in microradians. One microradian of deflection appears as a 1 mm change in sea surface height per 1 km of horizontal distance. Laplace's

equation allows the exact transformation of sea surface slope into gravity anomaly. One microradian error in slope translates into approximately 1 milligal (mgal) error in gravity. B) Over areas of thin sediment cover, the ratio of topography to gravity is primarily a function of topographic wavelength. A gravity field that is accurate to 1 milligal can recovery topography between wavelengths of 16 km and 160 km to an accuracy of better than 70 m. The short-wavelength part of the transfer becomes singular because of the smoothing of gravity by upward continuation. The long-wavelength part of the transfer becomes singular because isostatic compensation cancels the long-wavelength gravity due to seafloor topography. For wavelengths > 160 km, the topography/gravity ratio is highly dependent on the elastic thickness of the lithosphere so gravity cannot be uniquely inverted for topography. Both ship soundings and satellite altimeter data are needed to provide a global mapping of the seafloor topography. Existing sparse ship soundings are sufficient to constrain the long-wavelength (> 160 km) shape of the oceans. Ship soundings are also used to calibrate the topography to gravity ratio in over the intermediate wavelength band (160-16 km). Shorter wavelength topography (< 12-18 km) can only be recovered by swath bathymetry surveys. The resolution of seafloor structure within the achievable band of spatial is a strong function of the signal-to-noise ratio in the altimeter data, and a new mission with a more precise altimeter would make improvements of a factor of 5 in vertical precision, 2 to 3 in horizontal length, and 4 to 9 in horizontal area.

Figure 3. Bathymétrie déduite de l'altimétrie satellitaire. A) Dans l'océan, les masses d'eau ont tendance à s'accumuler au dessus des montagnes sous-marines à cause de l'attraction causée par les reliefs. Ainsi, en l'absence de vent, vagues et courants marins, il y a naturellement des « bosses » à l'aplomb des monts sous-marins et des « creux » au dessus des fosses : c'est cette propriété qui est utilisée par les satellites pour estimer, de manière approchée, la hauteur des reliefs sous-marins. La surface de l'océan au repos (en l'absence de toute perturbation océanique) correspond au géoïde, une surface équipotentielle en tous points perpendiculaire à la force de pesanteur locale. La déflexion de la verticale résultant des reliefs est égale à la pente du géoïde. Elle est mesurée en microradians (un microradian équivaut à 1 mm de variation de hauteur du géoïde par kilomètre de distance horizontale). L'équation de Laplace permet de convertir hauteur de géoïde en anomalie de gravité. Une erreur de pente d'un microradian équivaut à 1 mGal d'erreur en gravité. B) Dans les zones où la couverture sédimentaire est faible, le rapport entre gravité et topographie sous-marine dépend de la longueur d'onde de la topographie. Avec des anomalies gravimétriques précises à 1 mGal près, on peut déterminer la topographie avec une précision de l'ordre de 70 mètres pour les longueurs d'onde comprises entre 16 et 160 km. Une anomalie de topographie sous-marine de très courte longueur d'onde est à peine décelable (quasi nulle) à la surface de l'océan à cause de l'épaisseur de la masse d'eau ; ainsi, aux courtes longueurs d'onde, le rapport entre topographie et gravité (T/G) part à l'infini (en langage mathématique, c'est le résultat de l'opération dite de « continuation vers le haut »). Aux grandes longueurs d'onde (> 160 km), la topographie est compensée par des anomalies de masse en profondeur (situées sous la croûte), si bien que la topographie et la gravité ne sont plus vraiment corrélés. C'est pourquoi il est nécessaire d'avoir à la fois des données bathymétriques acquises par bateau et des données altimétriques pour déterminer la topographie des fonds océaniques à l'échelle globale. Les données bathymétriques existantes sont suffisantes pour contraindre les grandes longueurs d'onde (> 160 km) de la topographie sous-marine. Ces données permettent également de calibrer le rapport T/G dans la bande comprise entre 16 et 160 km. Pour obtenir le détail de la topographie (aux longueurs d'ondes < 12-18 km), une couverture bathymétrique totale, au moyen de sondeurs multifaisceaux. La résolution dans la bande [16 – 160 km] dépend de la précision (rapport signal / bruit) des données altimétriques. L'amélioration du rapport S/B d'un facteur 4 permettrait d'améliorer significativement l'estimation de la topographie dans cette gamme de longueurs d'onde.

Figure 4 (upper) Measured bathymetry (right column) and predicted bathymetry (left and center columns) for representative topography on the Mid-Atlantic Ridge, the East Pacific Rise, and the Gulf of Mexico. The Mid-Atlantic Ridge and East Pacific Rise show the characteristic abyssal-hill signature of slow and fast spreading ridges, respectively. While the current predicted bathymetry in the Gulf of Mexico is unable to resolved the salt-related mini-basins (outlined), the future predicted bathymetry reveals some of the more important structures; a global data set would be beneficial in frontier reconnaissance studies.

(lower) East-west spectra of the Mid-Atlantic Ridge and the East Pacific rise area bathymetry. For both areas, the corner wavenumber and roll-off exponent are 20 km and -2.8 , respectively. The total power is 493 m for the MAR and 209 m for the EPR. The noise spectra (dotted curves) for current and future bathymetric prediction is discussed in the following section. A signal to noise ratio of 1 defines the resolution limits of current and future bathymetric prediction. The current resolution for rough and smooth seafloor is 25 km and 45 km, respectively. Assuming a factor of 5 noise reduction in a future mission, the resolution improves to 12 and 17 km, respectively (i.e., 6-9 km half-wavelength). Note this improvement captures the corner wavenumber of 20 km.

Figure 4. Haut : bathymétrie mesurée (colonne de droite) et prédite (colonnes du milieu et de gauche) pour différents cas représentatifs provenant des dorsales Médio-Atlantique ou Est-Pacifique et du Golfe du Mexique. Les flancs des dorsales exhibent la signature caractéristique des collines abyssales produites à l'axe des dorsales lentes ou rapides, respectivement. La bathymétrie prédite actuelle ne permet pas de délimiter les mini-bassins associés aux diapirs de sel dans le Golfe de Mexico, mais un meilleur rapport S/B des données altimétriques permettrait d'obtenir un nouveau modèle bathymétrique présentant des améliorations significatives.

Bas : Aire (représentée dans le domaine spectral) de sections bathymétriques caractéristiques perpendiculaires à l'axe des dorsales Médio-Atlantique ou Est-Pacifique. Pour les détails, voir ci-dessus la légende en anglais, intraduisible en français courant.

Figure 5. The availability of accurate bathymetric data is critical for modeling major current systems such as the Kuroshio in the North Pacific [Metzger and Hurlburt, 2001]. The simulation in the left panel properly represents the islands and shoals within the Luzon Strait and the intrusion of the Kuroshio into the South China Sea. If the three model grid points representing small topographic features are removed (marked in blue on the left panel), the Kuroshio intrudes farther west (right panel) than indicated by observations.

Figure 5. La précision des modèles bathymétriques s'avère être d'une grande importance pour la modélisation des grands courants océaniques, tels que le Kuroshio dans le Pacifique Nord [Metzger and Hurlburt, 2001]. La simulation du panneau de gauche a été réalisée avec le modèle complet de topographie globale. Elle est relativement conforme aux observations. Si l'on retire les trois noeuds de la grille indiqués en bleu sur le panneau de gauche, on obtient (panneau de droite) que le Kuroshio pénètre plus profondément vers l'ouest à l'intérieur de la mer de Chine par le détroit de Luzon, ce qui correspond pas aux données.

Figure 6. Mixing rates in the ocean govern the rate at which the ocean absorbs heat and greenhouse gases, moderating climate. Global climate change forecasts are uncertain in part due to uncertainty in the global average ocean mixing rate. Mixing rates in the ocean vary geographically depending on bottom roughness [Polzin, et al., 1997]. (upper) Bathymetry of Brazil Basin, South Atlantic derived from ship soundings lacks the resolution needed to distinguish between rough and smooth seafloor. (center) Bathymetry derived from satellite altimetry and ship soundings resolves the rough seafloor associated with fracture zones but not abyssal hills. (lower) Mixing rates observed during an oceanographic survey across the Brazil Basin in the South Atlantic Ocean. Low mixing rates (purple) were found over the smooth topography to the west, and higher mixing rates (multiple colors) over the rough topography to the east.

Figure 6. L'absorption par l'océan de la chaleur et des gaz à effet de serre dépend de la façon dont se mélangent les différentes masses d'eau. La modélisation du changement climatique global dépend donc, elle aussi, de la vigueur de ces mélanges qui varient en fonction de la rugosité du plancher océanique [Polzin, et al., 1997]. (Panneau du haut) La topographie du bassin du Brésil (Atlantique Sud) déterminée à partir des seules données bathymétriques ne permet pas de déterminer la rugosité du fond. (Panneau du milieu) La topographie déduite de la combinaison des données bateau et des données altimétriques actuellement disponibles ne permet d'accéder à la rugosité associée à la présence des zones de fracture, mais pas à celle liée aux collines abyssales. (Panneau du bas) Taux de mélange des masses d'eau observés *in situ*. Les taux de mélange les plus faibles (violet) apparaissent dans les zones où la topographie est plutôt lisse ; les taux les plus élevés, là où la topographie est la plus accidentée.

Figure 7. Seamounts come in a range of sizes. The red dots shown here indicate the number of seamounts found with existing satellite altimeter data, as a function of seamount size [Wessel, 2001]. For seamounts 2 km tall and larger, the data are explained by a scaling rule (solid line). For heights less than 2 km, the red dots fall off the line because these more numerous small seamounts fall below the resolution of existing data. A new Bathymetry from Space mission should find these unmapped seamounts. An improvement in altimeter height resolution by a factor of 2 should increase the total number of seamounts mapped by 18-fold. The newfound seamounts will have important ramifications for physical oceanography, marine ecology, fisheries management, and fundamental science questions about Earth's magma budget and the relationship between volcanism and tectonics.

Figure 7. Classification (par taille) des monts sous-marins. Les points rouges indiquent les monts localisés à partir des données altimétriques existantes [Wessel, 2001]. La ligne continue noire représente une droite de régression effectuée à partir des données bathymétriques réelles, montrant que le nombre de monts diminue exponentiellement avec leur taille. La corrélation avec les données déduites de l'altimétrie est satisfaisante pour les reliefs de hauteur supérieure à 2 km, mais pas en dessous, ce qui suggère qu'il reste encore de nombreux monts sous-marins à découvrir, dont la hauteur est inférieure à 2 km. Une nouvelle mission altimétrique dédiée permettrait d'inventorier une bonne partie de ces monts sous-marins. L'inventaire complet des monts-sous-marins apporterait des éléments nouveaux dans de nombreux domaines de recherche appliquée (océanographie physique, écologie marine, halieutique), mais aussi fondamentale (géodynamique, bilan magmatique de la Terre, interactions entre volcanisme et tectonique).

Figure 8. Tsunamis are catastrophic shock waves that can flood coastal areas after a submarine earthquake or landslide. A submarine event on one side of an ocean basin can flood the coasts on the other side in a matter of hours. Careful modeling of the propagation and refraction of these waves is a key component of hazard mitigation. Model studies have shown that lack of information about the small-scale bathymetry of the ocean floor makes the estimated height of the flooding wave uncertain by 100% or more [Mofjeld, et al., 2004]. Here is a model of the tsunami generated by the December 5, 1977 earthquake in Kamchatka. Blue regions in the open ocean show the tsunami spreading outward, like a wave that forms after dropping a pebble into a pond. Rainbow colors indicate the percent change in amplitude attributed to fine-scale bathymetry. Image courtesy H.O. Mofjeld, NOAA PMEL.

Figure 9, d'après H.O. Mofjeld, NOAA PMEL Les tsunamis sont des ondes de gravité, principalement dues à des séismes ou à des glissements de terrain. Les systèmes d'alerte reposent sur le fait que les tsunamis se propagent bien plus lentement que les ondes sismiques. On peut donc en principe déclencher l'alerte avant l'arrivée de la vague. Pour affiner l'alerte (et éviter les fausses alarmes), il serait intéressant de pouvoir modéliser la hauteur de la vague, avant qu'elle n'arrive à la côte. Pour ce faire, il est nécessaire d'avoir un modèle bathymétrique aussi précise que possible. Des études réalisées par [Mofjeld, et al., 2004] montrent que les estimations de la hauteur de vague à la côte peuvent varier de 100%, suivant le modèle bathymétrique qu'on utilise. La figure ci-dessus indique une simulation de la hauteur de vague engendrée par le séisme survenu le 5 décembre 1977 au large du Kamtchatka. La simulation montre que le tsunami se propage comme une onde après un jet de pierre dans une mare. Les couleurs indiquent le rapport (exprimé en pourcentage) entre la hauteur de vague calculée avec un océan plat et celle calculée avec le modèle global de bathymétrie déduit des données satellitaires.

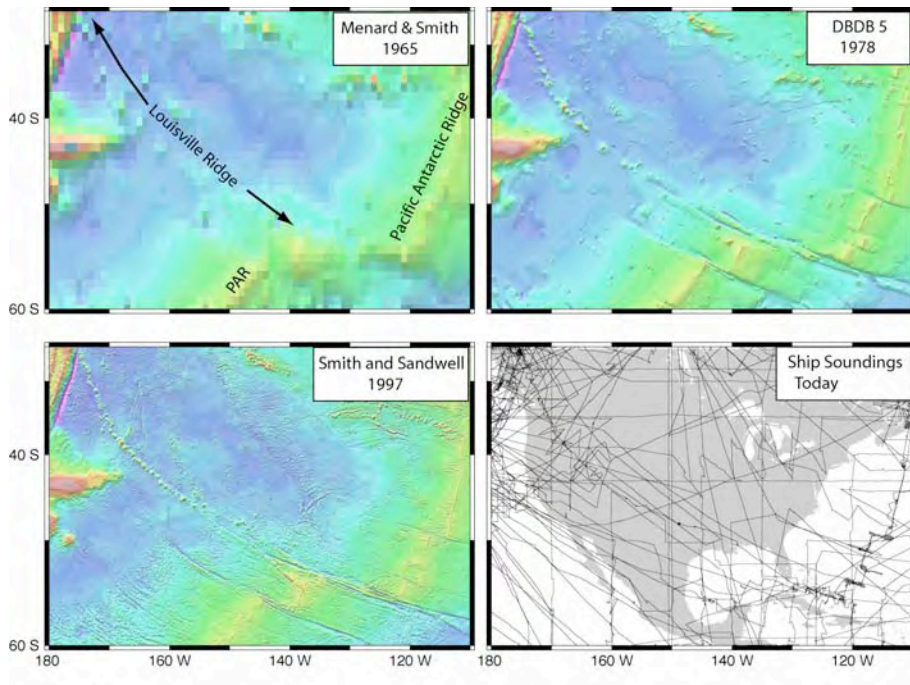


Figure 1

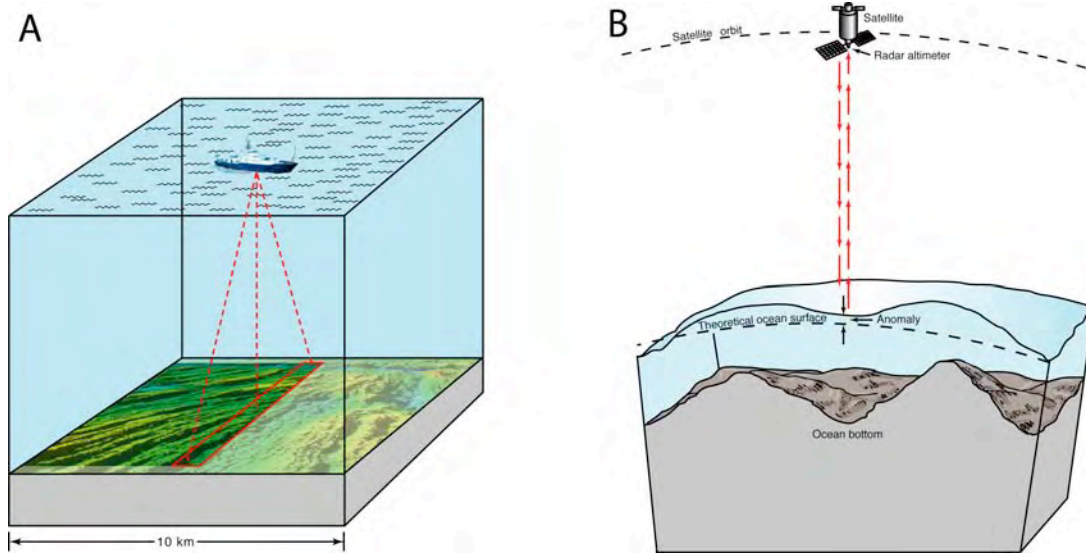


Figure 2

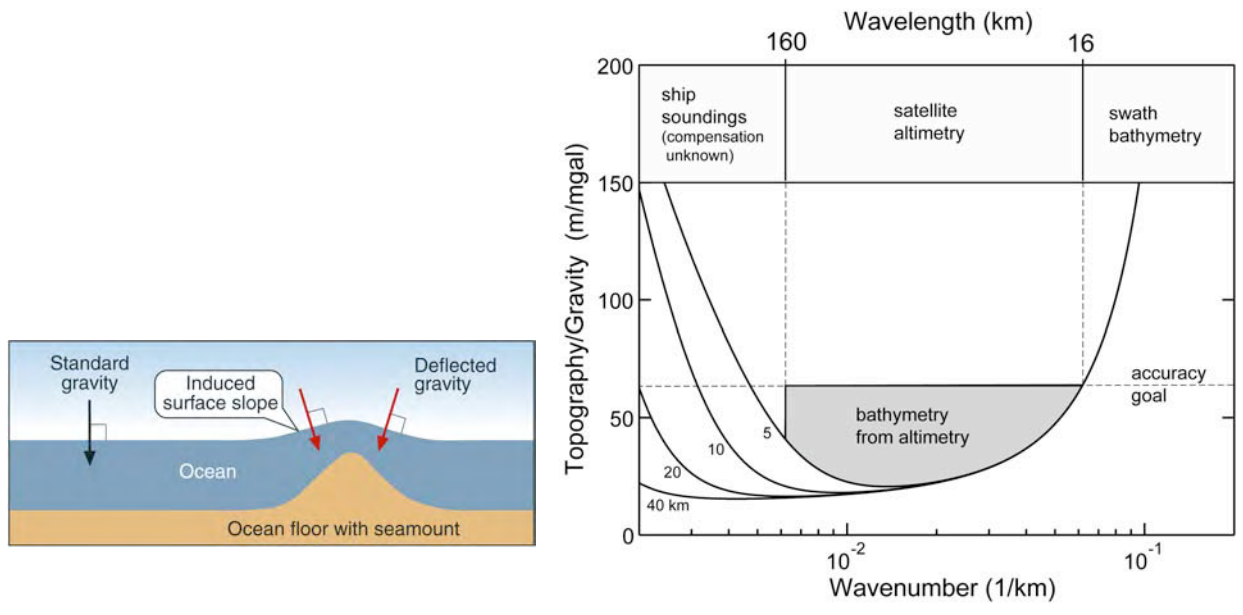


Figure 3

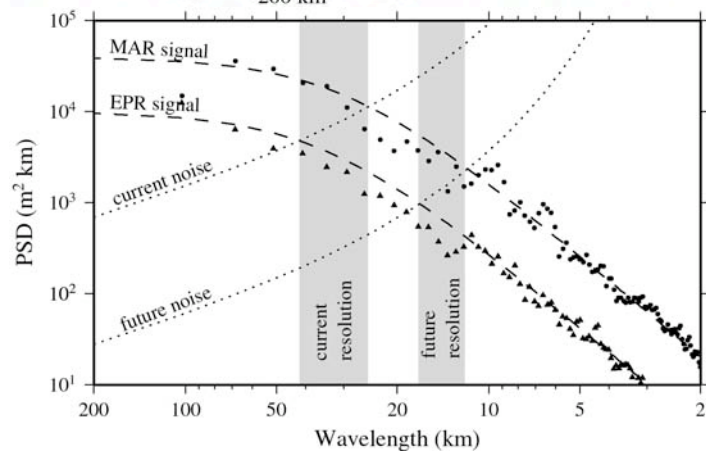
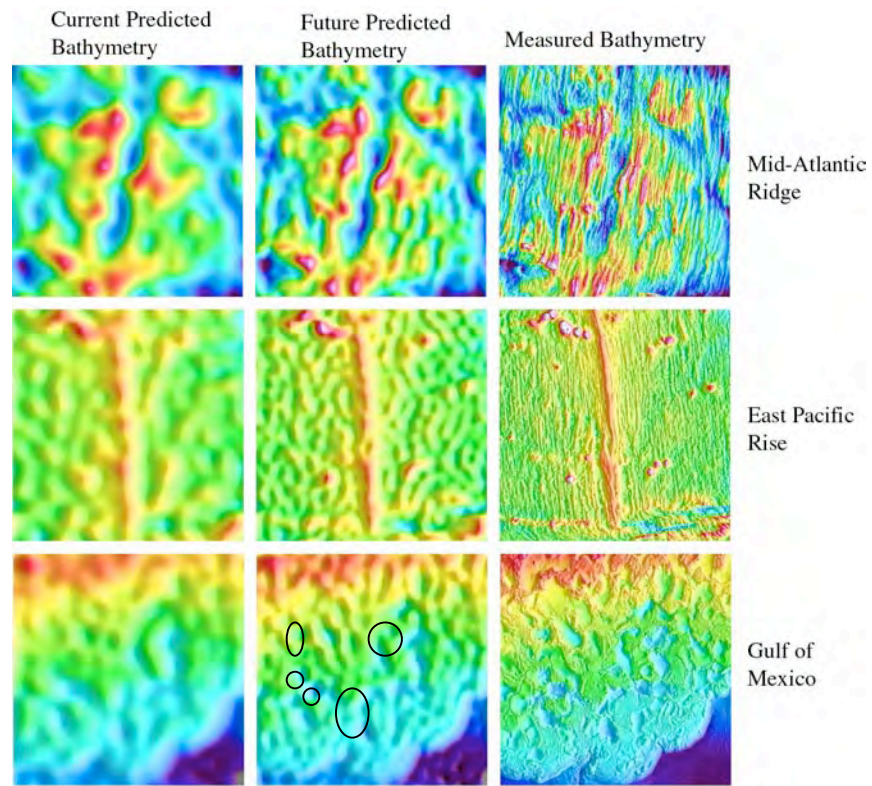


Figure 4

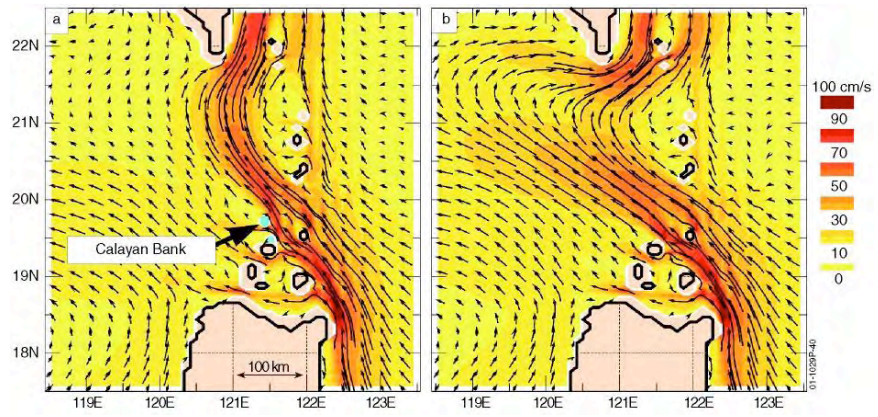


Figure 5

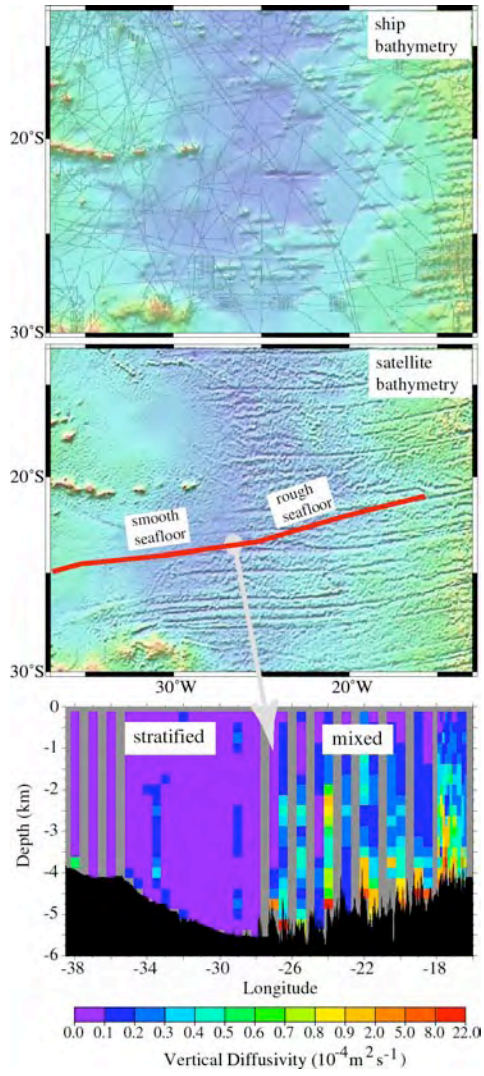


Figure 6

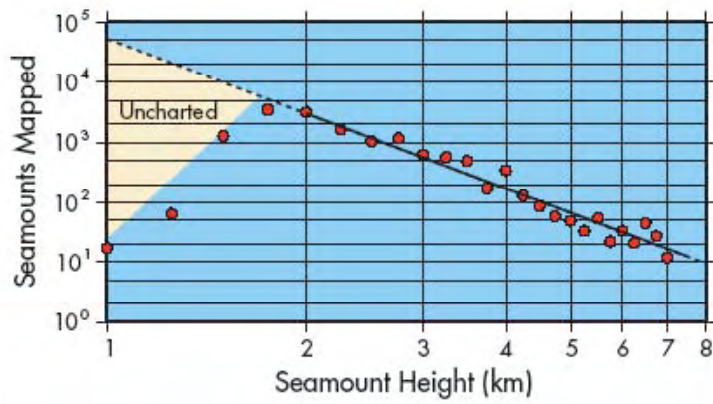


Figure 7

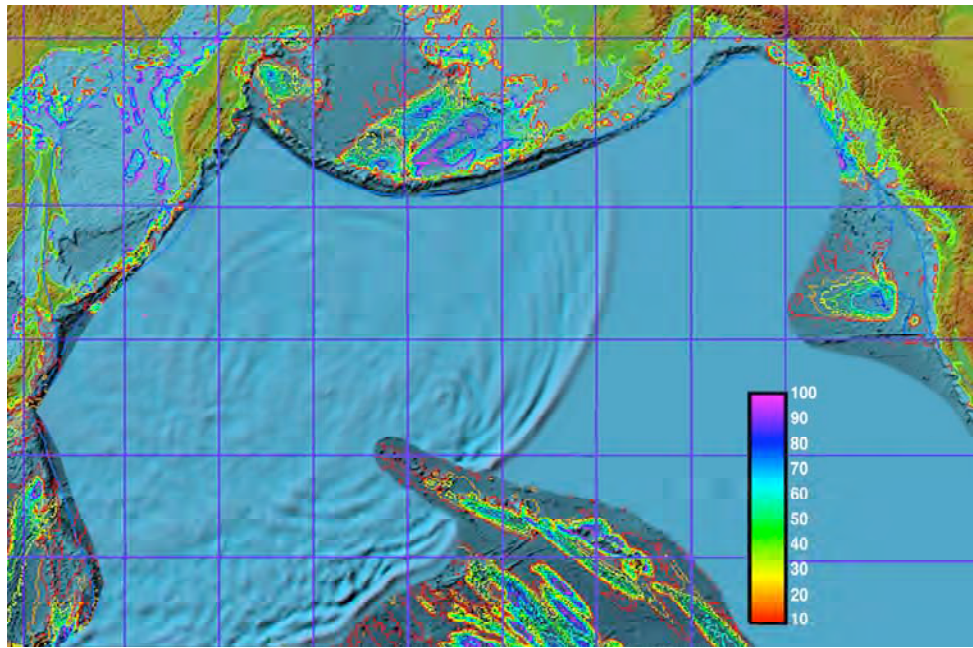


Figure 8

References

- Baudry, N., and S. Calmant (1991), 3-D Modelling of seamount topography from satellite altimetry, *Geophys. Res. Lett.*, *18*, 1143-1146.
- Brown, J., et al. (1998), *The Ocean Basins: Their Structure and Evolution*, 171 pp., Pergamon Press, Oxford.
- Carron, M. J., et al. (2001), A proposed international long-term project to systematically map the world's ocean floors from beach to trench: GOMaP (Global Ocean Mapping Program), *Inter. Hydr. Rev.*, *2*, 49-50.
- Cazenave, A., et al. (1996), High-resolution mean sea surface computed with altimeter data of ERS-1 (Geodetic Mission) and TOPEX-POSEIDON, *Geophys. J. Int.*, *125*, 696-704.
- Dixon, T. H., et al. (1983), Bathymetric prediction from Seasat altimeter data, *J. Geophys. Res.*, *88*, 1563-1571.
- Fairhead, J. D., et al. (2001), Satellite-derived gravity having an impact on marine exploration, in *The Leading Edge*, edited, pp. 873-876.
- Gille, S. T., et al. (2004), Seafloor topography and ocean circulation, *Oceanography*, *17*, 47-54.
- Haxby, W. F., et al. (1983), Digital images of combined oceanic and continental data sets and their use in tectonic studies, *EOS Trans. Amer. Geophys. Un.*, *64*, 995-1004.
- Jayne, S. R., et al. (2004), Connections between ocean bottom topography and the Earth's Climate, *Oceanography*, *17*, 65 - 74.
- Jung, W. Y., and P. R. Vogt (1992), Predicting bathymetry from Geosat-ERM and shipborne profiles in the South Atlantic ocean, *Tectonophysics*, *210*, 235-253.
- Kunze, E., and S. G. Llewellyn Smith (2004), The role of small-scale topography in turbulent mixing of the global ocean, *Oceanography*, *17*, 55 - 64.
- Menard, H. W., and S. M. Smith (1966), Hypsometry of Ocean Basin Provinces, *J. Geophys. Res.*, *71*, 4305-4325.
- Metzger, E. J., and H. E. Hurlburt (2001), The importance of high resolution and accurate coastline geometry on modeling South China Sea inflow, *Geophys. Res., Lett.*, *28*, 1059-1062.
- Mofjeld, H. O., et al. (2004), Tsunami scattering and earthquake faults in the deep Pacific Ocean, *Oceanography*, *17*, 38-46.
- Mofjeld, H. O., et al. (2001), Tsunami scattering provinces in the Pacific Ocean, *Geophys. Res. Lett.*, *28*, 335-337.
- Monahan, D. (2004), Altimetry applications to continental shelf delineation under the United Nations Convention on the Law of the Sea, *Oceanography*, *17*, 75-82.
- Mueller, R. D., et al. (1997), Digital isochrons of the world's ocean floor, *J. Geophys. Res.*, *102*, 3211-3214.
- Munk, W., and C. Wunsch (1998), Abyssal recipes II: Energetics of today and wind mixing, *Deep-Sea Res. I*, *45*, 1977-2010.
- Naar, D. F., and R. N. Hey (1989), Speed limit for oceanic transform faults, *Geology*, *17*, 420-422.
- Natland, J. H., and E. L. Winterer (2005), Fissure control on volcanic action in the Pacific, in *Plates, plumes, and paradigms: Geological Society of America Special Paper 388*, edited by G. R. Foulger, Natland, J.H., Presnall, D.C., and Anderson, D.L., pp. 687 - 710, Geological Society of America.
- Polzin, K. L., et al. (1997), Spatial variability of turbulent mixing in the abyssal ocean, *Science*, *276*, 93-96.

- Ramillien, G., and A. Cazenave (1997), Global bathymetry derived from altimeter data of the ERS-1 Geodetic Mission, *J. Geodynamics*, 23, 129-149.
- Sandwell, D. T., and W. H. F. Smith (1997), Marine gravity anomaly from Geosat and ERS-1 satellite altimetry, *J. Geophys. Res.*, 102, 10039-10054.
- Smith, W. H. F. (1998), Seafloor tectonic fabric from satellite altimetry, *Ann. Rev. Earth Planet. Sci.*, 26, 697-738.
- Smith, W. H. F., and D. T. Sandwell (1994), Bathymetric prediction from dense satellite altimetry and sparse shipboard bathymetry, *J. Geophys. Res.*, 99, 21803-21824.
- Smith, W. H. F., and D. T. Sandwell (1997), Global sea floor topography from satellite altimetry and ship depth soundings, *Science*, 277, 1956-1961.
- Tapley, B. D., and M. C. Kim (2001), Applications to Geodesy, in *Satellite Altimetry and Earth Sciences*, edited by b. L.-L. F. a. A. Cazenave, pp. 371-403, Academic Press, New York.
- Wessel, P. (2001), Global distribution of seamounts inferred from gridded Geosat/ERS-1 altimetry, *J. Geophys. Res.*, 106, 19,431-419,441.
- Wessel, P., and S. Lyons (1997), Distribution of large Pacific seamounts from Geosat/ERS 1: implications for the history of intraplate volcanism, *J. Geophys. Res.*, 102, 22459-22475.
- Yale, M. M., et al. (1995), Comparison of along-track resolution of stacked Geosat, ERS-1 and TOPEX satellite altimeters, *J. Geophys. Res.*, 100.

1 Global Estimates of Seafloor Slope from Single-Beam Ship Soundings

2 Joseph J. Becker and David T. Sandwell

3 Institute of Geophysics and Planetary Physics, Scripps Institution of Oceanography,

4 La Jolla CA 92093-0225

5 Submitted to JGR Oceans: August 14, 2006

6 Revised: January 26, 2007

7 Second revision: August 24, 2007

8 Third revision: December 19, 2007

9
10 Abstract

11 Rough topography on the ocean floor is a source of ocean mixing which is of interest to
12 both physical oceanography and climate science. Most mixing has been attributed to high
13 slopes of the large-scale structures of the deep ocean floor such as seamounts, continental
14 margins, and mid-ocean ridge axes. In this paper, we show the small-scale but ubiquitous
15 abyssal hills and fracture zones dominate the global map of rough topography. Much of
16 this rugged seafloor occurs in the Southern Ocean on the flanks of the Pacific-Antarctic
17 Rise and Southwest Indian Ridge. We present our results as a global map of the mean
18 slope of the ocean floor, and as a global map of the ocean floor above the M_2 critical
19 slope. We compare our results to multi-beam and satellite bathymetry data to show that
20 satellite bathymetry is not a valid proxy for multi-beam measurements, but edited single-
21 beam sonar data are adequate to provide a global perspective on features with horizontal
22 wavelengths as small as 2 km.

1 Introduction

2

3 In a classic paper, *Munk* [1966] assumed constant upwelling and estimated the eddy
4 diffusivity needed to maintain the observed abyssal ocean stratification as well as the
5 amount of energy needed to mix the abyssal ocean. The $O(10^{-4} \text{ m}^2/\text{sec})$ diffusivity [*Munk*,
6 1966] predicted was not found experimentally [c.f. *Osborn*, 1980]. Eddy diffusivity is
7 difficult to measure, but with the semi-empirical methods of *Osborn* [1980; 1972] and
8 *Dillon* [1982], reliable experimental results were obtained. Recent measurements show
9 that mixing is enhanced by orders of magnitude near rough topography [*Nash et al.*,
10 2007; *Polzin et al.*, 1997; *Toole et al.*, 1997]. *Munk and Wunsch* [1998] addressed the
11 missing diffusivity in the mid ocean and the increased mixing over rough topography by
12 proposing that tidal dissipation was a power source of mixing and mixing preferentially
13 occurred when internal tides flowed across steep slopes. There is an extensive body of
14 experimental, theoretical, and numerical research on the production of internal waves by
15 the interaction of tidal currents with variable topography [cf. [*Garrett and Kunze*, 2007].
16 *Baines* [1982] examined the simple case of horizontal tidal excursions impinging on a
17 uniform continental slope and found that for semidiurnal tides in a stably stratified layer,
18 there is a critical slope where conversion of the barotropic tide is most efficient. In the
19 deep ocean where the stratification is low, this critical slope ranges from 0.1 to 0.3 m/m
20 so only very steep topography can generate internal waves in this simplified model.
21 [*Llewellyn Smith and Young*, 2002] extended the model to show the shape of the
22 topographic spectrum determines the amount of energy conversion in an ocean of finite
23 depth with arbitrary stratification.

1

2 Satellite altimetry has been used to measure the global barotropic tide [*Kantha*, 1995], as
3 well as the location and magnitude of its global dissipation [*Egbert and Ray*, 2000; 2001;
4 2003]. The global dissipation studies indicated that the approximately 1/3 of the semi-
5 diurnal barotropic tidal dissipation occurs in the deep oceans, apparently over the mid-
6 ocean ridges (MOR) and seamounts. However, the dissipation maps do not have
7 sufficient spatial resolution to provide a clear correlation with seafloor structures [*Egbert*
8 *and Ray*, 2003]. The lack of resolution reflects the wide track spacing of Topex/Poseidon
9 altimeter profiles (~150 km) as well as the subtlety and difficulty of the measurements
10 presented in *Egbert and Ray* [2003].

11

12 In this paper, we present the global spatial distribution of seafloor slope and roughness in
13 the abyss (depth > 2000 m). In particular, we focus on abyssal hills and fracture zones
14 that extend over large parts of the ocean basins, especially on the lightly sedimented
15 flanks of the slower spreading ridges. If, as proposed by *Ledwell* [2000], most of the tidal
16 dissipation in the deep ocean occurs on abyssal hills, mapping their global distribution is
17 important. We also show a significant fraction of seafloor (4.5%) has slope greater than
18 the M_2 critical slope. Much of this super critical seafloor occurs in the Southern Ocean on
19 the flanks of the Pacific-Antarctic Rise and Southwest Indian Ridge. These high-slope
20 facets have either not been detected before, or have been grossly underestimated because
21 satellite bathymetry [*Smith and Sandwell*, 1997] does not resolve features having
22 horizontal scales less than 10 km.

23

1 Global Estimate of Critical Slope

2

3 While we are considering a more complete spectral analysis of the sounding data, a great
4 deal can be learned from a simple "critical slope" analysis. The internal tide literature
5 *Baines* [1982] describes topography as being either super or sub critical. A well-known
6 approximation for the critical slope of the topography is [*Baines*, 1982]

7

8
$$\alpha^2 \approx \tan^2(\theta_g) = \frac{(\omega^2 - f^2)}{(N^2 - \omega^2)} \quad (1)$$

9

10 where θ_g is the angle between the group velocity vector and the horizon, ω is the
11 frequency of internal wave (radian/sec) generated by the M_2 tide, f is the inertial
12 frequency and N is the buoyancy frequency. For waves of given frequency (always M_2 in
13 this paper) at given latitude the only unknown is the buoyancy frequency which depends
14 on the density profile,

15

16
$$N^2 = \frac{-g}{\rho} \frac{\partial \rho}{\partial z} - \frac{g^2}{c^2} \approx \frac{-g}{\rho} \frac{\partial \rho_\theta}{\partial z} \quad (2)$$

17

18 where z is the vertical coordinate, c is the speed of sound, ρ the in situ density, ρ_θ the
19 potential density, and g is the acceleration of gravity (9.8 m/s²) [*Knauss*, 1997].

20

21 A detailed global density profile is unavailable. We calculate an approximate buoyancy
22 frequency profile using the CSIRO MATLAB routines [*Morgan and Pender*, 2003] at

1 every depth and location in the 1° World Ocean Atlas (WOA) [Conkright *et al.*, 2002].
2 Noise in the WOA values of temperature and salinity made the calculated values of N^2
3 noisy and occasionally negative. To stabilize our estimate of N , we first removed
4 negative values of N^2 and other obvious errors, and then followed *St Laurent and Garrett*
5 [2002] by fitting N to an exponential function of depth.

6

$$7 \quad \ln(N) = c_0 + c_1 z \quad (3)$$

8

9 For depths that exceed the maximum depth in the WOA, we simply assumed N changes
10 only slightly at abyssal depths, and used the deepest WOA depth at that location rather
11 than extrapolate a fit to very noisy data. The calculated critical slope has at least two
12 significant sources of error. First, the value of N is based on the WOA and which is an
13 empirical data set with the usual potential for random and systematic errors. Secondly,
14 our N is an empirical fit to an exponential of depth [*St Laurent and Garrett*, 2002]; the
15 truth is substantially more complex. As a result, our critical slope calculation is a semi-
16 qualitative result.

17

18 To test the accuracy of our critical slope calculation we compared it to CTD data from
19 two WOCE cruises. Appendix I is a comparison of our fit to the WOA data and WOCE
20 CTD data along a meridian at 150 W between Alaska and Antarctica. We find good
21 agreement between the critical slope estimates from these two independent data sets
22 suggesting that the WOA data is adequate for this global analysis.

23

1 The global map of critical slope based on [Conkright *et al.*, 2002] is shown in Figure 1.
2 The map extends only to +/- 72°, so the M_2 turning latitudes at 75° are not visible. The
3 latitudinal trend toward a critical slope of zero at those turning latitudes is apparent, as is
4 the general decrease of N (increasing critical slope) with increasing depth. Low critical
5 slope occurs on the shallow continental margins, the crests of seamounts such as the
6 Hawaiian ridge, and along the mid-ocean ridges with depths between 2000-3000 m.
7 There is a prominent asymmetry between the North and South Pacific, east-west
8 asymmetries in the South Atlantic, across the equatorial East Pacific Rise, and across the
9 Ninety-East Ridge in the Indian Ocean. This asymmetry is also seen in the WOCE CTD
10 analysis provided in Appendix I.

11

12 Satellite Bathymetry Greatly Underestimates Seafloor Roughness

13

14 The slope of the ocean floor depends on the length-scale of interest since, for example,
15 individual pillow basalts can have vertical sides. The critical slope theory assumes that
16 the length scale of the topography is greater than the tidal excursions of ~200 m [Garrett
17 and Kunze, 2007]. A typical single beam echo sounder has a beam width of ~15° so in the
18 deep ocean (4000 m) it insonifies a zone about 1000 m across. Higher resolution (~200
19 m) is possible with modern multibeam systems but much of that data is collected at
20 transit velocities, which limits the resolution to several hundred meters.

21

22 Three types of measurement systems are used to map the topography and roughness of
23 the ocean floor. Single beam echo sounders, widely used since the 1960's, provide profile

1 of depth from thousands of research cruises (Figure 2). While coverage is widespread,
2 there are gaps as large as 200 km by 200 km, especially in the Southern Ocean.
3 Multibeam echo sounding, available on most large research vessels since the mid 1990's,
4 map 5-20 km wide swaths of seafloor at a horizontal resolution that depends on the depth
5 of the water; 200-500 m at 4 km depth depending on ship speed and swath width. Ideally,
6 the world's oceans should be exhaustively measured with multibeam bathymetry, but
7 only a small percentage of the ocean floor has been so measured [*Smith and Sandwell*,
8 2004]. The third approach combines the sparse ship soundings with dense satellite-
9 derived gravity anomalies to estimate depth and roughness [*Gille et al.*, 2000; *Smith and*
10 *Sandwell*, 1997]. Satellite bathymetry can only resolve features with wavelengths
11 between 20 and 160 km and misses most, if not all, of the small-scale roughness
12 associated with the abyssal hill fabric. While none of these three measurement systems
13 provides global coverage at the scales of interest (2 – 200 km), we show that the along-
14 track analysis of the single beam provides an acceptable compromise between coverage
15 and resolution if abyssal hills are assumed to be smoothly varying in slope over distances
16 greater than a few hundred kilometers [*Goff*, 1991].

17

18 To assess the accuracy and resolution capabilities of each of the three systems, we
19 compared multibeam, single beam, and satellite bathymetry along the track of an error-
20 free, but otherwise typical cruise near the Atlantis Transform Fault on the Mid Atlantic
21 Ridge (Figure 3). The multibeam data are from a 500-m grid provided by the Ridge
22 Multibeam Synthesis project [*Carbotte*, 2004] and is considered in this paper to represent
23 the "true" depth. The single beam data were filtered and differentiated, as discussed

1 below, to best match the multibeam slopes. Indeed the agreement between multibeam and
2 single beam data is quite good for both depth and slope. In contrast the satellite
3 bathymetry does not capture the smaller-scale topography associated with the abyssal
4 hills. This is evident in the slope comparison where the *rms* slope calculated from
5 satellite bathymetry (0.038 m/m *rms*) is much smaller than the slope derived from the
6 multibeam and single beam systems (0.095 and 0.111 m/m *rms*). The inability of satellite
7 bathymetry to accurately recover seafloor slope is illustrated in Figure 4, which shows a
8 cumulative histogram of the absolute value of the slope for each of the three systems
9 along the entire track line. Both sonar systems show that about 30% of the seafloor has
10 slope greater than 0.1 m/m while the satellite bathymetry indicates only 2% of the
11 seafloor of slope is greater than 0.1 m/m. This deficiency in the satellite bathymetry
12 makes it unsuitable for quantifying seafloor slope due to abyssal hills.

13

14 To further assess the accuracy and resolution of the single beam data, we compared
15 single beam slopes of our representative ship track (leg 19180015) to slopes derived from
16 a multibeam grid available at 200 m, 500 m, and 1500 m spacing. As noted above the
17 footprint of a single beam system in the deep ocean is ~1000 m but the along-track
18 sampling is 330 m at transit speed so the true along-track resolution is probably
19 somewhere between these two values. These grids were compiled by the Ridge
20 Multibeam Synthesis Project [Carbotte, 2004] and represent the best practices of the
21 marine geology and geophysics community. It should be noted that there is a tradeoff
22 between grid cell size and areal coverage so three resolutions are provided. While the
23 200-m resolution grids should provide the most accurate slope information, the coverage

1 is much less complete than the 500-m grid. The 1500-m grid has the most complete
2 coverage at the expense of lower resolution. To perform the slope comparison, the
3 gradient of the multibeam grid was sampled along the trackline of the single-beam profile
4 and the along-track slope was computed as the dot product of this gradient vector with
5 the ship direction vector. The *rms* difference in slope between the single-beam slope and
6 the along-track multibeam slope was nearly the same for all grids (0.094, 0.075, and .086
7 m/m respectively). These differences are due to many factors including navigational
8 errors, measurement errors in both systems, and the sampling and filtering of both data
9 types. The *rms* difference is generally less than the critical slope (0.1-0.3 m/m, Figure 1)
10 needed to excite internal waves in the deep ocean. In addition to *rms* difference, we
11 performed a regression analysis between the co-located slope profiles. A regression value
12 of less than one indicates that the single-beam slopes are underestimating the "true"
13 seafloor slope. A value of greater than one indicates either that the single-beam slopes
14 have enhanced slope due to measurement noise or that the multibeam grids are over-
15 smoothed. The regression was computed as the ratio of the standard deviation of the two
16 slope data sets [Laws, 1997]. The regression values for the 200-m and 500-m grids are
17 nearly one (0.98 and 1.08 m/m, respectively) indicating that the *rms* slope of the single-
18 beam data is closest to the *rms* slope of the 500-m grid. In contrast, the *rms* slope of the
19 single-beam data is 1.84 times greater than the *rms* slope derived from the 1500-m grid
20 suggesting that the 1500-m grid is too smooth to fully capture seafloor slope at a
21 wavelength of 2000 m. These comparisons demonstrate that the along-track slope derived
22 from a single-beam profile is similar in amplitude to the best multibeam grids at 500 m
23 resolution.

1

2 While single beam slope measurements are close to the multibeam "truth", they have not
3 been analyzed previously because the archived data are contaminated by many error
4 sources. There are three main types of problems with the single beam measurements.
5 First, the depth soundings can be inaccurate due to "blunders", scale factor errors, and
6 poor along-track sampling [*Smith*, 1993]. Second, older cruise data often contain large
7 navigational errors that place soundings in the wrong location. While this is an issue for
8 creating depth grids, navigation errors are not a problem for computing spatially averaged
9 along-track slopes. Third, the coverage is non-uniform and the slope can only be
10 computed along the track line of the ship. Track density is generally sparse in regions that
11 are remote, have extreme weather, or are topographically uninteresting (Figure 2). In
12 particular the abyssal plains and hills, (far from ports, mid-ocean ridges and other areas of
13 geologic interest), are poorly sampled. Since bathymetry derived from gravity data
14 became available in 1997, cruises have often been planned to avoid areas of smooth
15 topography. As a result, recent sounding data have a potential sampling bias toward
16 rough seafloor that is difficult to quantify.

17

18 Method

19

20 The most challenging issue related to the single beam data is that slope can only be
21 estimated along the track line of each cruise leg. In lightly sedimented areas, seafloor
22 fabric is dominated by abyssal hills (Figure 2c) that are elongated in the direction of the
23 fossil spreading ridge, because they were formed by ridge-parallel normal faulting and

1 volcanism [*Goff*, 1991; *Goff and Smith*, 2003; *Macdonald and Luyendyk*, 1985;
2 *Macdonald et al.*, 1996; *Smith*, 1998]. Because the abyssal hills have a preferred
3 orientation, a single beam profile must be oriented perpendicular to the hill to measure
4 the full magnitude of the seafloor gradient. This is illustrated in Figure 5 where we have
5 plotted the slope along the track line of many cruises against the magnitude of the
6 gradient vector derived from a 500-m multibeam grid. Theoretically, the along-track
7 slope should be less than the gradient, but in this example, there are deviations reflecting
8 the inconsistencies in the two types of data due to the inherent smoothing of the
9 measurement as well as the smoothing related to gridding.

10 While the single beam profiles measure only the along-track component of seafloor
11 slope, their coverage is much more complete than the coverage of the multibeam swaths
12 so they provide a better sampling of the global seafloor slope. We can partly overcome
13 the 1-D sampling of a 2-D topography by projecting the statistical properties of the
14 seafloor gradient to the statistical properties of along track slope. Appendix II provides an
15 analysis that demonstrates the magnitude of the gradient of a patch of sea floor is
16 typically $\pi/2$ higher than the along-track slope measured by a ship having a randomly
17 oriented trackline. The orientation of the ship tracks, with respect to the abyssal fabric, is
18 sometimes, but not always, random. Seagoing expeditions not focused on seafloor
19 geology, or cruises in transit across the basins, sample the abyssal fabric in an essentially
20 random direction. However, a cruise focused on geology and geophysics is typically
21 preferentially oriented perpendicular or parallel to the abyssal fabric (e.g., Figure 2,
22 bottom). Because of this possible sampling direction bias, we report mean slope without

1 scaling up by $\pi/2$. This conservative approach understates the extent of supercritical
2 seafloor.

3

4 Data Processing

5

6 The examples provided so far have used single beam data that are not contaminated by
7 errors in depth or navigation. Approximately 1/3 of the 4900 cruise legs of single beam
8 bathymetry data available from the GEODAS database [NGDC, 2005] have significant
9 errors. These 1800 cruises have never been used in the global satellite bathymetry maps
10 [Smith and Sandwell, 1997] even though, in many cases, the entire month-long set of
11 depth soundings had only a few outliers. The automatic algorithm used to screen out
12 obviously bad cruises generally failed to identify the occasional bad pings in good cruises
13 because the types of errors are so diverse. Typical errors include: navigation errors,
14 digitizing errors, typographical errors due to hand entry of older sounding, reporting the
15 data in fathoms instead of meters, incorrect sound speed measurements, and even
16 computer errors in reading punch cards [Smith, 1993]. Just one bad section of a cruise in
17 an isolated region introduces a seafloor topographic feature that does not exist and the
18 entire cruise is rejected.

19

20 About 5000 cruises of single beam soundings collected over the past 40 years and
21 archived at the National Geophysical Data Center [NGDC, 2005] have been hand edited
22 by comparing measured depth to satellite bathymetry (i.e., based on gravity only). These
23 data will be combined with multibeam data to refine the global satellite bathymetry grid

1 [Smith and Sandwell, 1997] and create a new global grid at 1 km resolution. This
2 involved the development of a graphical user interface program consisting of three linked
3 windows, the ship track, the along track profile, and a scatter diagram of altimetric versus
4 measured depth. Typical *rms* differences between the measured and satellite bathymetry
5 are 250 m. We expect the *rms* errors in the soundings to be less than 25 m [Smith, 1993]
6 so most of the bad soundings are obvious outliers. The analyst scans the profile data for
7 large deviations from the satellite bathymetry (typically > 500 m) and flags these data as
8 being suspect. The edited cruise is returned to the database with the suspect data flagged.
9 Using this tool, we have edited the approximately 30 million pings from the GEODAS
10 database.

11

12 These clean data were then low pass filtered and differentiated along-track to estimate
13 seafloor slope as discussed below using the software tools in GMT [Wessel and Smith,
14 1995]. The ship track profiles were pre-filtered with a Gaussian low pass filter having a
15 0.5 gain at a wavelength of 2 km. The 2-km filter is partly motivated by the expected
16 beam width of single beam sonar (~1 km) in the deep ocean [Smith, 2005]. Ship track
17 data are unequally spaced; e.g., the ship speed changes, but the ping rate is relatively
18 uniform. Moreover, the spacing of the older hand-digitized data is based on the seafloor
19 features. For example, flat abyssal plains sometimes have 4-km spacing between
20 soundings because the human digitizer determined that a finer spacing was unnecessary.
21 This uneven and sometimes large spacing does not strictly support a 2-km wavelength
22 resolution. We selected this resolution as a compromise because the widely spaced older
23 soundings presumably would have a smaller spacing if the human digitizer felt it was

1 needed to capture the actual seafloor slope. After low pass filtering, the data were
2 differentiated along-track at a minimum interval of 1/4 the wavelength of the low-pass
3 filter (500 m). More complex signal processing is not needed when the ship track data is
4 correctly edited.

5

6 The calculation of the fraction of seafloor above critical slope discussed below was done
7 in three steps in order to minimize the bias due to the uneven distribution of ship
8 soundings. First, we created two 0.1° longitude by 0.1° latitude grids - one consisting of
9 the total number of slope estimates in each grid cell and a second consisting of the
10 number of slope estimates (absolute value) that exceed the critical slope in each grid cell.
11 Second, these two grids were low pass filtered with a radial Gaussian filter ($\sigma=10\text{km}$) to
12 determine the number of slopes per 628 km^2 ; the integrated area under a radial Gaussian
13 is $2\pi\sigma^2$. Third, the fraction of seafloor with slope above the critical slope was computed
14 as the ratio of the two grids. Areas with less than one ping per 100 km^2 were not used to
15 avoid taking the ratio of very small numbers. For display purposes, the fraction of
16 seafloor above critical slope is median filtered and interpolated onto a 1° grid (Figure 7a).
17 This process combines the information in Figures 5 and 6.

18

19 Global Measurement of Sea Floor Roughness

20

21 The global map of spatially averaged seafloor slope is shown in Figure 6. Along-track
22 slopes were binned in a 0.25° longitude by 0.2° latitude intermediate grid and the mean
23 slope was calculated for each bin. The binning is done to reduce the bias due to uneven

1 sampling by the ship soundings. In particular, the ridge axes are sampled much more
2 densely than the abyssal plains. We find that seafloor slope varies more than an order of
3 magnitude throughout the deep oceans and depends on a combination of tectonic and
4 sedimentary processes. Large-scale features (> 40 km) such as continental margins, ridge
5 axes, fracture zones, trenches, and seamounts are sometimes associated with slope greater
6 than 0.05. These large-scale features are well resolved in bathymetry derived from
7 satellite-derived gravity anomalies and sparse ship soundings [*Smith and Sandwell,*
8 1997]. Such maps have been band-pass filtered between 20 and 160 km wavelength to
9 reveal the slope and roughness of the seafloor and to relate these bottom characteristics to
10 mesoscale variability [*Gille et al., 2000*] and ocean mixing [*Jayne and St Laurent, 2001*].
11 Using only ship soundings, we find that the global mean slope map is dominated by the
12 distribution of the smaller-scale abyssal hill topography and fracture zones. Abyssal hills
13 are generated at mid-ocean ridges by a combination of volcanism and normal faulting
14 [*Cannat et al., 2006; Lonsdale, 1977; Macdonald and Luyendyk, 1985*]. The amplitude
15 and wavelength of abyssal hills depends strongly on the rate of seafloor spreading [*Goff,*
16 1991; *Goff et al., 2004; Kunze and Llewellyn Smith, 2004*] that also controls the
17 morphology of the spreading ridge axis where they were formed [*Canuto et al., 2004;*
18 *Macdonald, 1982; Macdonald et al., 1988; Menard, 1967; Small and Sandwell, 1992*].
19 On older seafloor, a thick layer of sediment often covers the abyssal fabric. Sedimented
20 seafloor can be extremely flat at the scale of abyssal hills. In summary, there are basin-
21 scale variations in seafloor slope that are well explained in terms of variations in seafloor
22 spreading rate and the thickness of the sediments. These spatial variations in slope occur
23 over distances greater than a few hundred kilometers [*Goff and Jordan, 1989*] so the

1 sparse track sampling in the Southern Ocean (~40 km track spacing) is adequate for
2 characterizing global seafloor slope.

3

4 Fraction of Seafloor above Critical Slope

5

6 Given the slope along each ship track and the critical slope interpolated to the same
7 location we calculate the fraction of seafloor having slope above the critical slope. This
8 calculation is allows us to estimate the total area of super critical seafloor. It is also useful
9 because it at least partially addresses the issue of mixing hot spots. [*Nash et al.*, 2007]
10 suggest that mixing in the deep ocean is localized in a few small areas. Therefore, an
11 area's potential for mixing may not be the average critical slope, but the fraction of the
12 area that is super critical.

13

14 For comparison, we performed a similar analysis using the global 2-minute grid of *Smith*
15 *and Sandwell* [1997] (Figure 7b). Since the full gradient of the *Smith and Sandwell*
16 [1997] grid was calculated, we would expect slopes from the gradient of *Smith and*
17 *Sandwell* [1997] to be $\pi/2$ times greater than single beam slopes, and thus the fraction of
18 seafloor above the critical slope should be $\pi/2$ larger. Instead, we find the super-critical
19 fraction of seafloor for [*Smith and Sandwell*, 1997] to be substantially less than that
20 derived from the single beam soundings. This is because, as discussed above, satellite
21 bathymetry does not capture the full magnitude of the seafloor gradient because it only
22 resolves wavelengths > 20 km.

23

1 The ship data and the satellite bathymetry grid have similar super-critical seafloor
2 fraction for the large-scale structures of the ocean basins such as continental margins,
3 ridge axes, ocean trenches and back-arc volcanoes and intra-plate island chains such as
4 Hawaii. This is expected because these large-scale features are well resolved in the
5 satellite bathymetry grid. However, there are major differences (Figure 7a and 7b) on the
6 flanks of ridges especially in the Southern Ocean where the critical slope at the bottom of
7 the ocean is less than 0.2 m/m.

8

9 To quantify this observation we plot the area of seafloor with supercritical slope versus
10 ocean depth (Figure 8 - thick line). Seafloor spreading ridges lie at depths between 2000
11 m and 3000 m. The ridge flanks lie at depths between 3000 m and 4500 m. It is clear that
12 the fraction of supercritical seafloor on the ridge flanks is larger than the fraction of
13 supercritical seafloor on the ridge axes. A similar analysis using satellite bathymetry
14 arrives at just the opposite conclusion and suggests that the ridge axes are more important
15 than the ridge flanks. Indeed the total fraction of supercritical seafloor in the deep ocean
16 (> 2000 m deep) is 4.5% based on the single beam data and only 1.5% based on the
17 satellite bathymetry. These comparisons suggests that calculations based on slopes of the
18 [*Smith and Sandwell, 1997*] grid are substantially underestimating the area of super
19 critical seafloor, and it's location.

20

21 Discussion and Conclusions

22

1 We restrict our discussion to the deeper ocean areas (> 2000 m) where abyssal hills
2 dominate the seafloor slope, and where we expect that spatial variations in slope and
3 critical slope will be smooth relative to the characteristic spacing of the ship profiles. Our
4 estimate of the fraction of seafloor above critical slope shows some obvious global
5 patterns that deserve comment. The west flank of the southern mid-Atlantic Ridge is
6 prominent, but areas of rough seafloor in the Southern Ocean dominate the fraction of
7 seafloor above critical. In particular, the flanks of the Southwest Indian Ridge and the
8 flanks of the Southeast Indian Ridge, especially in the Australian-Antarctic Discordant
9 Zone (90° - 160° E) are prominent as are the flanks of the Pacific-Antarctic Rise, and the
10 flanks of the Scotia Sea Spreading Centers (50° - 60° S, 75° - 30° W). The presence of so
11 much super critical topography near the Antarctic Circumpolar Current (ACC) is striking.
12 We speculate that the ACC may be sweeping the sediment off the ridge flanks, creating
13 an area of rough topography in a strong current.

14

15 Our conclusions are: 1) The 40-year archive of single beam bathymetry provides a global
16 perspective on the slope and roughness of the seafloor although the data have some
17 significant shortcomings. First, the original data are highly heterogeneous because they
18 were collected with multiple generations of echo sounding and navigation technology and
19 were digitized and assembled by hundreds of scientists on tens of research vessels. By
20 visually editing 4900 cruises assembled at NGDC, we were able to extract seafloor slope
21 and roughness information for wavelengths greater than 2 km and confirmed the results
22 in small areas where complete multibeam coverage is available. A second problem with
23 the single beam bathymetry data is that the seafloor slope can only be estimated along the

1 trackline of the ship, which is usually not in the direction of maximum seafloor gradient.
2 Assuming the direction of the ship tracks is random with respect to the abyssal hill fabric,
3 we show that, on average, the along-track slope will be $2/\pi$ less than the magnitude of the
4 gradient. We use the along-track slope estimate as a proxy for seafloor slope knowing it
5 represents a lower bound on the actual slope.

6 2) The critical slope at the bottom of the ocean associated with conversion of the
7 barotropic M_2 tide was estimated from a global compilation of temperature and salinity
8 measurements [Conkright *et al.*, 2002]. Sparse measurements, especially in the Southern
9 Ocean, prevent the construction of a spatially detailed map of critical slope. We argue
10 that in the deep ocean (< 2000 m) spatial variations in temperature and salinity will be
11 small so this global representation may be qualitatively correct. Interpolating this critical
12 slope map to the locations of the measured seafloor slope, we estimate the fraction of
13 seafloor with slope that exceeds the critical value. In contrast to previous studies based on
14 altimetry-derived depth, we find large areas that have slope exceeding the critical value.

15 3) Our results are consistent with previous studies that show a high fraction of seafloor
16 above critical slope along the mid-Atlantic ridge and Hawaiian Chain but suggest that
17 barotropic tidal conversion dominantly occurs in the Southern Ocean where sediments
18 are thin and the abyssal hills have relatively high amplitude because they formed at a
19 fossil spreading rate less than the threshold value of 70 mm/yr. The global analysis shows
20 that the largest areas of super-critical slope are on the flanks of the seafloor spreading
21 ridges. The largest areas of super critical slope are the Southwest Indian Ridge flanks, the
22 Southeast Indian Ridge flanks, the southern Mid-Atlantic Ridge flanks, the Scotia Ridge,
23 and most importantly, the Pacific Antarctic Rise away from the ridge axis.

1

2 *Appendix I - Comparison of critical slope from WOCE P16 CTD casts and numerical fits*
3 *to WOA [2001]*

4

5 The global map of critical slope (Figure 1) shows obvious hemispherical variation with
6 the lower critical slope in the South Pacific than North Pacific. To verify this
7 hemispherical asymmetry, we compared our numerical fit of World Ocean Atlas (WOA)
8 2001 data [Conkright *et al.*, 2002] to the critical slope calculated from Salinity,
9 Temperature, and Pressure data (commonly referred to as CTD) from two World Ocean
10 Circulation Experiment (WOCE) repeat cruises in 2005/06. These cruises revisited the
11 “P16” line in the Pacific that runs along longitude 150W from Antarctica to Alaska with
12 a CTD cast taken at least once every degree of latitude from 72S to 56N. These particular
13 data were not used in the WOA 2001 analysis [Conkright *et al.*, 2002]. The 2005/2006
14 cruises had modern navigation and CTD instrumentation and they sampled the entire
15 water column from surface to approximately 10m above the bottom. A typical CTD
16 rosette has redundant sensors that are calibrated on shore and against each other on each
17 station. The noise present in the data is on the order of 1 part per thousand or better. This
18 level of instrument noise is inconsequential since the microstructure of the water column
19 dominates the instrumentation noise. The standard deviation of N due to the
20 microstructure was typically 0.25 *cph* in the deepest bin, which is a large fraction of the
21 total estimate of N so this environmental noise dominates. At one station in the North
22 Pacific at 28N, either an overturn was observed at the bottom, or there was a data error

1 large enough to create a negative N^2 . As in the cases of computing N from the WOA, this
2 value of N and the critical slope are both set to zero.

3

4 The CTD data from 190 casts were processed into critical slope at the bottom of the
5 ocean as follows. The “exchange” data in comma separated value (CSV) format from the
6 2005 repeat of the P16S line on cruise 33RR200501, and the 2006 repeat of P16N from
7 cruise 325020060213 were down loaded from the CLIVAR & Carbon Hydrography
8 Office (CCHDO) website [*Swift, 2007*] and processed using MATLAB software
9 [*MathWorks, 2007*]. For each of the depth casts, the CTD were processed using the
10 CSIRO algorithm [*Morgan and Pender, 2003*] of the UNESCO seawater equation of
11 state. The data for each cast were then binned and averaged at the WOA standard depths.
12 The deepest bin in each P16 station was compared to the numerical fit from the WOA
13 2001 data [*Conkright et al., 2002*]. The maximum depth of the water at P16 stations is
14 rarely more than 100 m deeper than the maximum standard depth in the WOA.

15

16 Estimates of critical slope from the WOA and P16 are plotted in Figure A1 and show
17 good agreement. Both estimates have an unknown uncertainty that is dominated by true
18 fluctuations in density gradient. Therefore we performed a robust regression [*Laws,*
19 1997] using a “bisquare” weighting function in the MATLAB robustfit function where
20 the model was constrained to go through the origin. The three slope estimates agree to
21 within 10% of each other and are consistent with a slope of one. The linear correlation
22 between the two approaches is 0.497. Our calculation of critical slope using the WOA is
23 slightly smaller than the experimental data (0.958 +/- 0.085), but it is within 5 percent of

1 the experimental results. The WOA data also show some anomalously high slopes that
2 are due to underestimating the density gradient. Considering that the microstructure of N
3 in the experimental data is approximately +/- 50%, we feel our use of a fit to the WOA to
4 estimate global critical slope is justified.

5

6 Given this level of agreement we believe the north-south asymmetry in critical slope,
7 shown in Figure 1, is real. Along this line of longitude the asymmetry is to be expected
8 because of the Pacific basin in the northern hemisphere is generally 1-2 km deeper than
9 the flank of the Pacific Antarctic Rise in the southern hemisphere and deeper ocean tends
10 to be more stratified than shallower ocean. In conclusion, a critical slope calculated from
11 WOA is error prone, but in good agreement with the more accurate CTD data.

12

13 *Appendix II - Statistical relationship between slope and gradient*

14

15 Assume the abyssal seafloor away from isolated seamounts and other distinct features is a
16 stationary and ergodic function [*Bendat and Piersol, 2000*]. The gradient of a randomly
17 oriented facet of sea floor is a random vector [*Goff, 1991*]. Our objective is to describe
18 the statistical properties of the gradient vector as well as to relate this to the statistical
19 properties of the slope vector. Following [*Goff, 1991*], assume the x - and y -components
20 of the gradient are independent, zero mean, and normally distributed with identical
21 variance σ^2 . As discussed by Freilich [1997], the histogram of the magnitude of this
22 random vector is a Rayleigh distribution ($x > 0$)

23

1
$$f_{Rayleigh}(x; \sigma) = \frac{x}{\sigma^2} \exp\left(\frac{-x^2}{2\sigma^2}\right) \quad (A1)$$

2

3 The mean value of the gradient g is

4

5
$$\bar{g} = \int_{g=0}^{\infty} g \cdot f(g; \sigma) dg = \sigma \sqrt{\frac{\pi}{2}} \quad (A2)$$

6

7 Given this statistical model for seafloor slope we can relate the probability distribution of
 8 along-track slope to the Rayleigh distribution of gradient. Consider a tilted facet of
 9 seafloor oriented at an azimuth of ϕ with respect to the track line of the ship. The
 10 measured slope of the seafloor is always less than or equal to the magnitude of the
 11 gradient and it is given by $s = g \cos \phi$. The distribution for along track slope is related to
 12 the probability distribution for gradient by

13

14
$$f(s; \phi, \sigma) = f_{Rayleigh}(s/\cos \phi; \sigma) \left| \frac{\partial g}{\partial s} \right| = \frac{s}{\sigma^2 \cos^2 \phi} \exp\left(\frac{-s^2}{2\sigma^2 \cos^2 \phi}\right). \quad (A3)$$

15

16 We need to integrate over all azimuths and normalize by 2π to obtain the distribution for
 17 a randomly oriented facet.

18

19
$$f(s; \sigma) = \frac{1}{2\pi} \int_0^{2\pi} f(s; \phi, \sigma) d\phi = \sqrt{\frac{2}{\pi\sigma^2}} \exp\left(\frac{-s^2}{2\sigma^2}\right) \quad (A4)$$

20

1 The Rayleigh distribution describing the gradient maps to a Gaussian distribution
2 describing the along track slope. An example of theoretical gradient and slope
3 distribution functions are shown in Figure A2 along with the histograms of observed
4 gradient and slope shown in Figure 5. While there are discrepancies between the actual
5 and model distribution functions, these simple ideas provide an approximate basis for
6 deriving seafloor gradient information from along-track slope profiles. In particular, it is
7 interesting to relate the mean along track slope to the mean gradient, ($s > 0$)

8

$$9 \quad \bar{s} = \int_0^{\infty} s \cdot f(s; \sigma) ds = \sigma \sqrt{\frac{2}{\pi}} = \frac{2}{\pi} \bar{g}. \quad (A5)$$

10

11 This relationship suggests the mean value of slope measured along a ship track is lower
12 than the gradient by a factor of $2/\pi$ (64%). In this paper, we compute mean slope along
13 ship tracks, and expect that the seafloor gradient is usually larger.

14

15 Acknowledgements

16 This paper benefited greatly from discussions with Walter Munk, Stefan Llewellyn
17 Smith, Shaun Johnston, Sarah Gille, and Jennifer MacKinnon. Scott Nelson of UCSD
18 edited the ship data with an astonishing rapidity and accuracy. We thank the associate
19 editor James Richman and the two reviewers for their many suggestions for improving
20 the manuscript. We also thank Walter Munk for originally proposing this study in 1999
21 using satellite bathymetry. That preliminary comparison suggested (incorrectly) that the
22 abyssal plains were not important in deep ocean mixing. The results were not published
23 because we speculated that the slope of the seafloor from satellite bathymetry greatly

1 underestimates the true seafloor slope. It has taken 8 years to go back, look at the raw
2 sounding data, and arrive at a more accurate assessment. This research was supported by
3 the Office of Naval Research (N00014-06-1-0140).

4

5 References

6

- 7 Baines, P. G. (1982), On Internal Tide Generation Models, *Deep-Sea Research Part a-*
8 *Oceanographic Research Papers*, 29(3), 307-338.
- 9 Bendat, J. S., and A. G. Piersol (2000), *Measurement and analysis of random data*, Third
10 ed., Wiley, New York.
- 11 Cannat, M., et al. (2006), Modes of seafloor generation at a melt-poor ultraslow-
12 spreading ridge, *Geology*, 34(7), 605-608.
- 13 Canuto, V. M., et al. (2004), Latitude-dependent vertical mixing and the tropical
14 thermocline in a global OGCM, *Geophysical Research Letters*, 31(16).
- 15 Carbotte, S. M. (2004), New Integrated Data Management System for Ridge2000 and
16 MARGINS Research, *Eos*, 85(51).
- 17 Conkright, M. E., et al. (2002), World Ocean Database 2001, Volume 1: Introduction, in
18 *NOAA Atlas NESDIS 42*, edited by S. Levitus, p. 159 pp., US Government Printing
19 Office, Washington, DC, Silver Springs, MD.
- 20 Dillon, T. M. (1982), Vertical Overturns - a Comparison of Thorpe and Ozmidov Length
21 Scales, *Journal of Geophysical Research-Oceans and Atmospheres*, 87(NC12), 9601-
22 9613.
- 23 Egbert, G. D., and R. D. Ray (2000), Significant dissipation of tidal energy in the deep
24 ocean inferred from satellite altimeter data, *Nature*, 405(6788), 775-778.
- 25 Egbert, G. D., and R. D. Ray (2001), Estimates of M-2 tidal energy dissipation from
26 TOPEX/Poseidon altimeter data, *Journal of Geophysical Research-Oceans*, 106(C10),
27 22475-22502.
- 28 Egbert, G. D., and R. D. Ray (2003), Semi-diurnal and diurnal tidal dissipation from
29 TOPEX/Poseidon altimetry, *Geophysical Research Letters*, 30(17), -.
- 30 Freilich, M. H. (1997), Validation of vector magnitude datasets: Effects of random
31 component errors, *Journal of Atmospheric and Oceanic Technology*, 14(3), 695-703.
- 32 Garrett, C., and E. Kunze (2007), Internal tide generation in the deep ocean, *Annual*
33 *Review of Fluid Mechanics*, 39, 57-87.
- 34 Gille, S. T., et al. (2000), Global correlation of mesoscale ocean variability with seafloor
35 roughness from satellite altimetry, *Geophysical Research Letters*, 27(9), 1251-1254.
- 36 Goff, J. A., and T. H. Jordan (1989), Stochastic Modeling of Seafloor Morphology - a
37 Parameterized Gaussian Model, *Geophysical Research Letters*, 16(1), 45-48.
- 38 Goff, J. A. (1991), A Global and Regional Stochastic-Analysis of near-Ridge Abyssal
39 Hill Morphology, *Journal of Geophysical Research-Solid Earth*, 96(B13), 21713-
40 21737.

1 Goff, J. A., and W. H. F. Smith (2003), A correspondence of altimetric gravity texture to
2 abyssal hill morphology along the flanks of the Southeast Indian Ridge, *Geophysical*
3 *Research Letters*, 30(24), -.

4 Goff, J. A., et al. (2004), The Contributions of Abyssal Hill Morphology and Noise to
5 Altimetric Gravity Fabric, *Oceanography*, 17(1), 24-37.

6 Jayne, S. R., and L. C. St Laurent (2001), Parameterizing tidal dissipation over rough
7 topography, *Geophysical Research Letters*, 28(5), 811-814.

8 Kantha, L. H. (1995), Barotropic tides in the global oceans from a nonlinear tidal model
9 assimilating altimetric tides. 1. Model description and results, *Journal of Geophysical*
10 *Research*, 100(C12), 25283-25308.

11 Knauss, J. A. (1997), *Introduction to physical oceanography*, 2nd ed., 309 pp., Prentice
12 Hall, Upper Saddle River, N.J.

13 Kunze, E., and S. G. Llewellyn Smith (2004), The Role of Small-Scale Topography
14 in Turbulent Mixing of the Global Ocean, *OCEANOGRAPHY*, 17(1), 55.

15 Laws, E. (1997), *Mathematical Methods for Oceanographers: An Introduction*, 343 pp.,
16 John Wiley, New York.

17 Ledwell, J. R., et al. (2000), Evidence for enhanced mixing over rough topography in the
18 abyssal ocean, *Nature*, 403(6766), 179-182.

19 Llewellyn Smith, S. G., and W. R. Young (2002), Conversion of the barotropic tide,
20 *Journal of Physical Oceanography*, 32(5), 1554-1566.

21 Lonsdale, P. (1977), Deep-Tow Observations at Mounds Abyssal Hydrothermal Field,
22 Galapagos Rift, *Earth and Planetary Science Letters*, 36(1), 92-110.

23 Macdonald, K. C. (1982), Mid-Ocean Ridges - Fine Scale Tectonic, Volcanic and
24 Hydrothermal Processes within the Plate Boundary Zone, *Annual Review of Earth and*
25 *Planetary Sciences*, 10, 155-190.

26 Macdonald, K. C., and B. P. Luyendyk (1985), Investigation of Faulting and Abyssal Hill
27 Formation on the Flanks of the East Pacific Rise (21-Degrees-N) Using Alvin, *Marine*
28 *Geophysical Researches*, 7(4), 515-535.

29 Macdonald, K. C., et al. (1988), A New View of the Mid-Ocean Ridge from the Behavior
30 of Ridge-Axis Discontinuities, *Nature*, 335(6187), 217-225.

31 Macdonald, K. C., et al. (1996), Volcanic growth faults and the origin of Pacific abyssal
32 hills, *Nature*, 380(6570), 125-129.

33 MathWorks, T. (2007), MATLAB, edited, The MathWorks, Natick, MA.

34 Menard, H. W. (1967), Sea Floor Spreading Topography and Second Layer, *Science*,
35 157(3791), 923-&.

36 Morgan, P., and L. Pender (2003), SEAWATER A Library of MATLAB Computational
37 Routines for the Properties of Seawater, edited, CSIRO Marine Research.

38 Munk, W. (1966), Abyssal Recipes, *Deep-Sea Research Part I-Oceanographic Research*
39 *Papers*, 13, 707-730.

40 Munk, W., and C. Wunsch (1998), Abyssal recipes II: energetics of tidal and wind
41 mixing, *Deep-Sea Research Part I-Oceanographic Research Papers*, 45(12), 1977-
42 2010.

43 Nash, J. D., et al. (2007), Hotspots of deep ocean mixing on the Oregon continental slope,
44 *Geophysical Research Letters*, 34(1), -.

45 NGDC (2005), GEODAS, edited.

1 Osborn, T. R. (1980), Estimates of the Local-Rate of Vertical Diffusion from Dissipation
2 Measurements, *Journal of Physical Oceanography*, 10(1), 83-89.
3 Osborn, T. R., and C. S. Cox (1972), Oceanic fine structure, *Geophys. Fluid Dyn.*,
4 3(321-345).
5 Polzin, K. L., et al. (1997), Spatial variability of turbulent mixing in the abyssal ocean,
6 *Science*, 276(5309), 93-96.
7 Small, C., and D. T. Sandwell (1992), An Analysis of Ridge Axis Gravity Roughness and
8 Spreading Rate, *Journal of Geophysical Research-Solid Earth*, 97(B3), 3235-3245.
9 Smith, W. H. F. (1993), On the Accuracy of Digital Bathymetric Data, *Journal of*
10 *Geophysical Research-Solid Earth*, 98(B6), 9591-9603.
11 Smith, W. H. F., and D. T. Sandwell (1997), Global sea floor topography from satellite
12 altimetry and ship depth soundings, *Science*, 277(5334), 1956-1962.
13 Smith, W. H. F. (1998), Seafloor Tectonic Fabric From Satellite Altimetry, *Annual*
14 *Review of Earth and Planetary Sciences*, 26(1), 697-747.
15 Smith, W. H. F., and D. T. Sandwell (2004), Conventional Bathymetry, Bathymetry from
16 Space, and Geodetic Altimetry *Oceanography*, 17(1), 8-23.
17 Smith, W. H. F. (2005), Personal Communication, edited.
18 St Laurent, L., and C. Garrett (2002), The role of internal tides in mixing the deep ocean,
19 *Journal of Physical Oceanography*, 32(10), 2882-2899.
20 Swift, J. (2007), CCHDO, edited.
21 Toole, J. M., et al. (1997), Near-boundary mixing above the flanks of a midlatitude
22 seamount, *Journal of Geophysical Research-Oceans*, 102(C1), 947-959.
23 Wessel, P., and W. H. F. Smith (1995), New Version of the Generic Mapping Tools
24 Released, *EOS*.
25
26

1 Figure Captions

2

3 Figure 1 Critical slope derived from temperature and salinity data [*Conkright et al.*, 2002]
4 interpolated and extrapolated to the bottom of the ocean. Black contour marks 3000 m
5 depth. The WOCE P16 line along 150W is also shown.

6

7 Figure 2 (a) Distribution of single beam depth profiles from 4900 cruises collected over
8 the past 40 years and archived at the National Geophysical Data Center. We have hand-
9 edited these data to remove blunders and outliers. (b) Distribution of single beam (black)
10 and multi-beam echo soundings (red) in the North Atlantic. Gray box shows area where
11 single beam, multibeam, and satellite bathymetry measurements were compared. (c)
12 Multibeam grid (500 m cell size) over the mid-Atlantic Ridge and Atlantis Fracture Zone.
13 Track lines are the single beam or center beam coverage used to relate 2-D gradients to 1-
14 D slopes.

15

16 Figure 3 Seafloor depth (top) and along-track slope (bottom) along the trackline of a
17 typical cruise near the Mid-Atlantic Ridge (MAR). Multibeam data were sampled from a
18 grid having 500 m cell spacing and represent the "true" depth and slope. Single beam data
19 were filtered and processed along track to best match the multibeam profile. This version
20 of satellite bathymetry was not forced to agree with available soundings so is
21 representative of the accuracy in areas having no shipboard coverage. The *rms*
22 differences are: single beam depth 48.4 m; satellite bathymetry 190.8 m; single beam
23 slope .066 m/m; multibeam slope .089 m/m.

1

2 Figure 4 Cumulative histograms of the absolute value of the seafloor slope along the
3 trackline from the three measurement systems. 30% of the multibeam and single beam
4 slopes exceed 0.1 m/m, while only 2% of satellite bathymetry slopes exceeds 0.1 m/m.

5

6 Figure 5 Magnitude of along-track slope of the seafloor from single beam data (Figure 1,
7 bottom) versus magnitude of gradient vector at the same locations from a 500-m
8 multibeam grid. Theoretically the 1-D slope should be less than or equal to the 2-D
9 gradient.

10

11 Figure 6 Mean slope of the seafloor filtered with a 60-km Gaussian filter and interpolated
12 on a 0.5° grid. Contour line at 3000 m depth highlights the deep ocean basins and shows
13 the ridges are not as steep. Mean slope commonly exceeds 0.05 m/m on the flanks of the
14 seafloor spreading ridges, especially the ridges spreading at a rate of < 70 mm/yr.

15

16 Figure 7 Fraction of seafloor having slope exceeding the critical slope for depth > 2000
17 m. (a) Fraction derived from single beam soundings. (b) Fraction derived from satellite
18 bathymetry [Smith and Sandwell, 1997, V8.2].

19

20 Figure 8 Area of seafloor with above critical slope as a function of depth. Thick curve is
21 from single beam data while the thin curve is from satellite bathymetry. Seafloor slopes
22 from satellite bathymetry clearly underestimate supercritical area with depth < 2000 m.
23 The critical slope calculation is unreliable for shallow depths < 2000 m.

1

2 Figure A1a) Scatter plot of critical slope calculated from WOA and P16 cruise data.

3

4 Figure A1b) Meridional plot of critical slope calculated from WOA and P16 cruise data.

5

6 Figure A2 Histograms of the magnitude of the slope (blue) and gradient (red) for the data

7 shown in Figure 5. The theoretical histogram for a Rayleigh distribution with a mean

8 slope of 0.152 m/m provides an adequate fit to the actual gradient distribution. Mapping

9 the gradient distribution into slope distribution provides an adequate fit to the actual slope

10 distribution. The mean value of the theoretical slope distribution is $2/\pi$ times the mean

11 value of the gradient distribution.

12

Figure 1)

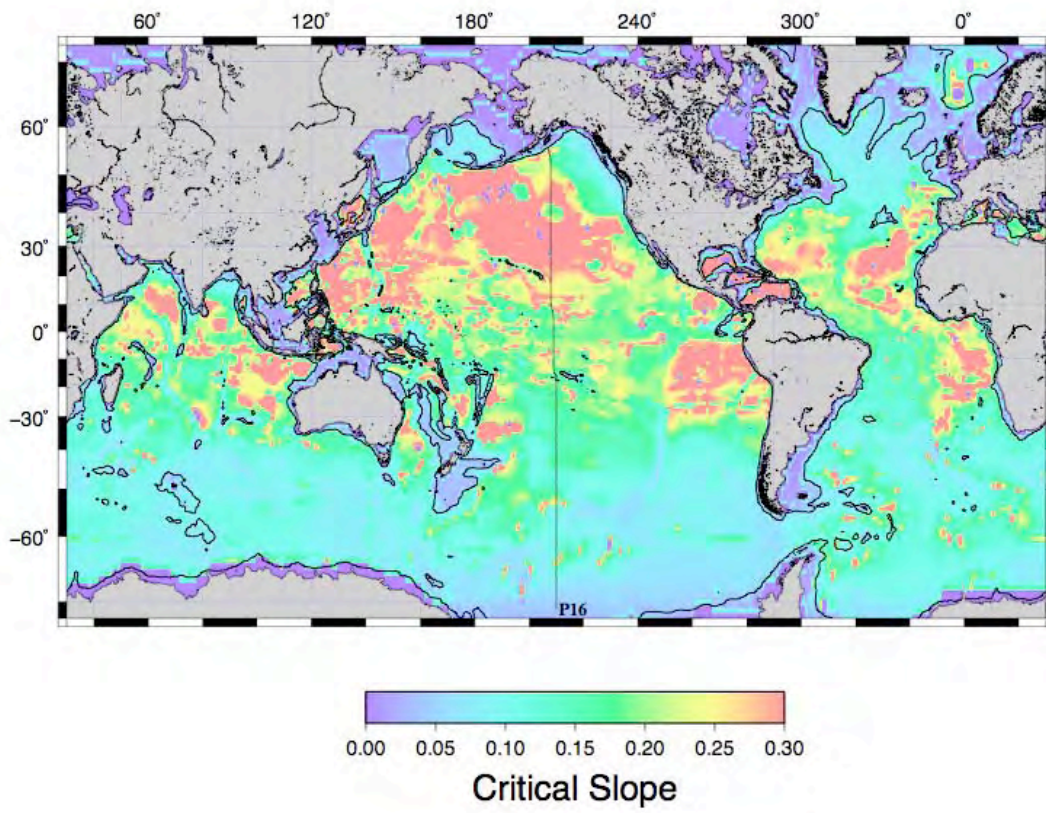


Figure 2a)

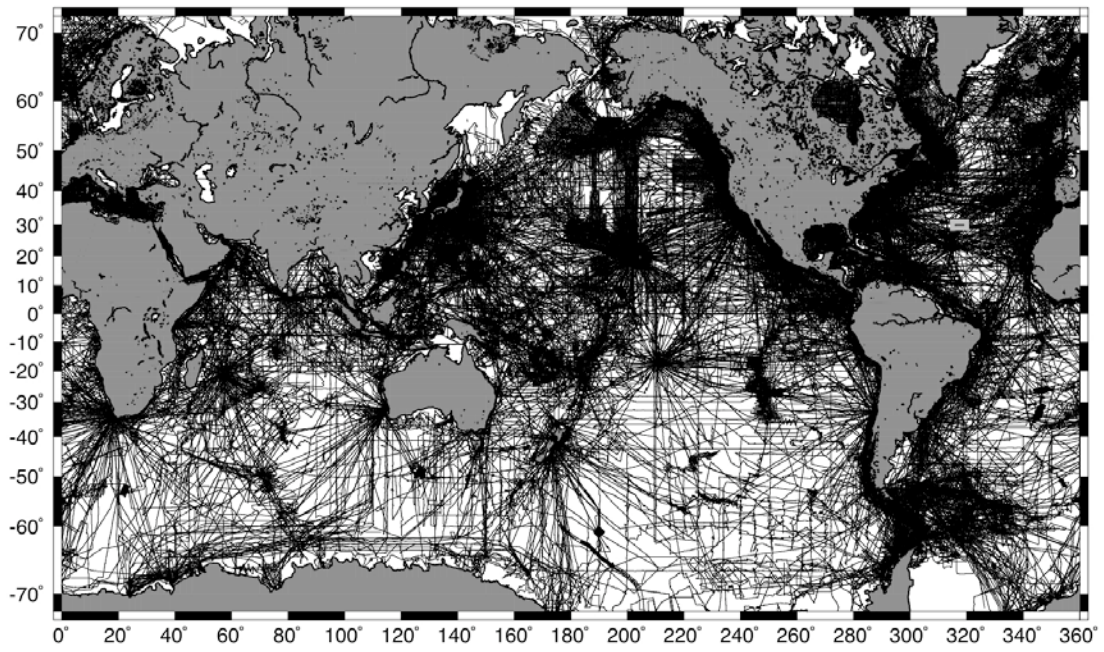


Figure 2b)

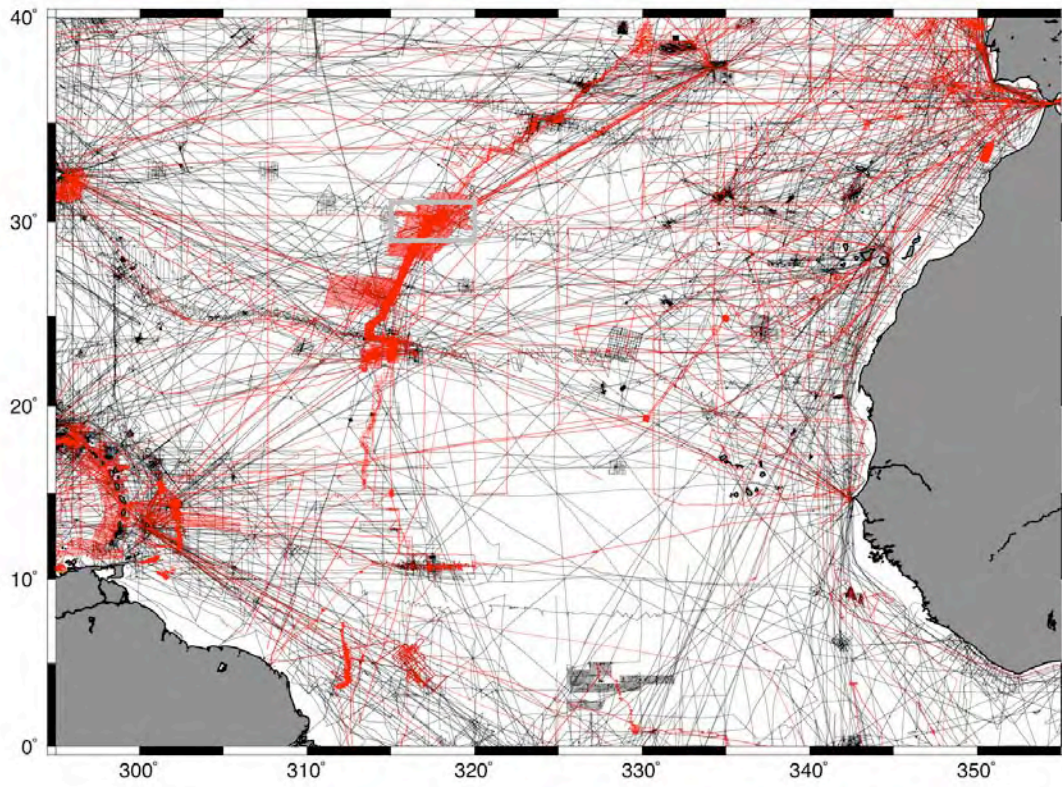


Figure 2c

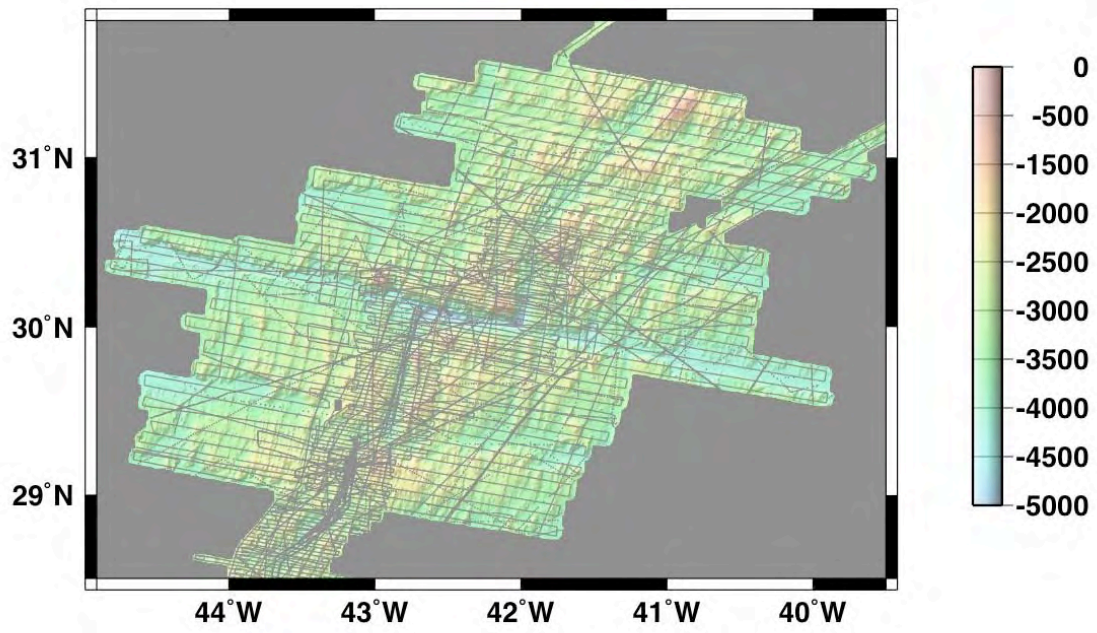


Figure 3)

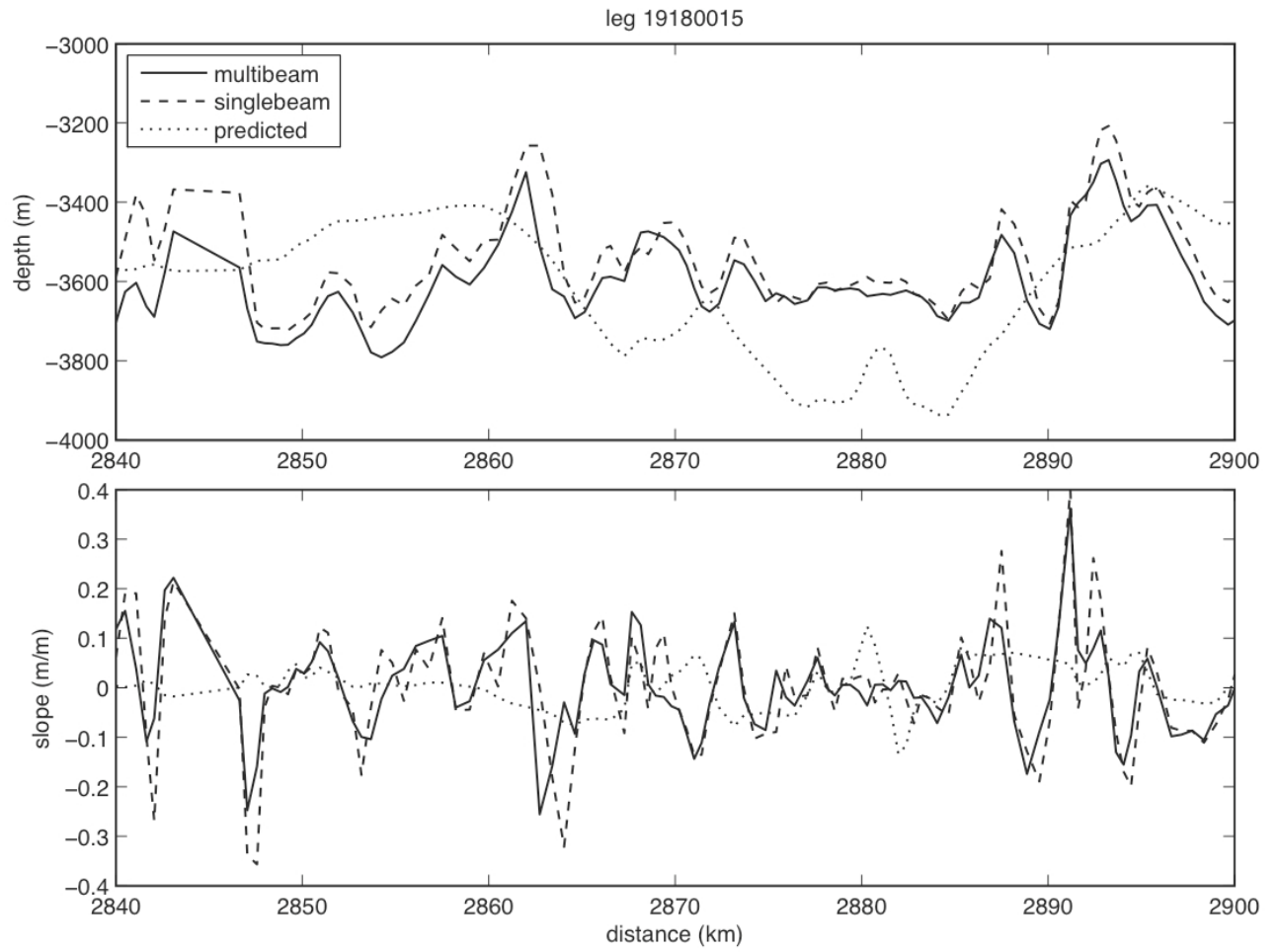


Figure 4)

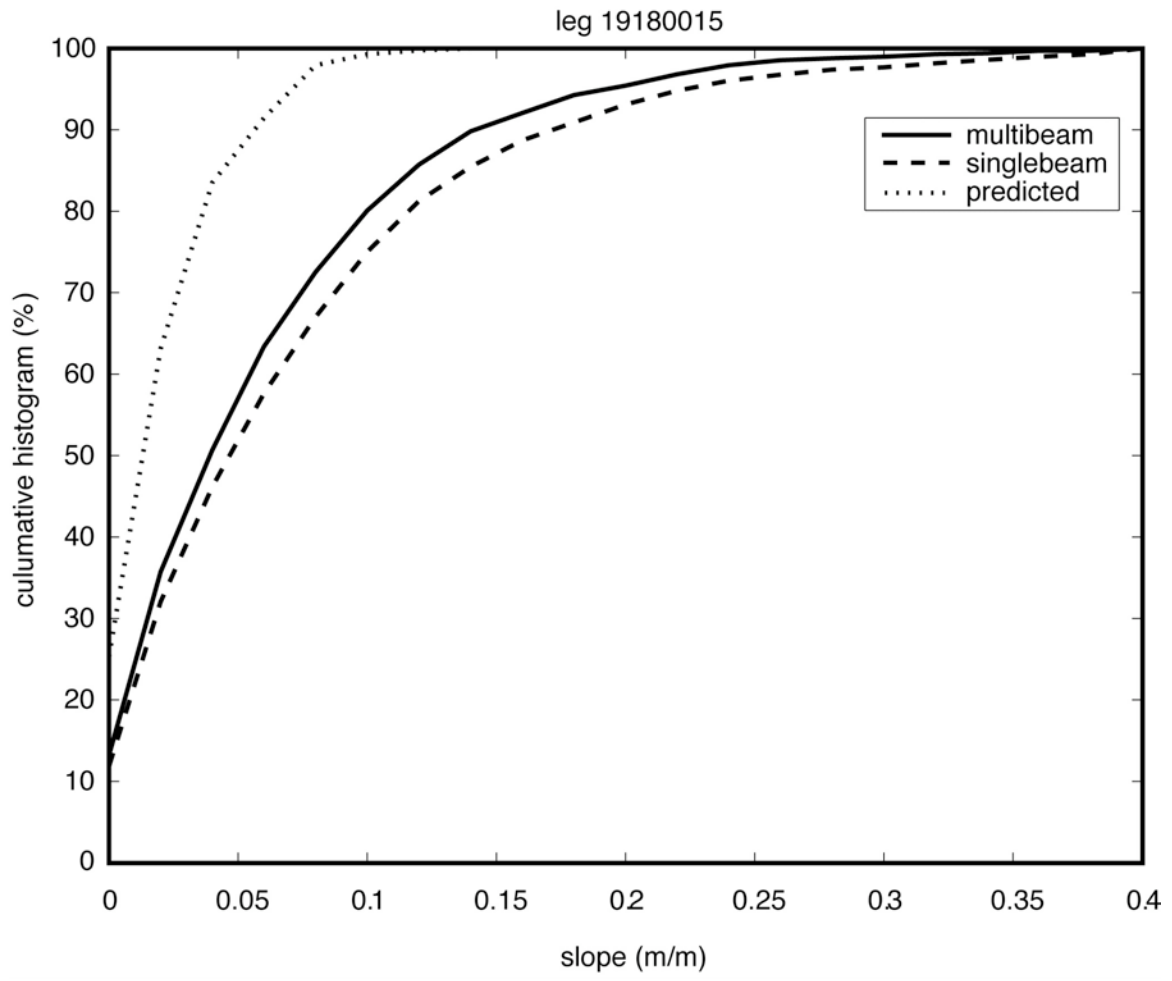


Figure 5)

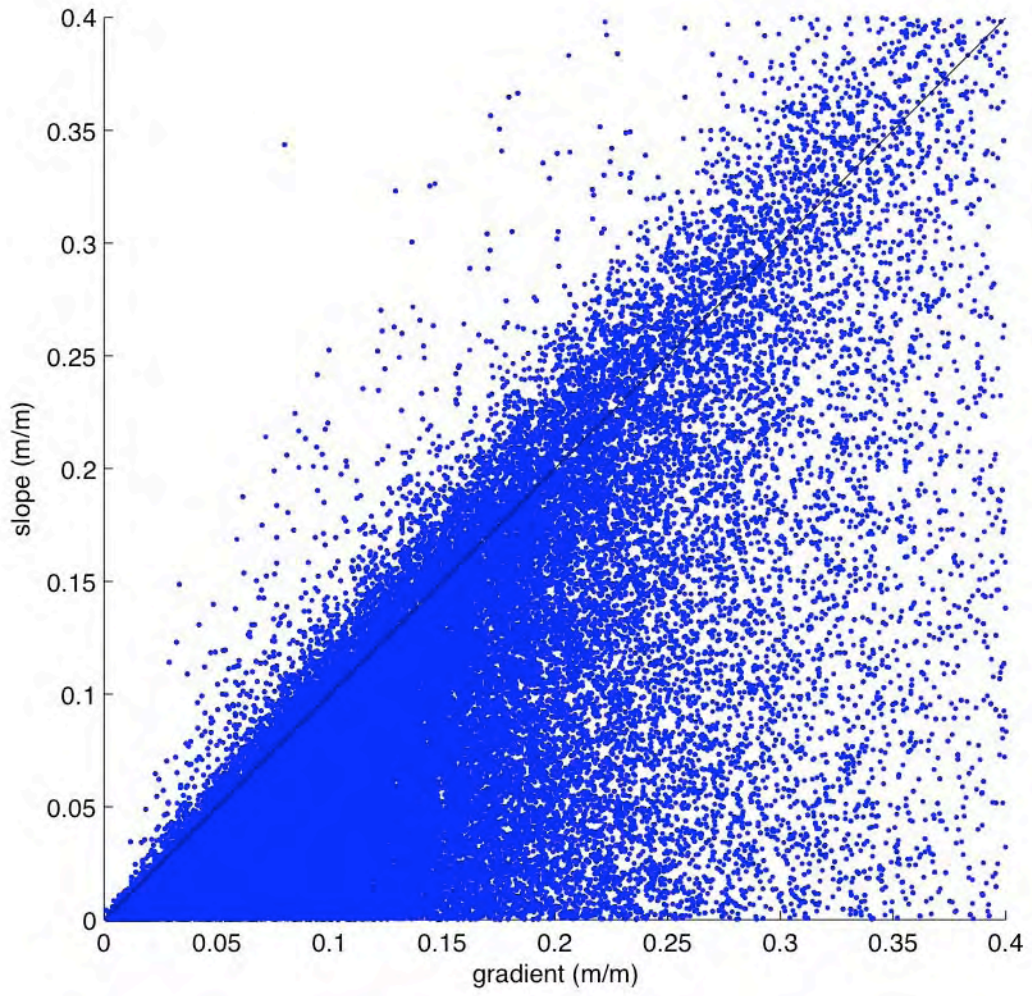


Figure 6)

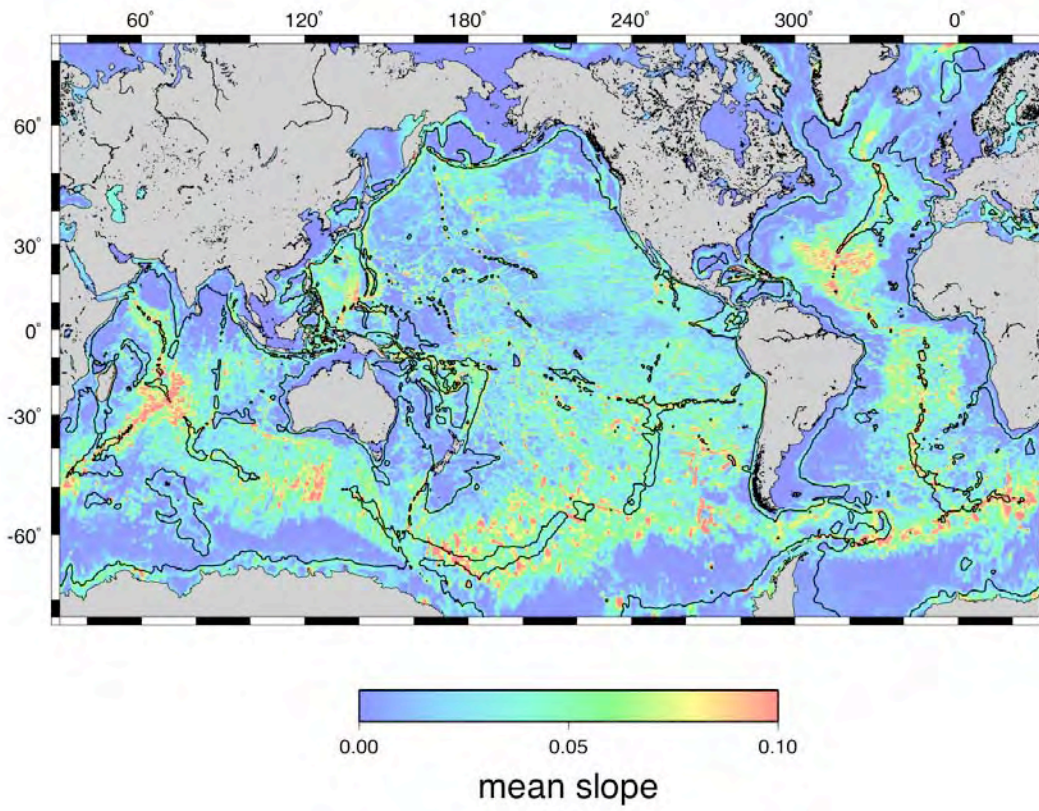


Figure 7a)

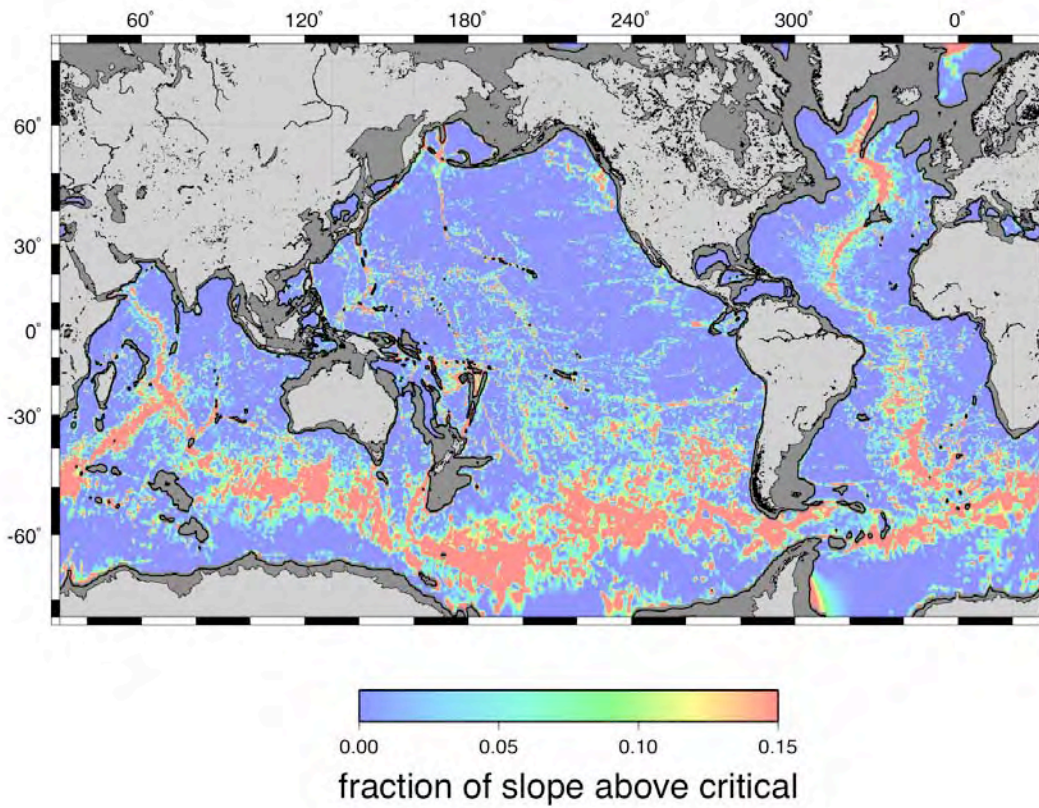


Figure 7b)

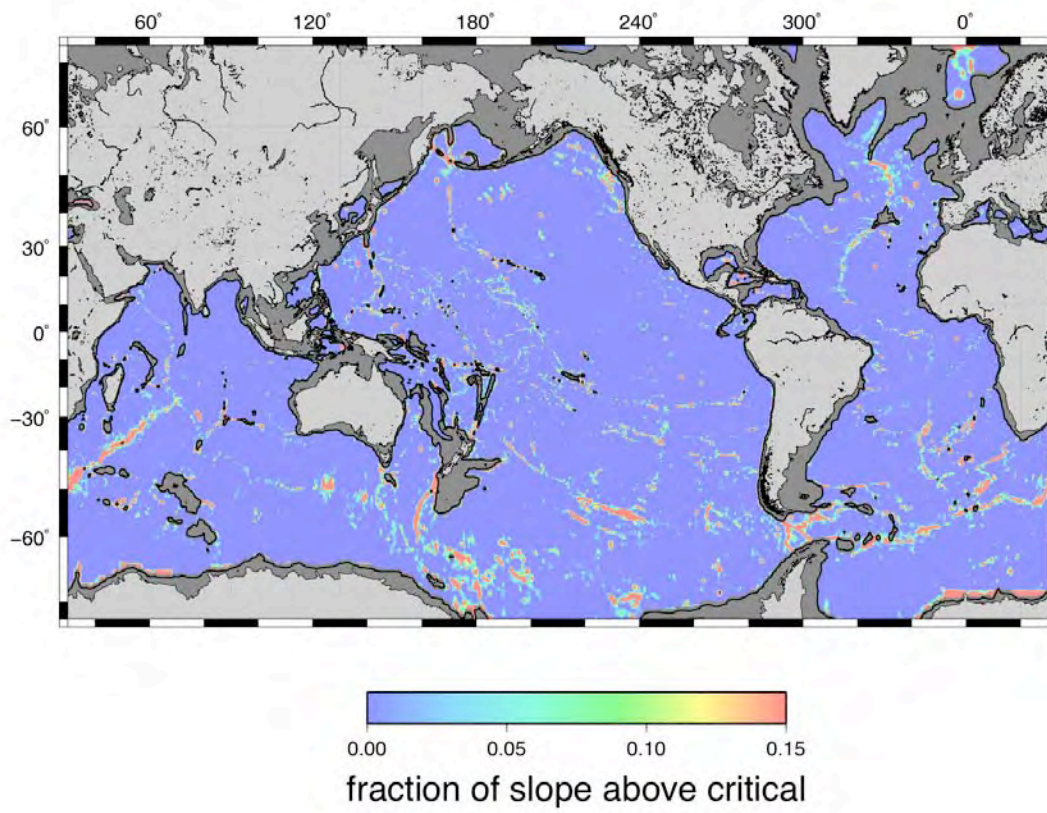


Figure 8)

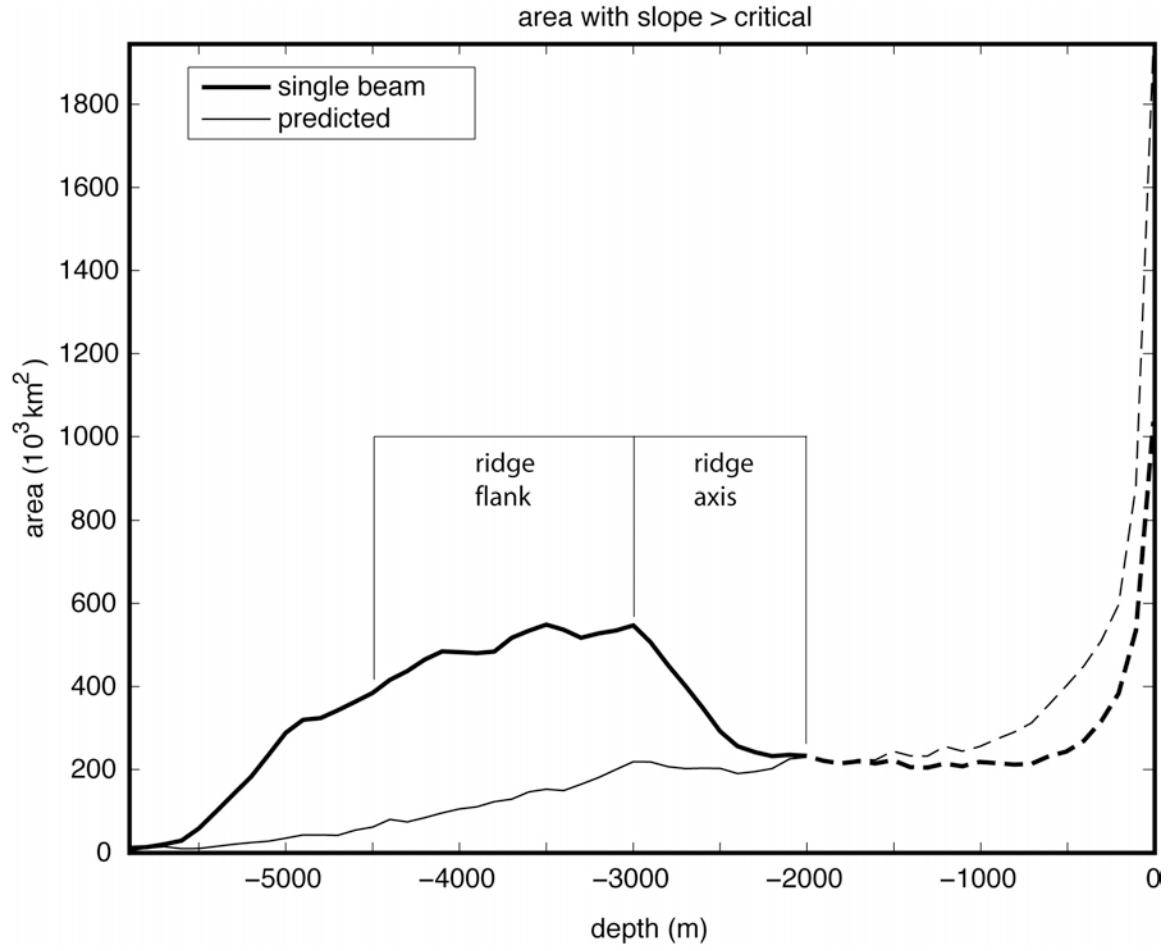


Figure A1a)

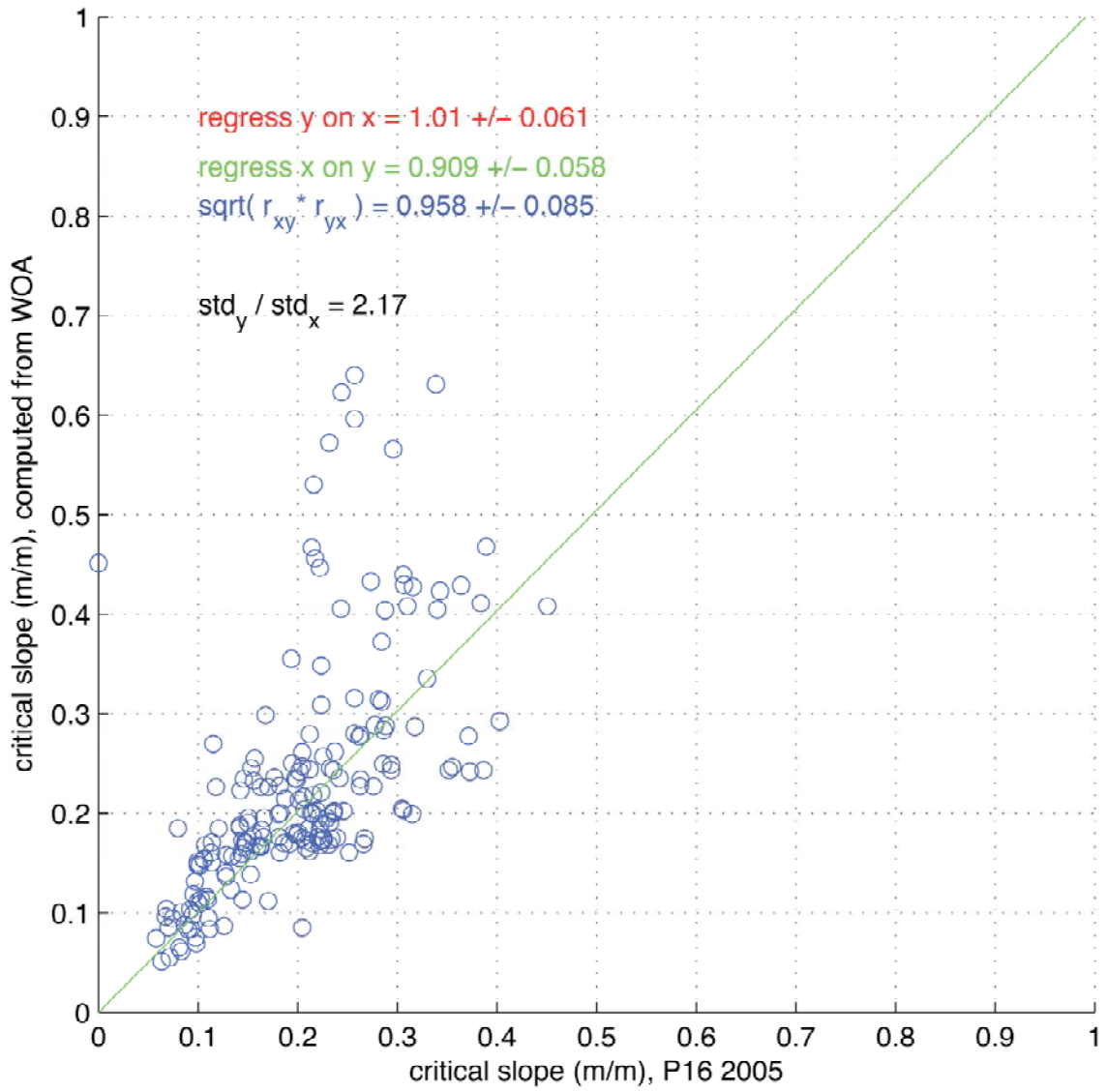


Figure A1b)

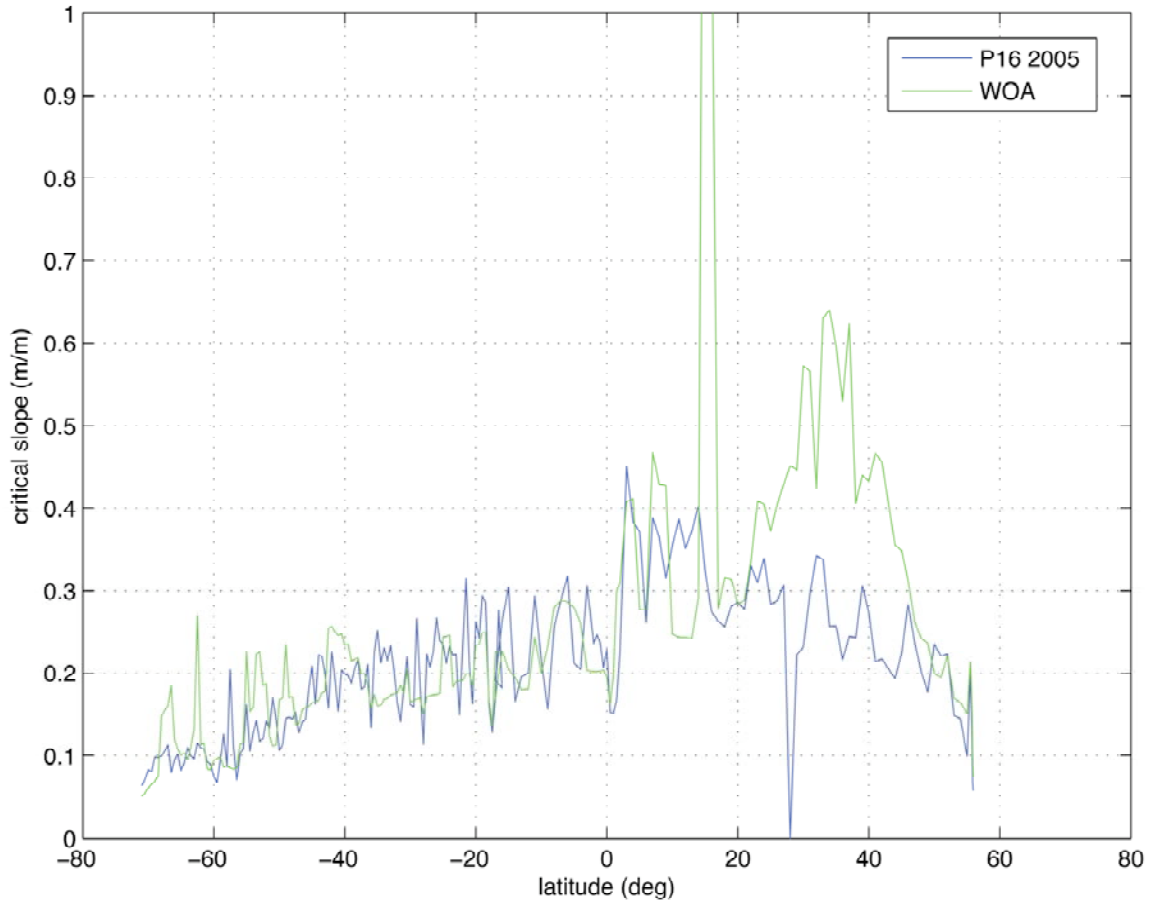


Figure A2)

